



This is to certify that the

dissertation entitled "A STUDY OF DIRECT PHOTON PRODUCTION AT THE CERN INTERSECTING STORAGE RINGS"

presented by

Carlos Walter Salgado-Galeazzi

has been accepted towards fulfillment of the requirements for

Ph.D. degree in Physics

Bernard G Pope

Major professor

Prof. B. G. Pope

Date August 3 1988



RETURNING MATERIALS:
Place in book drop to
remove this checkout from
your record. FINES will
be charged if book is
returned after the date
stamped below.

A STUDY OF DIRECT PHOTON PRODUCTION AT THE CERN INTERSECTING STORAGE RINGS

bу

Carlos Walter Salgado-Galeazzi

A DISSERTATION

Submitted to

Michigan State University

in partial fulfillment of the requirements

for the degree of

DOCTOR OF PHILOSOPHY

Department of Physics and Astronomy
1988

ABSTRACT

A STUDY OF DIRECT PHOTON PRODUCTION AT THE CERN INTERSECTING STORAGE RINGS

bу

Carlos Walter Salgado-Galeazzi

A measurement of direct photon production at high p_T from proton-proton collisions at the CERN ISR center of mass energy of \sqrt{s} = 63 GeV is reported. Arrays of lead glass calorimeters and multiwire proportional chambers were used as photon detectors. A single photon signal was extracted using a newly developed direct identification method. Backgrounds due to neutral meson decays were corrected by Monte Carlo simulation of the detector. Data for the direct photon cross section are presented in the transverse momentum range of 4.5 to 10 GeV/c and compared with QCD predictions. Constraints on the gluon properties of the nucleon and the QCD scale parameter $\Lambda_{\overline{MS}}$ are provided.

By using the lead glass arrays in conjunction with a drift chamber barrel detector inside a superconducting solenoid, accompanying charged particles were studied. The ratio of the number of positive to negative charged particles in the opposite side hemisphere and azimuthal distributions of accompanying particles are also presented.

ACKNOWLEDGEMENTS

I would like to thank my supervisor Prof. Bernard G. Pope for all these years of support and continued guidance. I am truly thankful to Prof. Pope and to Prof. James T. Linnemann for innumerable weekly meetings that made this research possible.

I would also like to thank the R110 collaborators that, while at CERN, introduced me to the experiment and the ISR environment. Especially, Drs. Leslie Camilleri, Hans-Jurgen Besch, Christoph Von Gagern, Timothy Cox and David Hanna. My stay in Geneva would not have been as pleasant without Mlle. Marie-Anne Huber's friendly support and excellent secretarial skills.

I thank Dr. Stuart Stampke for his critical review of this research and his analysis of the η^o data, and Mr. Bjorn Nilsen for his help with the EGS runs. I am very thankful to my office and Geneva apartment-mate Mr. Boyce Humphries for many discussions over particular and general physics topics. Thanks to Dr. P. Aurenche for providing us with programs to calculate the 2nd. order QCD predictions for the direct photon cross section.

My friend Dr. Felix Marti made possible my arrival to Michigan State University. To him and his family (Elida and Sergio) that became part of my family during these years, I am truly thankful.

"Muchas Gracias" to my wife Nayda M. Flores for her support and help during these last stressful years of analysis and thesis writing, and to my son Sebastian Carlos for providing much happiness.

TABLE OF CONTENTS

	Page
LIST (OF TABLESvii
LIST	OF FIGURESvii:
Chapter	· I INTRODUCTION.
I-1.	General Overview
I-2.	The R110 Experiment 2
I-3.	Brief Introduction to High p_T Physics 4
	Direct Photon Production at High p _T 11
	Overview of Experimental Techniques Used to
	Detect Direct Photons
Chapter	· II ACCELERATOR AND EXPERIMENTAL APPARATUS.
II-1.	The Intersecting Storage Rings (ISR) 35
II-2.	The I1 Intersection
11-3.	Apparatus Overview44
11-4.	The Solenoid
II-5.	The Drift Chambers
II-6.	The Back Lead Glass Arrays 55
II-7.	The Front Lead Glass Arrays 57
II-8.	The Shower Counters 59
11-9.	The Strip Chambers
TT-10	The Scintillators 64

Chapter III. - DATA TAKING.

III-1.	Control Room
III-2.	Calibrations
III-3.	Trigger Logic
III-4.	On-line Programs
III-5.	The Data 78
Chapter	· IV BASIC DATA ANALYSIS.
IV-1.	Overview of the Basic Analysis 82
IV-2.	Clustering in the Back Glass Arrays 81
IV-3.	Track Finding Algorithm 87
IV-4.	Energy Corrections 87
IV-5.	DSTing and B-Vetoing90
IV-6.	The B-veto Cut
IV-7.	General Cuts
IV-8.	Strip Chamber Clustering Algorithm100
Chapter	V SEARCH FOR A DIRECT PHOTON SIGNAL.
V-1.	Introduction111
V-2.	Further Strip Chambers Cuts112
V-3.	Search for a Variable to Distinguish
	Single from Multiphoton Showers Among the
	Trigger Clusters121
V-4.	The Main Method of Strip Chamber Analysis130
V-5.	Simulated Neutral Meson Decays137
V-6.	The B-veto Simulation140
V-7.	Simulated Single Photons149
v-8.	Simulated Single and Multiphoton
	o _t Distributions150
V-9.	A Front/All cut

V-10. Fits to the σ_t Distributions
V-11. Corrections to the Direct Photons Observed16
V-12. Statistical Errors173
Chapter VI RESULTS AND CONCLUSIONS.
VI-1. Fraction of Single Photons17
VI-2. Direct Photon to π° -meson and Direct Photon
to Neutral Meson Ratios19
VI-3. Direct Photon Cross Section192
VI-4. Systematic Errors199
VI-5. Comparison with QCD Predictions and with
Other Experiments204
VI-6. Direct Photon Event Correlations215
VI-7. Subtraction of the Neutral Meson Background216
VI-8. Estimation of Other Backgrounds22
VI-9. Charged Particle Distributions22
VI-10. Away Side Studies228
VI-11. Summary and Conclusions229
APPENDIX A: Single Photon Background from Neutral
Meson Decays233
APPENDIX B: Neutral Meson Decay Kinematics236
APPENDIX C: Shower Simulations (EGS Monte Carlo)248
APPENDIX D: Neutral Meson Decay Monte Carlo256
APPENDIX E: The η° Trigger Data261
LIST OF REFERENCES 26

LIST OF TABLES

		Page
Table	I-1:	Direct Photon Experiments 33
Table	III-1:	Data. Luminosities and Data Sets 79
Table	III-2:	Data. Condensed Tapes 80
Table	V-1 :	Cut Efficiencies141
Table	V-2 :	Values of the Parameters in the
		B-veto Simulation146
Table	VI-1:	Inside and Outside Values of the
		Parameters Used to Calculated the
		Cross Sections, Y/all and Y/ π° 190
Table	VI-2:	Results for the Inside Trigger193
Table	VI-3:	Results for the Outside Trigger193
Table	VI-4:	Final Error-Weighted Average Results of
		the Cross Sections, Y/all and Y/ π° 194
Table	A-1:	Neutral Meson Decays234
Table	C-1:	EGS4 runs254
Table	D-1:	Values of the Simulated Cut
		Acceptances in the Neutral Meson
		Decay Monte Carlo

LIST OF FIGURES

			Page
Figure	I-1	:	Hadron Scattering Kinematics 7
Figure	I-2.	a:	A) Drell-Yan process. B) First Order
			QCD corrections to Drell-Yan 13
Figure	I-2.	b:	Leading-order, quark-antiquark and
			quark-gluon QCD subprocesses 13
Figure	I-3	:	QCD Leading Order Diagrams for
			Direct Photon Production 14
Figure	I-4	:	Kinematics of Direct Photon
			Production A + B \rightarrow Y + X
Figure	I-5	:	Some Higher Order QCD Contributions
			to Direct Photon Production. a) Real
			Emission Diagrams to the Compton and
			b) the Annihilation. c) Virtual
			Corrections to Compton
Figure	I-6	:	Renormalization and Factorization
			Scheme Dependence of the Second
			Order QCD Direct Photon Cross Section. 24
Figure	I-7	:	Kinematics of Two-body Parton
			Scattering 26
Figure	I-8	:	Two-photon production diagrams 28
Figure	I-9	:	The Conversion Method
Figure	II-1	:	ISR Layout 36
Figure	II-2	:	Vacuum Pipe Cross Sectional View
			and Beam Density Profile 38
Figure	II-3	:	Rate vs Beam Displacement 40
Figure	II-4	:	I1 Intersection Layout 42
Figure	11-5	:	Overview of the R110 Apparatus in
			the Direct Photon Trigger Position 45
Figure	II-6	:	Sextant Definition
Figure	II-7	:	System of Coordinates

Figure	II-8 :	Coil Cross-sectional View 48
Figure	II-9 :	Drift Chamber Sector Assembly 51
Figure	II-10 :	Drift Chamber Cross-sectional View 52
Figure	II-11 :	Back Lead Glass Array 56
Figure	II-12 :	Front Lead Glass Array 58
Figure	II-13 :	Strip Chambers Cross-sectional View 62
Figure	II-14 :	Strip Chamber Layout 63
Figure	II-15 :	Position of MM Scintillators 67
Figure	III-1 :	Flow Chart of the Trigger Logic 75
Figure	IV-1 :	Flow Chart of the Analysis
Figure		View of the Apparatus91
•	IV-3 :	Geometry of the B Cut
Figure		B Counter Pulse Heights
Figure		Δz Differences in the B Counters 93
Figure	IV-6 :	Vertex Positions (Diamond) 96
Figure	IV-7 :	NaI Trigger Cut
Figure	IV-8 :	ΔY vs. ΔZ, Differences Between Charged
		Particle Hits and Trigger Position on
		the Back Glass Array 99
Figure	IV-9 :	Angular Correction to the Observed
		Front/All Ratio101
Figure	IV-10:	F/ALL Distributions for Various Δp_T
		Ranges in the Direct Photon Trigger.
		All Events and Events with Front/All
		Greater than 0.02102
Figure	IV-11:	Number of Clusters per Event in the
		Strip Chambers103
Figure	IV-12:	Gap Determination. Number of Clusters
		vs. Separation Between Two Charged
		Particle Hits in the Back Glass Array.104
Figure	IV-13:	Total Pulse Heights of Strip
		Chamber Clusters106

Figure	IV-14:	Widths (or Span) of Strip
		Chamber Clusters107
Figure	IV-15:	Pulse Height per Strip109
Figure	IV-16:	Variations Across the Chamber110
Figure	V-1 :	(Mean Pulse Height in Window)/w vs.
		Window Size (w) for the η° and Direct
		Photon Triggers114
Figure	V-2 :	Number of Strips per Cluster vs.
		Window Size (w) for the η^{0} and Direct
		Photon Triggers114
Figure	V-3 :	Half-Width at Half-Maximum of the
		Diff=(PHY-1.75.PHZ)/(PHY+1.75.PHZ)
		Distribution vs. Window Size (w) for
		the η^{0} and Direct Photon Triggers115
Figure	V-4 :	Distribution of the Differences
		Between Cluster and Shower Positions
		for the Direct Photon Trigger Data116
Figure	V-5 :	Distribution of the Differences
		Between Cluster and Shower Positions
		for the η^{o} Trigger117
Figure	V-6 :	Total Pulse Height of Clusters
		Inside a w= \pm 20 cm Window119
Figure	V-7 :	Total Pulse Height of Clusters
		Inside a w= \pm 5 cm Window120
Figure	v-8 :	Distribution of the Ratio
		Diff=(PHY-1.75.PHZ)/(PHY+1.75.PHZ)122
Figure	V-9 :	Fraction of Clusters in the Y and Z
		Views Inside the Matching Window for
		the Direct Photon Trigger Data123
Figure	V-10:	Fraction of Clusters in the Y and Z
		Views Inside the Matching Window for
		the η^{o} Trigger124
Figure	V-11:	Standard Deviation of Clusters Inside
		the Matching Window126

Figure	V-12:	Moments Method127
Figure	V-13:	Distance Between Photons vs. Asymmetry
		in Simulated π^{0} Decays and the
		Asymmetry Distribution ($\Delta p_T = 4.5-10$
		GeV/c)129
Figure	V-14:	o _t Distributions for Direct Photon
		Trigger Data at Various p _T bins for the
		Inside and Outside Triggers131
Figure	V-15:	$\sigma_{_{f V}}$ and $\sigma_{_{f Z}}$ Distributions for Direct
		Photon Trigger Data132
Figure	V-16:	Criterion of Limit Selection134
Figure	V-17:	Strip Chamber Analysis Flow Chart.
Figure	V-18:	$\frac{\Upsilon}{\Upsilon\Upsilon}$ mesons vs. p_T from the Neutral
		Meson Decay Monte Carlo135
Figure	V-19:	Probability of Observing a Shower in
		the Strip Chamber vs. Energy139
Figure	V-20:	Probability "tree" of the B-veto
		Logic without Associated Particles142
Figure	V-21:	Probability "tree" of the B-veto
		Logic with Associated Particles144
Figure	V-22:	Gatti-Mathieson Image Charge
		Distribution in λ Bins of 0.1152
Figure	V-23:	Mean of the σ_t Distributions vs.
		Energy for Single Photons from the
		η^{0} Trigger and Simulation155
Figure	V-24:	Maxima of the σ_{t} Distributions vs.
		Energy for Single Photons from the
		η^{o} Trigger and Simulation155
Figure	V-25:	Mean Pulse Height vs. Energy for
		Single Photons from the η^{o} Trigger
		and Simulation156
Figure	V-26:	Front/All vs. ot for the Direct
		Photon Trigger Data160
Figure	V-27:	Front/All distribution for 4 GeV EGS
		Electron Initiated Shower Simulation
		and A Cay Flantson PS Test Data 161

rigure V-28:	Front/All Distributions for the Direct
	Photon Data and EGS Simulation in the
	Range Δp _T = 4.5-5 GeV/c162
Figure V-29:	Front/All Distributions for Simulated
	Single Photons165
Figure V-30:	Front/All Distributions for Simulated
	Multiphotons166
Figure V-31:	Front/All Distributions for the Direct
	Photon Data and EGS Simulation in the
	Range Δp _T = 4.5-5 GeV/c After Rebalance
	of Front and Back167
Figure V-32:	C_{γ} Distributions for the p_{T} Bins of the
	Inside and Outside Triggers175
Figure VI-1:	Non-smeared σ_{t} Distributions for the
	Inside Trigger Single and Multiphoton
	Simulations, Direct Photon Trigger
	Data and Likelihood Fit for Various
	p _T (C.M.) Bins178
Figure VI-2:	Non-smeared o _t Distributions for the
	Outside Trigger Single and Multiphoton
	Simulations, Direct Photon Trigger
	Data and Likelihood Fit for Various
	p _T (C.M.) Bins180
Figure VI-3:	σ _t Distributions for the Inside Trigger
	Single and Multiphoton Simulations,
	Direct Photon Trigger Data and
	Likelihood Fit for Various p_{T} (C.M.)
	Bins183
Figure VI-4:	ot Distributions for the Outside Trigger
	Single and Multiphoton Simulations,
	Direct Photon Trigger Data and
	Likelihood Fit for Various $p_{\overline{T}}$ (C.M.)
	Bins186
Figure VI-5:	Ratio of Smeared to Non-smeared Versions

	of the	Direct Photon Cross Sections as
	Function	n of p _T (C.M.)189
Figure VI-	6: Y/all V	ersus p _T (C.M.)195
Figure VI-	7: Υ/π° Ve	rsus p _T (C.M.)196
Figure VI-		Photon Invariant Cross Section
	for the	Inside and Outside Triggers
	and the	ir Ratio198
Figure VI-	9: Direct	Photon Invariant Cross Section
	Compare	d with other ISR Experiments200
Figure VI-	10: Ratios	between Direct Photon Cross
	Section	s Measured in Other Experiments
		0205
Figure VI-	11: p _T ^{4.91} E	$\frac{do}{d^3p}$ vs. x_T , for Experiments
		A70 and R110207
Figure VI-	12: Gluon S	tructure Functions for the
	Duke an	d Owens [DUK84] Set I and II209
Figure VI-	13: Measure	d Direct Photon Cross Section
	Compare	d with QCD Predictions by
	Aurench	e et al. [AUR88]210
Figure VI-	14: Measure	d Direct Photon Cross Section
	Compare	d with QCD Predictions by
		uris et al. [ARG87]212
Figure VI-	$15: p_{T}^{6} \cdot E \cdot \frac{do}{d^{3}}$	vs. x _T , for Different QCD
		ions and Experimental Results
	for R80	6, R108 R110213
Figure VI-	16: "All" (Direct Photon + Neutral Mesons)
	Invaria	nt Cross Section vs. p _T (C.M.)
	for Exp	eriment R108 and R110214
Figure VI-	17: Represe	ntation of the o _{cut} for the
	Extract	ion of a Direct Photon Sample
	and Cor	rection of the Neutral Meson
	Backgro	und218
Figure VI-	18: Signal-	to-Noise Ratios vs. p _T for
	Various	Values of ocut
Figure VI-	19: Values	of θ vs. σ _{cut} 221
Figure VI-	20: Azimuth	al Distributions of Associated

	Particles for the Enriched Photon and
	Neutral Meson Samples in the $p_{\overline{T}}$ Trigger
	Range 4.5-6 GeV for Three Different
	p _{T track} Ranges226
Figure VI-21:	Azimuthal Distributions of Associated
	Particles for the Direct Photon and
	Neutral Meson Samples (After Background
	Extraction) for p_T Trigger Greater
	than 6 GeV and for Three Different
	p _{T track} Ranges227
Figure VI-22:	Ratio of the Number of Positive to
	Negative Charged Hadrons in the Away
	Side vs. z _F , for the Direct Photons
	and the Neutral Mesons Samples. Also
	QCD Predictions [HAL80] are shown230
Figure B-1:	Neutral Meson Two-body Decay
	Kinematics237
Figure B-2:	Geometry of the Neutral Meson Two-body
	Decay237
Figure B-3:	D_{\min} vs E for π° + YY and η° + YY243
Figure B-4:	Distribution of the Distance Between
	Photons for 5 GeV π° and η° Decays243
Figure B-5:	Dalitz Plot and Kinematics of Three
	Body Neutral Meson Decays245
Figure C-1:	EGS4 Detector Geometry251
Figure C-1 :	
Figure C-1 :	
Figure E-1 :	EGS4 Detector Geometry251

CHAPTER I

INTRODUCTION

I-1. General Overview.

This dissertation describes the detection and analysis of direct photons produced in proton-proton collisions at the CERN Intersecting Storage Rings.

The first chapter is mainly an introduction to the topic of direct photons, reviewing their importance in the present status of the phenomenology of Quantum Chromodynamics (QCD). An overview of the techniques utilized to detect direct photons and a list of experiments are also presented.

The second chapter describes the experimental apparatus used to collect the data included in this dissertation. A very brief description of the accelerator is included. In the description of the detector those parts that were particularly important for the present study are emphasized.

Chapters III and IV explain the data taking process and the basic analysis used. In chapter V the method of analysis used to determine the direct photon signal is introduced in detail. A

description of how backgrounds were calculated and extracted from the data sample is also included.

The final chapter presents results of a direct photon cross section in the transverse momentum (p_T) range of 4.5 to 10 GeV/c. Event correlations made from a direct photon sample are studied and the results presented. All these results are compared with QCD predictions and considered in the framework of perturbative QCD. A comparison with other ISR experiments is presented. Other experiments in different regions of \sqrt{s} (center of mass energy) are briefly discussed in order to complete the present status of direct photon physics.

I-2. The R110 Experiment.

The R110 experiment was the last of a series of experiments to look at proton-proton collisions at the CERN ISR intersection 1. From 1971 to 1974 the CERN-Columbia-Rockefeller collaboration (CCR), ISR experiment R103, used two walls of lead glass blocks coupled with planes of wire spark chambers to address the topics of direct single electrons, electron pairs and π° 's at high transverse momentum. This experiment was the first to observe a large cross section for the production of π° 's with large transverse momentum, thus opening a new branch of hadron physics. This large cross section was interpreted as being due to the hard scattering of partons (quarks and gluons) [BUS73].

A second generation experiment, R105, in collaboration with Saclay (CCRS) included a gas Cerenkov counter, additional spark chamber planes and a magnet. The collaboration continued to extend and improve

studies of e^+e^- production, π^o inclusive and single electron measurements, adding η^o , $\bar{\Lambda}^o$, Λ^o and K^o data to its work and resulting in many papers published between 1974 and 1976 [i.e. BUS76a].

In 1977 a completely new, third generation experiment involving CERN, Columbia, Oxford and Rockefeller (CCOR) performed ISR experiment R-108. The apparatus now consisted of a superconducting solenoid and a set of cylindrical drift chambers. The original lead glass was supplemented with twice as many blocks of the same cross sectional area but 15% longer. The performance of the drift chambers was reported in the 1978 Vienna wire chamber conference [CAM78] and papers published by the experiment from 1978 to 1982 included studies of high mass e^+e^- pairs (including the T); correlation and jet studies; π^0 inclusive spectra; direct photons; triple jets; and a novel method for analyzing $\pi^0\pi^0$ production [i.e. ANG78].

In order to increase the solid angle of the electromagnetic calorimeter, lead-scintillator sandwich counters were added inside the solenoid during July 1979 and the experiment was renamed R110. Columbia did not participate in this collaboration leaving the acronym as COR. In this mode the experiment collected a large luminosity of 63 GeV p-p data and also observed α - α , α -p and p- \bar{p} collisions. In 1981 R110 was modified with no change of experimental number. Additional lead glass walls were added in front of the originals, intended (in conjunction with proportional chambers) to provide a good Υ/π^0 discrimination. In November 1982 a group from Michigan State University joined the experiment forming CMOR. No change was made to the detector at this time and the physics goals remained basically the same. During the summer of 1983 α - α running became again possible and a group from Brookhaven

entered the experiment especially for the α - α and d-d analysis creating for this purpose BCMOR [ANG84a]. The detector was dismantled during the first months of 1984 after the closing of the ISR in December 1983.

I-3. Brief Introduction to High p_{τ} Physics.

When experiments at SLAC in the late 1960's started to probe the structure of the nucleon by inelastically scattering electrons off protons, it was revealed that the proton is composed of point-like objects. Feynman called them "partons" and they were eventually recognized to be consistent with the "quarks" of the original Gell-Mann Zweig model. These charged lepton scattering experiments probed the charge structure of hadronic matter. Complementary information was obtained with neutrino beams that coupled to matter via the weak interaction only, hence probing its weak structure. The scattering of hadrons enables us to explore the strong interaction structure. From hadron spectroscopy considerations a new quantum number called "color" was added to partons. A dynamics of partons was created based on this new property. This new field theory was called Quantum-Chromodynamics (QCD). The discovery of "asymptotic freedom", the decrease of the effective coupling at short distances, allowed use of perturbative techniques in QCD to calculate measurable quantities, for example high transverse momentum hadron scattering. On the other hand, "infrared slavery", the increase of the effective coupling at large distances, provided a mechanism to make plausible quark confinement. A selfconsistent gauge theory of the strong interaction was born by building on the field technology created by QED. Today QCD is an essential ingredient in the "Standard Model", SU(3)xSU(2)xU(1), that has motivated a new search for the grand unification of the fundamental forces. Very good reviews on perturbative QCD have been produced in the literature recently [REY81, DUK85, BUR80, YND83, QUI83].

The ISR was the first hadron machine to test QCD at high center of mass energy where the perturbative QCD predictions could be compared with the data. This dissertation deals with the study of strong interactions between the hadron components at the high center of mass energy of the ISR.

Among hadron reactions the production of particles that have a large component of momentum transverse to the beam direction (p_T) is a good example of a reaction in which the basic parton scattering process is fairly well separated from the more complex confinement mechanism which prevents the partons from escaping as free particles and causes them to reassemble into hadrons.

High energy hadronic interactions are characterized by the production of a large number of particles. In most of such events, the produced secondaries have small $\mathbf{p_T}$. The origin of these soft events at high energies is understood as the two particles being excited by passing each other and later becoming de-excited by, for example, bremsstrahlung. This is then a collective effect and difficult to study in the QCD perturbative framework.

A different thing happens when we consider large \mathbf{p}_T events. These events allow us to study directly the inner structure of the hadrons and their interactions and compare them with perturbative QCD

predictions that will be accurate at small values of the coupling constant (high energies).

The large transverse momentum events involve the "hard scattering" of a parton constituent of each of the hadrons. This process is similar to the one that allowed Rutherford, Geiger and Marsden [RUT11] to study the structure of the atom 80 years ago.

The partons involved are scattered at large \mathbf{p}_T but because of the QCD confinement of partons they materialized as a set of well collimated hadrons called "jets".

The simplest configuration of hard scattering shown in figure I-1 implies the existence of at least four jets. The beam and target jets (labelled "spectators") represent the soft interaction case. The other two are due to hard scattering. A trigger particle with high p_T signals a possible jet and defines it as the "trigger jet" or "same side jet" as opposed to the "away" or "opposite side jet".

In the parton model the inclusive hadronic reaction A + B + C + X is expressed in terms of the elementary elastic parton-parton cross section $d\sigma/dt$ for the reaction a + b + c + d, where a,b c and d are the parton components of hadrons A,B C and D that interact.

The inclusive invariant cross section for the hadronic reaction can be written as [LEA82]:

$$E_{C} \frac{do}{d^{3}p_{C}} (AB + CX) = a_{b}^{\Sigma} \int dx_{a} \int dx_{b} F(a_{c}x_{a};A) \cdot F(b_{c}x_{b};B) \cdot E_{C} \frac{do(ab + CX)}{d^{3}p_{C}}$$

(I-a)

and using the relation:

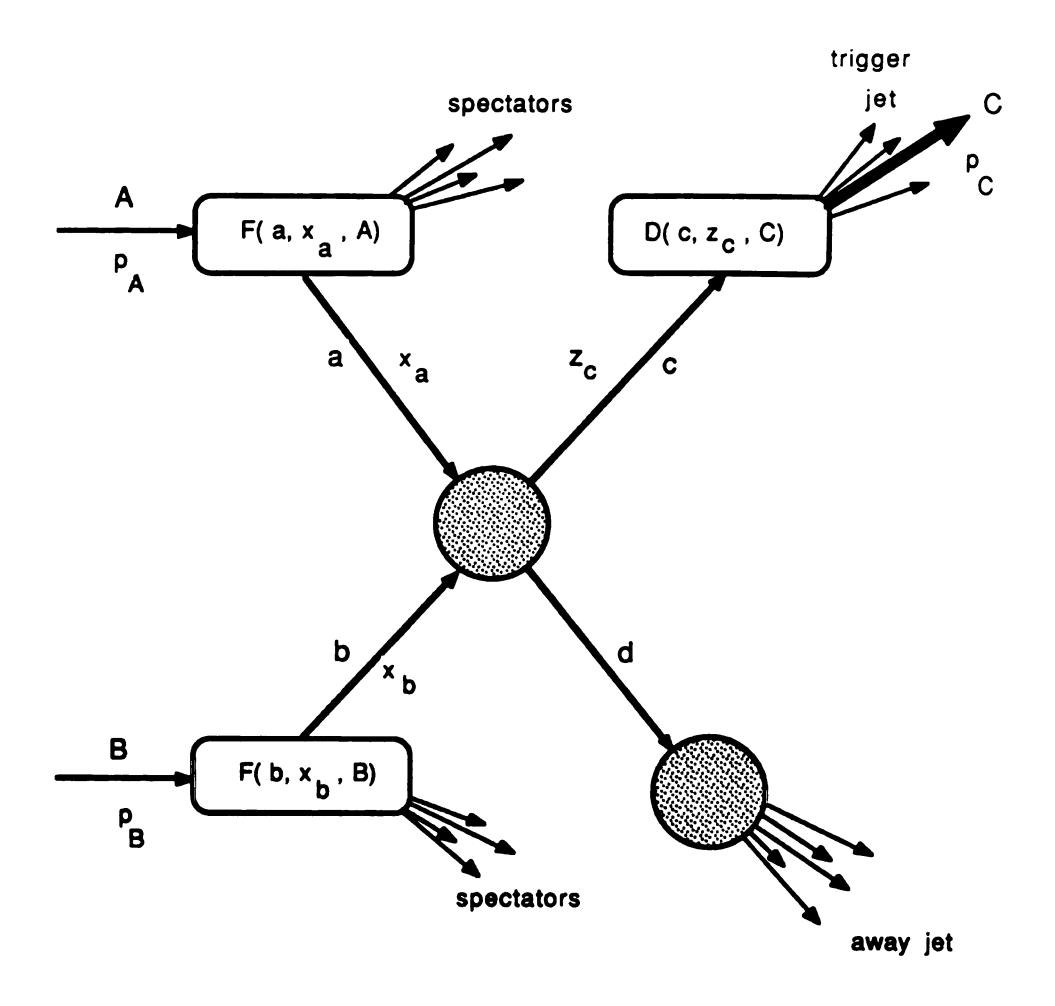


Figure I-1: Hadron Scattering Kinematics.

$$E_{C} \frac{d\sigma}{d^{3}p_{C}} (ab + CX) = c_{c} \frac{1}{\pi z} \cdot D(c_{c}z_{C};C) \frac{d\sigma (ab + cd)}{d\hat{t}}$$

written as:

$$E_{C} \frac{d\sigma}{d^{3}p_{C}} (AB + CX) = \sum_{abcd} \int_{x_{a}}^{1} dx_{a} \int_{x_{b}}^{1} dx_{b} \cdot F(a, x_{a}; A) \cdot F(b, x_{b}; B) \cdot \frac{D(c, z_{C}; C)}{\pi \cdot z_{C}} \frac{d\sigma}{d\hat{t}} (AB + CX) = \sum_{abcd} \int_{x_{a}}^{1} dx_{a} \int_{x_{b}}^{1} dx_{b} \cdot F(a, x_{a}; A) \cdot F(b, x_{b}; B) \cdot (I-b)$$

The functions $F(a, x_a; A)$ and $F(b, x_b; B)$ are called "structure functions" and represent the probability of finding the parton a with a fraction $x_a = q_a/p_A$ of the hadron A momentum. The momentum transverse to the beam direction is neglected (it is introduced later as a correction). $D(c,z_c;C)$ is called the "fragmentation function" and represents the probability that the produced parton c produces a hadron C with a momentum fraction $\mathbf{z_{C}}\text{=}\ \mathbf{p_{C}}$ / $\mathbf{q_{c}}\text{.}\ \text{s, t and u are the Mandelstam}$ variables (with a caret, s, t, u, when referring to the subprocess) and $x_a^m = -u/(s+t)$; $x_b^m = -x_a^m \cdot t/(s \cdot x_a^m + u)$ [REY81]. Therefore in making a prediction for the cross section we need to know the invariant cross sections for the parton sub-processes and also the structure and fragmentation functions of all the parton constituents that can contribute to the reaction. The sub-process cross sections are easily, at least to the first and second order, calculated directly from the appropriate perturbative QCD diagrams. But QCD makes no predictions for the form of the structure and fragmentation functions; they should be

extracted directly from the data. The structure functions of quarks have been studied in deep inelastic lepton-nucleon scattering processes (DIS) [DUK85].

The fragmentation functions of quarks and anti-quarks have been measured in e^+e^- machines [SAX85]. Dimensional counting rules can be also used to estimate these functions at least in the limit of $x \to 1$ (valence quarks) [BR075].

The most difficult problem is to determine these functions for the gluon constituents. Since the quark, anti-quark and gluon structure functions are related by the evolution equations [ALT77], using these equations one can calculate the gluon structure and fragmentation functions knowing the quark and anti-quark distributions. However, since gluons only interact via the strong force and we do not have in hand a parton probe the only way of directly extracting the gluon structure functions is from the more complicated hadron-hadron interactions.

We should look then for the simplest of these interactions. Simplicity is the principal advantage of the direct photon reaction, in which one of the strong vertices in the parton scattering diagram has been replaced by a better known electromagnetic vertex. Another kind of these interactions is high mass lepton pair production or the Drell-Yan process. This last topic also has been studied by the R110 experiment [ANG84b, HUM88].

However, the picture given by equation (I-b) is not complete. Actually we should include corrections referred to as "scaling violations" that are already important in the energy range covered by the ISR.

It was known for a long time that there is a roughly exponential cut off in the \mathbf{p}_T distribution of secondary particles for $\mathbf{p}_T < 1$ GeV/c. This phenomenon was usually interpreted in a thermodynamic approach to hadronic matter. It was believed that this exponential cut off would continue to hold at higher \mathbf{p}_T values. Using the parton model, Bjorken predicted that hard parton-parton interactions should produce a tail in the large \mathbf{p}_T distribution, which should exhibit a transition from an exponential to an inverse power behavior. This behavior was confirmed by the CCR data [BUS73]. This can be seen as the first confirmation of quark structure from a hadronic machine.

The CCRS, CCR and CCOR collaborations showed [BUS76a, ANG78] that the invariant cross section for production of neutral hadrons at high $p_{\rm T}$, mostly $\pi^{\rm o}$'s, follows a general scaling of the form:

$$E \frac{d\sigma}{d^3p} = p_T^{-n} \cdot (1 - x_T)^m \qquad (I-c)$$

where $x_T = 2p_T/\sqrt{s}$ and m = 10 and n = 8.4, valid for $p_T > 3$ GeV, a larger value of n than the value of 4 required by the Bjorken scaling. Various mechanisms were suggested to explain this phenomenon (i.e, CIM [SIV76]). However, it was perturbative QCD that explained the data, from the fact that the structure and fragmentation functions, and the strong coupling constant are actually dependent on the momentum transfer (Q^2) .

Beyond the simple parton model, in perturbative QCD, one must consider the contribution of more complicated scattering diagrams creating radiative corrections that give rise to momentum dependence of the structure functions and the coupling constant. The evolution of the structure functions has been given in a quantitative QCD approach by the "evolution equations" [ALT77]. The strong coupling constant "runs" with the momentum transfer and also produces scaling violations that should be taken into account [DUK85].

Another issue is the intrinsic transverse momentum of the parton, called k_T . There is much confusion about the role of k_T since it implies a transverse component of the incoming partons. Partons may acquire transverse momentum by gluon emission before scattering. Thus the high order QCD scattering diagrams produce k_T . The experimental values of $\langle k_T \rangle$ found in the literature lie between 0.4 GeV/c and 1 GeV/c.

It is customary to introduce a "K factor" (especially in lepton pair production) to parameterize the importance of the higher order corrections, define as [OWE87]:

$$K = 1 + \frac{HO}{Born} \tag{I-d}$$

where "HO" represents the high order prediction (or data), and "Born" the first order or Born term of the perturbative QCD expansion prediction.

I-4. Direct Photon Production at High p_T.

The investigation of simple diagrams in which one of the vertices is purely electromagnetic has been used for some time to study the fundamental physics of QCD. A well known example, is the Drell-Yan mechanism of production of high mass lepton pairs from a virtual photon produced at the parton level. In the first order, this proceeds via the

annihilation of a quark-antiquark pair contained in the colliding hadrons [DRE70]. In figure I-2.a the Drell-Yan production diagrams are shown (compare with the Direct Photon diagrams of figure I-3).

In hadronic collisions the overall inclusive yield of photons is comparable with that observed for pions (π^+, π^-) . Of course the main source of those photons is attributed to the rapid decay of neutral mesons as $\pi^0 \to \Upsilon\Upsilon$, $\eta^0 \to \Upsilon\Upsilon$ and other electromagnetic decays of directly produced hadrons. In addition, the production of direct (or prompt) photons, those produced directly from the high energy collisions of partons, is predicted by QCD [ESC75, FAR76].

The study of direct photon production offers an important tool for examining QCD and all of its associated phenomenology. A large yield of direct photons, particularly at large transverse momentum (p_T), supports the presence of point-like charged objects within the hadrons and provides means of studying the sub-structure of hadrons. However, there are some relatively weak sources of direct photons at low transverse momenta other than those mentioned above. Pion inner bremsstrahlung processes and the direct coupling of neutral vector mesons to photons produce direct photons in the low p_T energy range. At the p_T values studied in this dissertation QCD leading order processes should dominate.

Calculations based on the hard-scattering of partons predicted that the ratio Υ/π° production in hadronic reaction would exceed 10% at large p_T [FAR76]. This prediction was made before a direct photon yield at large p_T was first reported at the ISR in 1976 [DAR76].

Figure I-3 shows all the leading order contributions to direct photon production in hadronic reactions at large p_{T} , where a

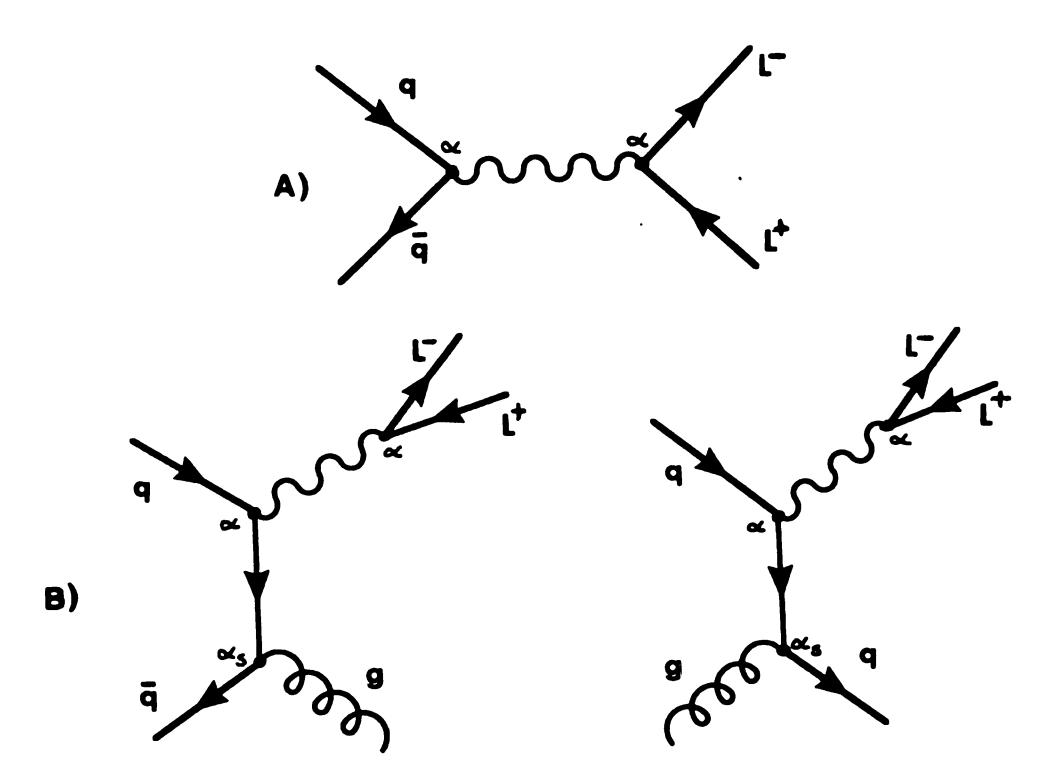


Figure I-2.a: A) Drell-Yan process. B) First Order QCD corrections to Drell-Yan.

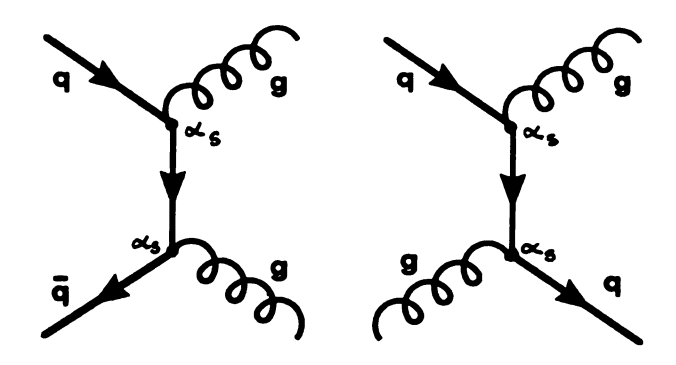
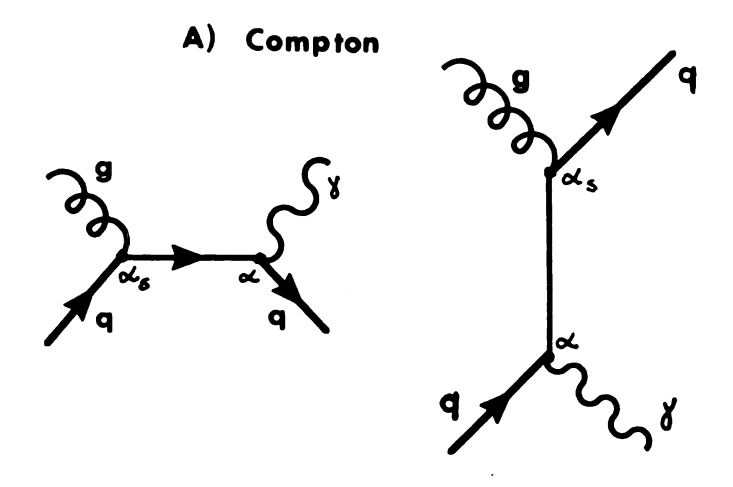


Figure I-2.b: Leading-order, quark-antiquark and quark-gluon QCD subprocesses.



B) Annihilation

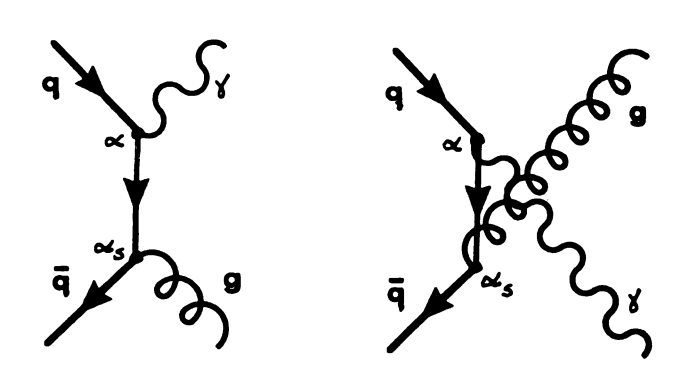


Figure I-3: QCD Leading Order Diagrams for Direct Photon Production.

perturbative expansion in QCD is expected to be valid. Diagram A is the QCD analog of Compton scattering, called the Compton graph or QCD Compton, and diagram B called the annihilation graph. These diagrams can be compared with the pure-QCD diagrams of order α_s^2 (where α_s is the strong coupling constant of QCD) of figure I-2.b. The photon emission probability relative to the gluon yield is reduced essentially by the ratio of α_s/α (α is the electromagnetic coupling constant). Thus one would expect the yield of direct photons to be reduced by a factor of 100. However what is really relevant to us is the ratio of direct photons to hadrons. Because hadrons are produced in jets and the jet production is a factor one hundred times bigger than single hadrons of the same p_T , the photon to hadrons ratio is expected to be approximately equal to one, at high p_T [FER84].

The importance of studying direct photon production comes from the fact that we have a good understanding of the electromagnetic (point-like) coupling of a photon to a quark. This process permits us to isolate the more complex quark-gluon dynamics and the hadron structure. In particular the diagrams of figure I-3 permit us to study the gluon component of the hadron. From the diagrams we can see that when a photon appears in the final state, either it is accompanied by a gluon, or the hard scattering was initiated by a gluon. If the contribution of diagrams A and B can be separated, direct photon production can be used to extract information on both the gluon fragmentation function and the gluon structure function inside hadrons.

Another advantage is that the direct photons emerge from the collision as free particles, and consequently provide first hand information about the hard scattering itself. In contrast gluons and

quarks fragment into hadrons (of reduced p_T) before they can be detected. The resulting hadrons must then be associated with their respective partons before the extraction of the physics of the hard scattering is possible.

This can be done but with difficulties that in turn create biases. For example, one might attempt to identify all of the fragments of a jet associated with a single parton hard scattering. Doing that one needs to select an energy or momentum requirement that will bias the energy or momentum distributions of the particles in the jet. Apart from the experimental difficulties in such a task there are theoretical difficulties in the definition of constituent jets. Nevertheless this technique has been used to extract information on the constituent scattering [JAC80]. Another possibility is to select a single hadron with large p_{τ} , hoping that its properties are related to those of its parent partons. The selection of a particle with high $\boldsymbol{p}_{\boldsymbol{T}}$ tends to bias the sample towards those events in which the fragmenting partons give most of their momentum to that single hadron. For single hadrontriggered experiments, it is difficult to identify which of the subprocesses for the scattering of partons contribute to the measured cross section. However a study of the charge correlations in the away jet can give some indication of the nature of the parton scattering.

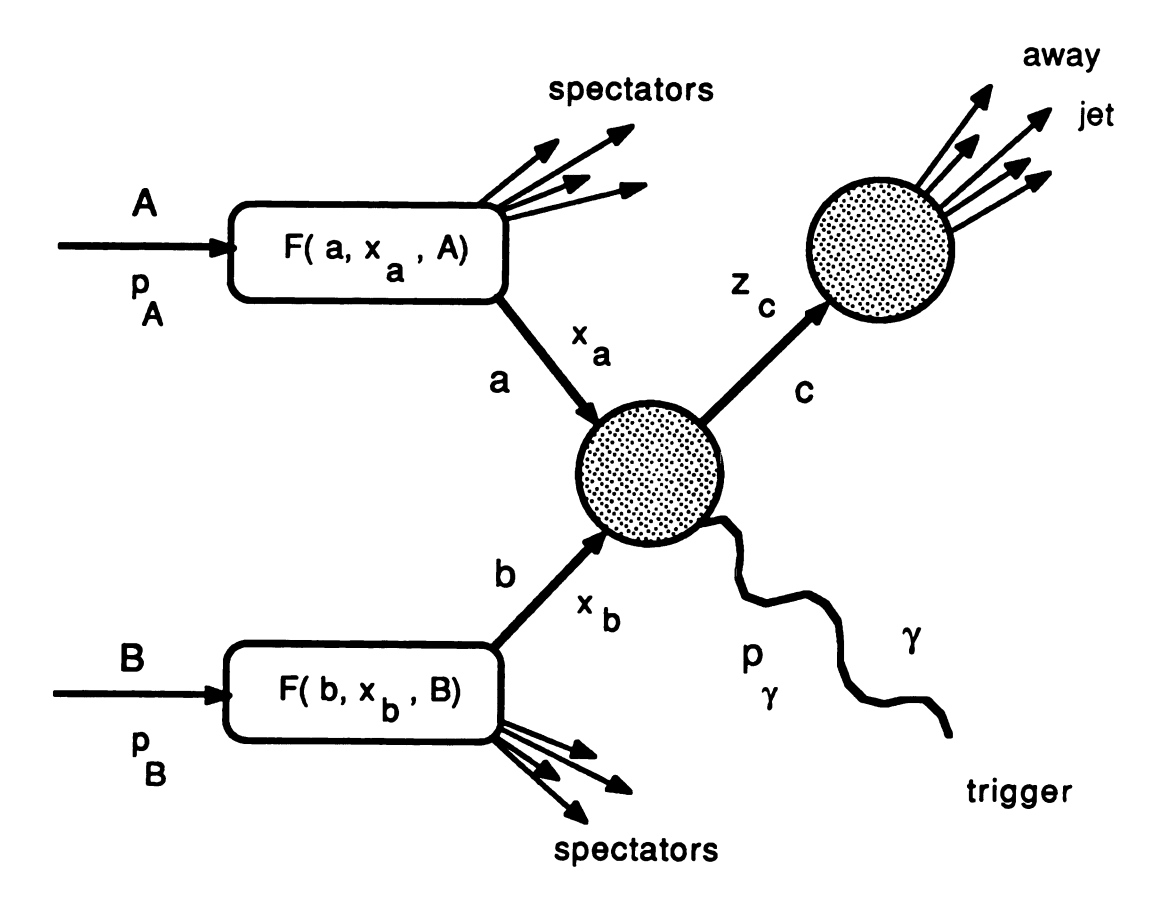


Figure I-4: Kinematics of Direct Photon Production $A + B \rightarrow Y + X$.

anything. The p_i are the four-vectors of the hadrons; \hat{s} , \hat{t} and \hat{u} are the Mandelstam variables for the subprocess.

From (I-b) the invariant cross section for the reaction can be written in the infinite momentum frame (where all masses can be neglected), in the following factorized form [LEA82]:

$$E_{\gamma} \frac{d\sigma}{d^{3}p_{\gamma}} (A+B \rightarrow \gamma+...) = \int dx_{a} \cdot dx_{b} \cdot F(a,A;x_{a}) F(b,B;x_{b}) \frac{E_{\gamma} d\sigma}{d^{3}p_{\gamma}}$$

(I-e)

where the invariant cross section for the subprocess a+b + c+Y is:

$$E_{\gamma} = \frac{\hat{s}}{d^{3}p_{\gamma}} = \frac{\hat{s}}{\pi} = \frac{\hat{s}}{d\hat{t}} \delta(\hat{s} + \hat{t} + \hat{u})$$
 (I-f)

The $\mathbf{x_i}$ are the fractions of the four momentum of the incident particles that are carried away by the partons. As for equation (I-a), the functions F are the "structure functions" of the partons inside the hadrons. Note that the fragmentation functions of partons do not appear in the cross section equation.

For the QCD Compton subprocess the elementary cross section is [FER84]:

$$\frac{d\sigma}{dt} (qg \rightarrow q\Upsilon) = -\frac{\pi \alpha \alpha_s}{3s^2} e_q^2 \frac{u^2 + s^2}{s \cdot u}$$
 (I-g)

and for the annihilation subprocess [FER84]:

$$\frac{d\sigma}{d\hat{t}} (q\bar{q} + g\Upsilon) = \frac{8\pi \alpha \alpha_s}{9s^2} e_q^2 \frac{\hat{u}^2 + \hat{t}^2}{\hat{u} \cdot \hat{t}}$$
(I-h)

where e_q is the charge of the interacting quark. For a large p_T process where production occurs at 90° in the (a,b) center of mass, $\hat{s} = -2\hat{u} = -2\hat{t}$, the cross sections for the two subprocesses are comparable. However, their respective contributions to the direct photon yield are clearly a function of the nature of the constituent distributions within the hadron (structure functions).

The $(\hat{s})^{-2}$ form in do/dt leads naturally to an inclusive photon cross section from equation (I-c) that scales in the parton model as p_T^{-4} . That is, if we assume that the structure functions depend only on the x_i and not on the momentum transfers (we are assuming scaling in the structure functions), then for any given $x_T=2p_T/\sqrt{s}$ and scattering angle θ in the center of mass, the cross section becomes:

$$E_{\gamma} = \frac{d\sigma}{d^{3}p_{\gamma}} \quad (AB \rightarrow \gamma + ...) = \frac{f(x_{T}, \theta)}{s^{2}} = \frac{g(x_{T}, \theta)}{p_{T}^{4}} \quad (I-i)$$

In fact, without scaling violations, the cross sections for production of jets, single hadrons and direct photons at large p_T should all follow this form, but with different forms for the functions $g(x_T)$, reflecting different parton-level processes. As we will see, the experimental p_T dependence for photons is closer to p_T^{-6} . This softer distribution can be explained by the presence of higher order corrections and scaling violations [BER82].

In perturbative QCD the strong running coupling constant has a Q^2 dependence, which, to the lowest order corrections in the gluon propagator [DUK85], is given by:

$$\alpha_{s}(Q^{2}) = \frac{12 \cdot \pi}{(33-2 \cdot f) \cdot \ln Q^{2}/\Lambda^{2}_{\overline{MS}}}$$
 (I-j)

where Q^2 is the square of an appropriate momentum transfer (of order p_T) that characterizes the collision, f is the number of flavors that contribute to the scattering, and $\Lambda_{\overline{MS}}$ is a parameter that sets the scale for Q^2 in the standard minimal subtraction renormalization scheme (\overline{MS}) . This expression is only valid for $Q^2 >> \Lambda^2$ (and $\ln Q^2 >> \ln[\ln Q^2]$) (leading-logarithm approximation), i.e., when $\alpha_s << 1$.

In perturbative QCD there are two kind of singularities that have to be considered before arriving at quantitative results. One kind are the mass singularities arising from diagrams as I-5(a), which can be factorized and separated from the subprocess scattering. The factorization theorem can be used to absorb these singularities into the uncalculated portions of the structure and fragmentation functions. In addition, there are ultraviolet singularities that arise from diagrams as I-5(c). The technique for regularizing these singularities is called renormalization. Therefore, every quantitative perturbative QCD calculation has at least two arbitrary scales which have to be chosen. If fragmentation to hadrons is involved a third scale appears. The degree of arbitrariness decreases when we consider more terms in the perturbative expansion. It is important, therefore, for the definition of the scales to calculate the next-to-leading order diagram contributions.

Some of the 3000 terms of the next order QCD diagrams [DOU84] that contribute to direct photon production are shown in figure I-5. Aurenche et al. [AUR84] have performed a detailed quantitative

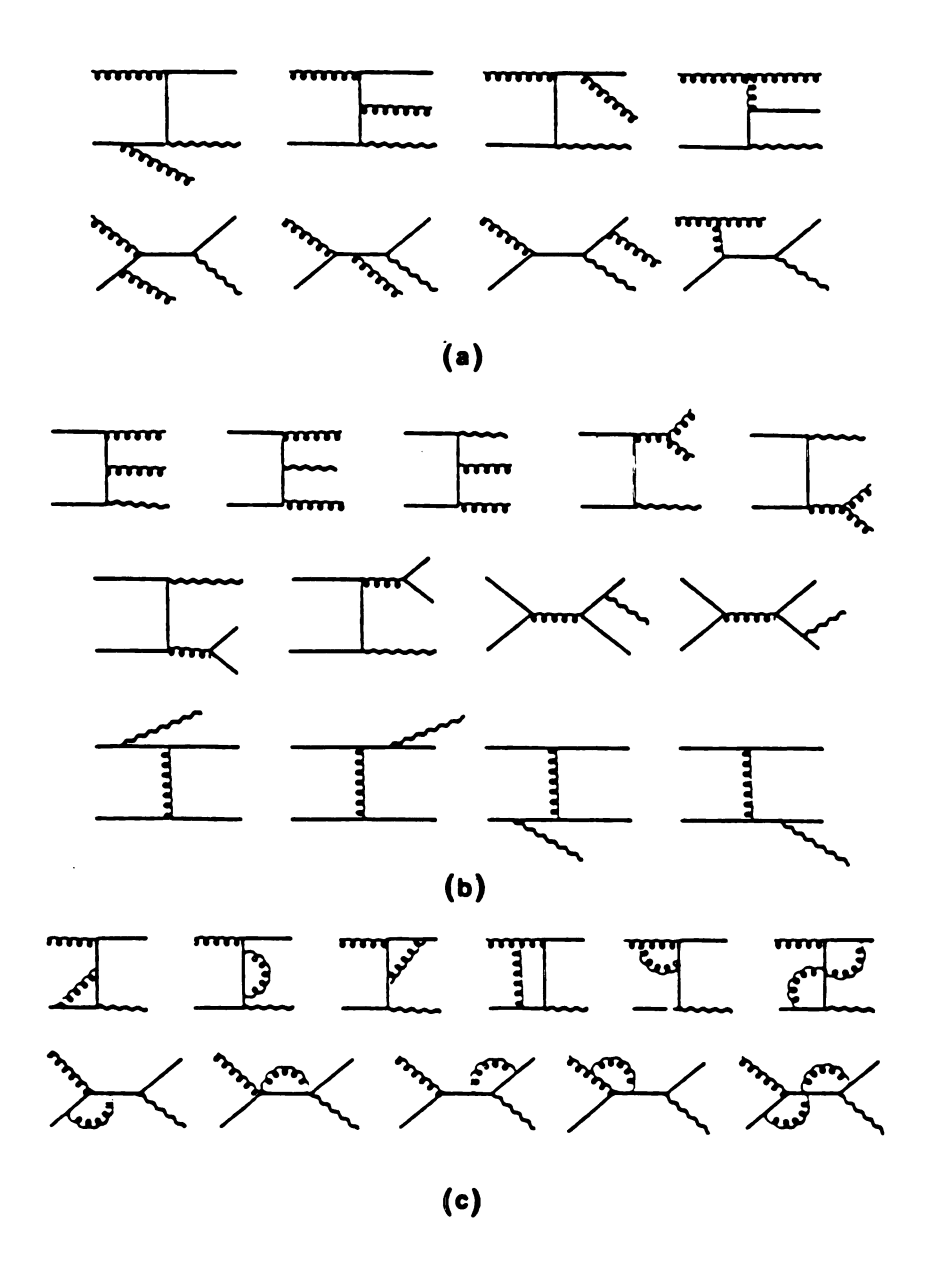


Figure I-5: Some Higher Order QCD Contributions to Direct Photon Production. a) Real Emission Diagrams to the Compton and b) the Annihilation. c) Virtual Corrections to Compton.

calculation of the invariant cross section at large \mathbf{p}_{T} beyond the leading order.

The authors of reference [AUR84] express the inclusive photon cross section as:

$$E \frac{do}{d^{3}p_{T}}(s, p_{T}, y) = \frac{do}{dyd^{2}p_{T}} = \frac{1}{1, j} \frac{1}{\pi} \cdot \int F(x_{a}, A; M_{s}^{2}) \cdot dx_{a} \cdot F(x_{b}, B; M_{s}^{2}) \cdot dx_{b} \cdot \frac{1}{s} \cdot \left\{ \frac{1}{v} \cdot \frac{do}{dv}(\hat{s}, v) \cdot \delta(1-w) + \frac{\alpha_{s}(\mu^{2})}{2\pi} \cdot \Theta(1-w) \cdot K_{i,j}(\hat{s}, \frac{\mu^{2}}{\hat{s}}, \frac{M_{s}}{\hat{s}}, \frac{M_{d}}{\hat{s}}, v, w) \right\}$$
(I-k)

where:

$$v = 1 - x_h \cdot (p_T / \sqrt{s}) \cdot e^{-y}$$

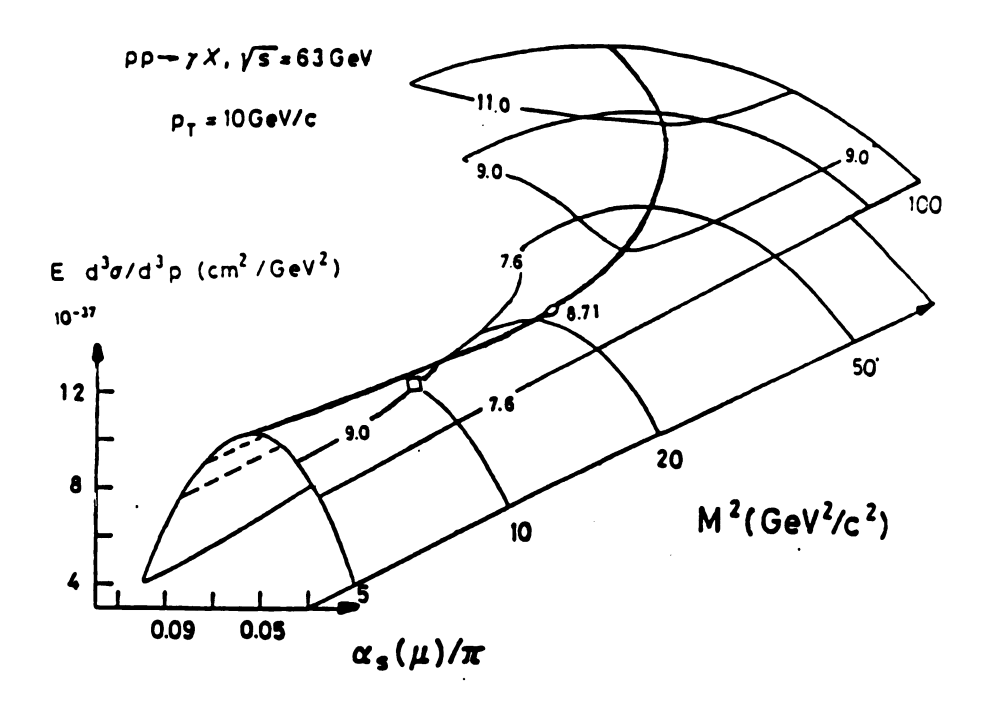
$$w = (1/v \cdot x_a) \cdot (p_T/\sqrt{s}) \cdot e^{-y}$$

and $y = \tanh^{-1}(p_z/E)$ is the rapidity of the photon. The indices i and j run over the parton content of the initial hadrons. do_{ij}/dv are the leading order QCD (Born) cross sections. The K_{ij} contain the finite next-to-leading order corrections. The masses M_s and M_d are parameters associated with the scale breaking of the structure and fragmentation functions.

Therefore to perform a detailed quantitative comparison of QCD and the direct photon data (i.e. invariant cross section), we need more than the gluon structure function and the QCD scaling $\Lambda_{\vec{MS}}$. The finite

order perturbative predictions are affected by ambiguities due to the choice of the renormalization (RS) and factorization (FS) schemes. They enter the calculations (I-h) via two parameters, μ the renormalization point (where the coupling constant $\alpha_s(\mu^2)$ will be defined); and M, the factorization mass. In most of the applications $\mu^2 = M^2 = Q^2$ is taken. Most present high-p_T phenomenological calculations choose $Q = \alpha \cdot p_T$ where $\alpha = 1$. Some calculations use $Q^2 = -\hat{t}$, \hat{s} or $2\hat{s}\hat{t}u/(\hat{s}+\hat{t}+u)$. There is no universaly accepted method to determined the QCD scales [CON86a].

This leaves us with a cross section which depends on the arbitrary parameters μ and M, E·do/d³p(s,p_T,y) = F($\alpha_g(\mu)$,M). Aurenche et al. have calculated this two-dimensional function as shown in figure I-6 [BAI86]. Different choices of μ and M (RS and FS) give numerically different predictions. In first order QCD calculations these quantities are not constrained, but they are taken "ad hoc" to agree with the data. In the next-to-leading order it is possible to define an "optimized second order QCD" using the "principle of minimal sensitivity" (PMS) [STE81]. Since the physical cross section is RS and FS independent, it is reasonable to require that a truncated perturbative calculation obeys at least a local stability condition in the parameters μ and M. This is done by choosing the saddle point in figure I-6 as the optimized second order QCD predictions. With the values of μ and M fixed, a comparison with the data is possible assuming $\Lambda_{\overline{MS}}$ and a set of structure functions. Duke and Owens [DUK84] have proposed two sets of structure functions called "soft" (lower momenta) (set I) and "hard" (higher momenta) (set II). The two sets differ chiefly in the gluon distribution. There is a correlation between the QCD coupling scale parameters $\Lambda_{\overline{MS}}$ and the shape of the gluon distribution [DUK84]. A soft gluon distribution (more low



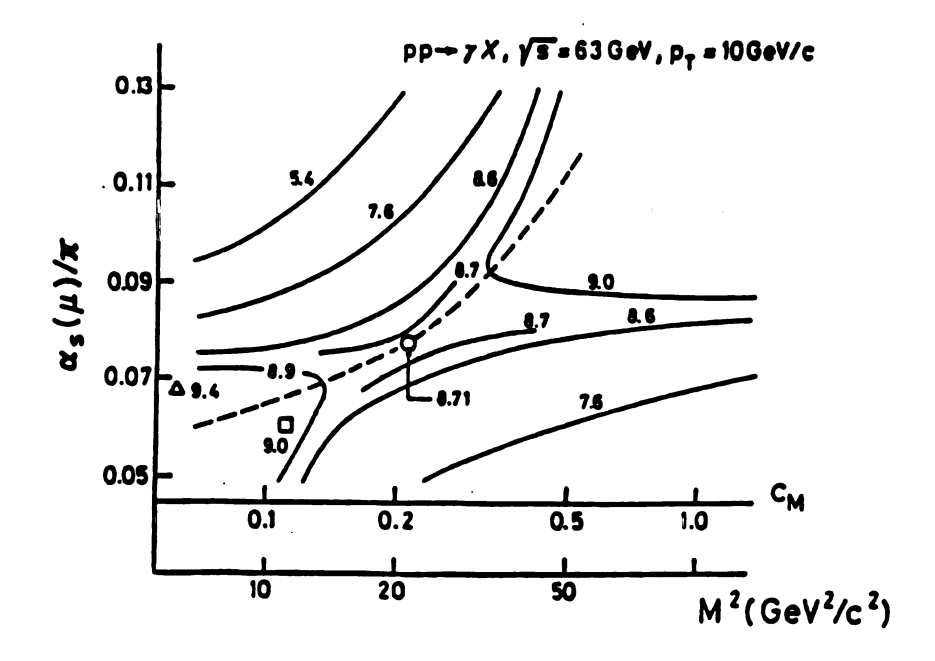


Figure I-6: Renormalization and Factorization
Scheme Dependence of the Second
Order QCD Direct Photon Cross Section.

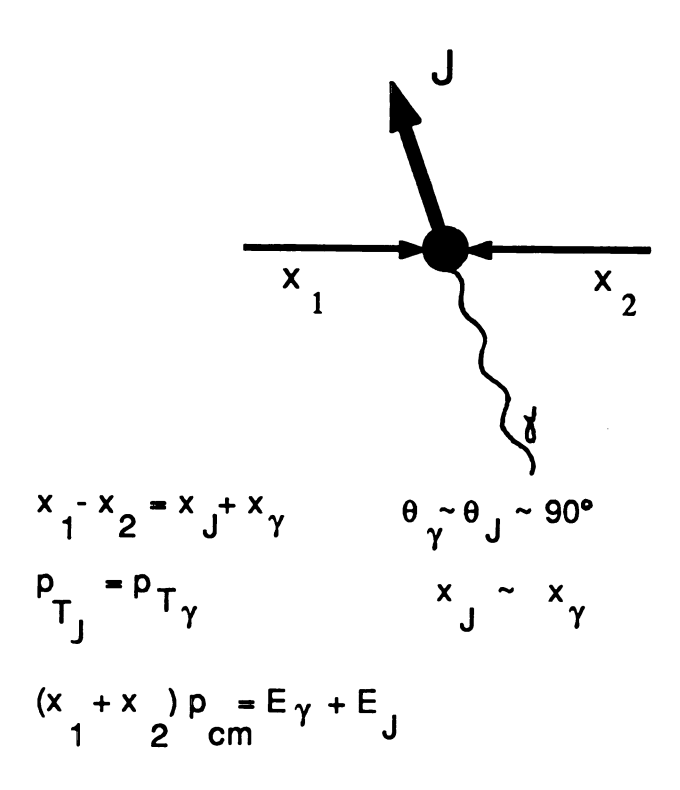
momentum gluons) results in a relatively smaller value of $\Lambda_{\overline{MS}}$, while a harder gluon distribution (more high momentum gluons) gives a bigger value of $\Lambda_{\overline{MS}}$.

Contogouris et al. [CON81] have developed another method to calculate the direct photon cross section to the next-to-leading order. They used the leading-logarithm approximation, k_T smearing and K factors calculated in the soft-gluon approximation by constant π^2 -terms [CON86b]. The scale is defined as $\mu^2 = Q^2 = M^2 = p_T^2$. There are in the literature opinions in favor and opposed to both methods [CON86a,OWE87].

Measuring the direct photon cross section then allows a comparison with a quantitative QCD prediction, although it does not allow a direct measurement of the parton distribution. There is a way of obtaining the parton distributions almost directly. If one can measure the double inclusive photon-away-jet cross section the two-body kinematics of the parton reactions are completely determined. The two body kinematics of the reaction are shown in figure I-7. In this case one can measure the gluon structure function. Further, the distribution of the hadrons in the jet will measure the fragmentation function D(z) of the quark (in the QCD Compton scattering) and of the gluon (in the annihilation process), provided one assumes that the valence structure functions are known, for example from DIS.

Halzen et al. [HAL80] have calculated the inclusive photon-jet cross section for the first order Compton diagram when photon and jet are both measured approximately at $\theta = 90^{\circ}$:

$$\frac{d\sigma}{d\eta_{\gamma}d\eta_{j}dp_{T}} = \frac{5\pi \cdot \alpha\alpha_{s} \cdot F_{g}(x, \mu) \cdot F_{2}^{ep}(x, \mu)}{3 \cdot x^{2}s^{3/2}}$$
(I-1)



Therefore:

$$x_1 = \frac{1}{2}p_{cm}(E_{\gamma} + E_J + p_{L\gamma} + p_{L)}$$

 $x_2 = \frac{1}{2}p_{cm}(E_{\gamma} + E_J - p_{L\gamma} - p_{L)}$

Figure I-7: Kinematics of Two-body Parton Scattering.

where $x = 2 \cdot p_T / \sqrt{s}$, $\eta = \ln(\cot \theta / 2)$ is the pseudo-rapidity and $F_2^{ep}(x,\mu)$ is the valance quark structure function as extracted from deep lepton-hadron scattering experiments.

One should first isolate Compton scattering if one wishes to use this method. One has more opportunities of doing that by comparing photon production with beams or targets of different anti-quark content. This is done particularly well with π^+ and π^- beams incident on fixed targets [FER84]. In our case, only proton-proton beams were used. We can make use of the fact that Compton scattering has been shown to be the dominant diagram [BEN83] in this kinematic regime. However, the bremsstrahlung contribution has been shown [AKE83] to contribute up to 30% in the p_T range of the ISR.

Another area where QCD predictions could be checked via direct photon data is the comparison of prediction for the associated event topology. I will reserve the discussion of this subject for chapter VI of this dissertation. All the topics discussed in this section have been extensively reviewed in an article by J. F. Owens [OWE87], and the work of the P. Aurenche, R. Baier, M. Fontannaz and D. Schiff in [AUR87].

Finally we should mention the hadroproduction of two photons in processes as shown in figure I-8 [OWE87]. The production of two photons has been measured at the ISR [AKE86] and the SPS [BAD86] and also QCD predictions have been made [AUR85, CON87]. However there are important sources of background, such as normal direct photon production (i.e., $qg + \gamma q$) with a second photon originated from bremsstrahlung from the recoiling parton. This contribution can be as large or larger than the

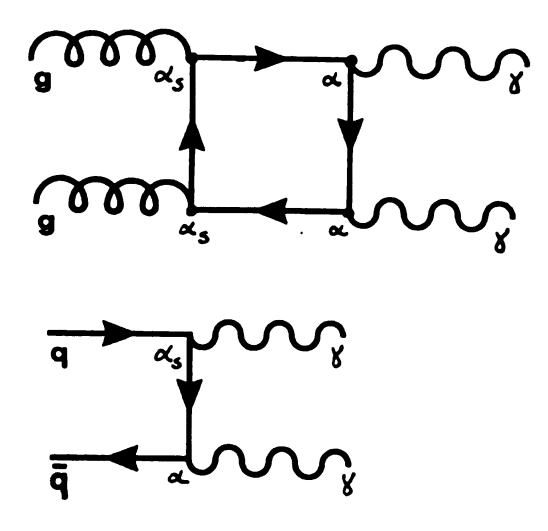


Figure I-8: Two-photon production diagrams.

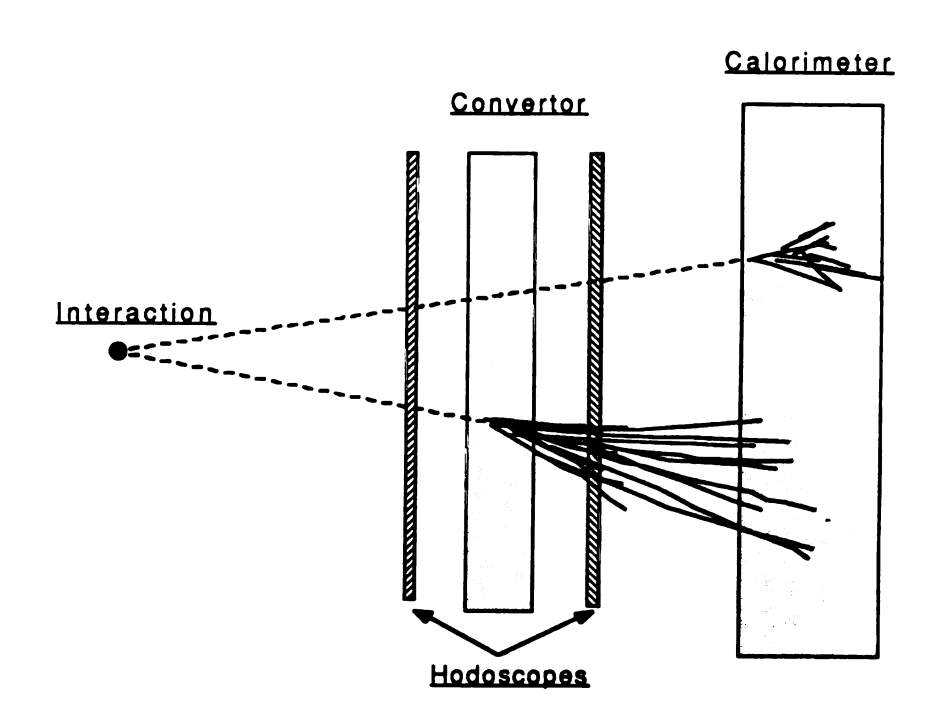


Figure I-9: The Conversion Method.

Born term subprocess. No attempt has been done to look for two photons in the present dissertation.

I-5. Overview of Experimental Techniques Used to Detect Direct Photons.

The principal problem in the study of direct photons is the background produced by non-direct photon sources. The primary source of background is the electromagnetic decay of neutral mesons such as π° + YY, η° + YY ...etc. These decays can contribute to the background in two different ways: (1) one photon from the neutral meson decay remains undetected thus yielding an isolated photon, and (2) the photons from the decay merge into one shower in the detector.

The two main techniques that have been used to isolate a direct photon signal from this background are called the "direct method" and the "conversion method". The "direct method" consists in recognizing the photons from the neutral mesons decays through a measurement of the meson mass or any other parameter provided by space-resolved photons. In the "conversion method", neutral mesons and photons are separated through the measurement of the conversion probability in a thin converter placed in front of the calorimeter.

The characteristics of the detector are determined by the detection method chosen (or viceversa). A direct method measurement requires a fine transverse segmentation to isolate every single shower, a good capability for detecting low energy photons and a large solid angle acceptance so that all photons from the neutral meson decays are

fully detected in the energy range of interest. The photons from the meson decays cover a broader range of energies than the direct photons. It is also important to achieve linearity in the energy response of the calorimeter, since one must be sure that the detector responds to one photon of energy E (i.e. a direct photon) the same as it responds to several photons of energies Σ E_i = E.

A good understanding of the neutral meson decay kinematics is important to undertake measurements of direct photons, from the experiment design to the analysis. See Appendix B for a detailed account of these kinematics. Two essential properties of the two-body meson decays (i.e. $\pi^0 + \gamma \gamma$) are the following. First, the energy distribution of each of the photons has a flat distribution between zero and the energy of the neutral meson, therefore the asymmetry of the decay, defined as $A = (E_1 - E_2)/(E_1 + E_2)$, runs with the same probability in the center of mass, between -1 and 1. Second, the distance between the two photons in the laboratory system, on the contrary, has a distribution of probability highly peaked near the minimum distance.

If we place our detector at a certain distance L from the π^0 decay, the minimum distance between photons is given, in the small angle approximation, by the relation $d_{\min} = 2 \cdot m_{\pi} \cdot L / E_{\pi}$. For example, in our case L=214 cm, therefore at $E_{\pi} = 5$ GeV $d_{\min} = 11.5$ cm, and for $E_{\pi} = 9$ GeV $d_{\min} = 6.4$ cm. These values put a constraint on the transverse segmentation of the detector and the possibility of isolating both photons from the π^0 decay.

The inefficiency in detecting low momentum gammas can also provide a substantial background of large p_T photons from asymmetric π° decays. The second most important contribution to the background comes

from the η° decay. The η° contribution to the background is reduced because the ratio of production is η° + YY / π° + YY = .21.

The conversion method relies on the fact that the probability of observing a photon conversion is greater for a neutral meson (more than one photon) than for a direct single photon. Such a detector would consist of a thin convertor surrounded by detectors that determine if conversion has occurred. This is sketched in figure I-9. The technique is to measure the fraction of events that show conversions in the convertor and compare this with the conversion probability expected from multi and single photons. In order to make a good measurement the absolute conversion probability must be known accurately, as must any non-linearity in the detector.

Comparing both methods we can find advantages and disadvantages for each of them depending on the goals, the p_T regime of study and the means to perform the measurements that we have. An advantage of the direct method is that most of the background can be measured and removed, so in an event by event basis a sample of direct photons can be isolated. This is then the best way to study event correlations or event structure properties. The advantage of the conversion method comes from the fact that it does not require as finely segmented a detector as the direct method and that it does not impose an intrinsic p_T limit on the measurement caused by the limit on the space resolution. Therefore this method has advantages if what we want is to study the cross section over a large p_T range, and up to high values of p_T . If the ratio of direct photons to background is high both methods could be competetive.

The first indications of a direct photon signal were produced at the CERN ISR using a direct method in 1976 [DAR76]. The results were

rather qualitative due to uncertainties in the systematics and the background subtractions. There were also at the same time indications of a possible direct photon signal at fixed target experiments at Fermilab [FER84]. The next experiment to show a signal of direct photons was R107 at the ISR, also using a direct method [AMA78].

Table I-1 shows a summary of the principal characteristics of all the experiments recently done or planned for the near future with the intention of looking for direct photons in hard scattering hadron collisions.

The more recent measurements of direct photons include experiments at the ISR, the fixed target SPS program, the fixed target program at Fermilab and the SppS collider at CERN. Previous ISR experiments that measured direct photons were R806 [ANA82], R108 [ANG80, ANG81] and the AFS collaboration using an open axial field magnet containing cylindrical drift chambers and sourrounded by an uraniumscintillator calorimeter [AKE85]. At Fermilab the experiments E95 [BAL80] and E629 [MCL83] measured direct photons at the Meson area, the former using a lead-liquid argon calorimeter of fine transverse segmentation. More recently the SPS fixed target program with WA70 using a lead-liquid scintillator electromagnetic calorimeter, drift and MWPC [BON87]. NA24 using Cerenkov counters, MWPC and a "photon position detector" consisting of lead sheets and proportional tubes of triangular cell shapes [DEM87] and NA3 using lead/scintillator strips and PWC with strips and pad read outs [BAD86], presented data studying direct photons. In the SPPS collider UA1 [DIC87], UA2 [APP86] and UA6 [BER87] also have presented data. UA6 looks at collisions of one of the collider beams with a H_2 jet to study high p_t phenomena at \sqrt{s} = 24.3 GeV.

Table I-1: Direct Photon Experiments.

			,		
Experiments	beam+target	√s GeV	max. p GeV/c T	Place	Method of detection
R 806	p + p	63	12	ISR	Direct
R 108	p + p	45,63	12	ISR	Conversion
E 95	p + Be	19.4 23,8	4	Fermilab	Direct
E 629	p+C , π ⁺ + C	19.4	5	Fermilab	Direct
AFS	$p + p, p + \overline{p}$	53,63	10	ISR	Direct
R 110	p + p	63	10	ISR	Direct
UA1	p + p	630	80	SppS collider	Conversion
UA2	p + p̄	540 630	43	SppS collider	Conversion
UA 6	p + p p + p	24	6-7	SppS	Direct
NA 3	p+C , π [±] + C	19.4	6	SPS	Direct
NA 24	$p + p$, $\pi^{\pm} + p$	24	6-7	SPS	Direct
WA 70	p + p , π [±] + p	23	6-7	SPS	Direct
E 705	p+D, $\pi^{\frac{1}{2}}$ +D	24	8	Fermilab	Direct
E 706	p+C , π [±] + C	<41	10	Fermilab	Direct
CDF	p + p	2000	40	Fermilab collider	Direct
D0	p + p	2000	?	Fermilab collider	Conversion

The R108 experiment and recently UA2 and UA1 are the only experiments to use a conversion method to measure the direct photon signal. Because the variety of accelerators used in all these experiments we have, by now, measurements over a broad range of center of mass energy (\sqrt{s}). For our case only the earlier experiments at the ISR are directly comparable with our data because they include measurements at \sqrt{s} = 63 GeV. In chapter VI of this dissertation I will discuss the results obtained by these experiments and compare them with those obtained in the present experiment.

The major contributions from Fermilab will come presumably from E705 (with a scintillating barium glass electromagnetic shower detector) [COX82] and E706, a second generation experiment (from E629) based on liquid argon calorimetry [FER86]. These are planned to run with improved detectors especially designed to detect direct photons. In addition the Tevatron collider experiments CDF [BLA88] and DO [D084] are planning to look for direct photons.

For a detailed account of all of these experiments I refer to the review article by T. Ferbel and W.R. Molson [FER84] or to the specific references.

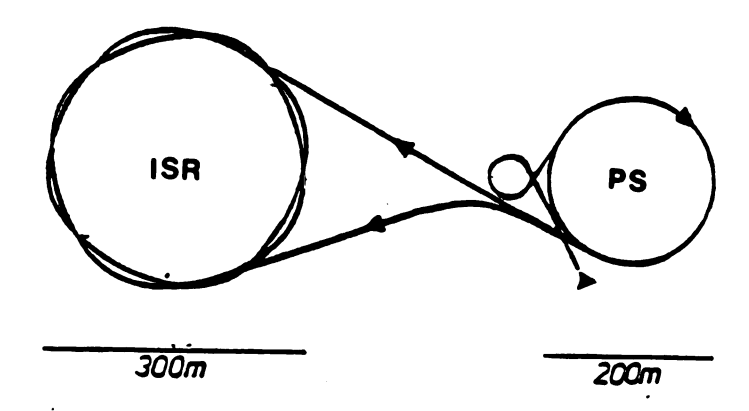
CHAPTER II

ACCELERATOR AND EXPERIMENTAL APPARATUS.

II-1. The Intersecting Storage Rings (ISR).

The Intersecting Storage Rings (ISR) was the first machine ever to store two continuous proton beams and make them collide [HUB77]. The ISR was composed of two almost circular rings in which protons circulated in opposite directions. A layout of the ISR is shown in figure II-1. Collisions occurred in 8 places, called intersections, numbered from 1 to 8 (I1 to I8) where the two beams collided at an angle of α = 14.77°. The protons were accelerated in the CERN PS (Proton Synchrotron) and injected into the storage rings through two transfer lines. The beam ejected from the PS was injected into one ring at a time and accumulated by successively stacking. Only a small acceleration was provided in the ISR to replace energy losses and maintain the same beam characteristics for a long period of time.

Because the ISR was a collider machine, almost all energy which was invested in the acceleration became available in the center of mass for reactions or particle creation. However due to the crossing angle between the beams, the proton-proton center of mass moved with a velocity of [JAC75]:



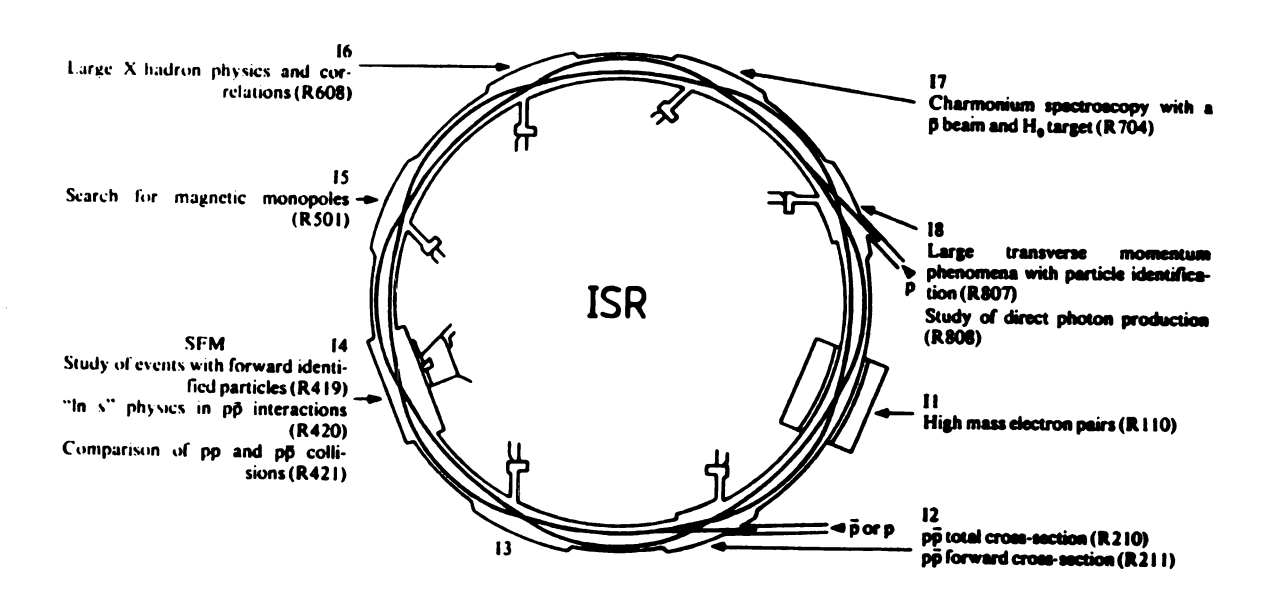


Figure II-1: ISR Layout.

$$\beta = v/c = \sin(\alpha/2) \cdot p/E$$
 (II-a)

with respect to the laboratory frame, where p is the particle's momentum and E is its energy. At the high energies at which the ISR run β was essentially independent of the beam momentum (E = p) and was equal to 0.129. The square of the total energy in the center of mass is given by [JAC75]:

$$s = 4 \cdot p^2 \cdot \cos^2(\alpha/2) + 4 \cdot m^2 \approx 4 \cdot p^2 \cdot \cos^2(\alpha/2)$$
 (II-b) where m is the proton mass.

The beams circulated inside vacuum pipes that had the cross section shown in figure II-2. Also shown is a typical beam density profile. The ISR could operate in a broad range of beam momenta and currents. An important quantity is the counting rate or number of collisions per unit of time which lead to a certain reaction. In a collider the rate can be calculated from the geometry of the beams, their density and their energy.

A usual way of giving the rate is to define the luminosity (L). The luminosity is defined as the rate per unit of cross section. For beams of rectangular cross section and uniform density, it can be shown [HUB77] that the luminosity is given by:

$$L = \frac{1}{\sigma} \frac{dN}{dt} = \frac{I_1 \cdot I_2}{c \cdot e^2 \cdot h \cdot \tan (\alpha/2)}$$
 (II-c)

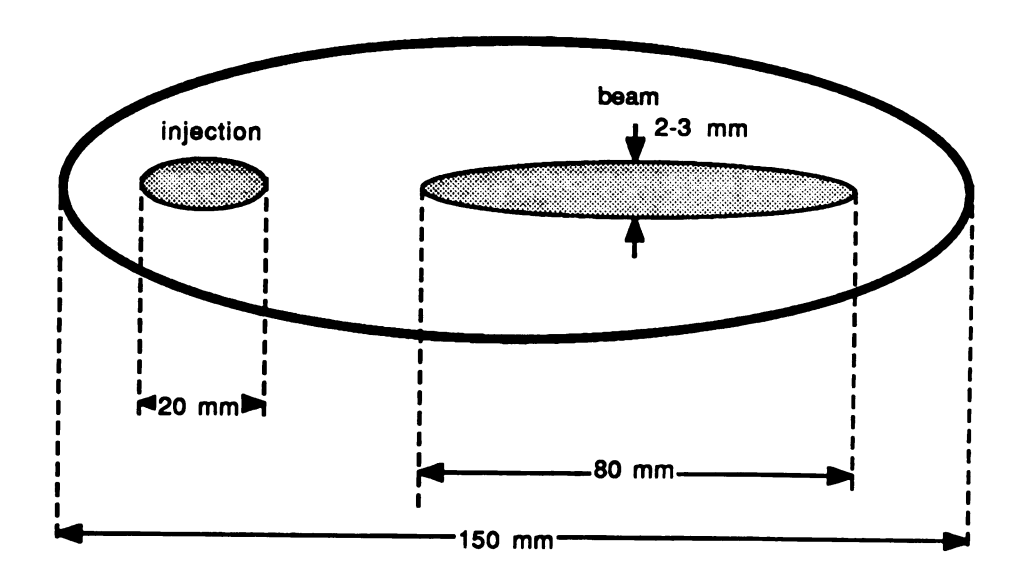


Figure II-2: Vacuum Pipe Cross Sectional View and Beam Density Profile.

where I_1 and I_2 are the beam currents in Amps, σ is the process cross-section in cm², dN/dt the counting rate, h the beam height in cm, e the electron charge and c the speed of light (assumed to be the velocity of the particles in the beam). L is normally expressed in units of cm⁻²s⁻¹.

In practice the luminosity was measured experimentally using the rates measured in the MM counters (described in section II-10 of this chapter). The experimental determination used the Van der Meer method [VAN68]. To account for the non-uniformity of the beams, h in equation (II-b) is substituted by an effective height $h_{\mbox{eff}}$. Then, the luminosity can be written as:

$$L = 10^{28} \cdot \frac{I_1 \cdot I_2}{h_{eff}}$$
 (II-d)

where I_1 and I_2 are measured in Amps, $h_{\mbox{eff}}$ in cm and the value of α for the ISR was introduced.

The value of $h_{\mbox{eff}}$ is obtained experimentally by making a plot of the rate as a function of the vertical beam displacement (Δz). A plot of this kind is shown in figure II-3. It has been shown [VAN68] that $h_{\mbox{eff}}$ is given by:

$$h_{eff} = \frac{\text{area under the curve}}{(dN/dt)_{max}}$$
 (II-e)

where $(dN/dt)_{max}$ is the maximum counting rate. Introducing the value of h_{eff} into equation (II-c) and knowing the beam currents the luminosity can be calculated. The ratio of the maximum counting rate to the luminosity is called the "monitor constant" (K):

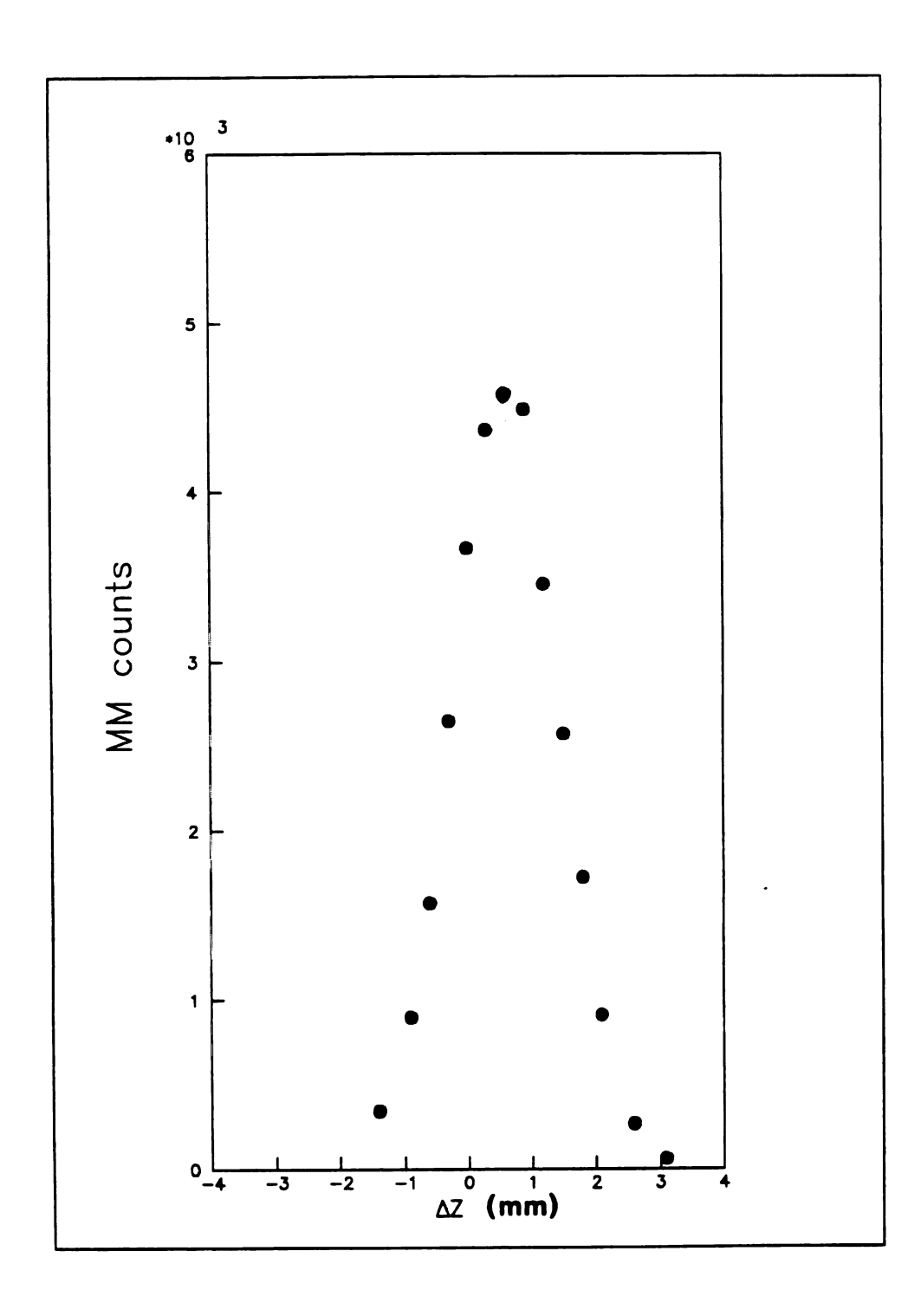


Figure II-3: Rate vs Beam Displacement.

$$K = \frac{(dN/dt)_{max}}{I.} \qquad (II-f)$$

As the observed rate is $\sigma \cdot L$, K is the effective cross section seen by the monitor. It depends only on the energy of the beams and the layout of the particular monitor. Once calculated, the monitor constant could be used directly (for a particular ISR stack) to convert MM counts to luminosity by $L = K \cdot (MM \text{ counts})$. The highest luminosity ever observed in intersection region I1 in proton-proton collisions was reached for 63 GeV running and was $6.31 \times 10^{31} \text{ cm}^{-2} \text{s}^{-1}$.

II-2. The I1 Intersection.

The detector used in this experiment was located at the intersection region 1 (I1), as shown in figure II-4. The p-p center of mass for I1 was moving towards the outside of the rings.

As can be seen from equation (II-b) there are other alternatives to increase the luminosity besides increasing the beam currents. One is to reduce the crossing angle and the other is to reduce the height of the crossing beams, that is what the "low- β " insertion does. I1 and I8 were the only two intersections equipped with low- β insertions.

The beam height is determined by the focussing and the emittance of the beam. The focussing is measured by the number of transverse oscillations (Q) which the particle performs per revolution around its equilibrium orbit. These are called "betatron oscillations". The area

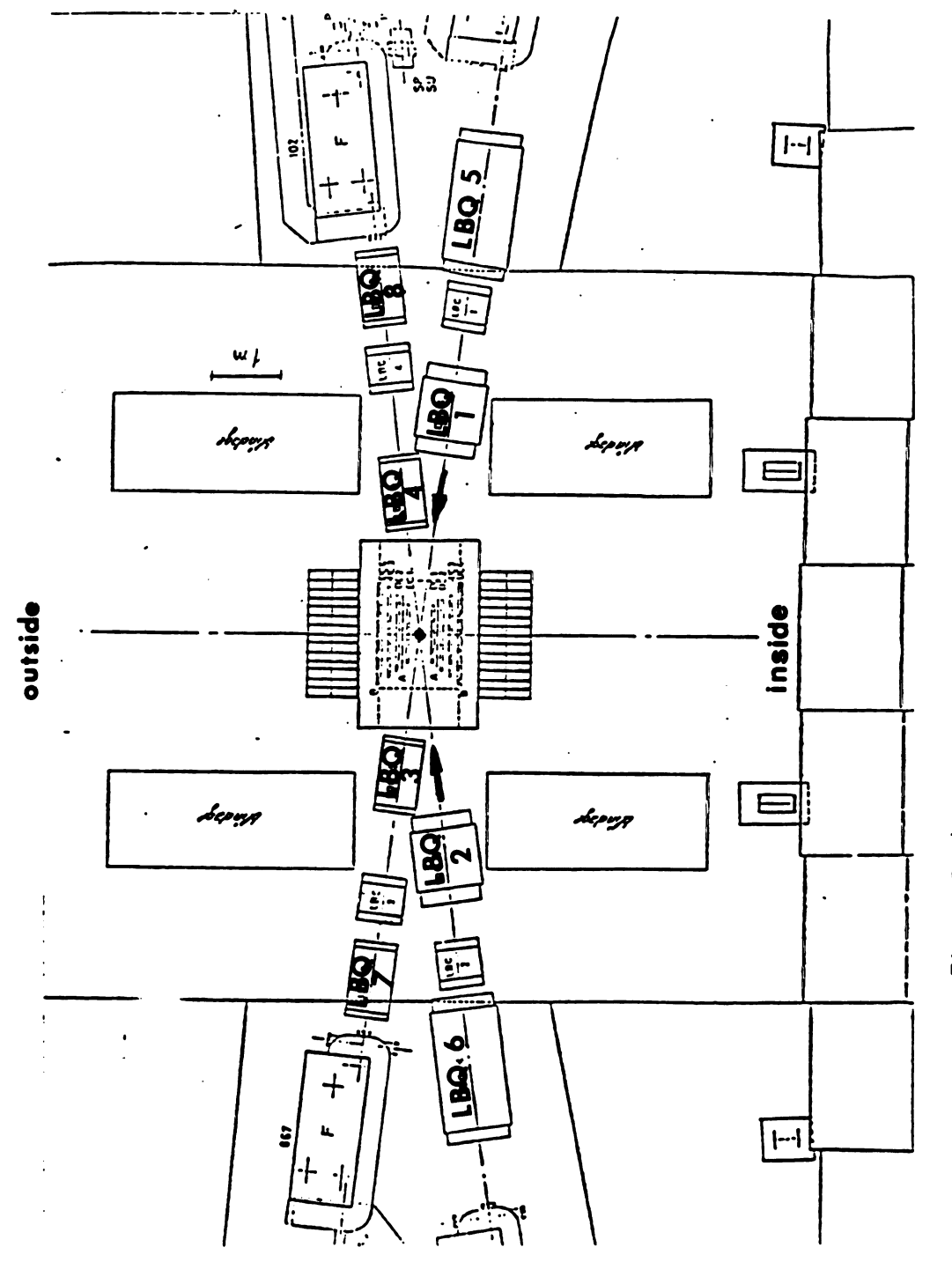


Figure II-4 : Il Intersection Layout.

inside the locus of motion in the phase plane of betatron motion is a beam characteristic and is called emittance (ϵ). Since transfer from one accelerator to another does not change its value, the emittance is determined by the PS.

It can be shown [HUB77] that the beam height h is related to $\boldsymbol{\varepsilon}$ and Q by:

$$h = 2 \cdot \sqrt{\frac{\varepsilon}{\pi} \cdot \frac{R}{Q}}$$
 (II-g)

where R is the radius of the particle's orbit. The wavelength of the betatron oscillations λ_{β} varies as a function of the azimuth (s). It can be written as:

$$\lambda_{g} = \frac{2 \cdot \pi \cdot R(s)}{Q}$$
 (II-h)

or also expressed as $\lambda_{\beta} = 2 \cdot \pi \cdot \beta(s)$ where $\beta(s)$ is called the "betatron function". Therefore,

$$h \sim 2 \cdot \sqrt{\frac{\varepsilon}{\pi} \cdot \beta_{VI}}$$
 (II-1)

where β_{VI} is the vertical β -function in the intersection. A low- β means lower h and thus greater luminosity. Therefore, in order to increase the luminosity it is sufficient to increase the focussing locally. This was done by four quadrupoles lenses for each beam; two before and two after the intersection. In the case of I1 a factor of 2.2 in luminosity was gained over a standard interaction region. The 8 quadrupoles (LBQ1-LBQ8) layout that provided the extra field for low- β focussing is shown in

figure II-4. All data presented in this dissertation were taken with the low-β magnets on.

The I1 vacuum pipe consisted of a 1mm thick titanium cylinder with conical ends (see figure II-15).

II-3. Apparatus Overview.

The R110 detector was designed for several specific physics purposes. These were to study high mass e e pair production and in general high $\textbf{p}_{_{\boldsymbol{T}}}$ processes where an electromagnetic energy deposition trigger could be used. Over time other topics were also studied. These included jet structure studies, pp-pp comparisons, α - α , d-d and p-p comparisons, direct photon production and high mass π° pairs. To achieve these purposes an electromagnetic calorimeter with a large coverage was designed to trigger on electromagnetic deposition. A charged particle momentum measurement system was also included. The detector can be separated into two main parts: 1) the electromagnetic calorimeter and 2) the high magnetic field spectrometer composed of drift chambers and a superconducting solenoid. Various scintillation counters and proportional chambers were also included. The detector covered almost 2π in azimuthal angle ϕ but with very different detector characteristics. The figure II-5 shows a general view of the detector. The azimuthal angle was divided in sextants as shown in figure II-6. Sextants 1, 3, 4 and 6 were covered by lead-scintillator shower counters and 2 and 5 by the lead-glass Cerenkov arrays. The main components for the purpose of this dissertation were the lead glass arrays in sextants 2 and 5. In the

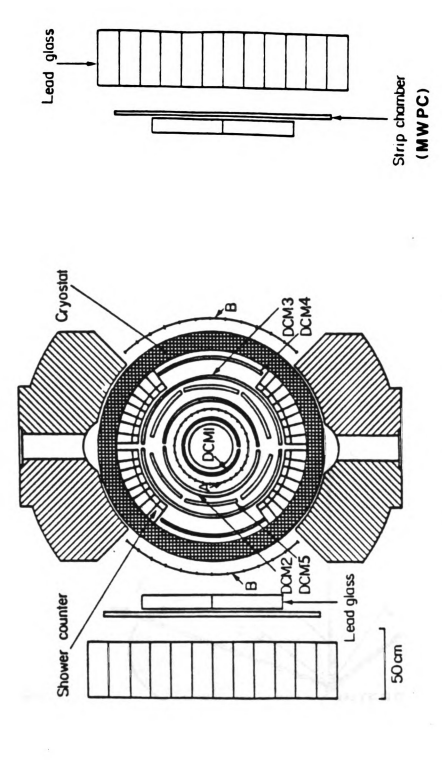


Figure II-5: Overview of the R110 Apparatus in the Direct Photon Trigger Position.

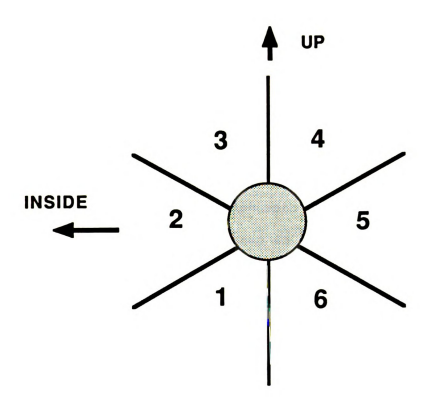


Figure II-6: Sextant Definition.

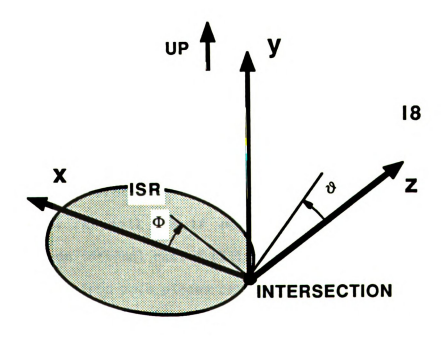


Figure II-7: System of Coordinates.

S • ... I: (: y) Ţęş ¥a; lat 0.: rad ₩as cy] the

tigh

trigger used for this dissertation one of the lead glass arrays, the one used in the trigger, was moved away from the intersection region (back glass front face at 236 cm) to increase the angular resolution of the apparatus. The other array was kept in its original position (back glass front face at 144 cm), closer to the intersection, as shown in figure II-5. (Triggers were taken with each array alternately retracted). The specifics of the trigger will be discussed later in the dissertation.

The system of coordinates used in the R110 experiment is (see figure II-7): a right-handed x,y,z with: x, towards the inside of the ISR rings; y, vertically up; z, along the solenoid axis (towards I8). The 0,0,0 is at the center of the solenoid. For cylindrical coordinates (r,ϕ,z) $\phi=0$ is along x, and the ϕ increases anti-clockwise (from x to y), with $-\pi < \phi < \pi$.

II-4. The Solenoid.

The magnet was a superconducting solenoid with a field of 1.4 Tesla [MOR77a, MOR77b]. The advantage of using a superconducting magnet was that a high field could be produced while having a small amount of material between the intersection region and the lead glass arrays outside the magnet. The coil itself was 170 cm long with an external radius of 89 cm and an internal radius of 70 cm. The magnetic flux path was completed by soft iron pole pieces capping the ends of the solenoid cylinder. Stray field not confined to the return yoke interfered with the external detectors, thus preventing operation of the magnet at any higher field. The uniformity of the field was checked to be within 1.5%

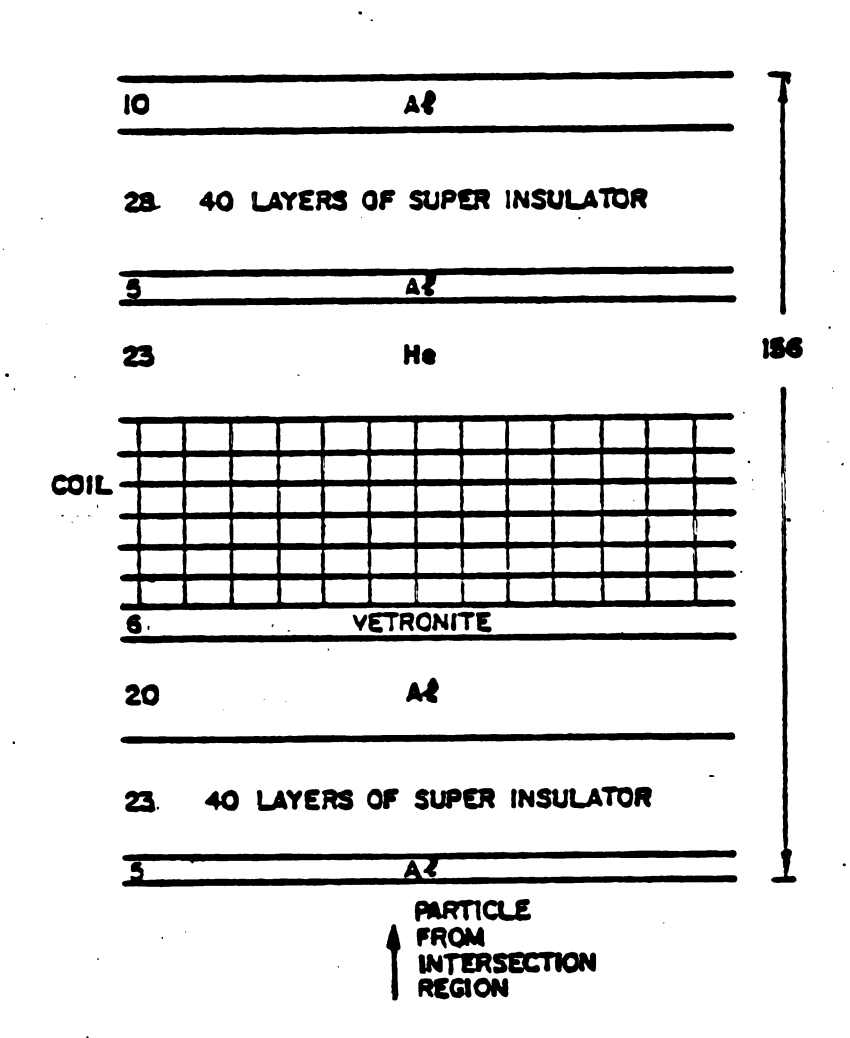


Figure II-8: Coil Cross-sectional View.

ove:

bein

pass

to t laye

stra

prov

by a

goin them

aver.

15-7

ieng

syst time

Part

in th

Was ne

over the warm bore (138 cm in diameter), with the worst non-uniformity being near the holes in the iron end pieces through which the beam pipes passed.

Particles reaching the B counters and the lead glass arrays had to traverse the coil and its aluminum dewar. The coil winding was five layers of a conductor that consisted of niobium-titanium superconducting strands embedded in a copper wire matrix and given mechanical strength by a steel core; strips of pure aluminum surrounding this matrix provided a current path and thermal sink in the event of the magnet going normal. The layers were partially wrapped in an insulator to hold them apart while allowing free circulation of the helium. The total average thickness of material in the solenoid coil was: 7.5 cm of Al, 1.25 cm of fiberglass, 0.12 cm of steel, 0.075 cm of Cu, and 0.025 cm of Nb-Ti. This structure corresponds to a thickness of 1.0 radiation lengths (see figure II-8).

While the magnet itself was quite reliable, the refrigeration system was considerably less dependable; significant amounts of running time were lost due to compressor problems.

II-5. The Drift Chambers

The drift chambers provided momentum analysis of charged particles over the full azimuth by measuring their radius of curvature in the magnetic field of the solenoid. Because of the high magnetic field produced by the superconducting solenoid only a small lever arm was needed to measure the momenta of charged particles up to a few GeV.

t o

> the Fig Con

5)

de

tur sha

:h

à.

ec (a

aul:

Ĩħ,

?\$\$!\$(

Maper:

The chambers were cylindrical, but constructed in sectors previously assembled in the laboratory (see figure II-9) [CAM78]. There were at least four sectors in any azimuthal direction and five in some places. Three complete cylinders, DCM1-DCM3 were in place and six of the ten sectors (DCM4,DCM5) of a chamber, (which prior to the addition of the shower counters were used as a fourth complete cylinder), were inserted in available spaces between DCM2 and DCM3. In front of the lead glass acceptance they remained outside DCM3 (as indicated in figure II-5).

Each sector had two drift chamber gaps of an adjustable field design. A diagram is shown in figure II-10. There was an offset between the drift cell in the two gaps to help in the resolution of the left-right ambiguity. Every gap had a cathode plane on both its surfaces consisting of printed circuit copper strips. The 20 μ m gold plated tungsten sense wires, with a tension of 40 g, alternated with field-shaping wires of 100 μ m copper beryllium stung at a tension of 100 g. The gap width was 0.6 cm. The sense wires were held at 0.3 cm from the cathode planes by means of glass beads placed every 50 cm along the wire and maintained at a voltage of 1.7 kV.

The time recorded on a sense wire measures the azimuthal coordinate of a particle hit. For the measurement of the Z coordinate (along the wires) delay lines were glued opposite to each sense wire. The times of the induced pulses (caused by electromagnetic shower multiplication on the sense wires) in these were read out at each end. The delay lines were chosen to have a high impedance (550 Ω) and low resistence/impedance ensuring good voltage/noise rejection and low dispersion. Close tolerance specifications during manufacture led to

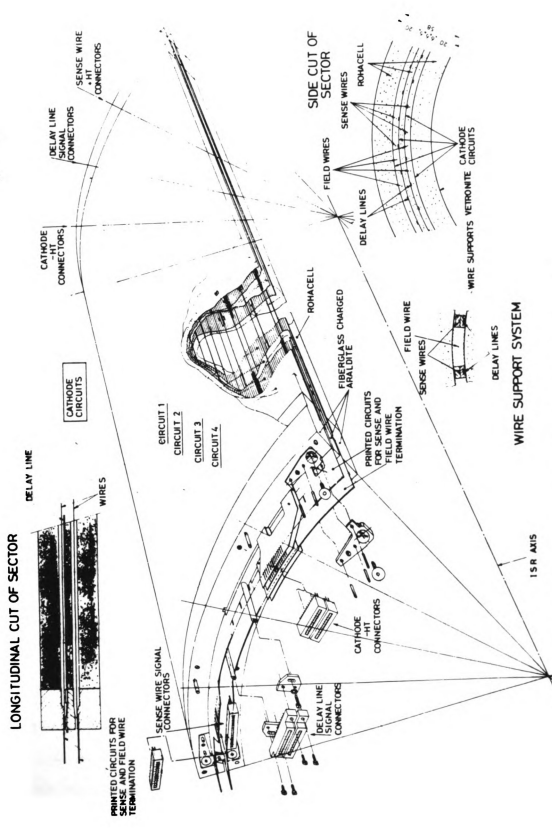


Figure II-9: Drift Chamber Sector Assembly.

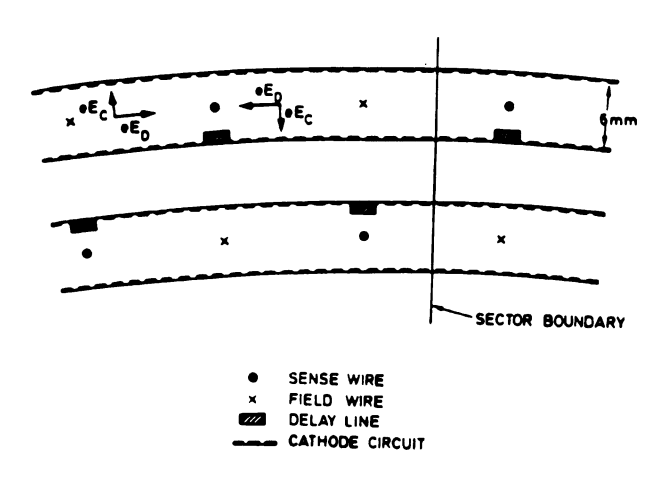


Figure II-10 : Drift Chamber Cross-sectional View.

line to line variation in velocity (2.3 ns/cm nominal) being less than 3 % and the internal reflections less than 1 %.

The basic cylindrical shape of the chambers was formed of moulded Rohacell (This is a polymethacrylimide foam manufactured by Rohm Gmbh.). These main forms were mounted in precision diecast aluminum end pieces. Since Rohacell is hygroscopic an outer layer of vetronite (fiber glass) was added to exclude moisture. In the case of DCM1-DCM3 the end pieces were semi-cylinders and contained several sectors. Each group of sectors mounted in their end piece could be alignmened as a unit.

In order to compensate for the Lorentz force on the drift electrons caused by the solenoid field, the voltages supplied to the individual cathode strips were adjusted to result in a field pattern with both a tangential drift angular component Ed, and a compensating radial component Ec as shown in figure II-10. The voltage on the cathode strips could be individually adjusted to account for the magnetic field effect. The choice of Ec and Ed is dependent on the gas used in the chambers. A monatomic gas would yield a drift velocity proportional to the drift field, which would complicate the operation of the chamber since a good position resolution requires a precise knowledge of the time-distance relationship. This relation is less critically dependent on the exact details of the electric field pattern in the chamber if one chooses a polyatomic gas, in which excitation of low-lying energy levels causes a saturation in drift velocities: once above some critical electric field value a velocity plateau is reached. The gas selected was a 50-50 % by volume mixture of Argon and Ethane, which resulted in an Ed of 1.0 kV/cm and an Ec of 1.2 kV/cm. The drift velocity was approximately $0.5 \times 10^7 \, \text{cm/s}$. For these chambers this corresponds to a maximum drift time of $0.5 \, \mu \text{s}$.

The drift chambers were powered by DanFysik Supplies. Current monitoring devices were set to turn off the high voltage if the currents drawn by the chambers became too large. The voltages to individual drift chamber cathode strips could be controlled using plug-in cards from the counting room.

Placing the chambers in a test beam (at the CERN PS) allowed the extraction of some chamber parameters such as the delay line velocities [NIC82]. However, the presence of the magnetic field, the interacting beams and the need of a precise chamber position (alignment) meant that the other parameters had to be measured in place.

Alignment and the correct parametrization of the time-distance relation are crucial for obtaining a good momentum resolution. The alignment was carried out between running periods. Data were taken with the magnet on using the "Y" counters (see section II-10.f) triggering in cosmic rays. Tracks were fitted using a simple time-distance relationship and the exact position of the chamber half-cylinders was adjusted in the off-line analysis to minimized these residuals. This was an iterative process.

The time-distance relationship has to be obtained for the actual data taking conditions. The time-distance relation was parametrized by a quadratic in time multiplied by a small angular dependence. These factors were different for each gap. The best position resolution was obtained with a r.m.s. of 400 μ m. This was converted to momentum resolution with a Monte Carlo which generated points of well defined tracks and observed position resolutions. The overall momentum

of [N

> ta in

> > ph se

Th Pr

tr. de

ar:

We Wr

Ty:

0n1

resolution obtained was $\Delta p/p = 0.07 \cdot p$ (p in GeV), varying with the number of points and event multiplicity between values of 0.03p to 0.15p [NIC82].

II-6. The Back Lead Glass Arrays.

The lead glass arrays were the same as used in the R108 experiment [BEA74,ANG78]. The operation of a lead glass detector is based on the principle of total energy absorption. Photons or electrons incident on the lead glass initiate a shower of secondary electrons and photons. The refractive index of this SF5 lead glass (for composition see Appendix C) was such (1.67) that the electrons in the shower radiate Cerenkov light until they have a kinetic energy of less than 127 keV. This light was collected by phototubes at the end of the glass blocks. Provided that the lead glass array is made so thick that it contains all the shower, the light collected will be proportional to the energy deposited.

The back glass array of 17 radiation length-deep blocks (figure II-11) ensured that the majority of the shower was contained within the array. An array consisted of 168 SF5 lead glass blocks arranged in a 12 (vertical) by 14 (horizontal) matrix, the overall dimensions of which were 180 cm by 210 cm. Each block was 15cm square, including its wrapping which was aluminized vinyl and soft iron foil with an outer mylar layer to ensure electrical isolation [BEA74]. The blocks were mostly 40cm long (17 radiation lengths) but the outermost blocks were only 35cm and were arranged as seen in figure II-11. An RCA-8055 5"

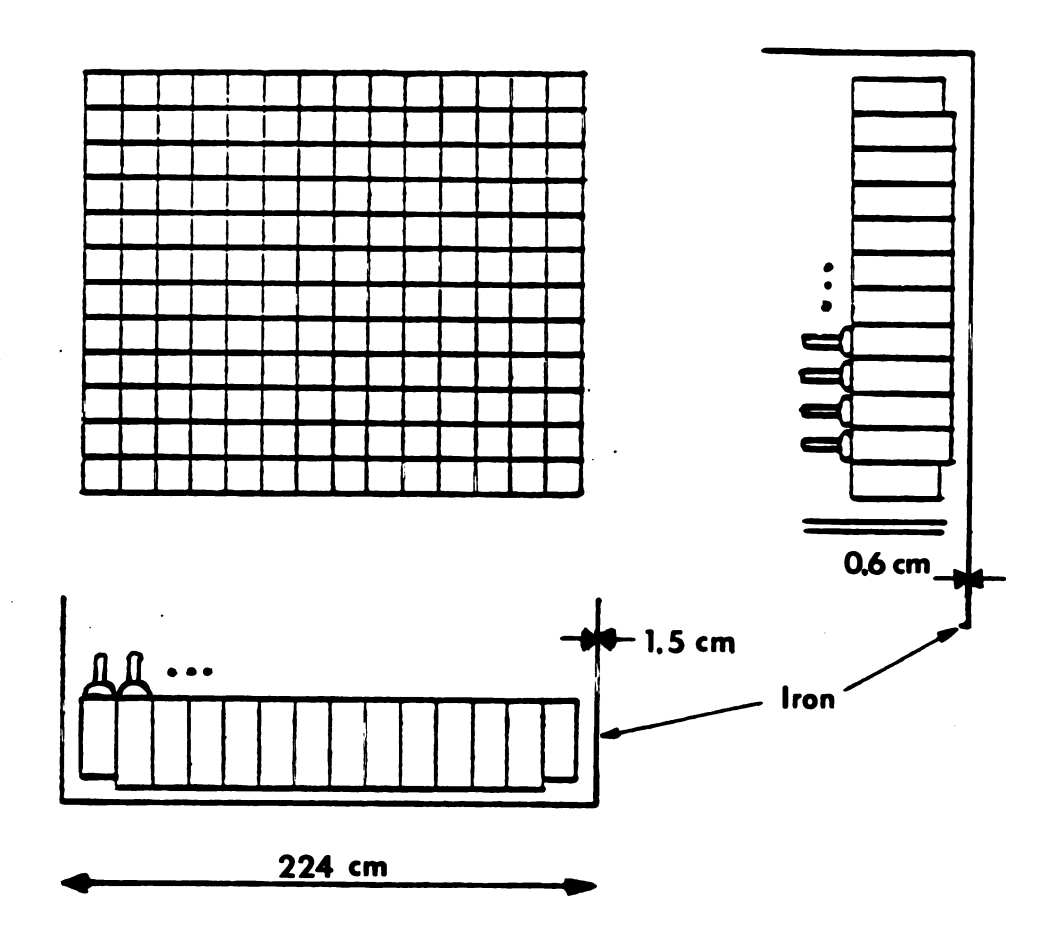


Figure II-11 : Back Lead Glass Array.

photo-multiplier tube was glued to the back face of each block using HE10 optical glue. Every block had a small light source on its front face
to facilitate calibration (This will be explained later).

The high voltage supplies to the lead glass arrays were Heinzinger HN 3200-0405. The output of these were fed into Oxford made stepping boxes which supplied 20 outputs in increments of 20 or 40 volts. Matrix boards and Zener diodes pegs then allowed the individual photomultipliers to be supplied to within 5V of the optimum value.

The tubes were surrounded by a μ -metal magnetic shield and the whole array was further shielded from the solenoid fringe field by an iron cage consisting of a 6 mm thick plate of 247 cm by 224 cm front face, and 1.5 cm thick, 88 cm deep sides. The arrays were mounted on a train which permitted them to be withdrawn when the ISR was being filled with protons. This feature was necessary to prevent radiation damage to the glass (yellowing). They also provided mobility to allow the retraction of an array as discussed above.

II-7. The Front Lead Glass Arrays.

Original to the R110 experiment was an extra lead glass Čerenkov counter array in front of the old (back) array sandwiching the MWPC (Strip Chambers). This new array consists of 34 blocks, of the same material the back glass arrays were made of, arranged as shown in figure II-12. The overall dimensions of the array were 102 cm by 141.6 cm (Y by Z). Each block was 10 cm square. The vertical blocks were 50.2 cm long and the horizontal 35.2 cm long. The total array was then approximately

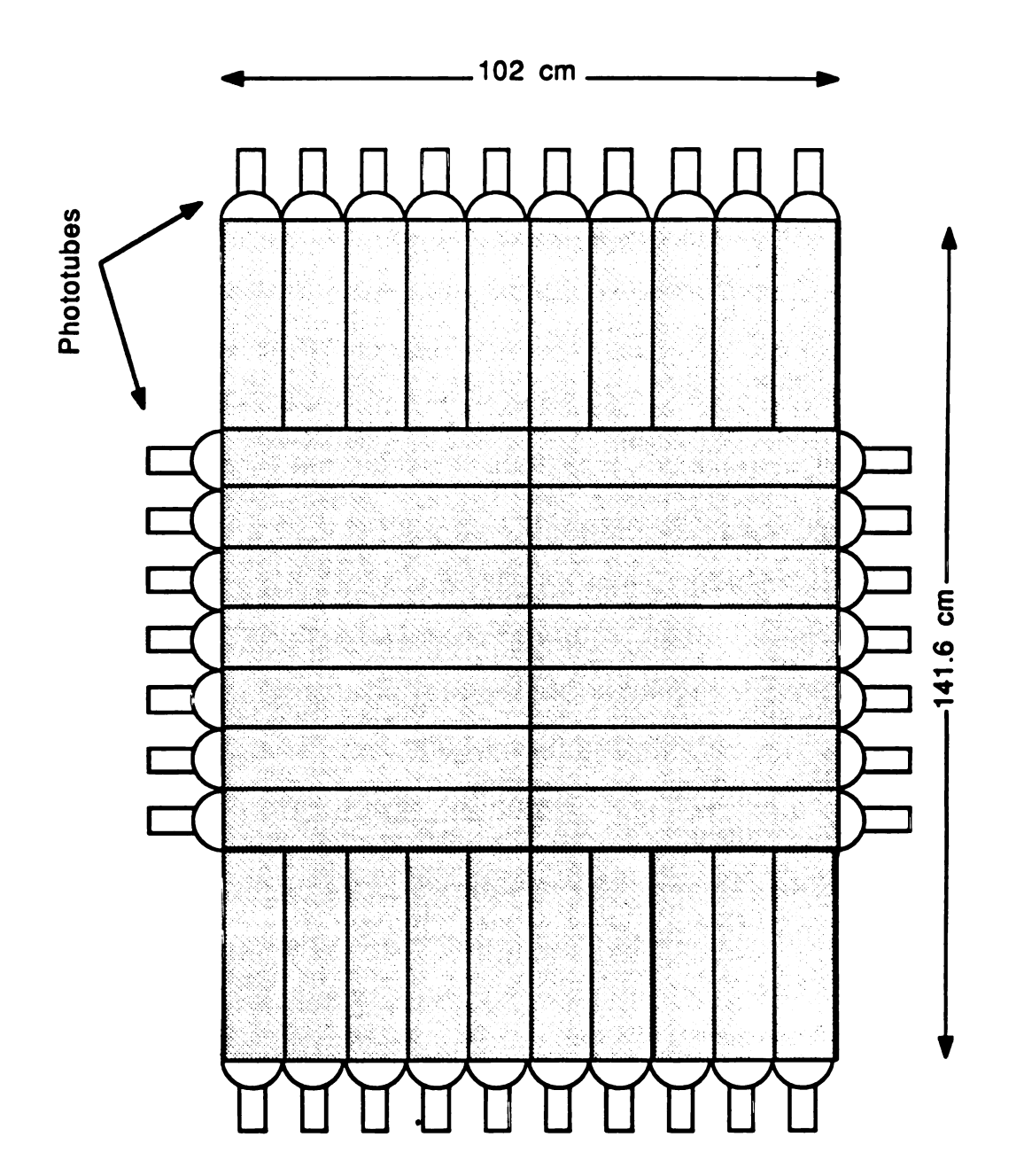


Figure II-12 : Front Lead Glass Array.

4.2 radiation lengths in depth. The phototubes collecting the Cerenkov light were at the sides (as shown in figure II-12), therefore the collected light travelled perpendicular to the direction at which the particles struck the glass. This made the light collection in the front glass less efficient. Due to the complicated geometry of these arrays they were used mainly for energy and not position measurements.

In order to improve angular resolution the strip chambers and glass arrays were placed about two meters from the intersection. It was undesirable to allow the shower to spread before measurements in the strip chambers were made. The addition of this new array provided an active converter close to the strip chambers. By requiring non-conversion in the solenoid coil (using the B counters) the showers measured in the strip chambers were restricted to those that have been produced in the front glass array.

II-8. The Shower Counters.

The shower counters consisted of 32 azimuthal segments, grouped into 4 sets of eight, two modules above and two below the intersection region. Each set of eight (SCM1-4) was an independent instrument encased in its steel box. The shower counter layout is seen in figure II-5.

Because of the return yoke of the magnet, a substantial fraction of the solid angle could not be easily instrumented for electromagnetic detection outside the magnet; the shower counters overcame this difficulty by being inside the solenoid. The construction chosen was a wedge-shaped sandwich of lead and scintillator the principle of which

e: ţ, :: 10 ez 010 a f ea (рох pox and was to integrate the electromagnetic shower curve by sampling it at several points in its development. The counters consisted of 16 layers each of 0.5 cm thick lead followed by 0.4 cm thick scintillator. The first four layers of scintillator were read out separately and called C counters. The remaining 12 layers constituted the D counters. A shaped supporting iron plate was necessary before the first layer of lead; this was 0.6 cm thick for the upper modules and 0.3 cm for the lower.

The segments were individually wrapped in aluminum foil and it was necessary to put two layers of 100 µm thick mylar between segments during construction (for lifting). The light from the scintillator was collected at both ends of each segment. Thus each module of eight segments was monitored by 32 phototubes, four per segment; two on each end of a segment; one reading the first 3.6 radiation lengths, the other the last 10.7 radiation lengths. The 105 cm long shower counters were located inside the solenoid, but the phototubes were outside; 85 cm long light guides going through holes drilled in the pole pieces were employed. These butted onto the internal light guides via a dry joint, close contact being insured by mechanical pressure.

For calibration purposes an optical fiber capable of delivering a flash of light to each of scintillators was attached to each end of each segment. These left the solenoid and were glued into a "flasher box" containing a krytron light source. An additional fiber left this box and entered a reference counter phototube. There was one flasher box and one reference tube per shower counter module.

P 0: Ϋâ ٧ņ 8.5

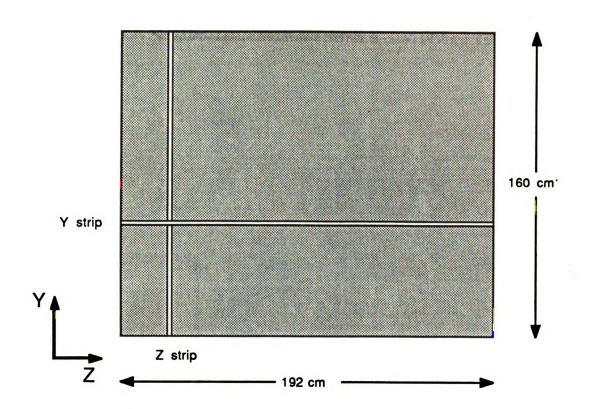
II-9. The Strip Chambers.

The most important part of the detector for this dissertation was the strip chambers. They were designed for the purpose of isolating single photon showers produced in the front glass.

The chambers were multi-wire proportional chambers (MWPC) [DIM78] with 200 cm (horizontal) by 180 cm (vertical) active area sandwiched between the two glass arrays (see figure II-13). For photons converting in the front glass, these chambers allowed considerably better spatial resolution than that afforded by the back glass array alone.

The 1000 anode wires per chamber were 20 µm gold plated tungsten strung vertically in a pitch of 2 mm and held in three places along their length by support wires. They were maintained at 4.5 kV. The support wires, which ran horizontally, were electrically isolated from the anodes. There were cathode planes each side of the anodes at a distance of 1.0 cm. They consisted of 0.8 cm wide 35 µm thick etched copper strips on a 75 µm Kapton board at a spacing of 1.0 cm (resulting in a 2 mm gap between strips). The 160 strips on the plane nearest the intersection region ran horizontally, while the 192 strips on the other plane ran vertically. Both sets of cathode strips were read out, so that Y and Z coordinates were available. However, this gave projected signals of the showers along Y or Z rather than a fully two dimensional view.

Figure II-13 shows a view of the chamber cross-section. The walls of the chambers were constructed of 0.9 cm thick styrofoam to which the cathodes boards were glued with abundant Epoxy (to give support). All this was inside a 230 μ m thick polythene gas envelope.



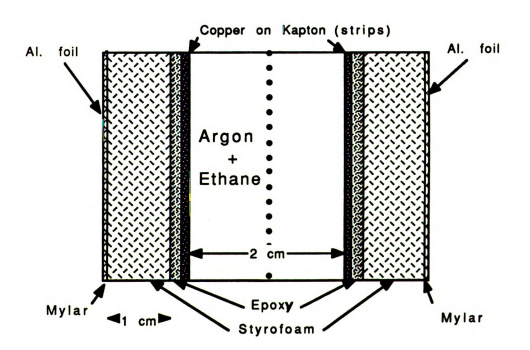


Figure II-13 : Strip Chambers Cross-sectional View.

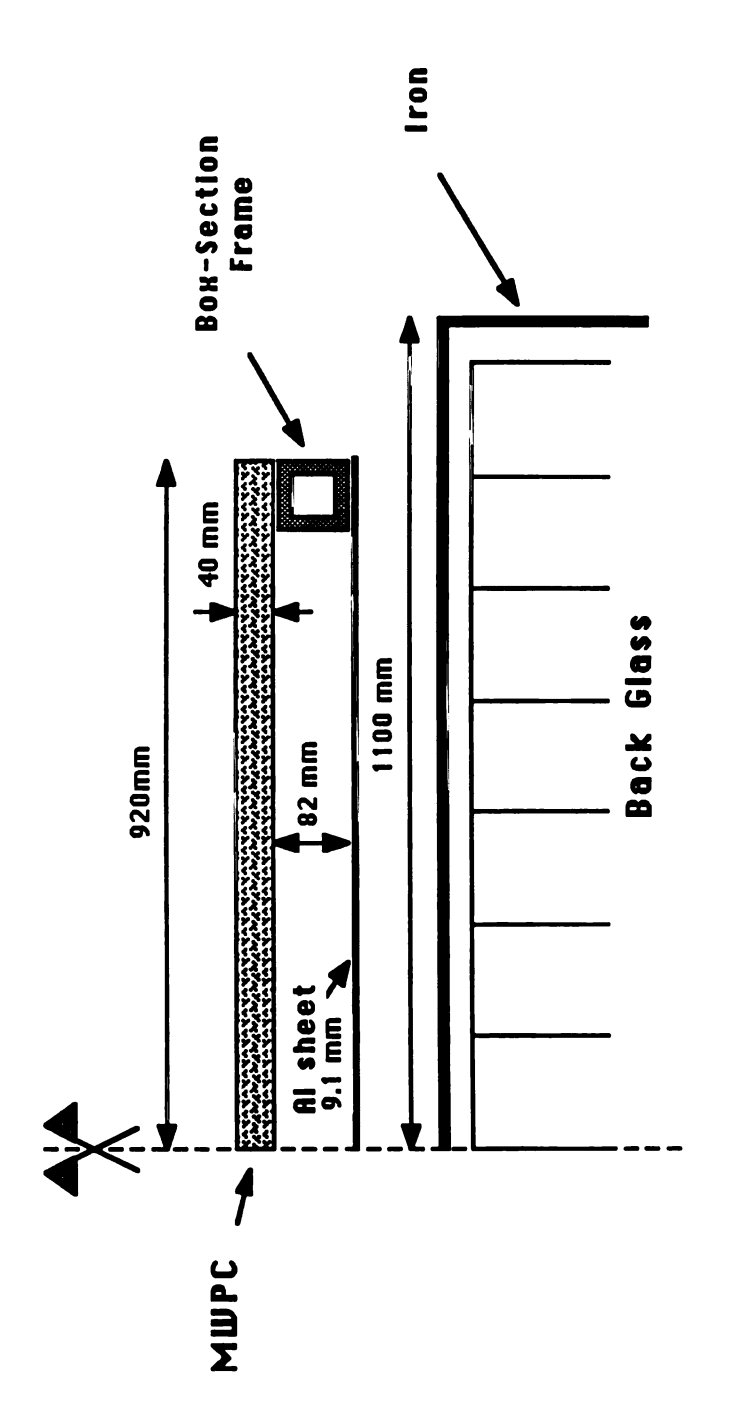


Figure II-14 : Strip Chamber layout.

Furthermore, the whole chamber (including the first pre-amplifiers) was placed inside a Faraday cage of aluminized mylar. Outside the gas bag, but still inside the Faraday cage, towards the back glass, was a 0.91 mm aluminum plate as a strong back for the chamber assembly. The resulting total thickness was about 0.02 radiation lengths. In figure II-14 a diagram of the total array is shown. The gas used was a mixture by volume of 70% Argon and 30% Ethane with a 0.1% addition of Freon to help prevent sparking problems.

The strip chambers were powered by DanFysik supplies. The 704 signals from strips in the strip chambers were fed immediately into preamplifiers with an appropriate input impedance. These drove buffer amplifiers, mounted near the chambers, via co-axial cable. The buffers supplied push-pull outputs to 120 m of twisted pairs cable which went to the counting room. ADCs designed and built at Columbia University then digitised the pulse height from all strips [DIM78]. A hardware processor supplied CAMAC with pedestal-subtracted digitized amplitudes for all the ADCs with a non-zero content. In this way the amount of redundant information written to tape was minimized.

II-10. The Scintillators.

a.- The A counters. The A scintillators formed a complete barrel hodoscope of 32 counters 87.5 cm long around the intersection region at a radius of 26.5 cm (figure II-5) between DC1 and DC2. They were 0.6 cm thick and were physically demountable in two half-cylinders which had 0.1 cm thick aluminum covers on each surface. The total thickness of the

A counters was 0.036 radiation lengths. The counters were read out by Mullard XP2230 high gain phototubes at both ends after a curved length of light guide consisting of 1.88 cm diameter Perspex between 186 cm and 226 cm long. Because of the long light guides and thickness of the scintillators the resolution of the A counters was limited by photoelectron statistics; only a few per minimum ionizing particle being expected.

The A counters were very close to the intersection region therefore the light guide damage yellowing by radiation was severe; at one time during the course of the R110 experiment it was found necessary to heat treat the guides to recover transmission properties. Timing was the primary function of the A counters. The phototubes selected had a 1.6 ns rise time. They could also give information regarding the number of charged particles produced in an event or "multiplicity". Their times were recorded in the same system as the drift chamber read out and were used as the zero time of the event. Thus the resolution of the drift chambers depended in part on the time resolution of the A counters.

b.- The B counters. These counters formed a partial cylinder of 184 cm long and 1.0 cm thick scintillator slabs at a radius of 90 cm just outside the coil dewar, covering all the solid angle not covered by the return yoke (figure II-5). There were 24 in all; each was 11 cm wide and covered an azimuth angle of approximately 7°. The light guides were short, and 56 AVP phototubes had sufficient gain as to be used. High voltage for the B counters was supplied by means of two 32-channel LeCroy HV 2032s which were adjustable to ± 1 Volt. They also were used to supply high voltage to other scintillators (ST and MM, see below).

The B counters have been used in various ways in our experiment. For the present dissertation, the most important was to indicate when a photon had converted to charged particles and started a shower in the coil. It was also possible to extract longitudinal position information on the basis of time differences between the pulses from either end of the counter, or from the relative pulse heights.

c.- The L counters. The L counters were maintained and operated by the ISR division. A copy of the signals was supplied to the R110 counting room and used for background monitoring.

The L counters were 10 m upstream in pairs separated by 3 m and measuring 25.5 cm by 21 cm, with 1 cm thick scintillator. A coincidence was formed between the pair of scintillators in pairs and a background count was recorded for each hit. They were useful to verify beam losses, since as the beams spread the background rate measured by these counters increased. The ISR operator acted to remove particles at the periphery of the beams when the L count rate became too large.

d.— The MM counters. These were the main luminosity monitor counters. There were eight scintillator slabs measuring 43 cm by 20.5 cm mounted in pairs on four of the corners of the magnet. Due to the presence of the low-β quadrupoles, our intersection was more crowded than most intersection regions. Rather than placing the luminosity monitors near the beam pipe, where they would intercept more events, they were placed one on each side of the intersection, see figure II-15. From the interaction region and looking inwards these appeared top-right

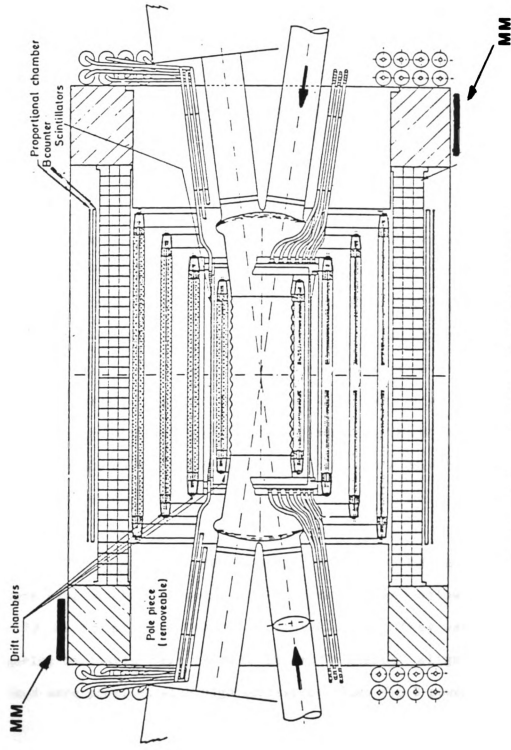


Figure II-15: Position of MM Scintillators.

and bottom-left, looking outwards they were top-left and bottom-right; thus an interaction producing back to back particles would have hit two sets of MM counters, one top set and one bottom set; a coincidence of four scintillators in this combination was defined to be the real event. As explained before, the rate of such coincidences was used to measure the luminosity in our intersection.

- e.- The ST counters. A 190 cm long vertical scintillator 7.5 cm wide and 1.0 cm thick was positioned behind each glass array. They could be moved by remote control behind each column of blocks in the glass array. Triggering on energy deposition in the ST's ("straight through") gave data containing a substantial proportion of muons or hadrons that did not interact in the lead glass. These deposited a characteristic amount of Cerenkov light in the lead glass blocks, which could then be used as a calibration check and stability monitor. The ST counters were read out at both ends and a trigger was defined as a coincidence between pulses from each end.
- f.- The Y counters. 105 cm long, 15 cm wide, 1.0 cm thick, the Y counters were mounted on top of the return yoke and below it. There were 12 in total, each read out at both ends. They were used for triggering on cosmic rays to help in drift chamber alignment. These counters were provided with high voltage by Fluke 415 B power supplies.

CHAPTER III

Data Taking and Calibrations

III-1. Control Room.

Most of the electronics and a Hewlett-Packard (HP) 2000 minicomputer were situated in a room just outside the experimental area. From there experimenters were able to monitor and control the collection of data. Single-person shifts lasting eight to thirteen hours covered the data-taking which, due to the high reliability of the ISR often covered several days of continuous running.

The trigger thresholds were set by hand on the electronics and rates were monitored during data taking. The HP 2000 mini-computer allowed the experimenters to have on-line access to the data collected. Event dumps and special histograms made it possible to monitor the data quality.

The lead glass arrays were moved by remote control to the desired position and fully retracted when the ISR beams were stacked. The position and movements were viewed through a closed-circuit TV monitor. Information from the ISR beams were constantly monitored and direct communication was maintained with the ISR control room. This made

possible interaction with the beam handling in order to reduce the beam-associated backgrounds.

The writing of the data to tape was controlled by the HP 2000. The speed of tape writing depended on the trigger selected and the instantaneous luminosity of the ISR. A typical 1600 bpi tape for the triggers under discussion was filled with raw events in about 45 minutes.

III-2. Calibrations.

Calibration refers here to the process of determining the energy scale of the calorimeter. I will only describe in detail the calibration of the lead glass arrays used in this dissertation.

We can distinguish two kinds of calibrations done during the experiment. First is the initial calibration, where the calorimeter is exposed to an energy standard to determine the energy-to-signal relation. The initial calibration of each individual block of the arrays was done with an electron beam at the CERN PS before our MSU group joined the collaboration and is described elsewhere [NIC82]. The second is maintanance calibration, an on-site calibration done during the running of the experiment to track changes in the parameters determined in the initial calibration. There are many time-dependent effects in the energy-to-signal relation. An important factor in this experiment has been the radiation damage of the glass and material of transmision (wires and light guides). Other sources can include geometrical or structural changes, aging of the electronic read-out, etc.

I will describe here only the on-site calibration of the glass arrays. The back lead glass arrays were monitored using light sources produced by sodium iodide (NaI) crystals doped with Am^{2*1}. The Am^{2*1} decay produces 5 MeV α particles and these produce scintillation light pulses in the NaI which are constant and well defined in nature since the range of the α particles is much less than the size of the crystals. Typical rates were 100-150 scintillations per minute. A source container was in a small aluminum can with a glass window glued onto the front face of the lead glass block. The lead glass calibration could vary with time due to glass yellowing by radiation damage, or changes in the phototube gains, etc. The NaI pulse heights were measured at the end of every ISR stack (ISR running period, 3 to 12 days). The glass blocks were calibrated by the known energy equivalence of the NaI scintillations (originally measured at the same time in the electron beam PS calibration).

There were two problems associated with this procedure. First, NaI is hygroscopic so the crystal must be well sealed. If moisture were to enter the crystal, the light characteristics would be irreversibly changed. At first 40% of the sources were found to have this problem due to manufacturing errors. A second batch of sources, after many talks with the manufacturers, was found to behave better.

To correct for this problem a second method of calibration was also used for the glass. This used a special trigger called "straight throughs". The ST counters situated behind the array triggered on particles (charged hadrons) going through the glass blocks. The spectrum formed by the Cerenkov light of these particles had a broad peak which

was found to have an energy equivalence of about 450 MeV. These runs were performed every two or three stacks and monitored NaI changes.

The front glass arrays were also calibrated using Am^{2*1} sources in NaI. They were monitored by a flasher system similar to the one used for the shower counters [NIC82]. The flasher system was used before every ISR stack. The method of monitoring the glass blocks with respect to the reference NaI was to generate a flash of light from a Krytron tube, a fixed fraction of which went to each block and to a separate "reference counter" phototube. The light from the Krytrons was fed to the block beside the phototube end. The Krytron tubes were mounted in small boxes ("flash boxes") from where the optical fibers carried the light to the blocks. Measuring the NaI to flasher ratio in the reference counter and the flasher to signal ratio in the blocks allowed one to transport the reference to each block.

The calibration of the NaI to flasher ratio in the reference counters and the flasher to a 4 GeV electron beam ratio was performed at the PS and is described elsewhere [NIC82]. For the front glass a correction was applied to the phototube voltages in order to account for changes in the glass calibration.

III-3. Trigger Logic.

In collider machines at high energies the rate of interactions is enormous, therefore it is necessary to select which events will be recorded. The requirements for the data to be recorded are defined by

the "trigger logic". In this experiment all the main triggers involved electromagnetic energy deposition in the calorimeters.

The R110 experiment ran normally with four or five simultaneous triggers. More than one trigger could be satisfied at the same time. Since the trigger used to collect the data presented in this dissertation required a different lead glass arrays position than the other triggers, no other trigger involving back glass energy deposition could run at the same time. However, triggers requiring energy deposition only in the shower counters were taken simultaneously.

Our experiment had two levels of triggering decision. A fast hardware (electronic) trigger made decisions using analog pulses from the phototubes and controlled whether the event was digitized. Then a software trigger using digitized data in a HP2000 mini-computer placed more stringent requirements on the events. This latter will be referred to as "on-line" filtering. The trigger used in this dissertation was called "glass singles with half-back geometry". It was designed to require at least one energy cluster in the back glass array with an energy greater than a certain threshold.

The "glass singles" trigger looked for electromagnetic energy deposited in the glass arrays, adding the energies in the front and back glass arrays. The lead glass block voltages were adjusted so that a given pulse height from any tube was equivalent to the same energy. Thus the sum of pulses was in principle equal to the total energy deposited.

The trigger took advantage of the segmentation of the arrays to attempt to trigger on single particles. The two photons from the decay of a neutral pion of 5 GeV/c transverse momentum (in the ISR center of mass) will fall within a 3 x 3 matrix of the glass 95% of the time for

to f fı Ē(du de 510 the inside array and 98% of the time for the outside array. The difference is due to the opposite sign of the Lorentz transformation in the two sides. Requiring that the pulse height in a 3 x 3 matrix exceeded a threshold would act as a good single particle detector.

There are, however, one hundred and twenty 3 x 3 submatrices in each array and this would require an enormous number of discriminators. To avoid this, a set of blocks in four adjacent rows and the set of blocks in four adjacent columns defined what was called "roads" and "cols". Each array was divided into six "roads" and five "cols", offset from each other by two rows or columns respectively. Every possible 3 x 3 submatrix in a array lies entirely within exactly one overlap region of a "road" and a "col". The trigger required that one "road" and one "col" satisfy individual discriminator levels in coincidence with a higher discriminator level being satisfied by the sum of the side.

Figure III-1 shows a flow chart of the "Glass singles" trigger logic arrangement. The phototube signals were fed to a splitter-mixer system where part of the signal (about 1%) was diverted from the ADC's to the trigger logic electronics.

The splitter-mixer system provided four kinds of output (in figure III-1). The first output defined the NaI trigger. Each signal from an entire column of blocks was added and discriminated. A multiplexer under CAMAC control then selected one column at a time during the block calibration run to record NaI events.

The second and third outputs permitted one to look for energy deposition in the 3 \times 3 matrix "cluster". The second output sums all the blocks in a column, then the column sums in sets of three in all

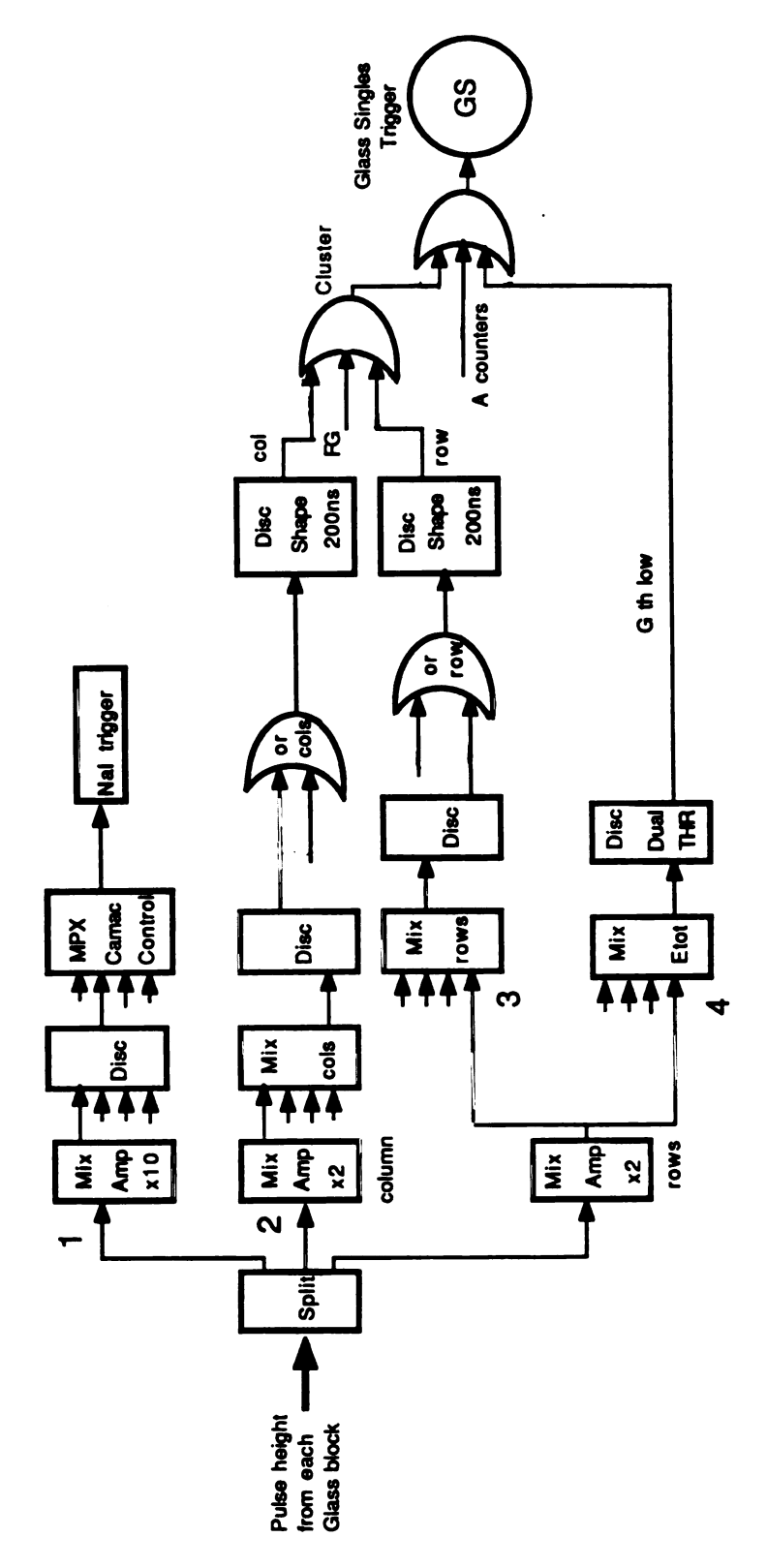


Figure III-1: Flow Chart of the Trigger Logic.

possible combinations of neighboring columns (cols). The third kind of output does the same for rows of blocks (roads).

A coincidence between a "road" and a "col" then defined a 3×3 array (cluster). The energy in this 3×3 array was added to the energy found in the front glass array. If the total energy was greater than the energy threshold taken, the event was recorded.

As previously stated, each lead glass array was set to produce the same pulse height for the same incident energy. Therefore the linear sum of the pulse heights in any set of blocks would be proportional to the energy deposited. Since the arrays are approximately at 90° to the beam line the energy deposited is approximately equal to the transverse momentum. Thus an energy threshold (pulse height cut) will generate a trigger for events satisfying a minimum transverse momentum. This was made with the fourth output. The threshold, cluster busy signal and an A counter signal were then put in coincidence to define the glass singles. At normal ISR luminosities reached in intersection I1 ($\sim 5 \times 10^{31}$ cm $^{-2}$ s $^{-1}$), the rate of taking data resulted in about 4 events/sec.

Other triggers used in our experiment are described elsewhere [ANG82, HUM88, NIC82, YEL81]. They included ETOT, the total energy deposited in all electromagnetic calorimeters (jet studies); PAIRS, that required two clusters, each above a given threshold, with the sum of these being greater than a second threshold (electron pairs studies). Some requirements in spatial position of the clusters could also be demanded.

Another trigger used to gather data for the analysis presented in this dissertation was the η° trigger. The hardware trigger consisted

of "glass singles" events where either side could trigger. In addition the B counters were used in veto and a requirement of a signal in the A counters was also required. The logic representation of the trigger was:

$$(\mathtt{A} \geq 1) \cdot \big\{ \mathtt{G}_{\mathtt{I}}(3.0) \cdot (\bar{\mathtt{B}}_{\mathtt{4}} \cdot \bar{\mathtt{B}}_{5} \cdot \bar{\mathtt{B}}_{6} \cdot \bar{\mathtt{B}}_{7} \cdot \bar{\mathtt{B}}_{8} \cdot \bar{\mathtt{B}}_{9}) + \mathtt{G}_{\mathtt{0}}(3.5) \cdot (\bar{\mathtt{B}}_{\mathtt{16}} \cdot \bar{\mathtt{B}}_{\mathtt{17}} \cdot \bar{\mathtt{B}}_{\mathtt{18}} \cdot \cdot \bar{\mathtt{B}}_{\mathtt{19}} \cdot \bar{\mathtt{B}}_{\mathtt{20}} \cdot \bar{\mathtt{B}}_{\mathtt{21}}) \big\}$$

 ${\bf G_I}$ and ${\bf G_O}$ represent "glass singles" hardware logic, with the energy threshold used shown in parentheses. The B counter number used in the veto appear as subscripts (see figure IV-3 for B counter number definitions).

Another configuration used for the η° data gathering was a "double glass trigger" that took two cluster triggers having a summed energy greater than a given threshold. More details of these η° triggers are given in Appendix E.

III-4. On-line Programs.

Various checks on the detector could be requested via the HP 2000 mini-computer. There were programs to check minimum ionizing peaks in the A and B counters, glass and shower counter calibration, ADC's and TDC's pedestals and the drift chamber and strip chamber read-out. The programs to control the front glass and the shower counter calibration through the flasher system and the "straight through" program also were run through the HP-2000.

An on-line filtering program sharpened the trigger by executing a CAMAC read on the glass ADCs, going now to two dimensional 3×3

clusters, not projections. The program searched for the highest energy 3 x 3 submatrix centered on a block with energy greater than 400 MeV and required an energy threshold on each. This on-line filter was measured to be 100% efficient (in terms of events eventually processed) and decreased the trigger rate by a factor of four from the rate satisfying only the hardware trigger.

The events which satisfied the trigger were then read in full by the computer and written to a magnetic tape. Each magnetic tape, called a raw tape, held about 8000 events. The information in the ADCs for the lead glass and the scintillators, and the pattern units and scalers was read first as a fixed length buffer. The scalers counted the number of counts received from the luminosity monitors since the previous event was read, the pattern units contained information about the kind of trigger the event has satisfied.

This information was followed by the information from the TDCs for the scintillators and drift chambers. During the reading process the on-line computer compiled histograms on most of the information read. These histograms were viewed regularly on a terminal to monitor the data acquisition process.

III-5. The Data.

The data for this dissertation was collected mostly during 1983, the last year of ISR running. We took a total integrated luminosity of 8.54×10^{37} cm⁻². A total of 928 raw data tapes were written resulting in about 8×10^6 total events registered, with about 80% satisfying the glass

Table III-1: Data. Luminosities and Data Sets.

Data Cot	Trigger	Luminosity	Events	T	Events in
המומ ספו		cm ⁻²	on Con	naw lapes	raw tapes
December 192	mixed eta/gam	•			047,000
	4.5 GeV inside	1.27×10	39990	114	974,000
October '83	outside	1.29 210 37	79109	700	
	Inside 4,5 GeV	2.12	73916	207	2,568,000
Spring '83	inside 3 5/4 5	2.09 x10 37	62086	959	000
B	outside	0.64	53234	767	2,109,000
Before '82	ins/out 3.5/4.5	1 13×10 37	143011	955	000 666 6
		1.13810	1166+1	533	2,22,000
TOTAL		8.54×10	452,246	928	7,883,000

Table III-2: Data. Con Tapes.

CON TAPE	SET	TRIGGER	Integrated Luminosity cm-2	number of events	# of ISR runs
1	DEC'83	MIXED 4.5 GEV INS	1.27X10 37	39,990	145
2	OCT'83	4.5 GEV INS	1.92X10 37	63,883	145
3	OCT'83 Sp. B filter	4.5 GEV INS	0.20X10 37	10,033	27
4	OCT'83	4.5(5) GeV outside	1.29x10 37	79,109	165
5	SPRING'83	4.5 GEV INS	1.83x10	43,000	173
6	SPRING'83	3.5 GEV INS	0.26x10 37	19,086	37
7	SPRING'83	4.5 GEV OUT	0.64x10 37	53,234	73
8	BEF'82	4.5 GEV INS dedicated	0.13x10 37	24,153	34
9	BEF'82	4.5 GEV OUT dedicated	0.21x10	24,722	30
10	BEF'82	MIXED 3.5/4.5 ins/out	0.53x10 37	47,189	48
11	BEF'82	MIXED 3.5/4.5 ins/out	0.26x10 37	47,847	40
total			8.54x10 37	452,246	917

singles trigger. The corresponding total number of events written on the condensed (CON) tapes, after various cuts described in the next chapter, was 452,246.

Most of these direct photon runs were done in three periods of approximately one month each, one in Spring, another in the Fall and the last in December of 1983. Some runs from early 1982 are also included in this dissertation.

A special η° trigger run was performed during Spring '83 where an integrated luminosity of 1.91×10^{37} cm⁻² was taken. The December'83 run was a combined direct photon/ η° trigger trigger that collected a luminosity of 1.27×10^{37} cm⁻².

The characteristics of the different data sets, run periods and luminosities accumulated are shown in Tables III-1 and III-2.

CHAPTER IV

BASIC DATA ANALYSIS

IV-1. Overview of the Basic Analysis.

The method of analysis can be divided into two main stages. In the first, performed mainly at CERN, we went from the raw data tapes to the data summary tapes (DSTs) and then to so-called condensed (CON) tapes. The second stage is the search for direct photons.

First I will describe all of the analysis up to the analysis of the strip chambers information. This is the basic analysis with the purpose of producing a clean sample of strip chamber showers (mainly produced by neutral mesons or direct photons). The search for direct photons was done by analysing the strip chamber data and will be described in the next chapter.

This chapter describes the analysis from the raw tapes to CON tapes and general cuts made afterwards. This includes re-clustering in the back glass array, tracking, vertex finding and energy corrections. The analysis of the CON tape includes cuts on the number of clusters in the back glass, the fraction of energy deposited in the front glass and the tracks pointed to the trigger cluster. Figure IV-1 shows a flow chart of the analysis.

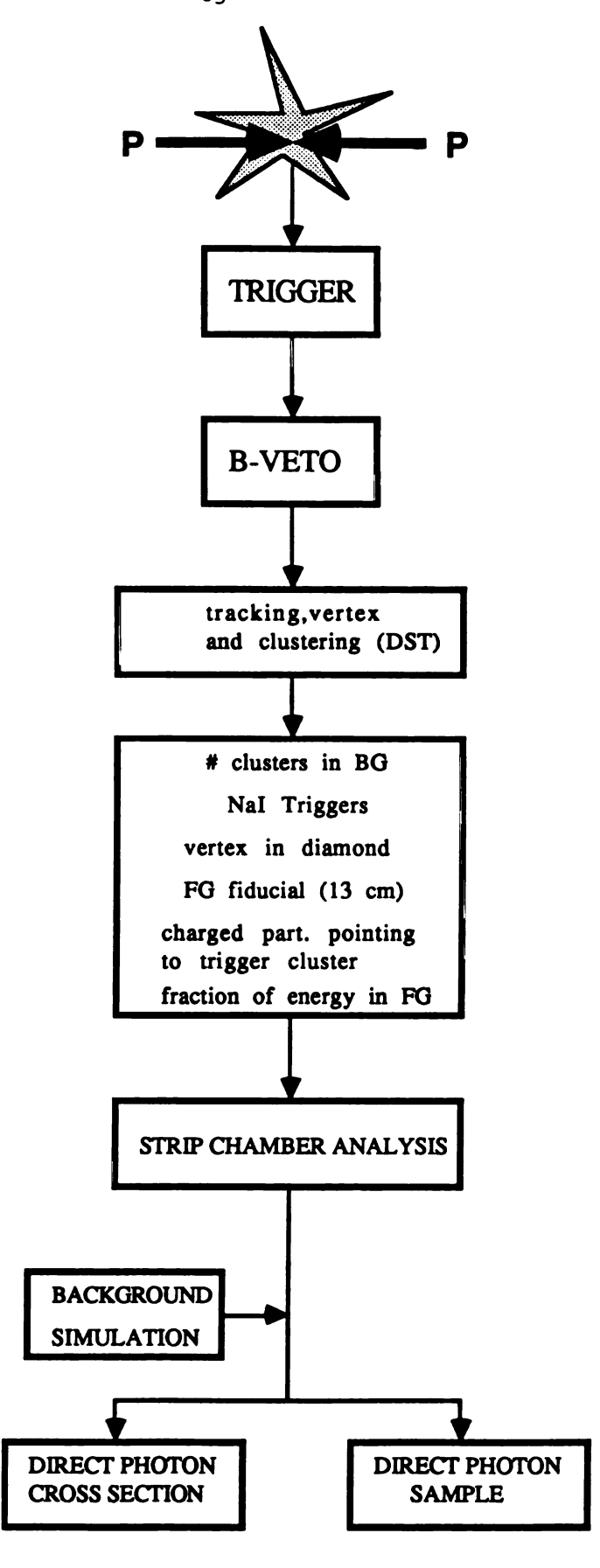


Figure IV-1: Flow Chart of the Analysis.

For the making of a DST tape the B counters were put in veto. This important cut will be explained in detail in section 5 of this chapter. The strip chamber clustering algorithm is introduced at the end of the chapter.

IV-2. Clustering in the Back Glass Arrays.

The standard R110 clustering algorithm to search for clusters in the back glass was used at the CON tape analysis level. First a search for all blocks with energy greater than a seed energy ESEED = 0.3 GeV was done. These blocks were taken as seeds for clusters. Neighbors with energies above a cut-off, EMIN = 0.02 GeV, were added to the seed block and a cluster was formed.

These clusters were then checked to ensure that their shapes were inconsistent with side splash (beam protons interacting in the shielding) or cosmic rays. With this purpose a maximum number of rows, columns and total number of blocks in a cluster was defined, ROWMAX = 4, COLMAX = 4 and NBLMAX = 9, respectively. A minimum energy of a block which can cause a cluster size to be considered too large was fixed on EMCUT = 0.1 GeV. The clusters were also rejected if their energies were above a maximum energy (BLKMAX = 50 GeV), discriminating against possible NaI triggers, if the block with the maximum energy in the cluster was in the edge of the array, or if all of their energy was contained in one block.

At the DST level a different set of values was used for these parameters to relax the restrictions and keep more data for further

studies. They were: NBLMAX = 20, ROXMAX = 5, COLMAX = 5, ESEED = 0.15

The calculation of the cluster positions was done in two steps.

The the first step the center of gravity of the cluster at the front face

the back glass was calculated as:

$$Y_{cg} = \frac{\sum_{i=1}^{n} y_i \cdot E_i}{n} ; Z_{cg} = \frac{\sum_{i=1}^{n} z_i \cdot E_i}{n}$$

$$\sum_{i=1}^{n} E_i$$
(IV-a)

where n is the number of blocks in the cluster, (y_i, z_i) the coordinates

their geometrical centers and E, their energies.

The above calculation approximates an integral over shower shape

by putting all the energy in a block as concentrated at the geometrical

center, which is obviously correct only when the block size is much

larger than the shower. The second step corrects for the fact that the

center of gravity of the energy deposition (cluster) is not at the front

face of the glass and that the energy is not concentrated in the block

center.

The method [ANG82] is based on the study of the longitudinal and ransversal development of a shower. Studying the longitudinal evelopment of the shower inside the glass it was found that the maximum curred around 14.3 cm deep in the glass. The center of gravity was sumed to be at 15 cm from the front face of the back glass in the rection of the shower.

An exponential shower profile [AKO77] of the form:

 $E(r) = E_0 e^{-\left|r\right|/b}$ was taken, where the shower was assumed to have a radial symmetry, r is the radial distance from the center peak, E_0 is the maximum energy at the center and b is a parameter to be adjusted experimentally.

A routine was developed to take the first order position calculations and correct them using a shift in distance due to the exponential assumption. It can be shown [ANG82] that the corrections are given by:

$$\Delta Y = b \cdot \sinh^{-1} [(Y_0/1) \cdot \sinh(1/b)]$$

$$\Delta Z = b \cdot \sinh^{-1} [(Z_0/1) \cdot \sinh(1/b)] \qquad (IV-b)$$

where 1 is the half length of the front face of a block, 1= 7.5 cm; and Y_0 and Z_0 are the positions of the first order center of gravity relative to the geometric block center $(Y_0 = Y_{cg} - Y_{block}, Z_0 = Z_{cg} - Z_{block})$. The parameter b was empirically determined in a test performed at the CERN PS resulting as:

$$b = (1.0+0.4/E) \cdot (1.0+3.0 \cdot \theta)$$
 cm (IV-c)

where θ is the angle of incidence in the XY plane or XZ projection (according to the direction in which the shift is calculated) and E is the cluster energy as measured in the back glass in GeV.

This correction has been shown to improve the position resolution of the back glass. Although is not totally free from errors since it does not include shower fluctuations, the fact that the exponential profile is only a first approximation (a two component exponential profile is more adequate) and the asymmetries caused by angular differences of incident particles.

IV-3. Track Finding Algorithm.

The track finding was a complex and slow process using an average of 2 seconds of computing time per event on the CDC 7600. It has been already fully explained elsewhere [YEL81, NIC82]. Tracks were found starting from points in the outside drift chambers and working inwards. Once preliminary tracks were found, they were fitted to circles in the xy projection, and straight lines in the radius-z projection. This was possible due to the uniformity of the magnetic field over the volume considered. The preliminary track list was then reduced by not allowing more than one track to share a point, except in the innermost drift chamber. A track was required to have at least five points.

When all tracks had been found and fitted, the track parameters were written to DST's, together with all the space points used on the tracks. The corresponding momentum was determined from the radius of curvature of the circle that was the best fit to the points. The Ascoli method [POR79] was used to fit the circle. When the alignment constants were changed, the tracks were refitted from the space points but without going to the track finding again.

IV-4. Energy Corrections.

It was found during PS tests [NIC82] that the response from the phototubes of the lead glass counters decreased when the incident beam was not normal to the block faces. This is because the pulse height from the phototubes is a measurement of the Cerenkov light actually

collected, not necessarily proportional to the energy deposited. The optical properties of the glass, geometry and properties of the conection between phototube and glass influence the amount of light collected by the photocathode.

Defining \mathbf{E}_{raw} as the energy measured by the glass arrays by adding the individual blocks of the clusters, then, the angular dependence of the measured energy studied in the PS calibration has the empirical form:

$$E_{BG} = (1.0 + 0.22 \cdot \theta) \cdot E_{raw(BG)}$$
 (IV-d)

where θ is the incidence angle of the particle with respect to the normal to the face of the back glass array in radians. The angular acceptance in this trigger resulted in a θ range of 0 to 0.28 radians. Therefore, the energy corrections were never greater than 6 %.

Due to the asymmetric geometry of the front glass, the front glass energy measurements were less accurate. The clustering in the front glass was done in two separate passes. First the blocks in the array were associated with back glass clusters. In case of overlap between front clusters the energy in shared blocks was allocated in proportion to the total (front + back) energy of the two clusters.

The second pass considered blocks not assigned to clusters in the first pass. Among these, blocks with energies above FGESEED= 0.05 GeV were potential cluster seeds. Each seed formed a cluster with its immediate neighbors. As each cluster was formed its blocks are removed from consideration as seeds. Only the first pass clusters were relevant

for the energy of the triggering shower; but the second pass clusters could be used, for example, in a cleaning cut.

Test data taken at the CERN PS [NIC82] used a small array of blocks in a front-back geometrical arrangement. Angle and position corrections were extracted for the raw energies measured by the phototubes. The expression for the correction was:

$$E_{FG} = [1/(1+C_1 \cdot \Theta)] \cdot [(1+A)/(\exp(\Delta L/\alpha_1) + A \cdot \exp(\Delta L/\alpha_2)]$$
 (IV-e)

where θ is the angle of incidence to the face of the block in radians and ΔL the distance between the incident particle hit on the glass face and the position of the beam during calibration. The empirical constants are: $A_{short} = 0.126$, $A_{long} = 0.063$, $\alpha_1 = 1650$ cm, $\alpha_2 = 21.4$ cm and $C_1 = .465$. The short and long subindeces refer to the block sizes.

To obtain the energy of the shower we should add the energy losses of the shower going through the detector. Figure IV-2 shows an apparatus diagram where is possible to see for a typical direct photon trigger shower the parts of the apparatus crossed. The main energy losses were due to the crossing of the magnetic coil and the iron walls in between arrays. Since the events analysed in our case went through a B-veto cut that assure non-conversion in the coil, there were practically no losses in the coil. The most important loss was in the iron cage of the back glass array.

The iron losses were estimated by running a EGS (Electron-Gamma shower simulation Monte Carlo) simulation of the detector. The details are explained in Appendix C. This simulation estimates a 5 % loss in the iron for all energies. This value is consistent with the energy

scale factor found to minimize the rms width of the η° mass peak in the η° data. A small angular dependence of the correction was also found, but in the angular acceptance of the trigger, this additional correction was always less than 1%, and felt to be negligible.

Thus, the total energy in the glass arrays including corrections, is:

$$E_{glass} = E_{BG} + E_{FG}$$
 (IV-f)

IV-5. DSTing and B-vetoing.

Each DST contained about 8000 events. They already included different cuts to improve the data selection. The introduction of new calibration and alignment constants produced a new energy re-evaluation and some events were now rejected when the energy threshold was applied. The introduction of a event veto using the B counters was of the most importance.

The "B-veto cut" was very important for the analysis and therefore will be discussed at several points throughout this dissertation. The main purpose of this cut was to eliminate triggers produced by conversions in the solenoid coil.

If the conversion (photon or multiphoton) occurred in the coil the resulting shower will deposit the equivalent of at least one minimum

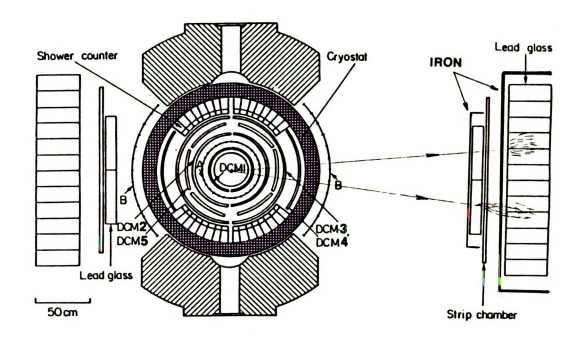


Figure IV-2: View of the Apparatus.

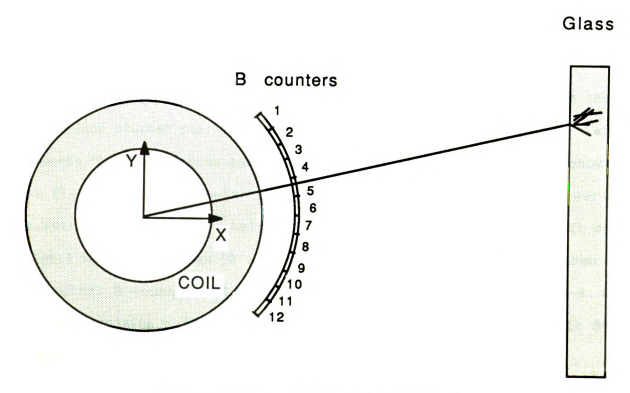


Figure IV-3 : Geometry of the B Cut.

ionizing particle signal in the B counters. This cut was implemented when writing the DSTs from raw tapes.

In order to speed up the analysis, CON (condensed) tapes from DST's were written which contained the relevant information in the fewest possible words. This information excluded the track points but included the track parameters and a vertex position. The maximum number of events in a CON tape was about 80,000.

IV-6. The B-veto cut.

We rejected events that started showering in the magnet coil by demanding no shower signal in the B counters, since such showers would have spread more before reaching the strip chambers than showers starting in the front glass. Then, the front glass was the prime converter for the strip chamber shower sample.

The B-veto cut was performed in the following steps. First the back glass cluster position (trigger cluster position) was projected towards the event vertex and the B counter traversed was found, as shown in figure IV-3. The pulse height signals of this B counter were examined. If the pulse height from at least one phototube (left or right) was greater than 50 counts, the signal was described as a shower. A typical B counter pulse height spectrum is shown in figure IV-4. A minimum ionizing particle signal in the B counter corresponds to 80 counts [ANG81].

If the pulse height in at least one counter end was then greater than 50 counts, we checked the Z position of the shower as given by the

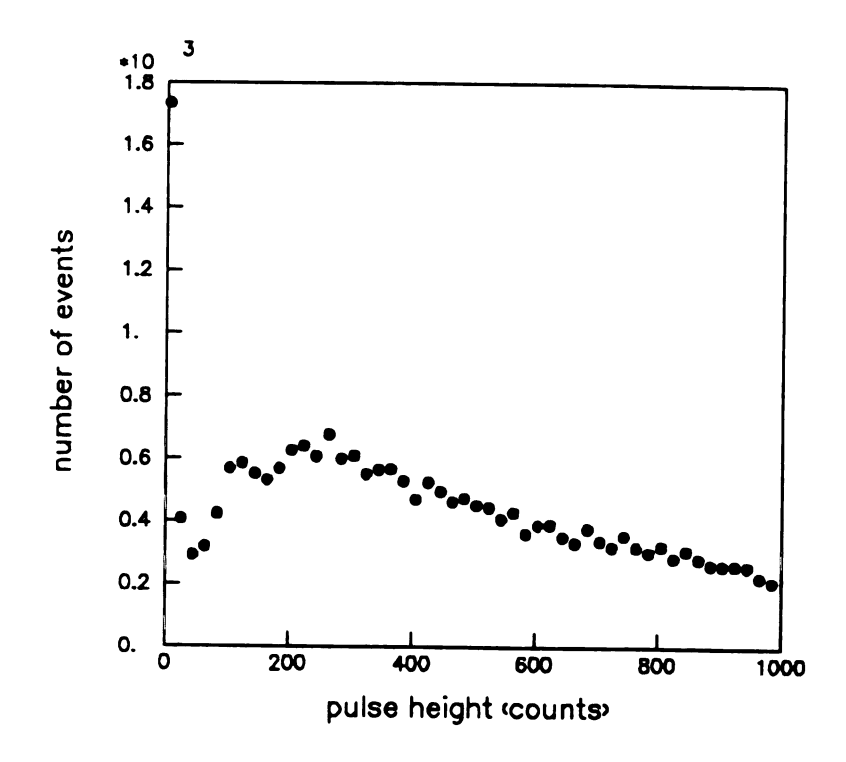


Figure IV-4: B Counter Pulse Heights.

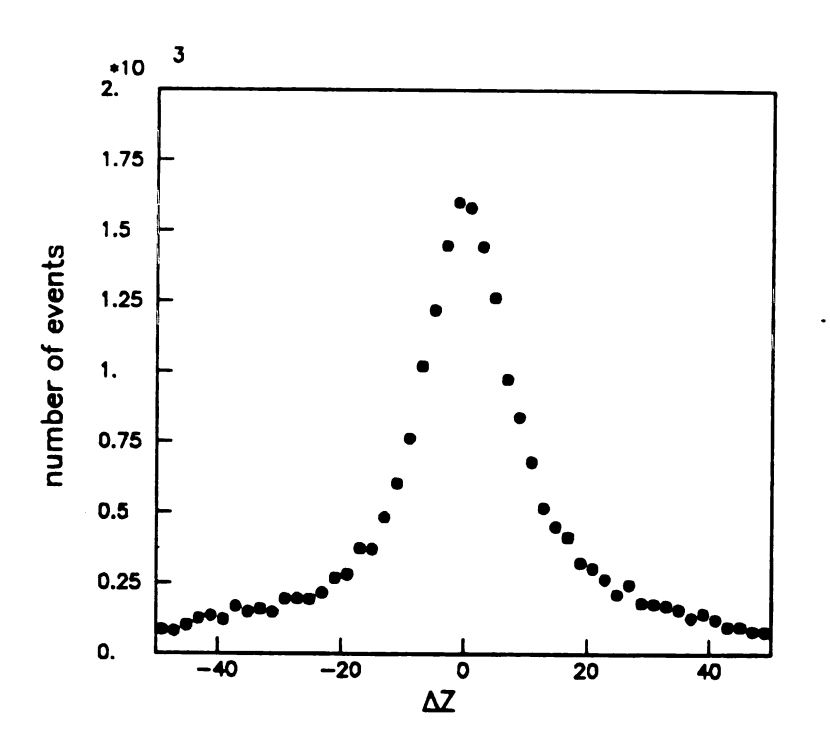


Figure IV-5: Az Differences in the B Counters.

counter. A typical ΔZ distribution is shown in figure IV-5, where ΔZ is $Z_B^ Z_{trigger}$, Z_B^- is the shower position as determined by the B counter (see section II-10) and $Z_{trigger}^-$ the projected back glass shower position in Z. If ΔZ was less than \pm 20 cm, we concluded that the shower registered by the B counter was associated with the trigger cluster. Therefore, the shower started in the magnetic coil and the event was rejected.

When the projected shower position was near the edge of a B counter (within a 25% of the length to the border), the adjacent counter was analyzed in the same way but adding the pulse height of respective adjacent ends, since the shower could be shared between both counters.

The pulse height cut of 50 is below the minimum ionizing particle peak of 80 counts, so we expect a good efficiency in vetoing showers that originated in the magnetic coil. Charged particles from the trigger cluster may also cause the vetoing of the event, the overall efficiency of this cut is discussed in section V-6.

IV-7. General Cuts.

After track finding in the drift chambers, a common vertex was determined in order to find out if the event was consistent with a real beam-beam interaction. The vertex finding process was iterative. For the first iteration the vertex was considered to have $y_0 = 0$. The first iteration vertex was then found by the average of the track interceptions with the y = 0 plane. Then the tracks were approximated by straight lines tangent to the point of nearest approach to this final

vertex. For the second iteration a second vertex was found for these straight lines. Tracks whose χ^2 for pointing to the vertex were too high (more than 30 away) were rejected. Iteration continued until no more tracks were rejected.

The event vertex was required to be inside a volume defined by the beam intersection region. Figure IV-6 shows a two dimensional histogram of X-Z ("diamond") and a histogram in Y of the vertex positions found in the direct photon data. The requirements for the vertex were: $|x_0| \le 5$, $-6 \le y_0 \le 20$ and $|z_0| \le 50$, where x_0 , y_0 , z_0 are the coordinates of the vertex in cm. Events with vertices outside this region were rejected. Such events may be produced by a beam-vacuum pipe, or beam-residual gas, or cosmic ray interaction.

Another cut made at this stage was to reject triggers caused by charged particles interacting in the NaI sources intended for calibrating the lead glass. The lead glass pulse heights summed over the whole array were analysed using two different ADC gates, a long 600 ns gate: (X), and a short 200 ns gate: (Y). Since the rise time of the electromagnetic interactions (Cerenkov light) was shorter than the pulse of the NaI scintillation, comparing the energy reading with both gates it was possible to veto the NaI initiated triggers.

Figure IV-7 shows X vs. Y for the data collected. The events under the diagonal are NaI trigger candidates (X>Y). A cut was implemented requiring $Y \ge (1.15 \cdot X - 45)$ for $X \ge 300$.

The front glass array phototubes stood in front of the back glass acceptance (see figure II-12). To reject events where part of their energy could be produced by showering in the phototubes a fiducial geometrical cut was proposed. A Monte Carlo study of neutral meson

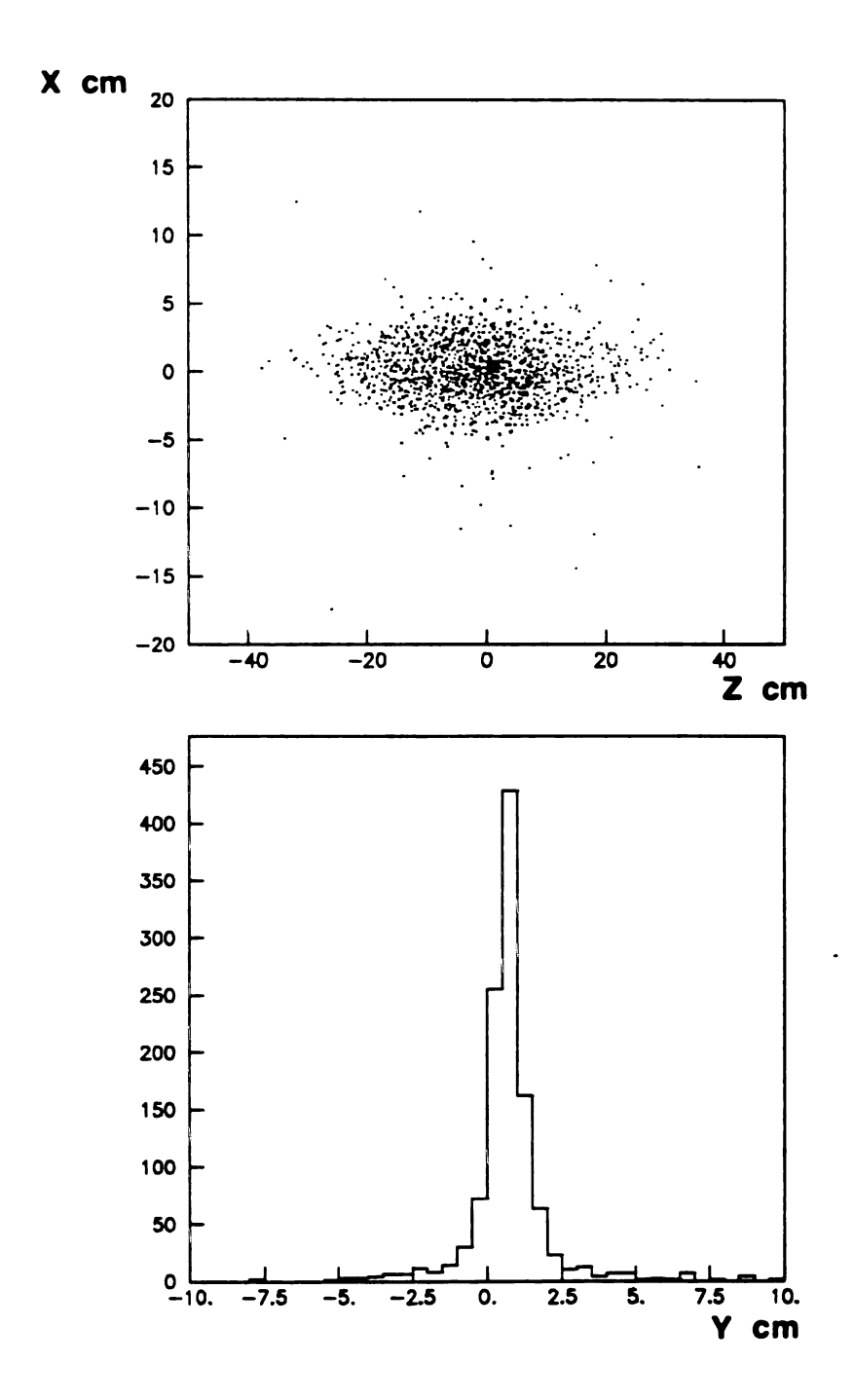


Figure IV-6: Vertex Positions (Diamond).

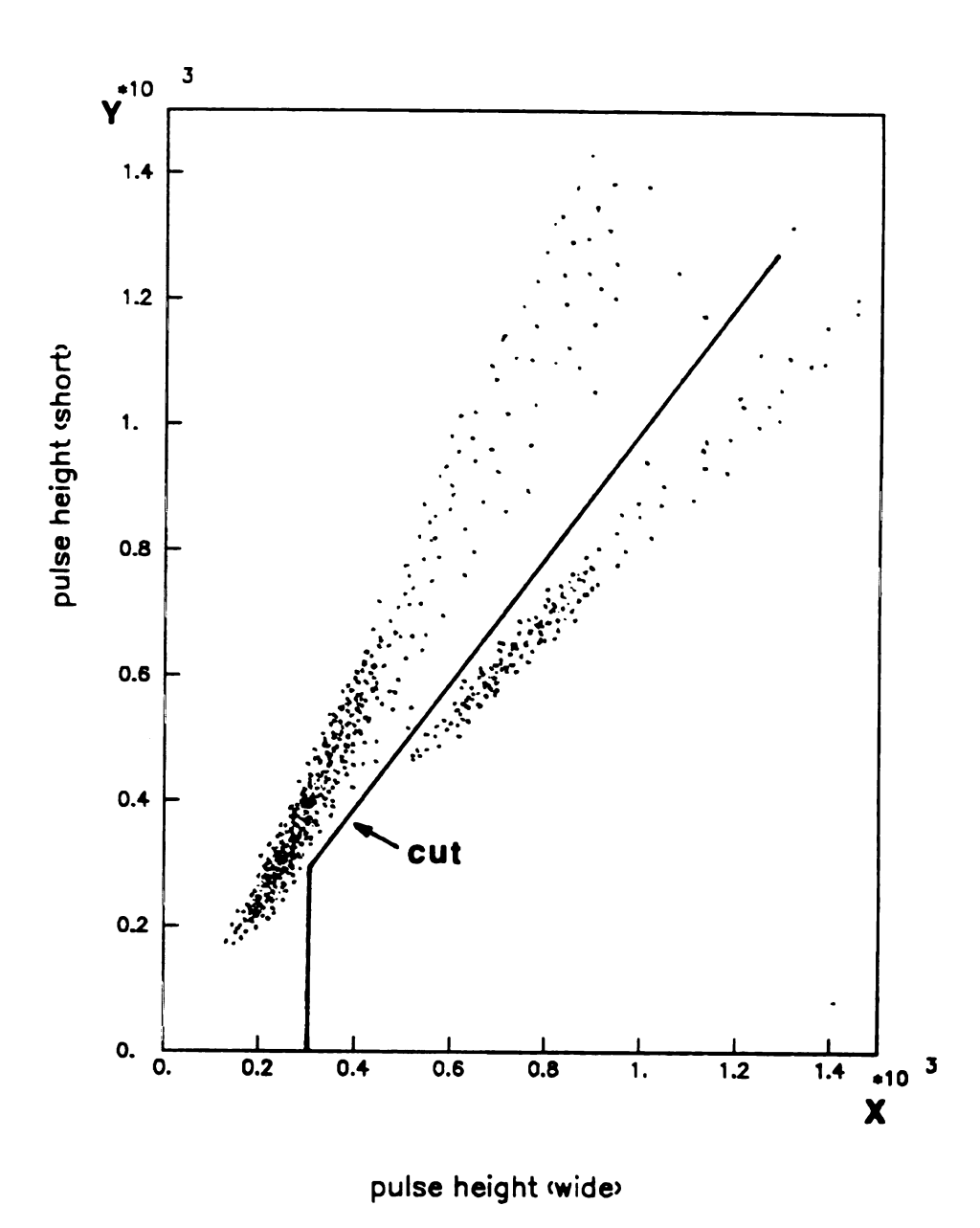


Figure IV-7: NaI Trigger Cut.

decays in the detector showed that for a trigger shower to have both photons of the decay inside the front glass array 90% of the time, the fiducial would have to be placed at 13 cm inside the front glass geometrical boundary.

The B veto cut was, of course, not 100% efficient (see section V-6). There were tracks pointing to the trigger zone (back glass cluster) still after the B veto cut was applied. Figure IV-8 shows the distribution of charged particles hits as extrapolated from the drift chamber measurements in a Y-Z view of the front face of the back glass array. Events with at least one charged track pointing to a region of ± 25 cm in Y and Z of the back glass trigger position were vetoed. The efficiency of this cut to discriminate between trigger associated charged particles and charged hadron backgrounds will be discussed in section VI-8.

The fraction of the energy of the shower deposited in the front glass is of great importance. As was stated in chapter I, a longitudinally segmented calorimeter could separate, using the conversion method, direct photons from the neutral meson background. The parameter used to measure the fraction of the shower energy deposited in the front glass was defined as: Front/All (F/ALL) = energy in the front glass, with all the corrections to the energy discussed in section IV-6 applied. The front glass calibration constants derived from the PS test data were obtained with a beam at normal angle of incidence. A correction for extra front glass energy deposited at finite angles had to be performed. The PS test data has shown that the corrected form of F/ALL is given by:

$$F/ALL = (F/C_{\Theta}) / E_{shower}$$
 (IV-h)

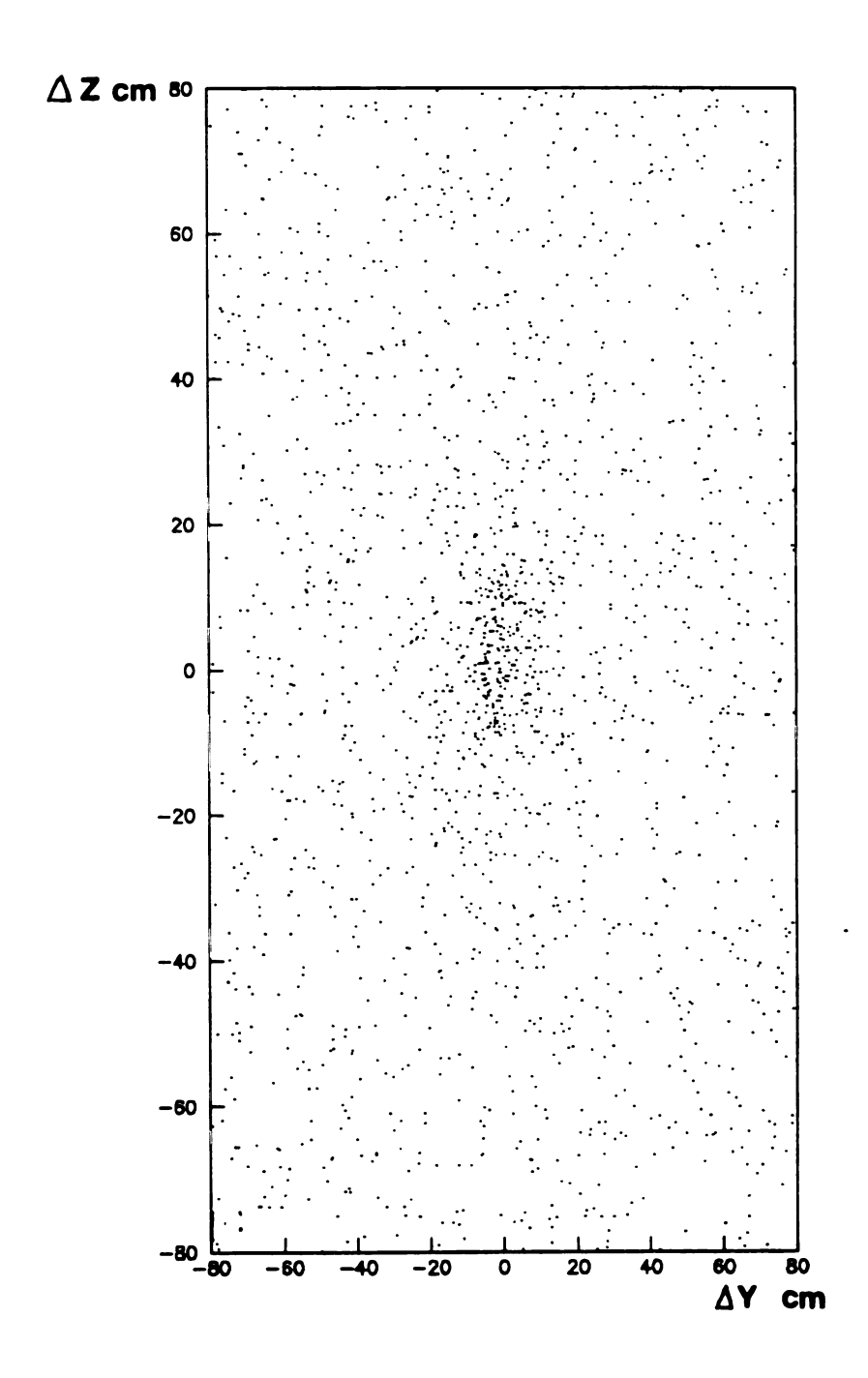


Figure IV-8: ΔY vs. ΔZ , Differences Between Charged Particle Hits and Trigger Position on the Back Glass Array.

where the angular dependence, fitting the PS data at different angle of incidence, is given by:

 $C_{\theta} = \beta_1 + \beta_2/\cos\theta + \beta_3/\cos^2\theta$; with $\beta_1 = -2.946$, $\beta_2 = 5.77$ and $\beta_3 = -1.818$. Figure IV-9 shows C_{θ} vs (cos θ). Figure IV-10 shows F/ALL distributions for the direct photon data at different p_T ranges. There was an important cut applied to the data using F/ALL. The cut and its efficiency will be discussed in section V-9.

IV-8. Strip Chamber Clustering Algorithm.

The strip chamber information is given by pulse height and strip position, 1 to 160 in Y and 1 to 192 in Z. We use the notation (i,ph_i) where i is the strip number and ph_i is the associated pedestal subtracted pulse height.

The strip chamber clustering algorithm looks for strips with pulse height greater than a given minimum value (in this case IPHCUT = 20, equal to the pedestal), to be used as a "cluster seed". All contiguous strips with pulse height greater than 20 counts were added to the "cluster". Figure IV-11 shows typical cluster frequency distribution for the Y and Z projections.

For a uniform illumination of the chambers by charged particles and a large mean separation between tracks, we expect that the distribution of the distances (d) between the clusters will have the form: $e^{-d/k}$, where k is a constant (by analogy with Poisson statistics). This would give a a straight line on a semi-logarithmic plot. Figure IV-12 shows a semi-logarithmic distribution of the distance between two

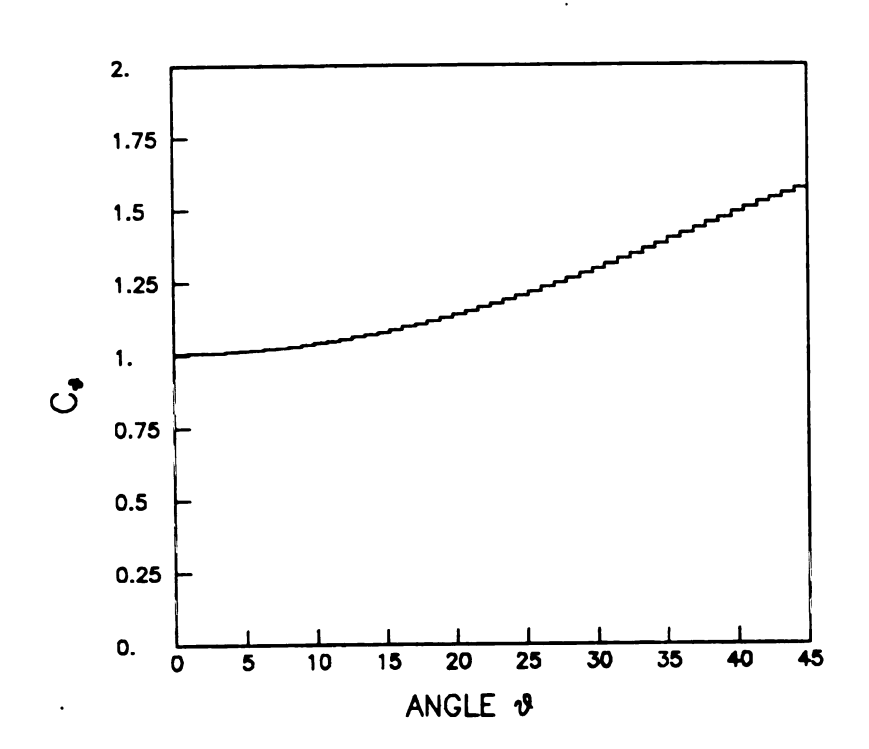


Figure IV-9: Angular Correction to the Observed Front/All Ratio.

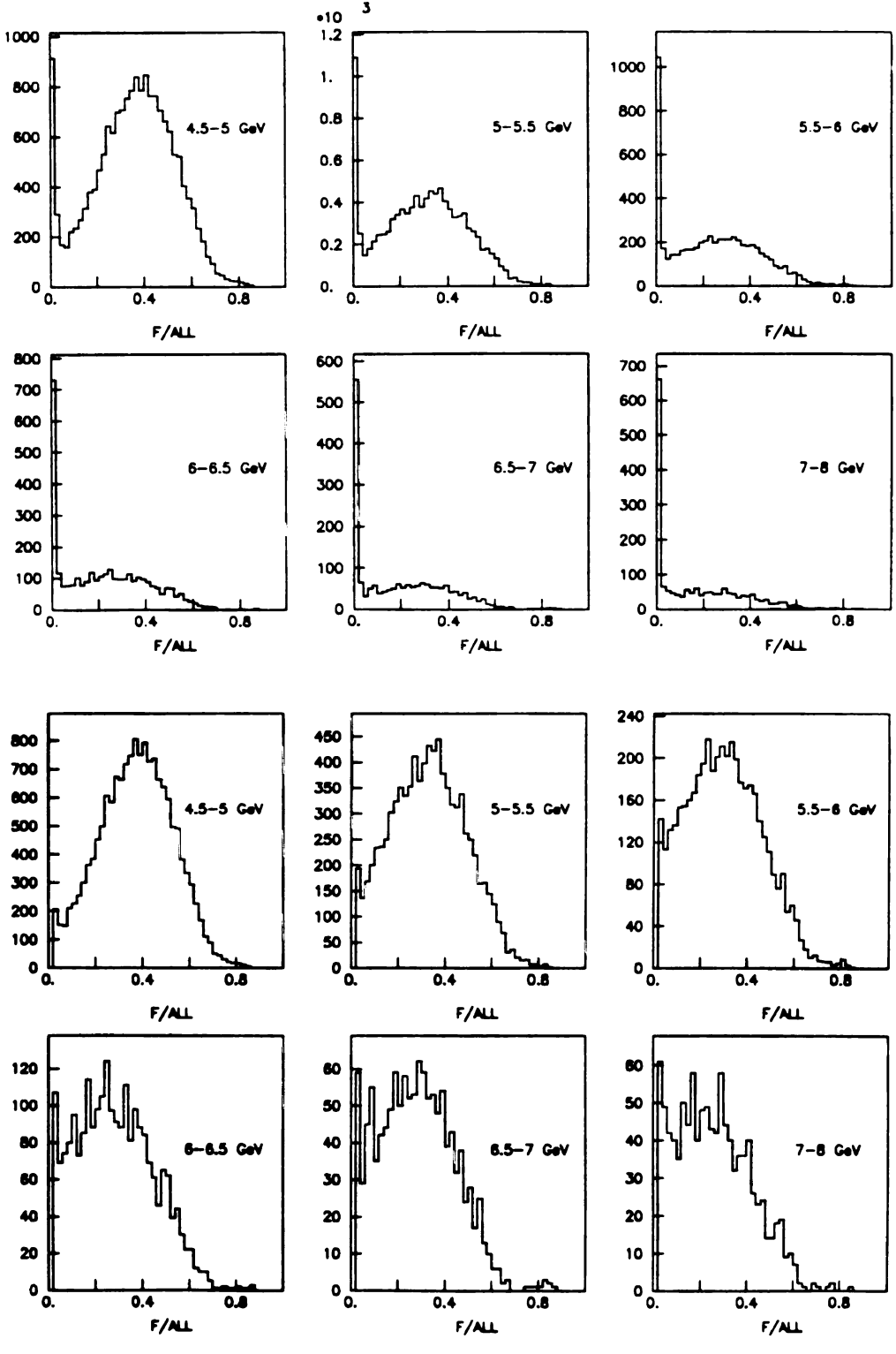


Figure IV-10: F/ALL Distributions for Various Δp_T Ranges in the Direct Photon Trigger. All Events and Events with Front/All Greater than 0.02.

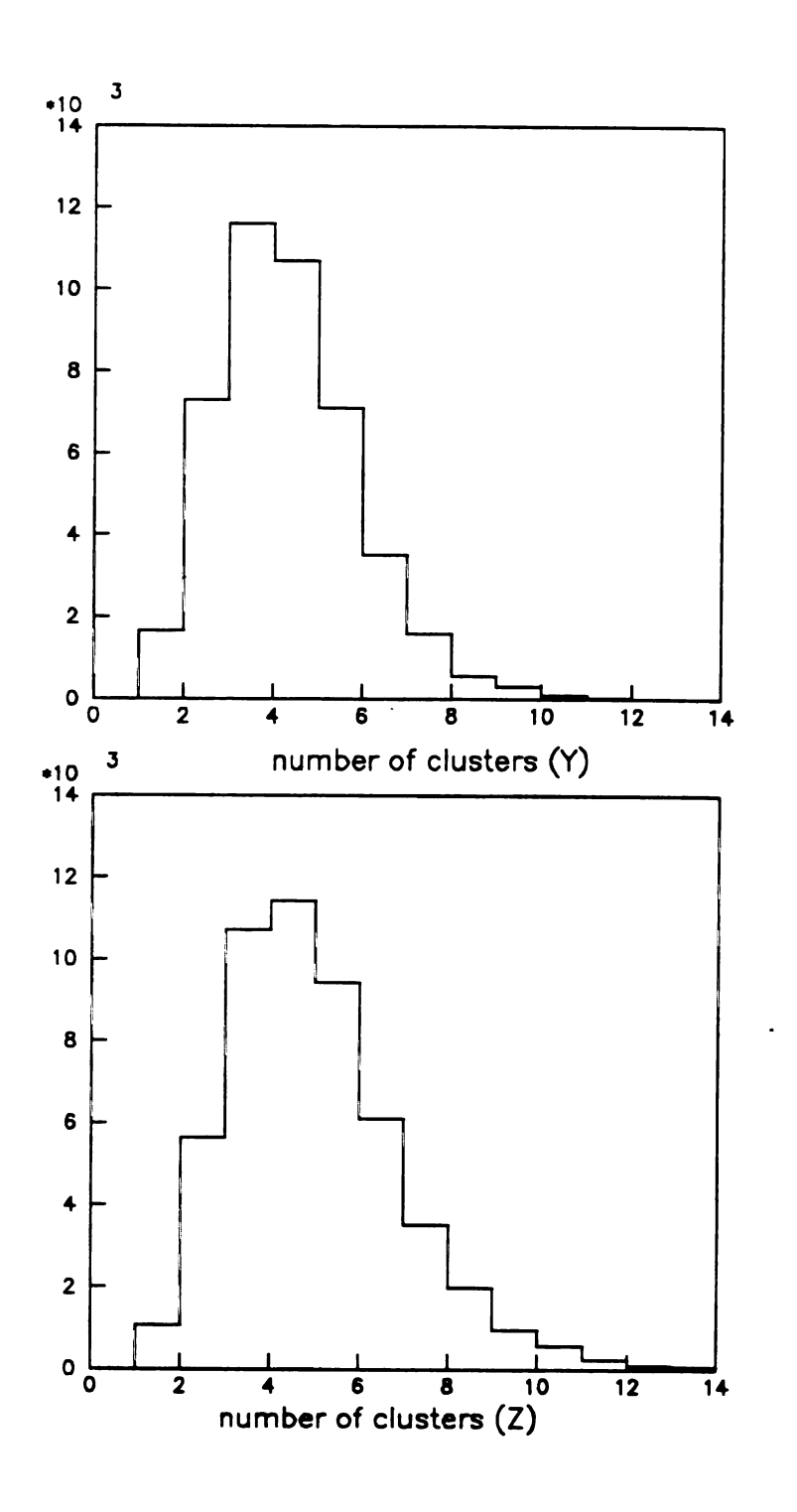


Figure IV-11: Number of Clusters per event in the Strip Chambers.

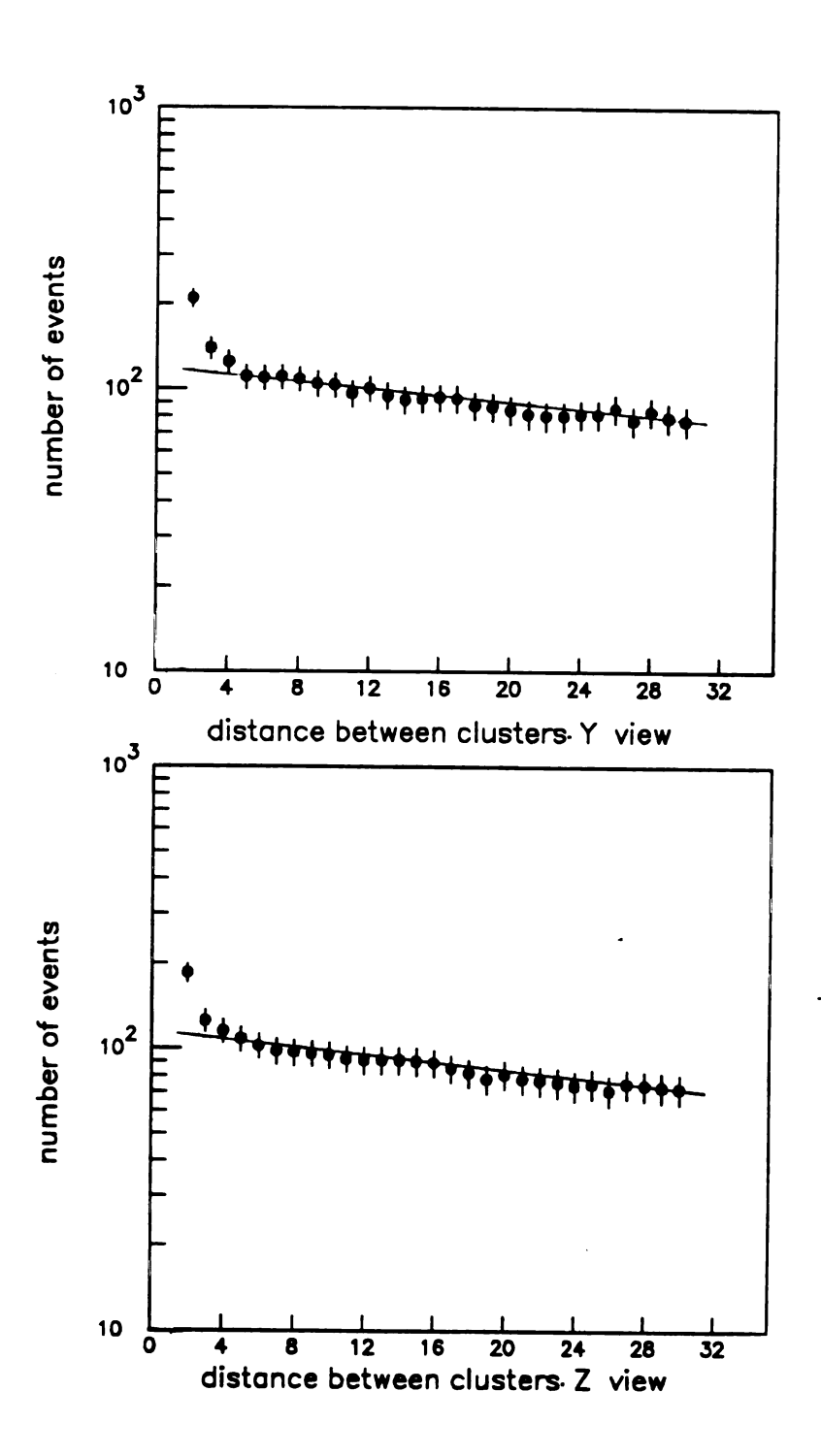


Figure IV-12: Gap Determination. Number of clusters
vs. Separation Between Two Charged
Particle Hits on the Back Glass Array.

clusters in the chamber. We verified that each track is associated with a cluster. Thus, the enhancement from the straight line at small values of the distance indicates that we had artificially created extra clusters and we should merge clusters with distances less than this inflection point. In other words, clusters should be merged across a "gap". This gap is defined as the minimum number of strips with pulse height less than 20 counts needed to define a break between adjacent strip chamber clusters. The plot in figure IV-12 suggests a value of 4 strips for the gap. A second method used to determine the gap was to study the balance between the Y and Z planes signals (pulse height) as a function of the gap. These studies suggested a similar value for the gap.

Thus, we saw that the minimum distance between edges of two distinguishable clusters was greater than 4 strips (4 cm). This was a fundamental limit in our ability to separate multiphoton from single photon showers.

Several parameters describing the clusters were calculated from the pulse height information. The position was defined as the pulse height weighted average location of the strips of the cluster.

position =
$$\langle i \rangle = \frac{\sum i \cdot ph_i}{\sum ph_i}$$
 (IV-i)

 $\langle i \rangle$ is a real number. The width or span is essentially the number of strips belonging to the cluster (including any gaps). If L_1 is the first strip number of the cluster and L_2 the last, the width is defined as:

width or span =
$$W = L_2 - L_1 + 1$$
 (IV-j)

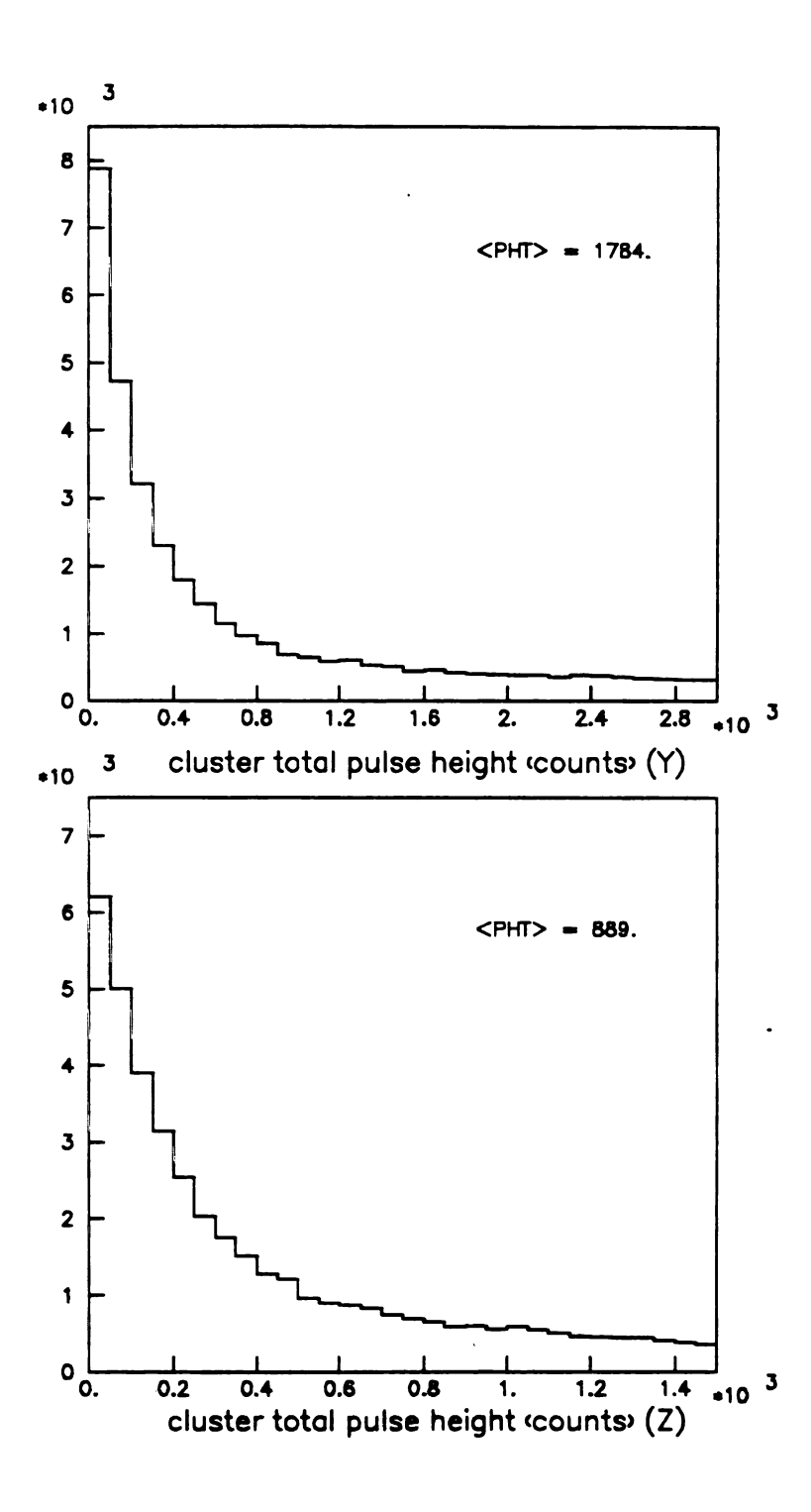


Figure IV-13: Total Pulse Heights of Strip Chamber Clusters.

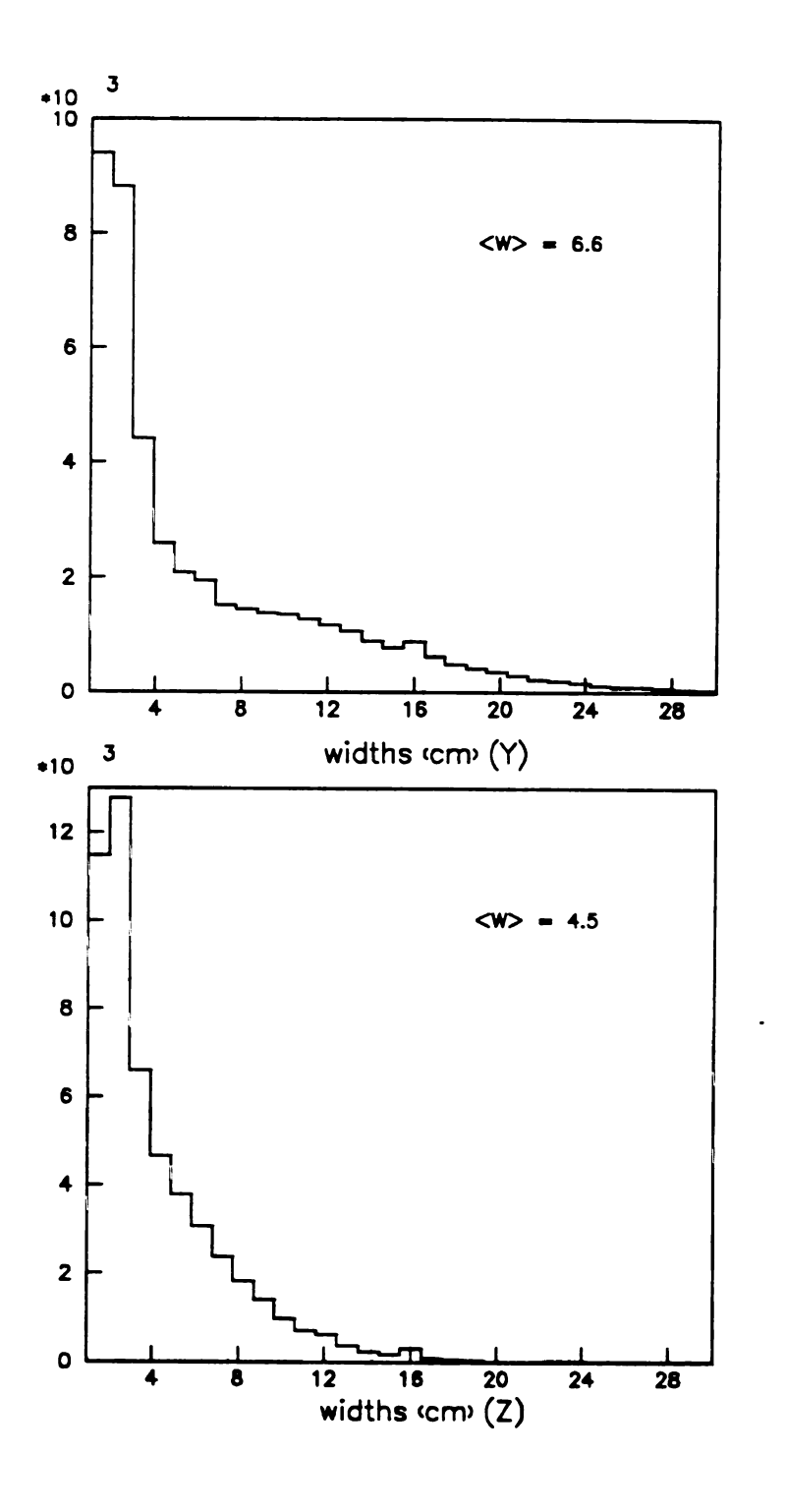


Figure IV-14: Widths (or Span) of Strip Chamber Clusters.

the widths are expressed in cm. The R.M.S (a) is the standard deviation of the pulse height distribution of the cluster calculated from a continuous histogram, given by:

$$RMS^2 = \sigma^2 = \langle i^2 \rangle - \langle i \rangle^2 + 1/12$$
 (IV-k)

where

$$\langle i^2 \rangle = \frac{\sum ph_i \cdot i^2}{\sum ph_i}$$

Histograms of total cluster pulse height and width for the inside and for the Y and Z planes are shown in figures IV-13 and 14.

Each pulse height $,ph_{\underline{i}}$, measures the integrated signal along the i strip. We did not have a two dimensional description of the shower in the (y-z) plane, only a projection of the shower ionization along that axis.

Figure IV-15 shows data histograms of ph_i for the y and z planes. There is a ph_i cut of 20 counts at the hardware level. For both planes an exponential fall-off is seen. The mean pulse height for the y plane (389) is similar to the pulse height for the Z plane (311).

The variation of strip chamber parameters across the chamber was also studied. The results are shown in figure IV-16. The values of $\langle PH_y/E \rangle$ vs. Z, $\langle PH_z/E \rangle$ vs. Y, $\langle W_y/E \rangle$ vs. Y and $\langle W_z/E \rangle$ vs. Z are plotted. E is the shower energy, PH the total cluster pulse height and W the cluster span. There is a small increase in pulse height as one gets away from the center of the chamber. This relative variation can be as high as 25% at the edges for the Z view, but smaller than 8% for Y view. However, there is no variation in W (span).

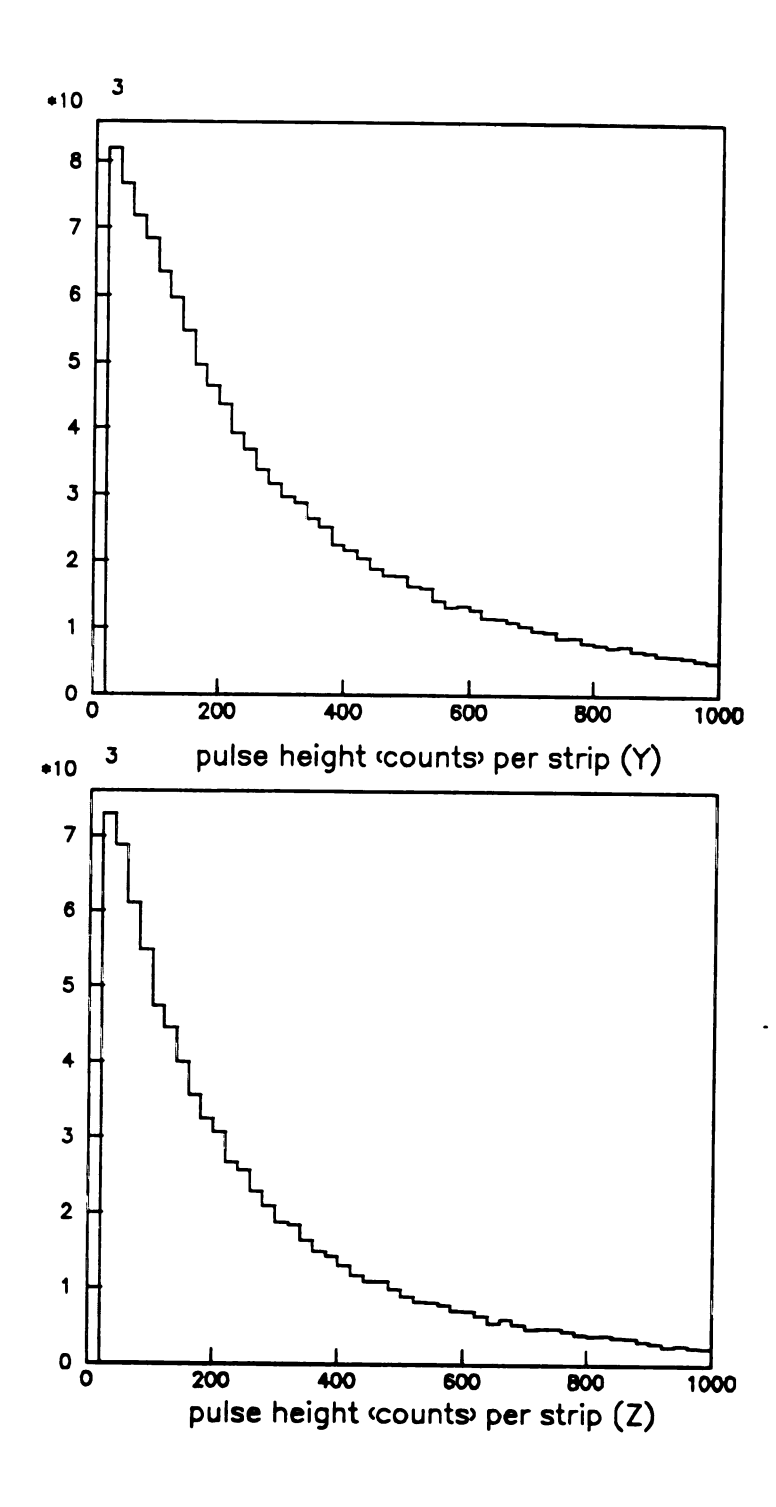


Figure IV-15: Pulse Height per Strip.

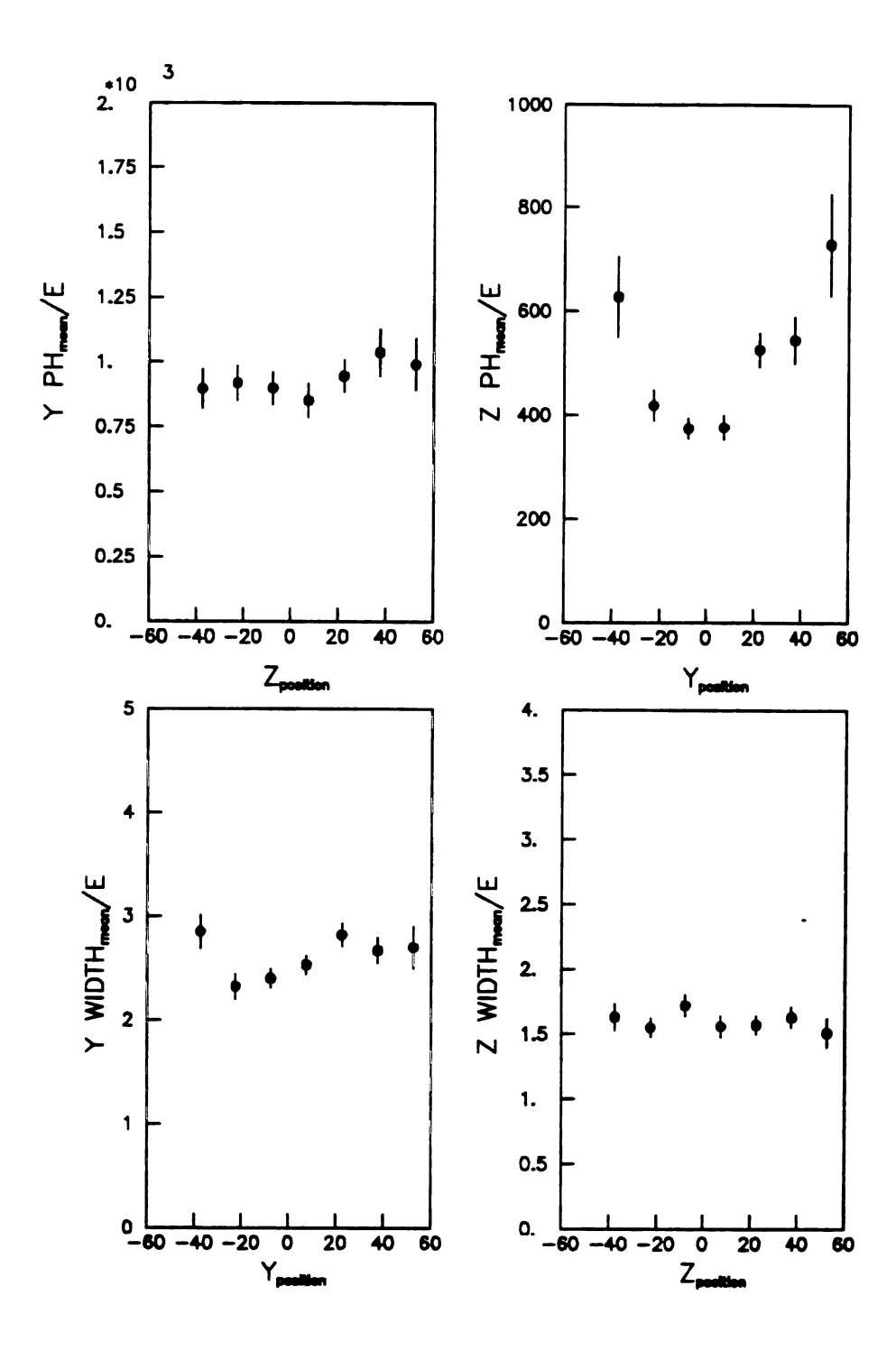


Figure IV-16: Variations across the chamber.

CHAPTER V

SEARCH FOR A DIRECT PHOTON SIGNAL

V-1. Introduction.

The chief purpose of the multiwire proportional chambers in the R110 detector was to identify multiphoton showers among the back glass single cluster triggers.

In principle, each cluster in the strip chamber could be equated with a single photon shower. Under this hypothesis, counting the number of clusters in the strip chamber region in front of the back glass trigger cluster one could measure directly the number of photons contributing to the back cluster. In practice, this was not the case.

As will be discussed throughout this chapter, due to the intrinsic fluctuations of the showers, the important contribution of low-energy large-angle delta rays and the asymmetric properties of the chamber read out, the task was much harder than expected.

To overcome these difficulties a special method of analysis was developed. The method essentially compares a strip chamber shower property of the data with Monte Carlo simulations of the same property for single photon and multiphoton produced showers. The distribution

from the data is fitted with the single and multiphoton distributions to obtain their relative contributions to the data sample.

This chapter explains how the property for comparison was chosen. The description of the single- and multiphoton- initiated shower Monte Carlos and chamber simulation is included together with the method of fitting the single and multiphoton distributions to the data. The background and acceptance corrections are also discussed, and the chapter ends with the description of the statistical error calculations.

V-2. Further Strip Chamber Cuts.

Two main cuts were applied to select from all strip chamber clusters those associated with the shower: a matching chamber window and a total pulse height cut for the cluster inside this window.

The "matching window" is defined as the strip chamber region around the projected back glass cluster position where one finds activity associated with the shower. The determination of the matching window is important because it has direct influence on the efficiency and purity of the strip chamber information. A "matching window" of size w in cm, is a window covering ± w cm about the center position and is thus 2w cm wide on each view. The same size was used in both Y and Z projections.

Two independent determinations of the window were made, one for the η^0 trigger and one for the direct photon trigger data. Most of the single back glass clusters of the η^0 trigger sample (after a mass cut) are produced by a single photon (see Appendix E). However, for the

direct photon trigger most of the single back glass clusters are produced by $\pi^{\circ} \rightarrow \Upsilon\Upsilon$ decays merged in the back glass. Therefore we expect activity in a wider region for the direct photon trigger than for the η° trigger.

In the chamber, the shower signal is superimposed on a background produced, for example, by other particles of the same event. Because of the jet structure of the events, we expected this background to be concentrated around the trigger cluster, although the background level had been reduced by cuts already applied to the data. Superimposed on the background we expect a region of greater activity from the trigger shower. The edges of this region would be characterized by a strong variation of cluster parameters as a function of the window size. This variation depends on the transverse shape of the shower and on background properties. Several parameters have been studied as a function of the window size. Figures V-1, V-2 and V-3 show parameter variations with w (window's size) for the n° trigger data.

An inflection point in these distributions would give a natural place to set the window values. However, the inflection points of the curves are not very well defined. Analysing all of these curves we have chosen w = 15 cm as the minimum size of the window that can be taken without losing shower information for the η° trigger data. The same parameters for the direct photon trigger are also shown in figures V-1, V-2 and V-3. We have chosen a window of w=20 cm in this case.

Figures V-4 and V-5 show the distance between projected back glass position and the cluster position in the Y-Z planes for direct photon trigger data and for η° trigger data. For the direct photon data there is a "two shoulder" structure as expected from having a second

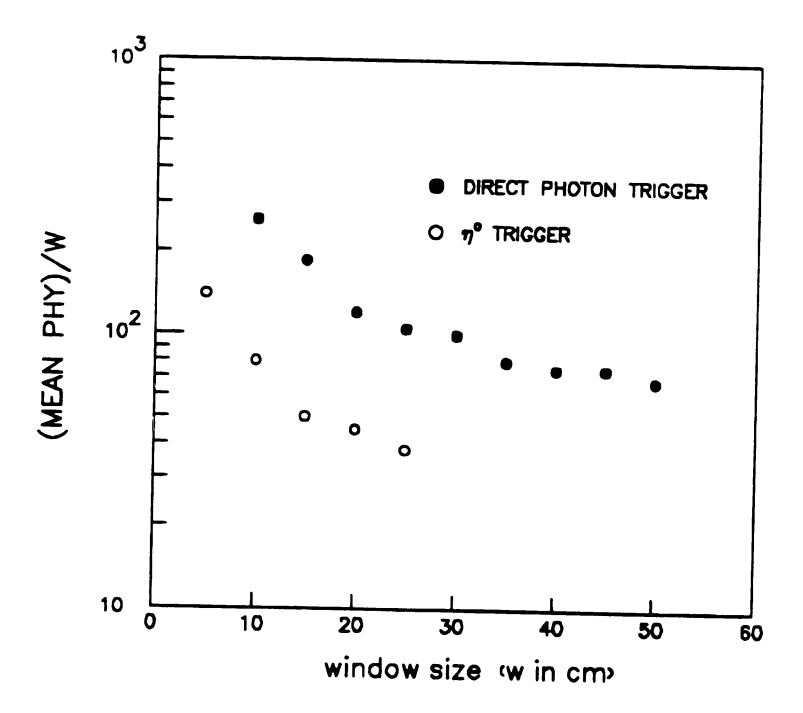


Figure V-1 : (Mean Pulse Height in Window)/w vs. Window Size (w) for the $\eta^{\,0}$ and Direct Photon Triggers.

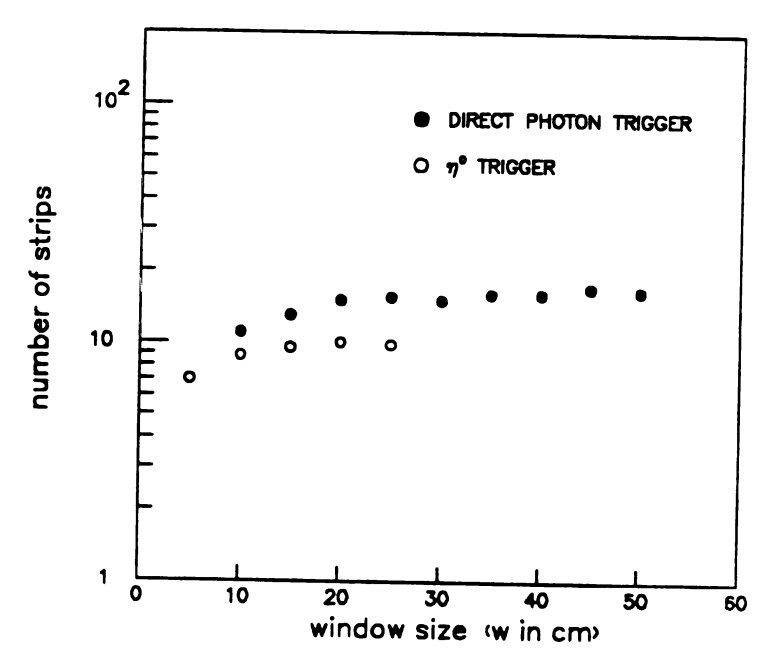


Figure V-2: Number of Strips per Cluster vs. Window Size (w) for the $\eta^{\,0}$ and Direct Photon Triggers.

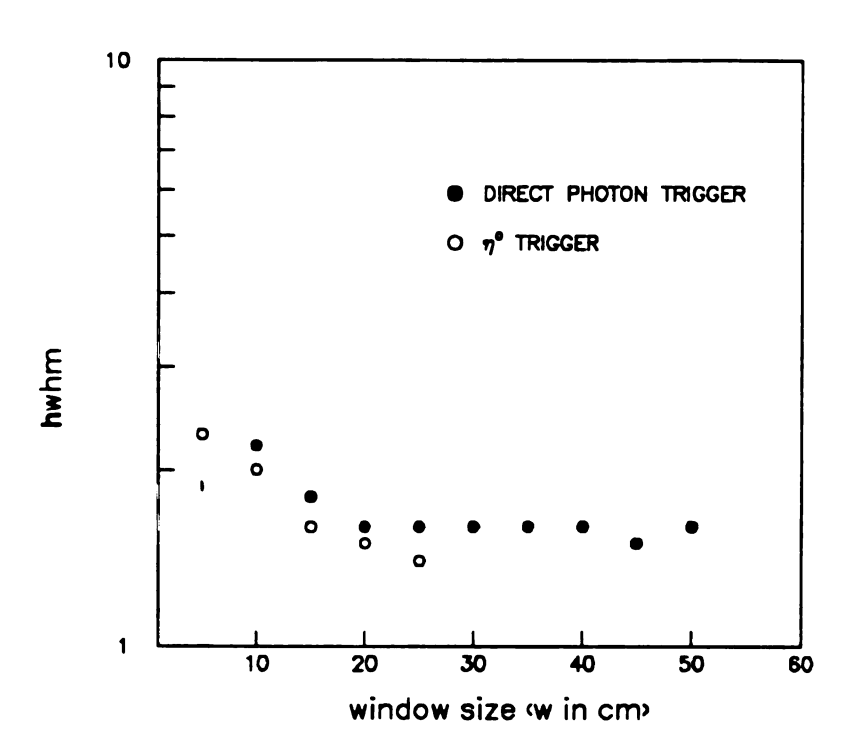


Figure V-3: Half-Width at Half-Maximum of the $\frac{\text{diff=(PHY-1.75 \cdot PHZ)/(PHY+1.57 \cdot PHZ)}}{\text{Distribution vs. Window Size (w) for the η^0 and Direct Photon Triggers.}$

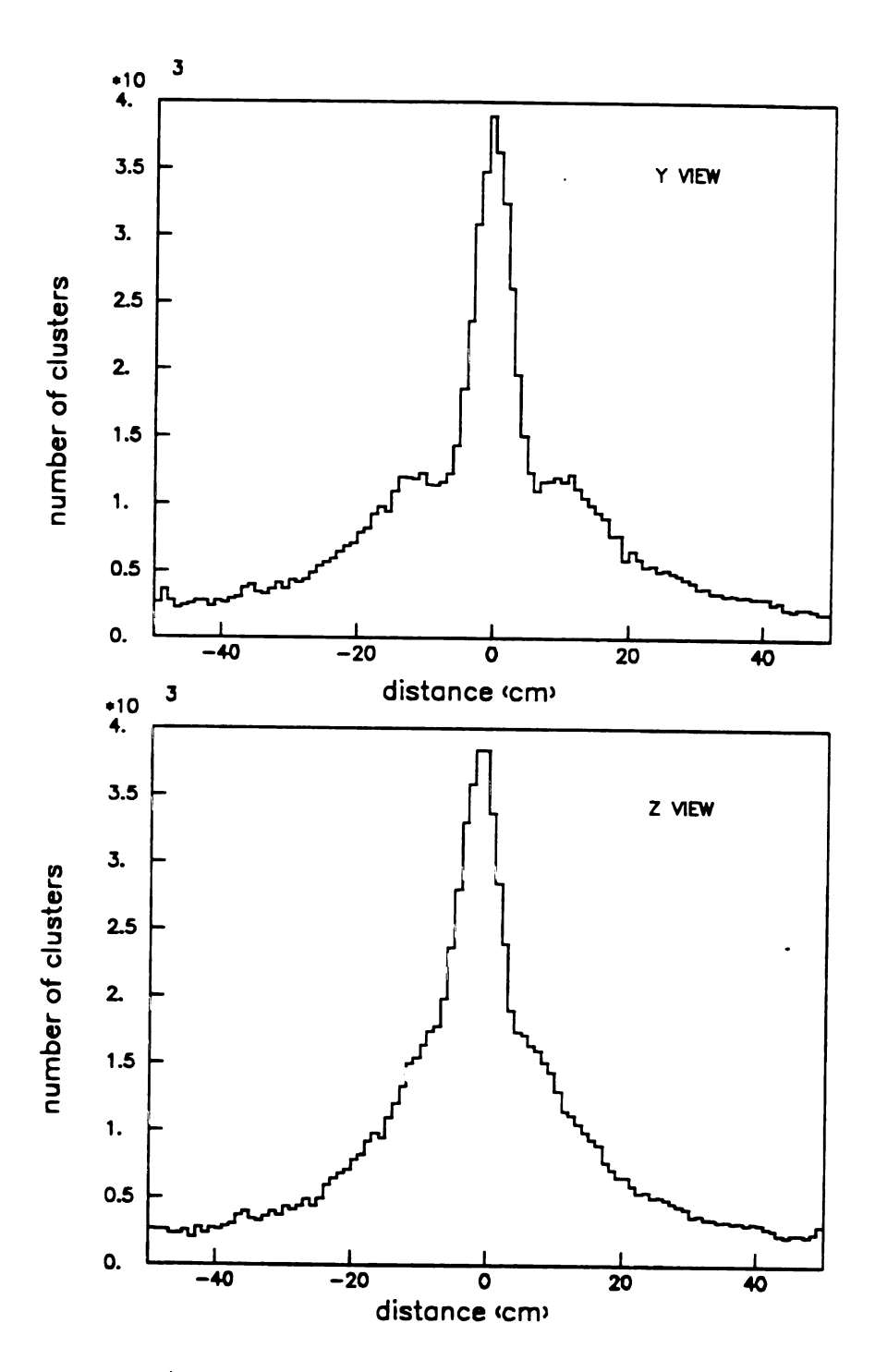
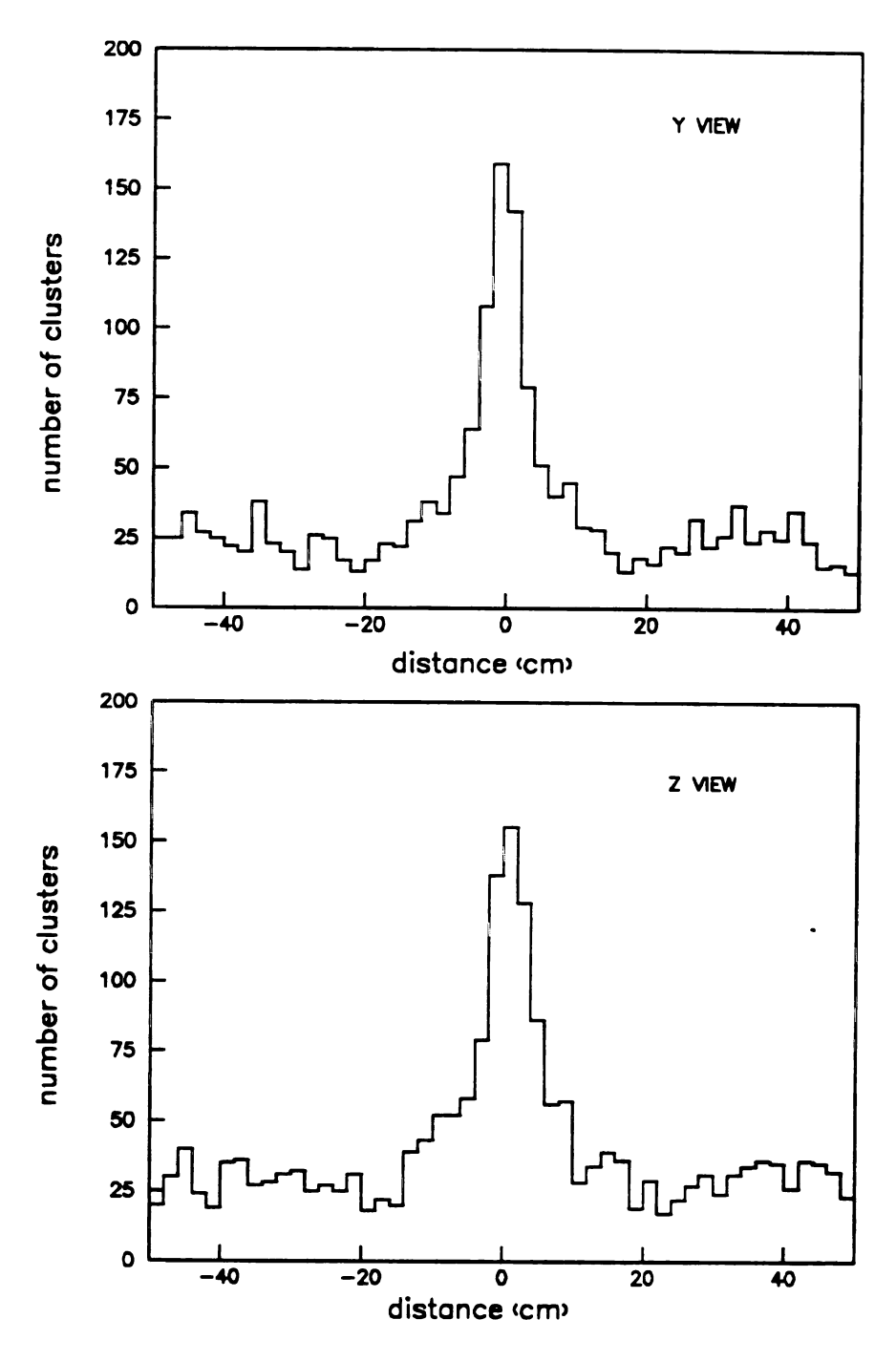


Figure V-4: Distribution of the Differences

Between Cluster and Shower Positions
for the Direct Photon Trigger Data.



resolved photon from meson decay. Because we want both photons to be inside the window for our study, we need w = 20 cm as the minimum possible window. This agrees with our previous result of 20 cm as a reasonable value.

A smaller window could be used for the η° trigger where no second photon is present. Because we want the same window size for comparison, we used a window of w = 20 cm for both analyses.

Another cut for cluster selection was done on the total pulse height of the clusters. Figures V-6 and V-7 show total pulse height distributions for all clusters with positions inside a w = 20 cm and a w = 5 cm matching window, for the direct photon trigger and the η° trigger.

An interesting pattern emerges for the 5 cm window clusters, which are clusters whose positions match very well with back glass showers. There are many low pulse height clusters, which we associate with noise in the strip chamber. After a minimum, the distribution begins to rise at higher pulse heights, which one could reasonably expect of a shower. It is reasonable, then, to associate this 5 cm window with the chamber activity of a single photon shower. We want to cut out the noise without losing any shower signal, especially from low energy photons of asymmetric meson decays. We chose the minimum possible value of the pulse height that still rejected most of the noise. A value of 400 counts in Y and 200 counts in Z was adopted. By studying charged particles hitting the chambers, the pulse height associated with the minimum ionizing particle deposition has been measured to be about 120 counts for the Y plane and 75 for the Z plane.

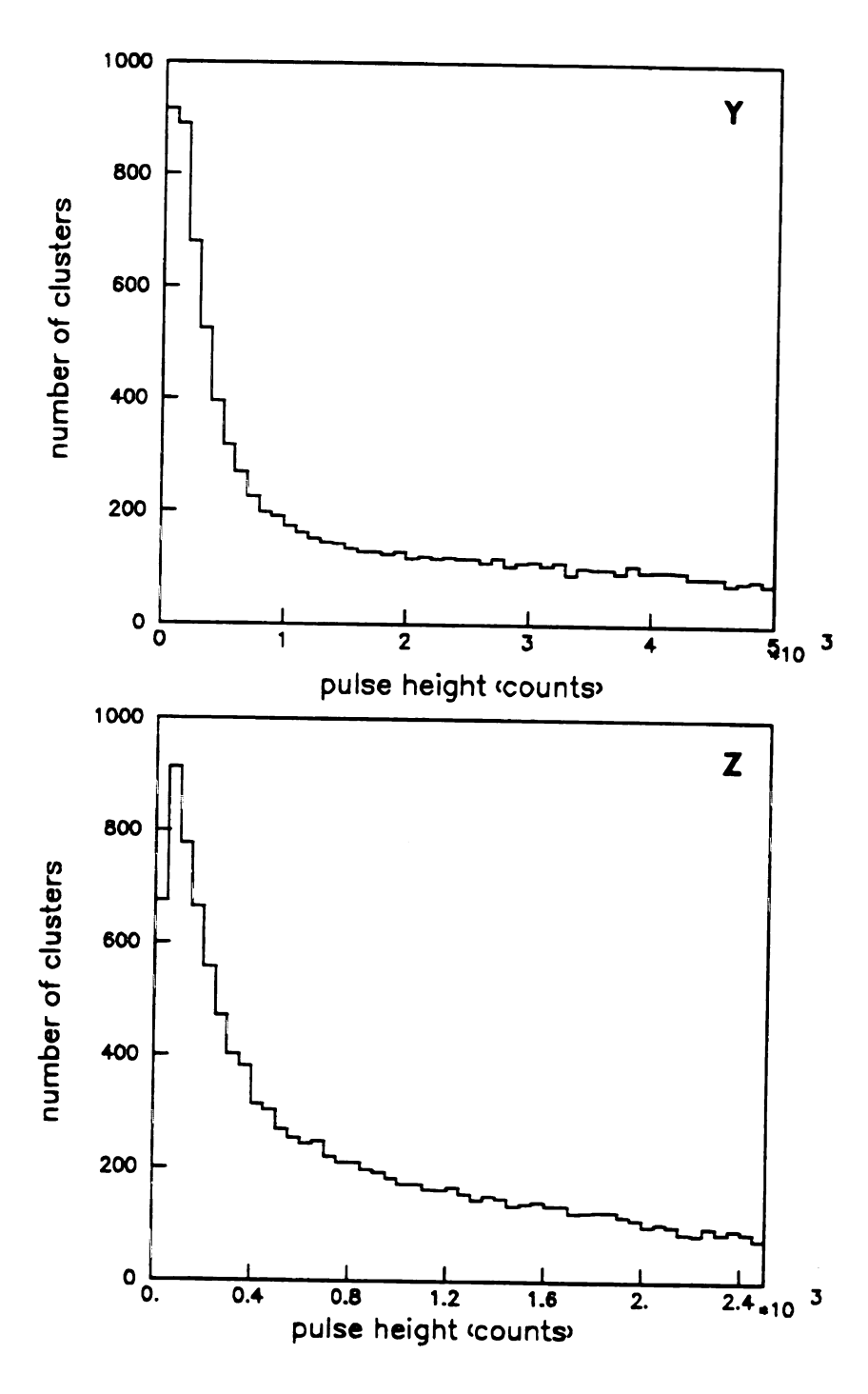
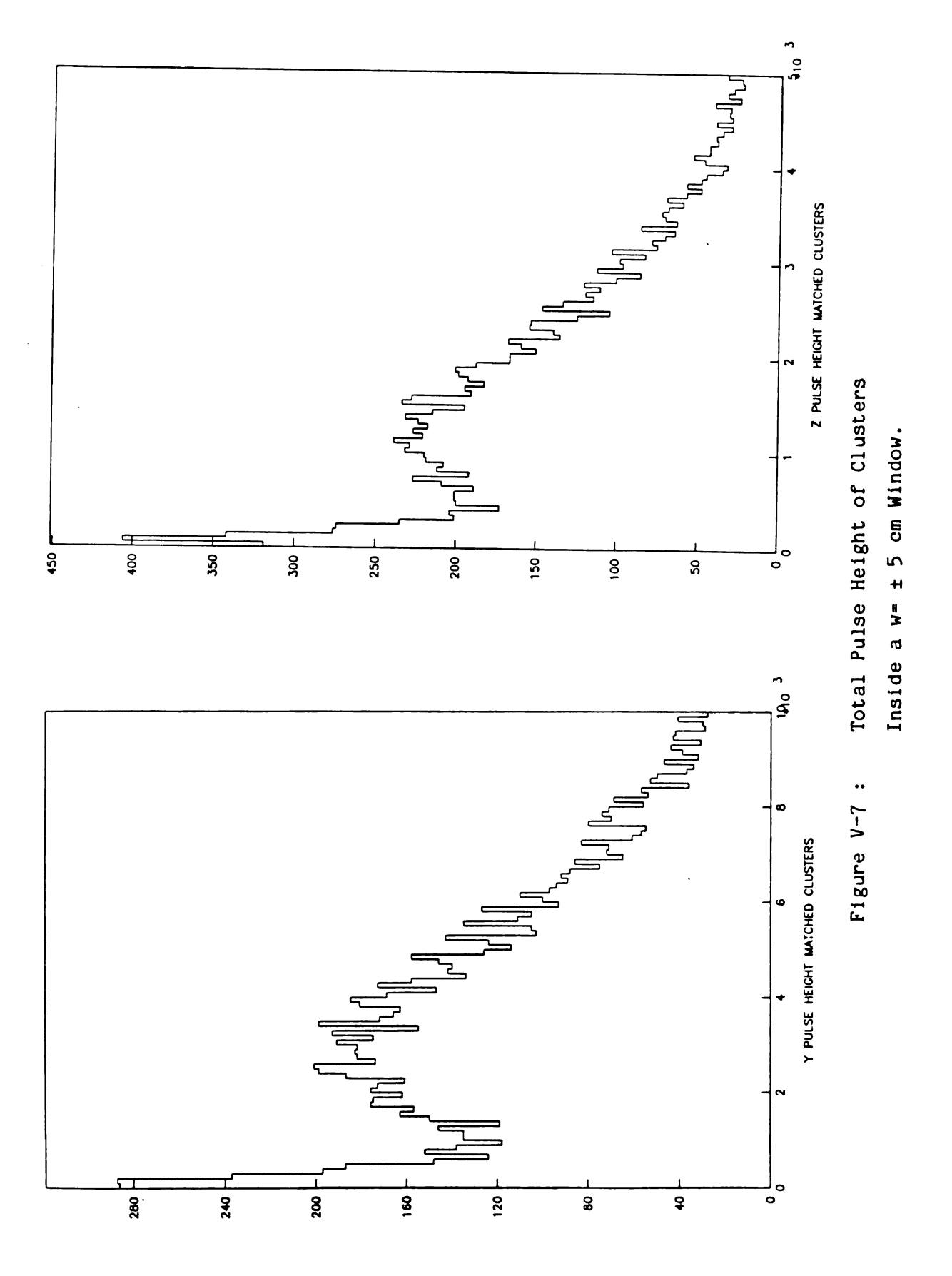


Figure V-6: Total Pulse Height of Clusters Inside a $w=\pm 20$ cm Window.



Another chamber property extracted from the information in figure V-7 is that the mean pulse height of the clusters in the Y view (3440) is about twice the value for the Z view (1804). Figure V-8 shows the distribution of the ratio (PHY- α -PHZ)/(PHY+ α -PHZ) for all clusters in a matching window of w= \pm 20 cm. A value of α = 1.75 was chosen for plotting. As the mean of the distribution shown is greater than zero, a larger value of α is needed to balance the Y and Z pulse heights. The particular value of α depends of the cuts used to select the chamber information. α values ranged between 1.7 and 2.1, but 2.0 was the value used for the analysis reported here.

V-3. Search for a Variable to Distinguish Single from Multiphoton Showers Among the Trigger Clusters.

The search for a variable to distinguish among single and multiphoton initiated showers is, of course, the core of the analysis.

If we equate one shower to one strip chamber cluster, the job of separating single- from multi-photon triggers is reduced to counting the number of clusters within the chamber matching window. Figure V-9 shows, in a matrix form, the fraction of clusters in the Y and Z matching windows for different p_T ranges in the direct photon trigger data. In the matrices there are many off-diagonal counts (especially important are the (1-2) and (2-1) components), making for a considerable ambiguity in the number of showers associated with the event.

After analysing figure V-9 it can be asked whether the original hypothesis of equating showers and clusters is correct. Looking at the

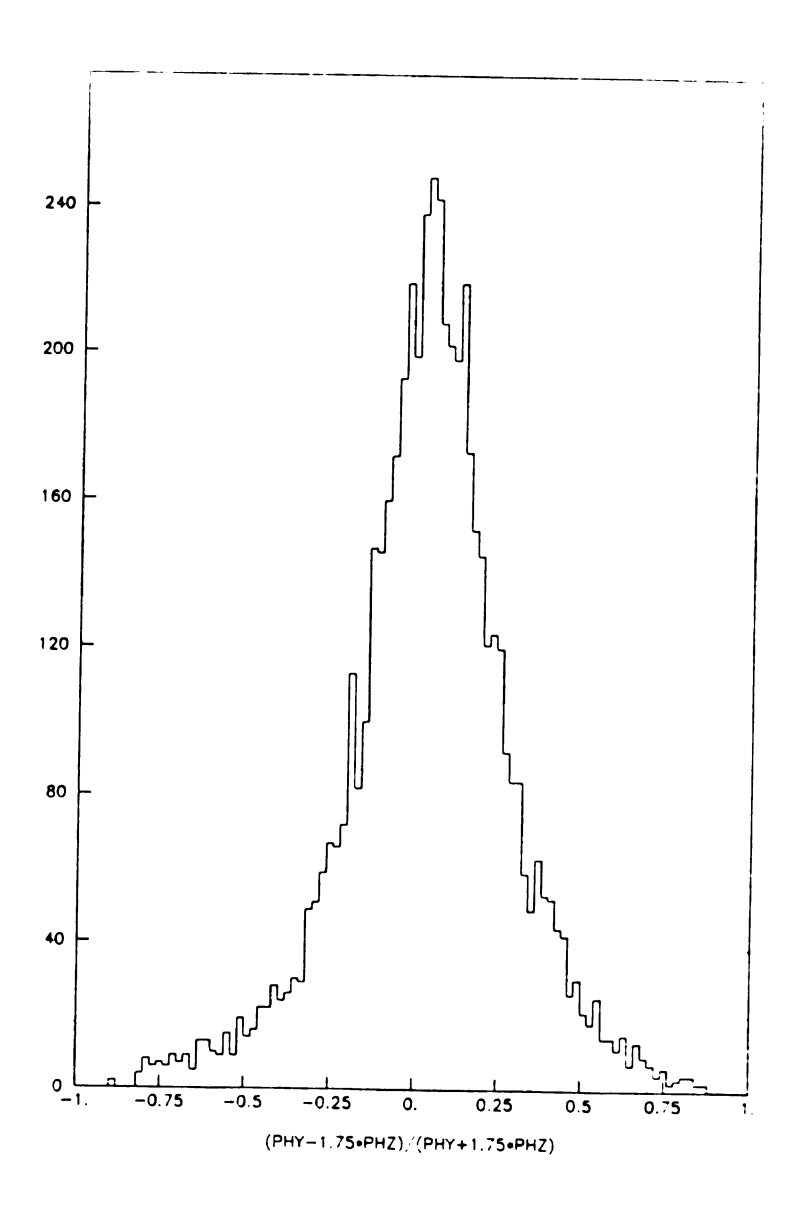


Figure V-8: Distribution of the Ratio diff=(PHY-1.75.PHZ)/(PHY+1.75.PHZ).

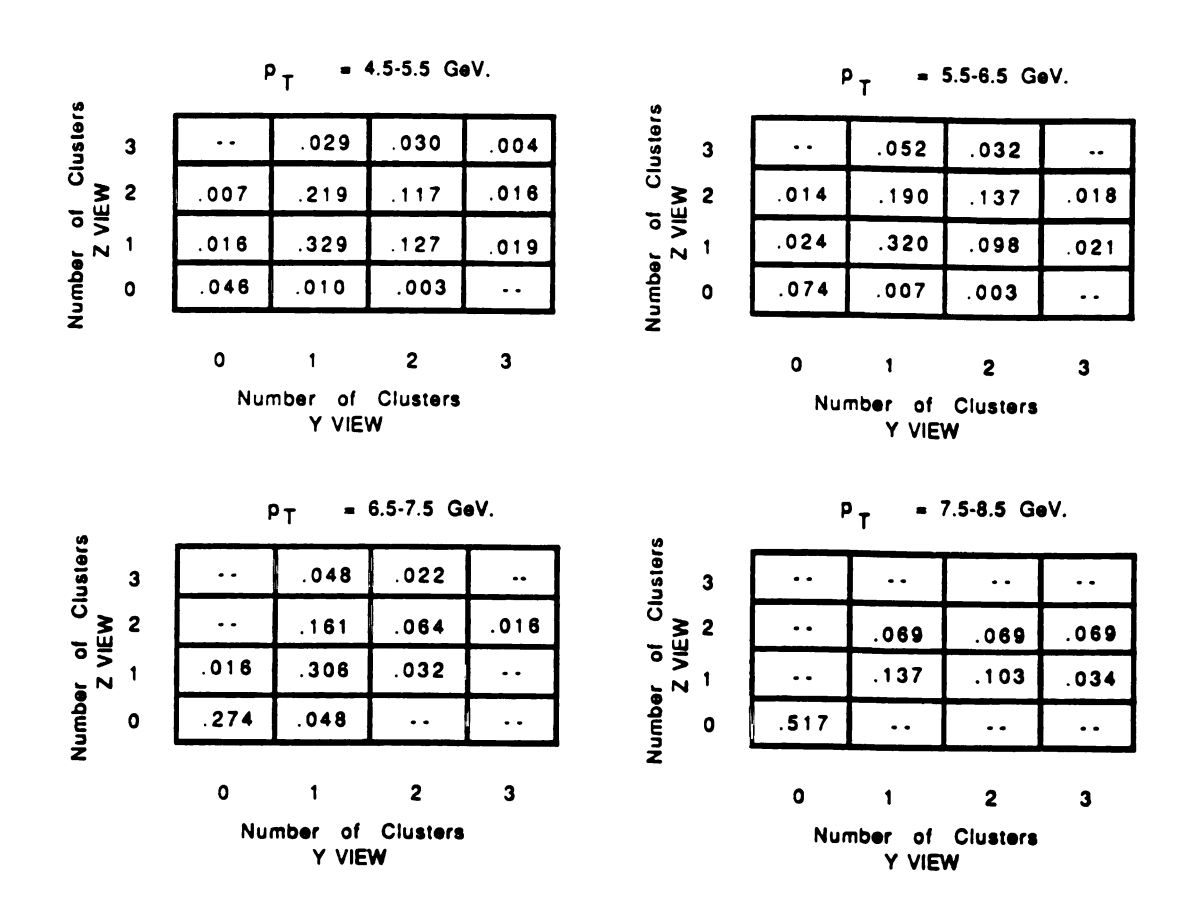


Figure V-9: Fraction of Clusters in the Y and Z Views Inside the Matching Window for the Direct Photon Trigger Data.

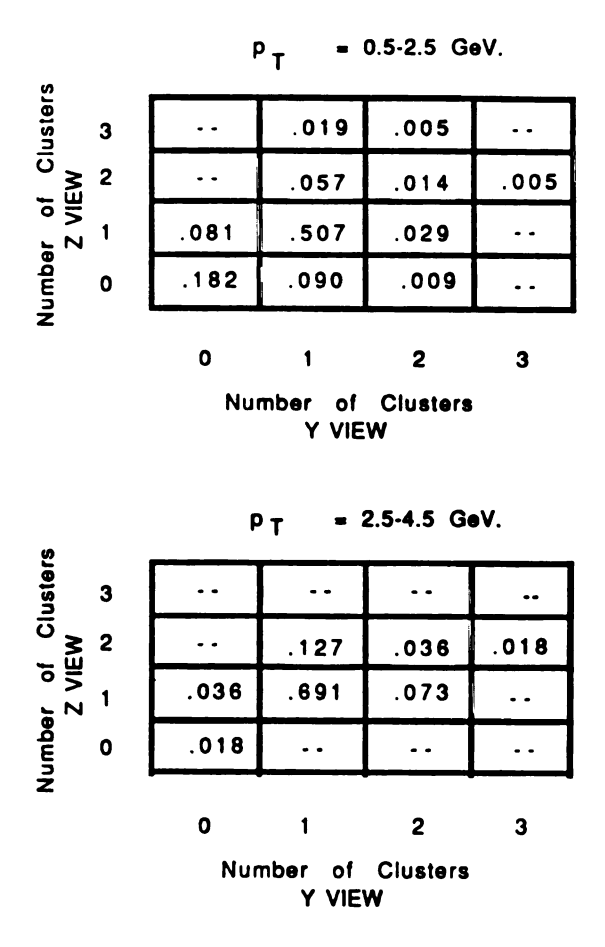


Figure V-10: Fraction of Clusters in the Y and Z $\mbox{ Views Inside the Matching Window for the n° Trigger.}$

single photon sample from the n° trigger data we obtained the matrix shown in figure V-10. It clearly shows that multiple clusters are associated with a single photon shower. This is caused in part by shower fluctuations (as was later demonstrated by the EGS simulation, Appendix C). The inverse phenomenon is also expected to occur as two nearby clusters can merge, producing a single cluster. For example, in meson decay the photons can coalesce into a single chamber cluster. This is made worse by the fact that we are only looking at the Y and Z projections of the shower. Clearly, the geometry and properties of the strip chamber make the direct method of counting the number of clusters an impractical method of separating single and multiphoton triggers.

We then studied the shape of the clusters and the shape of the chamber pulse height distributions in the matching windows on an event by event basis. The shape of a distribution can be studied by analyzing its moments. Figure V-11 shows the second moments (standard deviations) for the individual clusters inside the matching window. There is no obvious structure, for example in the form of a two component distribution, to allow us to separate single from multiphoton showers. The third (skewness) and four (kurtosis) moments were also studied, and showed similar behavior.

An effort was made to adapt the "moments method" [JOH75] to our case. The motivation for the "moments method" is shown in figure V-12. It tries to obtain the distance between two distributions by knowing their standard deviations and areas. The total standard deviation is given by:

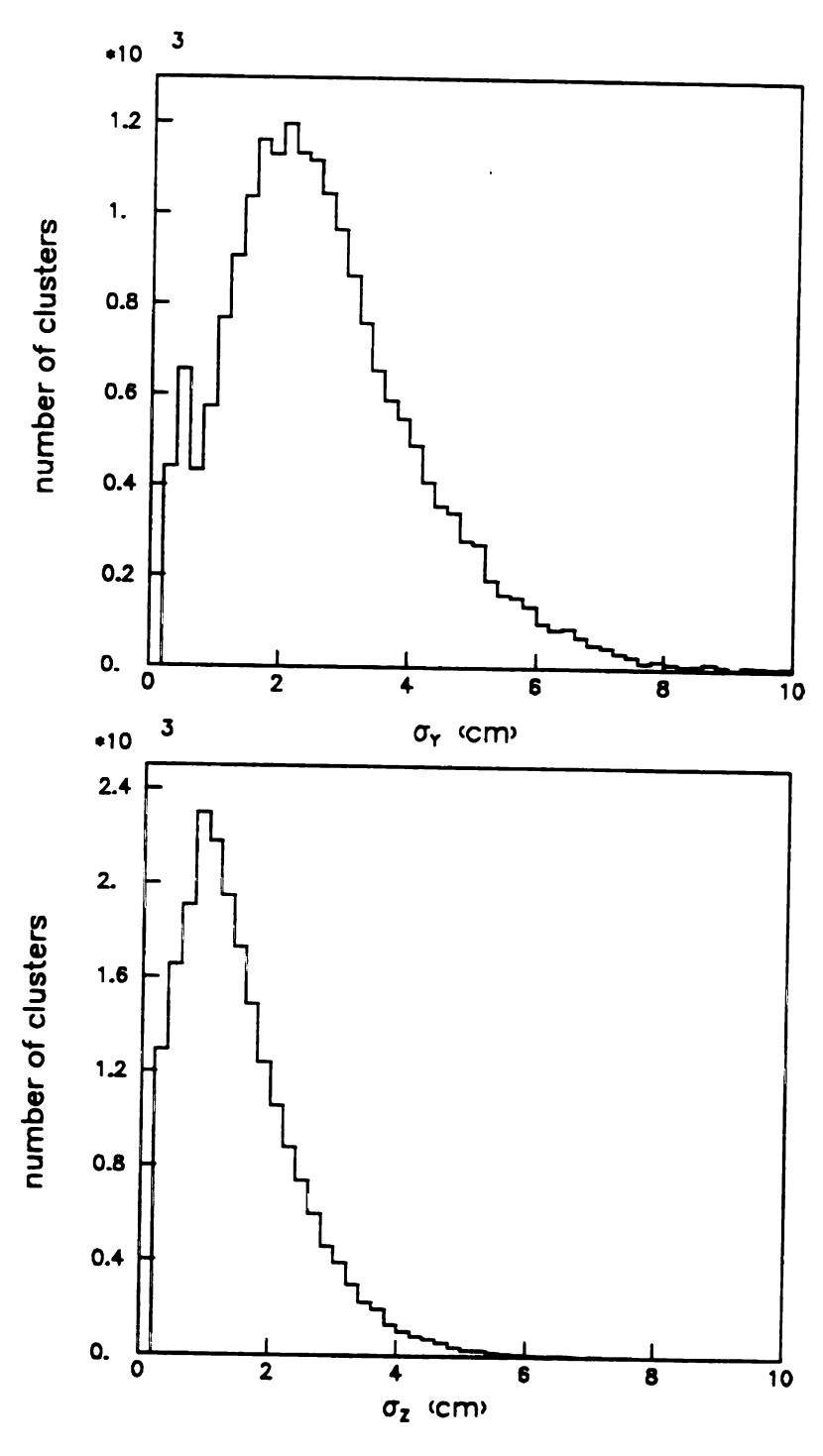


Figure V-11: Standard Deviation of Clusters Inside the Matching Window.

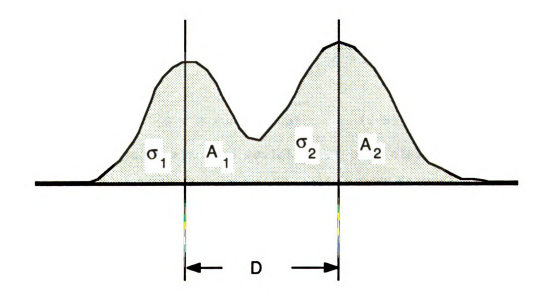


Figure V-12: Moments Method.

$$\sigma_{\rm T}^2 = \frac{\sigma_1^2 \cdot A_1^2 + \sigma_2^2 \cdot A_2^2 + 4 \cdot A_1 \cdot A_2 \cdot (\sigma_1^2 + \sigma_2^2 + D^2)}{(A_1 + A_2)^2}$$
 (V-a)

where σ_1 and σ_2 are the standard deviation of each distribution, A_1 and A_2 their respective areas (energies) and D the distance between centers.

Assuming equal area and equal standard deviation of the two distributions (clusters), the distance between means (cluster centroids) is given by:

$$D = 2 \cdot \sqrt{\sigma_T^2 - \sigma_S^2} \qquad (V-b)$$

where σ_T is the joint standard deviation of both distributions and σ_S is the standard deviation of each of the distributions. Full application of the method requires two dimensional knowledge of the shower and knowledge of the standard deviation of a single shower.

In our case, we defined a variable applying the formula for each view:

$$d_{Y} = 2 \cdot \sqrt{\sigma_{Yt}^{2} - \sigma_{Ys}^{2}}$$
 $d_{Z} = 2 \cdot \sqrt{\sigma_{Zt}^{2} - \sigma_{Zs}^{2}}$ (V-c)

and combined them as $d=\sqrt{d_Y^2+d_Z^2}$. This formula gives the correct separation (d) in the case of symmetrical decays of the neutral mesons. However, the asymmetry distribution of π° 's, even after acceptance effects, is almost flat between -1 and 1, figure V-13. (Asymmetry = (E_1-E_2) / (E_1+E_2) , where E_1 and E_2 are the energies of each photon in the decay). After investigating the use of this variable it was decided that the assumptions do not match the data closely enough, and the uncertainties introduced by the assumptions are too important for a good use to be made of this method.

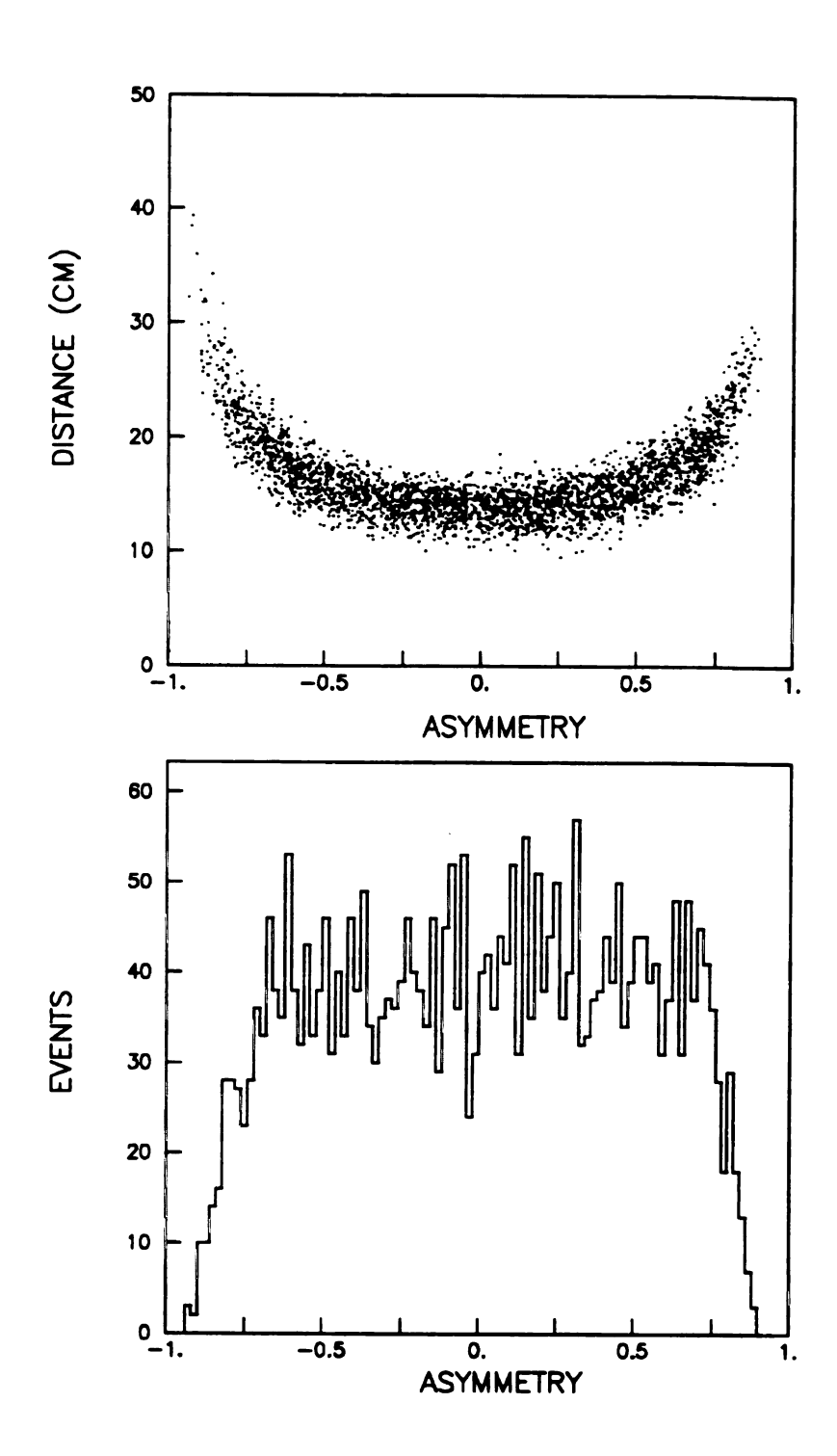


Figure V-13: Distance Between Photons vs. Asymmetry in Simulated $\pi^{\,o}$ Decays ($\Delta p_T^{\,=\,}4.5\text{--}10$ GeV/c) and the Asymmetry Distribution.

Another proposed method was to utilize the ratio of the energy deposited in the front glass array (front) to the total energy deposited (all) as a statistical method of separation. The method compares the front/all distributions obtained from the direct photon trigger data (figure IV-9) with single photon and multiphoton distributions from Monte Carlo simulations.

In addition to the difficulty of the simulation (discussed in section V-9) the separation power of this variable is very poor since the single and multiphoton distributions overlap over a wide range, making the separation either inefficient or ineffective.

V-4. The Main Method of Strip Chamber Analysis.

The variable finally chosen was the result of a simplification introduced in the moments method. The variable $\sigma_{\rm t}$ (total RMS) is defined as:

$$\sigma_t = \sqrt{\sigma_y^2 + \sigma_z^2}$$
 (V-d)

This variable directly combines the Y and Z plane standard deviations (σ_y and σ_z) without the introduction of any extra assumptions. Figure V-14 shows the σ_t distributions for the direct photon data trigger at different p_T ranges. The Y and Z standard deviations are calculated with <u>all</u> the strip chamber information found in a 40 cm matching window ($w = \pm 20$ cm).

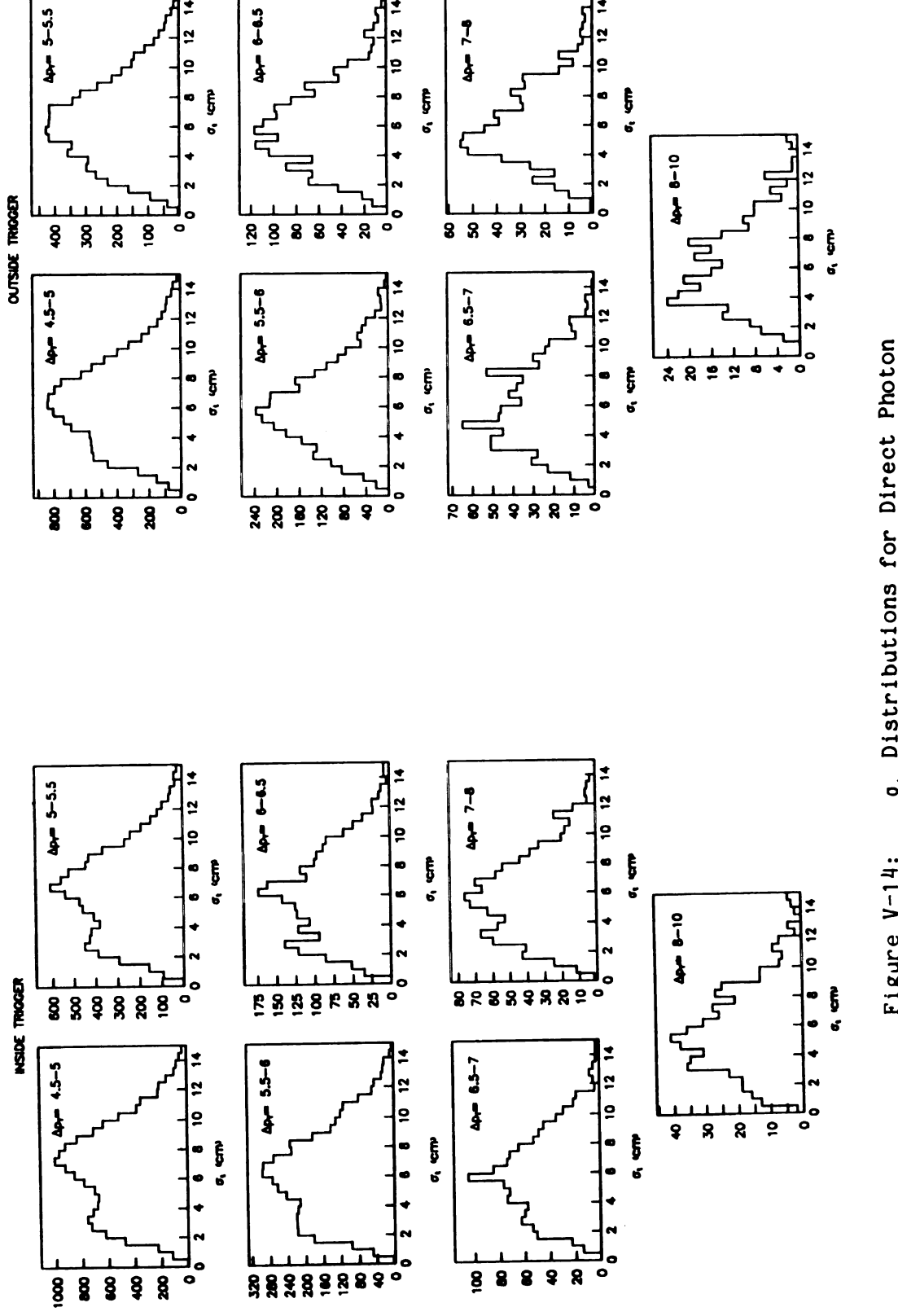


Figure V-14: o_t Distributions for Direct Photon Trigger Data at Various p_T bins for the Inside and Outside Triggers.

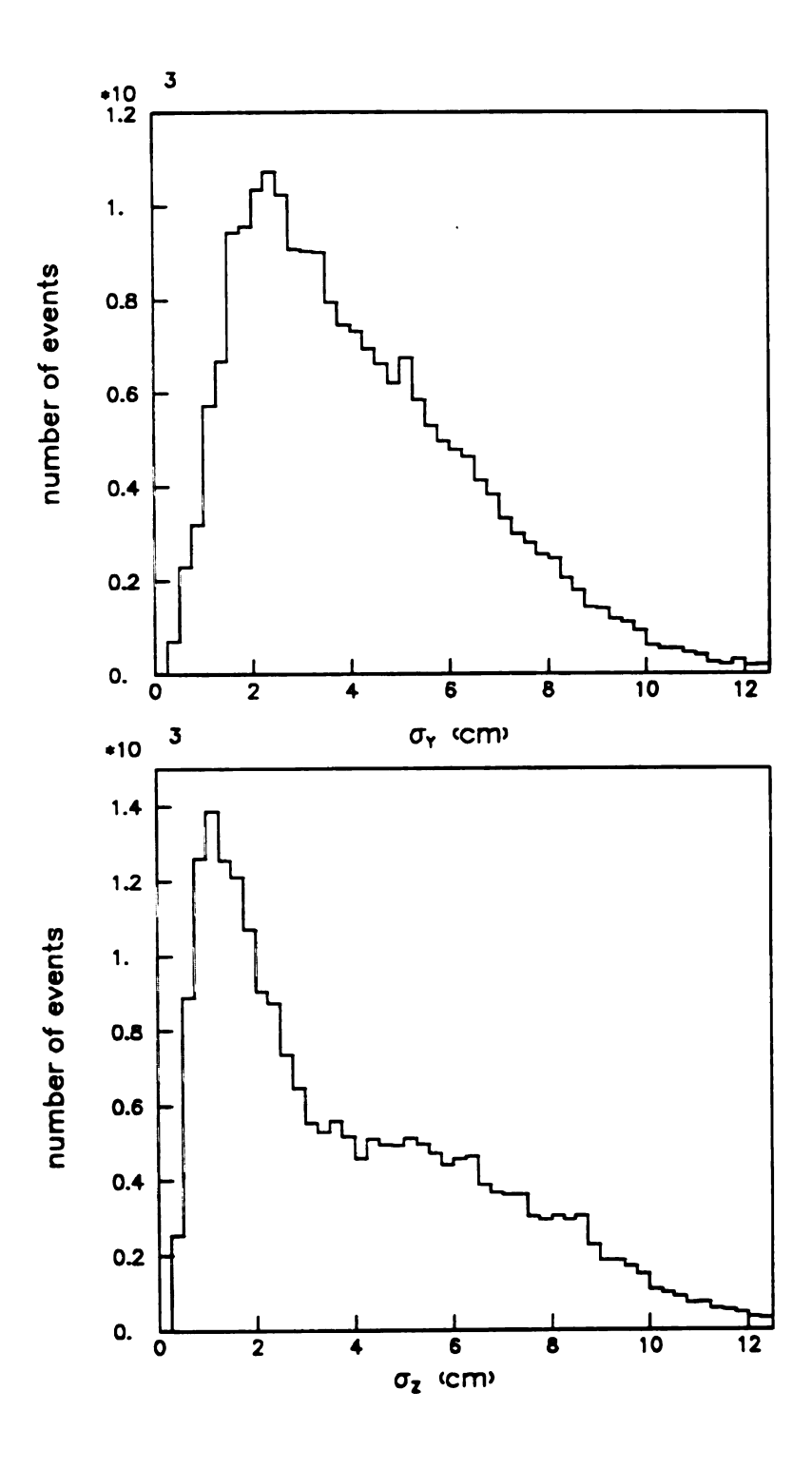


Figure V-15: $\sigma_{\mathbf{y}}$ and $\sigma_{\mathbf{z}}$ Distributions for Direct Photon Trigger Data.

Compared with other distributions discussed above, a remarkably good two component distribution was found. It is interesting to notice that this two component distribution is not shown in the projections σ_y and σ_z of figure V-15. Since the separation between two decay photons from a neutral meson need not be aligned along either projection; only when both are added do they produce a realistic picture.

Clusters were used to fix the lower and upper limits of the strip range in which σ_y and σ_z were calculated. Only clusters with positions inside the matching window and pulse height greater than 400 counts in Y and 200 in Z were considered. Figure V-16 illustrates the criterion for limit selection. The left edge of the left-most cluster inside the window was taken as the left edge, and the right edge of the right-most cluster inside the matching window as the right edge of the "information window".

A flow chart of the strip chamber analysis is shown in figure V-17. The method consists in fitting the $\sigma_{\rm t}$ distributions of the direct photon trigger data to simulated single photon and multiphoton (neutral meson decays) distributions.

The single and multiphoton of distributions are based on EGS shower simulations and Monte Carlo detector simulations. The EGS (Electron-Gamma Shower) simulation is described in Appendix C. It propagated through the detector single photon initiated showers in a range of energies between 0.5 to 10 GeV. For each event generated, the energy deposited in each chamber strip was obtained. Further simulation of the strip chamber response translated this energy deposition to pulse height counts. This "chamber response algorithm" that transformed the

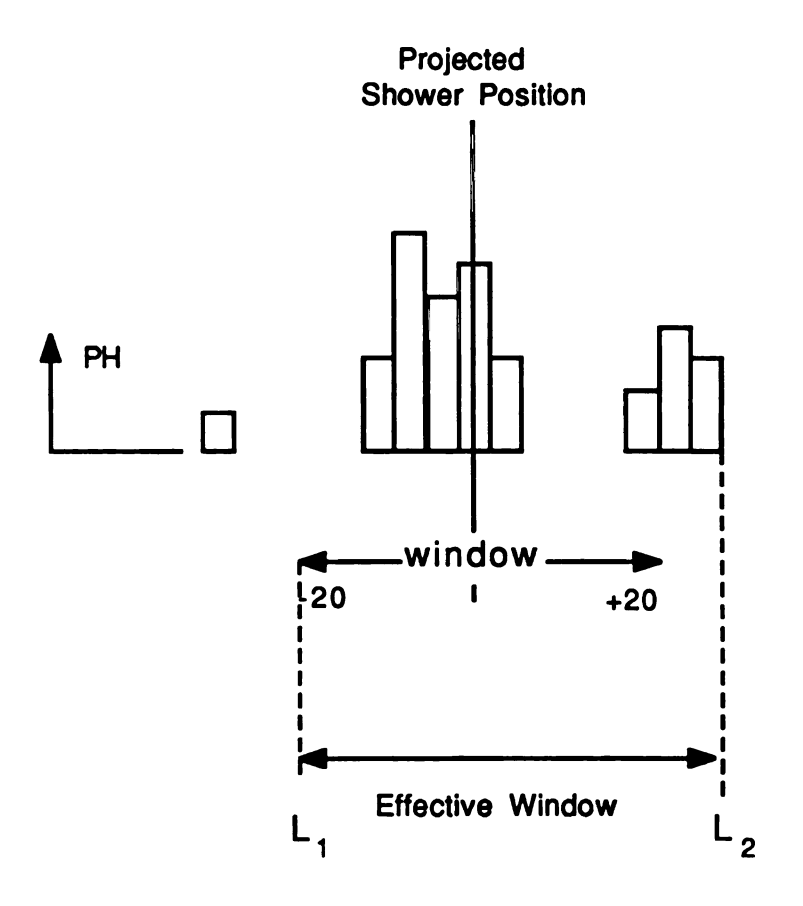


Figure V-16: Criterion of Limit Selection.

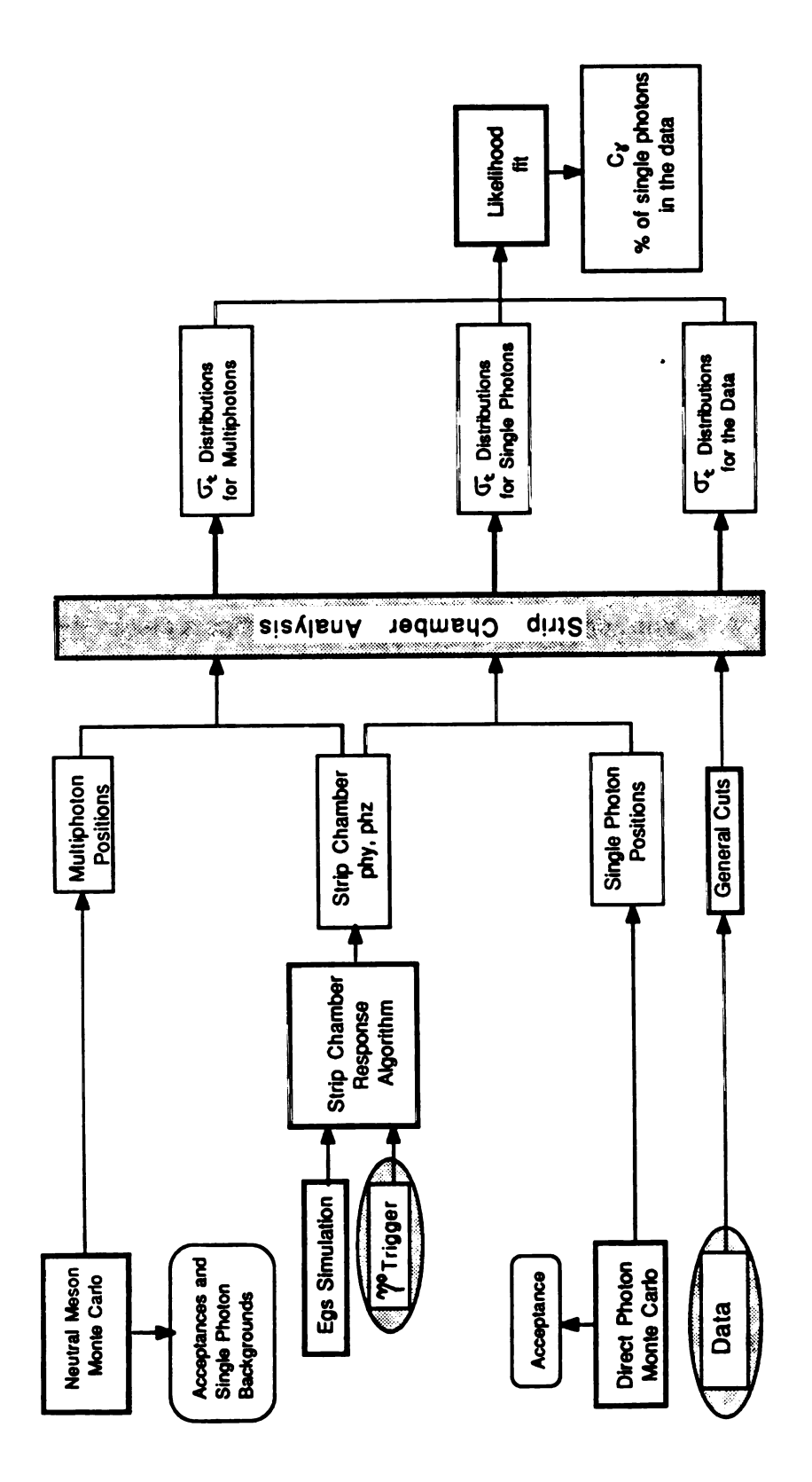


Figure V-17: Strip Chamber Analysis Flow Chart.

energy deposited in each strip to pulse height counts will be discussed in section V-8. A sample of single photon showers from the η° data trigger (described in Appendix E) was utilized to normalize the EGS output.

A sample of direct photons hitting the chambers was generated via Monte Carlo (MC) in the energy range of 4.5 to 10 GeV. Strip chamber pulse height information was attached to these strip chamber hits ("positions"). We then produced a simulated direct photon sample in the appropriate energy range. The details of this MC will be explained in section 6.

Another Monte Carlo, described in the next section, generated neutral mesons and traced their decay photons into the detector. The trigger and all other cuts were also simulated by this MC. The photon positions at the strip chambers were calculated. As with the single photon simulation, photons with appropriate energies were then taken from the EGS generated strip chamber information ("EGS bank") and inserted at these positions. A sample of neutral meson decays in the appropriate energy range was thus generated. Again, the "chamber response algorithm" was then convoluted with these energy depositions to simulate the pulse height response to these multiphoton decays.

The simulated $\sigma_{\rm t}$ distributions for single and multiphotons were then fit to the data. As described in section 8, a likelihood fit with one free parameter gave the fraction of single and multiphoton produced showers in the data sample. The fraction of single photon produced showers was corrected for background and detector acceptance in order to obtain the fraction of direct photons produced. These corrections were evaluated using the single photon and neutral meson decay Monte Carlos

mentioned above. An important background to single direct photons, corrected with this MC information, came from the asymmetric decays of neutral mesons in which one of the photons missed the detector acceptance or was too weak to produce a signal in the strip chamber.

V-5. Simulated Neutral Meson Decays.

One of the most important parts in the analysis was to formulate a Monte Carlo simulation of the detector in such a way that by introducing the various physics processes that we expected to observe, we could calculate the acceptances, evaluate the main single photon backgrounds, and create a pure neutral meson decay sample from which to calculate the multiphoton σ_+ distributions.

The main background processes in direct photon production are those involving production of neutral mesons. The neutral mesons included in the Monte Carlo are described in Appendix A. A detailed description of the Monte Carlo is included in Appendix D. The MC includes the geometrical acceptance of the apparatus, the trigger requirements and all of the cuts (requirements applied to the data during the analysis). It also takes into account resolution effects.

The MC was used in several ways. One was to calculate the acceptance for the neutral mesons, $\mathbf{A}_{\mathbf{m}}$, defined as:

Since we generated neutral mesons in a specific interval in y (rapidity) and ϕ (azimuthal angle), the A_m calculated refers specifically to this solid angle ($\Delta y = \pm 0.8$, $\Delta \phi = \pm 0.6$ rad).

Another important quantity derived from the MC is the number of neutral mesons that manifest themselves as single photons in the detector (especially in the strip chamber), because only one of the decay photons is detected. The number of strip chamber single photons produced by the decay of neutral mesons is given by the ratio:

In the p_T range of our experiment these single photons are produced mainly from asymmetric meson decays and multiphotons are mostly double-photons, predominantly π° decays. Figure V-18 shows $\frac{\gamma}{\gamma\gamma}\Big|_{m}$ vs. p_T for the neutral mesons studied.

The MC also provides a sample of pure multiphoton decays as seen by the strip chamber. Using this sample the \mathfrak{o}_t distributions of multiphotons used in the fits were created.

Another output of this MC is the number of events that do not produce a signal in the strip chamber. These events produce showers which are totally contained in the front glass and/or do not produce an appreciable signal in the chamber. Combining the results of this MC with the EGS simulation we can calculate the probability that this can happen, shown in figure V-19 as function of p_T .

This probability was in fact observed to be much higher in the data than predicted by the Monte Carlo. There are other possible explanations for these events. They can be produced from beam-pipe or

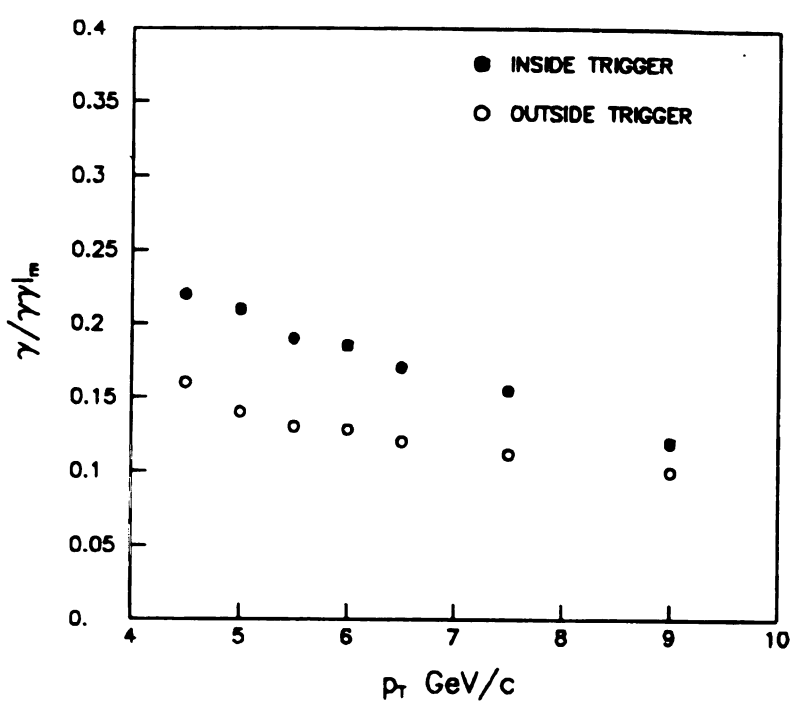


Figure V-18: $\frac{\Upsilon}{\Upsilon\Upsilon}$ mesons vs. p_T from the Neutral Meson Decay Monte Carlo.

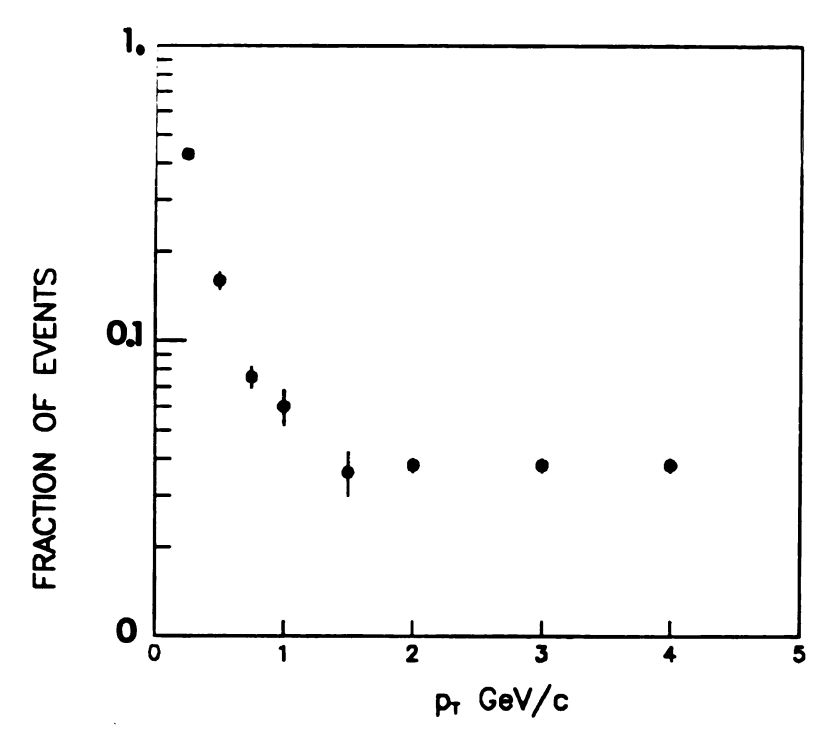


Figure V-19: Probability of Observing a Shower in the Strip Chamber vs. Energy.

beam-gas interactions (side splashes, etc.) or by hadron interactions in the lead glass. The total number of these events contaminating the data was reduced by requiring more than 14 % of the total observed energy to be in the front glass, as will be discussed in section V-9.

V-6. The B-veto simulation.

The B counters were used to veto all single photon triggers converting in the coil. As explained before (section IV-6), the B-veto was not implemented at the trigger level but was used early in the analysis (while writing Data Summary Tapes, DST's) to include only events that did not convert in the magnetic coil. As shown in table V-1, the B-veto is, quantitatively, the most important cut applied to our data. It is important, therefore, that we understand its effects and make the appropriate corrections to the observed signal.

The cut has two parts. First we check for the pulse height in both ends of the B counter hit by the triggering particle. If each of the pulse heights is less than 50 counts, we conclude that the trigger-particle did not convert in the coil. Second, if either pulse height is greater than 50 we check its position. If the B counter position of the trigger-particle (as measured by time differences in the B counters) is inside a ± 20 cm window around the projected position of the trigger, the event is vetoed; otherwise the event is accepted.

The probability of a photon crossing through one radiation length of material (coil, at normal incidence) without conversion is given by $v(E) = .453 + .031 / \sqrt{E}$ [YEL82]. For the average energy of

Table V-1 : Cut Efficiencies.

Analysis Cuts ^p = 4.5 - 10 GeV/c	Acceptance (%)	
	ins	out
Clustering in the Back Glass	94	90
Vertex position	95	95
Nal triggers	99	99
Multi-clusters	95	90
Front Glass geometrical acceptance	67	67
B-veto	38	41
Front/All cut	85	82
Signal in Strip Chamber	99	99

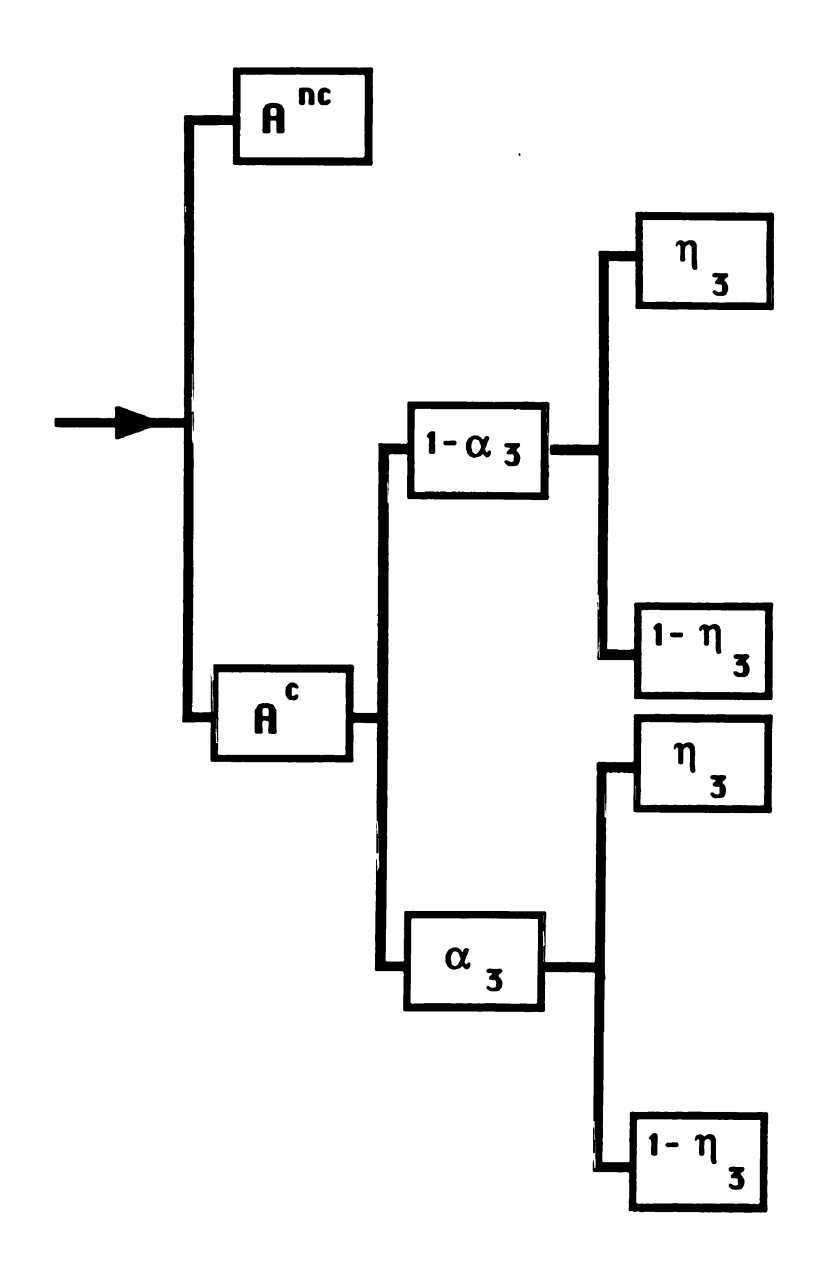


Figure V-20: Probability "tree" of the B-veto
Logic without Associated Particles.

approximately $\langle E \rangle = 5$ GeV in our sample, the non-conversion probability is then $\langle v \rangle = .467$; and the probability of conversion is given by $(1 - \langle v \rangle) = .533$. For n photons the probability of non-conversion is $A^{nc} = v(E)^n$, and the probability of conversion $A^c = (1 - v(E)^n)$.

To check for angular effects in the B-veto, a slightly simplified model, using $\exp(-7/9)$ and $\exp(-7/9\cos(\theta))$ for the normal and oblique conversion probabilities, was done. The angle of incidence θ distribution was taken from the neutral meson Monte Carlo. The result was a change in the B veto acceptance from 0.341 to 0.336.

For the B-veto we have to consider two efficiencies: α_s , the probability of detecting the pulse height associated with the conversion and η_s , the probability of the position measured by the B counter being outside the window. Since our pulse height cut is less than one m.i.p (83 counts) we will assume $\alpha_s = 1$. Figure V-20 shows the probability "tree" of a trigger-particle through the veto logic; the probability of passing the veto is given then by

 $A_0 = \Sigma \ PASS = A^{C} + A^{C} \cdot \eta_3 \cdot \alpha_3 + A^{C} \cdot (1 - \alpha_3) \cdot \eta_3 \qquad (V-g)$ and, with the assumption that $\alpha_3 = 1$:

$$A_o = A^{nc} + A^c \cdot \eta_3$$
 (V-h)

The presence of particles associated with the trigger particle complicates the situation described in figure V-20. Each of the "branches" of figure V-20 opens now to a group of "2" order" diagrams represented in figure V-21.

Let us define the following quantities, f: fraction of triggers with associated particles in the region covered by the B cut; α_1 : the probability of a track depositing enough pulse height in the B counter to pass the cut; α_2 : probability of a track plus a shower (conversion)

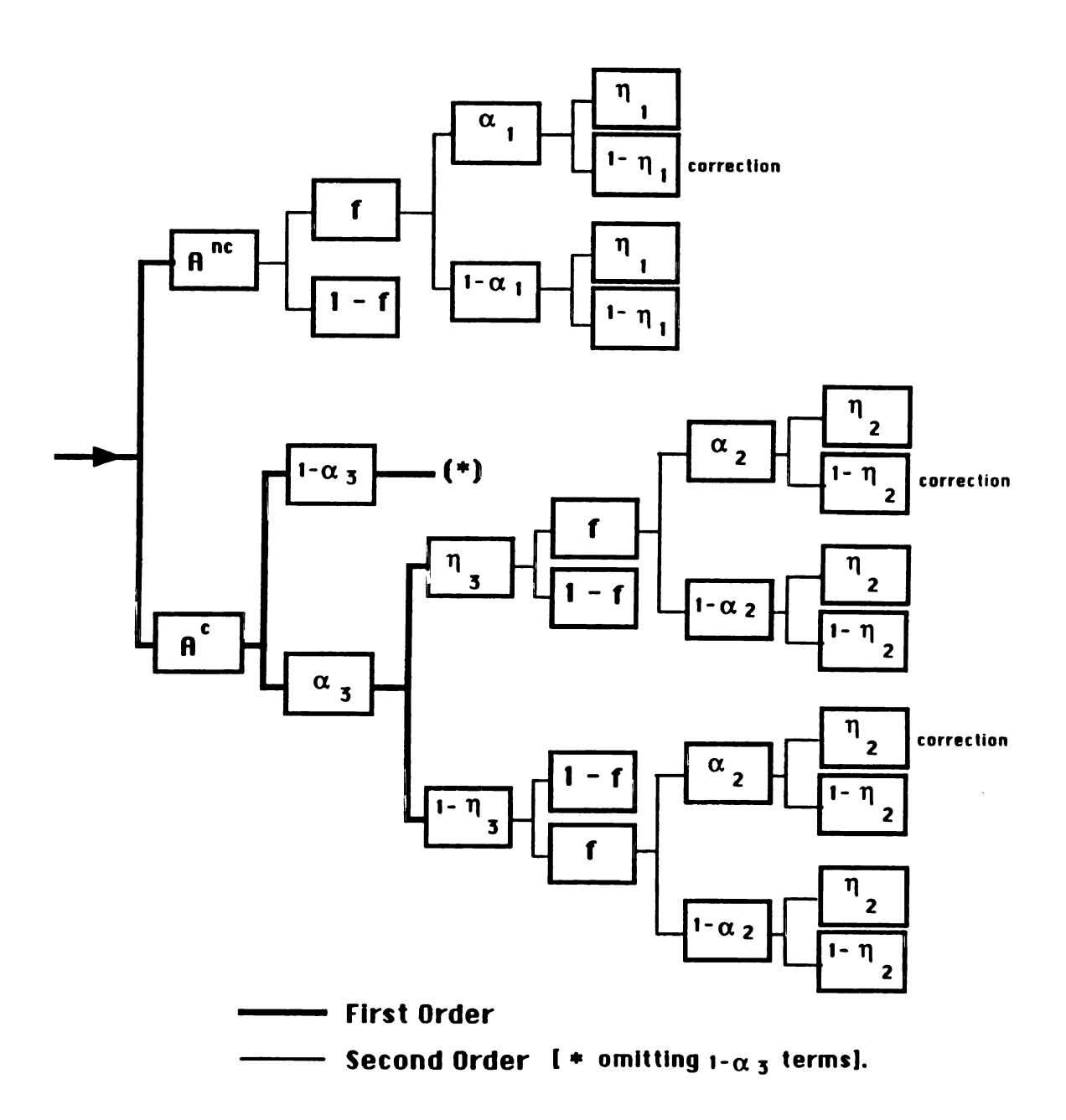


Figure V-21: Probability "tree" of the B-veto
Logic with Associated Particles.

depositing enough pulse height in the B counter to pass the cut; η_1 : the probability for a B counter position of a track being outside the Δz window and η_2 : the probability for a B counter position of a track plus a shower (conversion) being outside the Δz window.

Figure V-21 shows the probability "tree" for all the possibilities encountered by a trigger-particle going through the B-veto logic. If formula (V-g) is viewed as a sum of all the terms represented by the first order diagrams, then figure V-21 shows that each gets a correction term:

$$A = A^{\text{nc}} - A^{\text{nc}} \cdot f \cdot \alpha_1 \cdot (1 - \eta_1)$$

$$+ A^{\text{c}} \cdot \alpha_3 \cdot \eta_3 - A^{\text{c}} \cdot f \cdot \alpha_3 \cdot \alpha_2 \cdot \eta_3 \cdot (1 - \eta_2)$$

$$- 0 + A^{\text{c}} \cdot f \cdot \alpha_3 \cdot \alpha_2 \cdot \eta_2 \cdot (1 - \eta_3) \qquad (V-i)$$

The probability of passing the B veto, the B-veto acceptance, is now (with $\alpha_3=1$):

$$A = A^{\text{nc}} + A^{\text{c}} \cdot \eta_3 - f \cdot A^{\text{nc}} \cdot \alpha_1 \cdot (1 - \eta_1) + f \cdot A^{\text{c}} \cdot (1 - \eta_3) \cdot \alpha_2 \cdot \eta_2 - f \cdot A^{\text{c}} \cdot \eta_3 \cdot \alpha_2 \cdot (1 - \eta_2)$$

$$(V-j)$$

and after some algebra we obtain the expression:

$$A = A^{nc} \cdot [1 - f \cdot \alpha_1 \cdot (1 - \eta_1)] + A^{c} \cdot [\eta_3 + f \cdot \alpha_2 \cdot (\eta_2 - \eta_3)]$$
 (V-k)

We have to calculate 4 sets of these parameters. For the direct photon and meson events and for the inside and outside detectors. We average over any energy dependence. The values are given in table V-2.

Table V-2: Values of the Parameters in the B-veto simulation.

	inside photons	inside mesons	outside photons	outside mesons
f	.11	.21	.13	.32
α_1	.87		.87	
α_2	1.		1.	
α_3	1.		1.	
η,	.56	.26	.56	.34
η2	.54	.20	.54	.28
η_{3}	.19		.27	

f : fraction of triggers with associated particles

 α_1 : probability of a track to pass the B pulse height cut

α 2 : probability of a track plus a shower to pass the B pulse height cut

 $lpha_{3}\;$: probability of a shower to pass the B pulse height cut

 η_1 : probability for a B counter position of a track being outside the z window

 η_2 : probability for a B counter position of a track plus a shower being outside the z window

 η_3 : probability for a B counter position of a shower being outside the z window

We have a CON tape in which the B-veto was not applied. We used these data (which contains both inside and outside triggers) to measure the fraction f for π° 's, by counting the number of associated particles within \pm 4 degrees in azimuthal angle from the trigger position (a region comparable with the B counter geometrical acceptance).

To measure the f value for direct photon triggers we assumed that direct photons have no associated particles other than the spectators (i.e. we ignored the bremsstrahlung process). The value of f for the direct photon trigger is then the spectator level that was measured at an azimuthal angle of 90 degrees from the trigger position, well away from either the recoil jet or the trigger.

The value of α_1 , the efficiency of the B counter for tracks [ANG82] is α_1 = 0.87. Since we assumed α_3 = 1, therefore α_2 = 1. The value of η_3 was measured directly from the non-B veto CON tape considering only triggers with no associated particles at \pm 4 degrees in the azimuthal angle (ϕ) of the trigger position. η_1 for π^0 's was calculated from a Δz histogram from the non-B veto data where only triggers with no conversions in the coil (B counter pulse heights less than 50 counts) were considered. The η_2 value for π^0 's was obtained directly from the Δz histogram of all the non-B veto data.

For the direct photon value of η_1 , a Monte Carlo was written to calculate the Δz histogram. This MC produced tracks from a flat distribution in y (rapidity). One particle per trigger was considered, and the value of Δz = [track - trigger] was calculated.

The η_2 value for direct photons was calculated using the same MC mentioned before but the B counter position was obtained as the average between track and trigger, therefore a value of Δz = {(track + trigger)

/2 - trigger} was calculated. This averaging is appropriate for cases where the position is calculated using time differences of two ends [LIN82].

veto acceptance with that measured for the non-B veto data (a mix of direct photons and mesons). From table V-1 the measured are, A_{ins} = 0.38 and A_{out} = 0.41. We had to assume a fraction of photons in the sample. Based on previous results of experiments R108 [ANG80] and R806 [ANA82] we took Y/all = 0.1. Also needed is the fraction of single photons resulting from asymmetric meson decays. These numbers came from the meson decay MC: Y/ π ° = 0.081 for the inside and Y/ π ° = 0.047 for the outside. These values gave the following sample composition: inside, a=83% π °'s; b=7% Y from π ° and c=10% direct photons; outside: a=86% π °'s; b=4% Y from π ° and c=10% direct photons, then: A = a·A $_{\pi}$ °+ b·A $_{\pi}$ °+ c·A $_{\gamma}$. Applying equation (V-k) with all the values of table V-2 we obtained for the inside A $_{\gamma}$ = 0.569; A $_{\pi}$ ° $_{\gamma}$ = 0.506; A $_{\pi}$ ° $_{\sigma}$ = 0.339; A = 0.374 while the measured value was 0.38. For the outside A $_{\gamma}$ = 0.606; A $_{\pi}$ ° $_{\gamma}$ = 0.527; A $_{\pi}$ ° $_{\sigma}$ = 0.392; A = 0.418 while the value measured was 0.41.

If associated particles were ignored (f = 0), the values obtained are A_{γ} = 0.568, $A_{\pi^0\gamma}$ = 0.568, A_{π^0} = 0.366 and A= 0.40 for the inside, and A_{γ} = 0.611, $A_{\pi^0\gamma}$ = 0.611, A_{π^0} = 0.429 and A = 0.45 for the outside. We take the agreement between calculated and measured values as evidence that a B-veto consisting of a pulse height cut and a Z-position cut is well understood.

Comparing A^{nc} with the sets of values, with, and without associated particles, we concluded that the most important correction to the non-conversion acceptance comes from the inclusion of the position

resolution of the B counters. However the effect of the associated particles is also noticeable, especially in the π° component.

In the analysis, formula (V-k) was introduced directly in the Monte Carlo simulation of the total acceptance (where various neutral meson decays are considered) to account for multiphoton triggers with more than two photons.

V-7. Simulated Single Photons.

As previously stated there was a single photon Monte Carlo that produced the same kind of output as the Neutral Meson decay MC described in section V-5. The geometrical acceptance, trigger and requirements (cuts) were the same as utilized for the neutral meson MC, as explained in Appendix D.

The kinematics are, of course, different and more simple. We start by producing photons using the Aurenche et al. [AUR84] p_T distribution for y=0 prediction using Duke & Owens set I structure functions [DUK84]. We take a uniform rest-frame angular distribution in ϕ (azimuthal angle) and a flat distribution in rapidity. We produce photons in the rapidity interval of $\Delta y=\pm~0.8$ and in $\Delta \phi=\pm~0.6$ rad; the same used in the neutral meson MC.

The acceptance for direct photons, A_{γ} , is calculated by applying all the geometrical and analysis requirements, just as in the case of the neutral mesons. A sample of pure single photons as seen in the chambers is produced with the correct p_T distribution within each of the p_T bins utilized in the p_T fits. It is assumed that the single photon

background from the neutral mesons has nearly the same \mathbf{p}_T distribution as the real photons. Therefore we take these $\mathbf{\sigma}_t$ distributions to be the distribution of all the single photons in the chamber (direct photons plus single photon background).

V-8. Simulated Single and Multiphoton o, Distributions.

To obtain the simulated \mathfrak{a}_{t} distributions for single and multiphoton decays we combine the EGS simulated strip chamber shower information with photon positions generated by the Monte Carlos described in previous sections.

The EGS output provided the energy deposition by strip in the chamber. The simple scaling of the energy to pulse height using the η° trigger data for normalization is not enough. The σ_t distributions produced in this way are clearly in disagreement with the data.

Of course, what is missing is the response of the chamber to the signal. This is difficult to simulate. Strip chamber properties have been studied by the Charpak group at CERN [CHA70, BRE77]. These studies concentrated on position resolution using MWPCs. Various sources of errors are presented, some related to the algorithm to calculate positions [CHA78], others to the chamber geometry [GAT79] and charge collection, or to systematic errors of external source such as electronic cross talk [PIU82].

A good model of the way the signal is read-out by the cathode strips is available [SAU77]. However, each chamber possesses its individual signal-response relation. Essentially, the ions and electrons caused by the ionization of the chamber gas start moving with different speeds due to the electric field in the chamber towards their respective opposite sign poles. When the electrons are very near to the anode wires, the high field present there gives to the electrons enough energy to start an "avalanche". The electrons of the avalanche are rapidly captured by the anode. The positive ions, however, form a very slow moving cloud moving towards the cathode. This positively charged cloud, on the time scale of the electronic read-out, can be approximated to be at the wire position. The induced image of this charge in the cathode strips is what is detected.

The electrostatic problem of the distribution of induced charge has been resolved analytically [ERS82,MAT84,VAN86,GAT79]. The charge distribution is given by the Gatti-Mathieson [MAT84] formula:

$$\Gamma(\lambda) = K_1 \frac{1 - \tanh^2(K_2\lambda)}{1 + \tanh^2(K_2\lambda)}$$
 (V-1)

where $\lambda=x/H$, x is the coordinate along the cathode plane, H is the distance between wires and strip cathodes, $K_2=\pi/2\cdot(1-\frac{1}{2}\cdot\sqrt{-K_3})$. The parameter K_3 , that depends on H, the wire spacing and the wire radii, was taken from [MAT84], $K_3=0.05$ for our chamber geometry. K_1 is a normalization constant such that $\int \Gamma(\lambda) d\lambda = 1$. Figure V-22 shows the Gatti-Mathieson distribution for our chamber parameters. We used the G-M distribution to spread each wire energy deposition among adjacent strips.

Other properties also have to be taken into account. The gain fluctuations between strips [CHA78] account for some smearing of the signal. To simulate it, we used a Gaussian distribution with a R.M.S. given by $\Delta PH/PH = \alpha_{C}$. We also introduced a Gaussian noise, with mean at

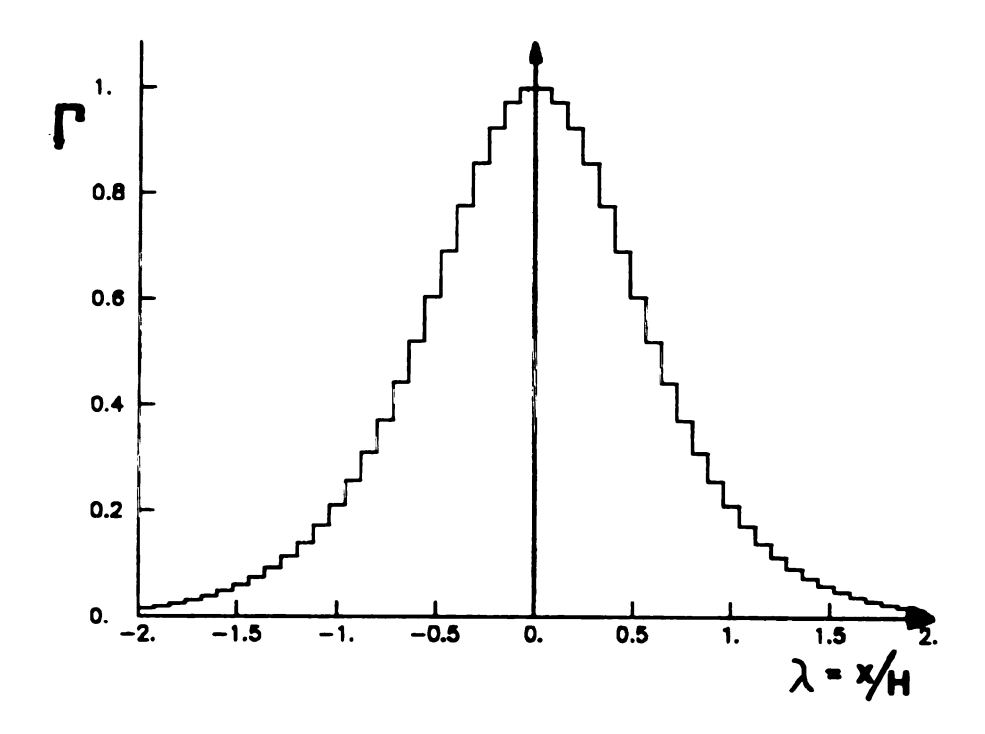


Figure V-22: Gatti-Mathieson Image Charge Distribution in λ bins of 0.1.

the calculated value of the pulse height and a standard deviation of α_N counts, to account for random noise in the strip read-out electronics. Where α_G and α_N are parameters to be determined (values given in next page).

Further improvements of the simulation require information on the specific characteristics of the chamber such as geometry (wire spacing, wire-strip spacing, etc.) [GAT79] as well as electronic read-out and connections between components [PIU82]. Unfortunately we were not able to increase further the accuracy of our simulation. First the simulation was done long after the detector was dismantled and precise written information was not available. Second, we lacked an accurate model of how to proceed. The chambers showed an asymmetry between the Y and Z views. This was related, presumably, to read-out characteristics; Y strips run perpendicular to the anode wires, while Z strips run parallel to them. The electrical coupling characteristics of the Z strips was thus different. The positive charge of the ions created in the avalanche could induce a positive charge in the adjacent anode wires. The Z strips running parallel to this wires would see a lower charged anode and then could get more positive. This would affect the shape of the signal in the Z view. This phenomenon is likely to be of less importance in the Y view since the wires are perpendicular, thus integrating the signal over various wires. This effect has not been simulated.

To summarize, the "chamber response algorithm" is composed of: an energy to pulse height scaling of the form PH = α_{PH} •E , the Gatti-Mathieson charge distribution formula, strip by strip gain fluctuations and random noise. The values of α_{PH} , α_{G} and α_{N} were adjusted through the

normalization using the η° trigger data. As explained in Appendix E, these data provided a sample of single photons in the energy range between 0.5 to 4 GeV. The 2 GeV bin was used as normalization point. As was proven later (see section VI-1) the most important feature is to make the σ_{t} distribution maxima to agree. Thus the values were chosen such that MC σ_{t} maxima, mean σ_{t} and mean pulse height agree with η° data. Figures V-23, V-24 and V-25 show the values of mean σ_{t} , σ_{t} distribution maxima and mean pulse heights for single photons from η° trigger and simulations as function of the energy. The values chosen were: σ_{N} = 17, σ_{C} = 0.2 and σ_{PHV} = 44000, σ_{PHV} = 22000.

For the single photon sample we took events generated with the single photon MC and simulated chamber energy deposition of each event choosing from the EGS shower bank (the set of energies between 0.5 and 10 GeV generated by EGS) a shower with the appropriate energy. We need to interpolate since the energies of the generated events have a continuous distribution within the bin, but the EGS runs were made for discrete energies. The EGS runs used for the single photon simulations are at 4,5,6,7,8 and 10 GeV. For example, if we want to create a strip chamber shower at 4.73 GeV we have to interpolate the properties from the 4 and 5 GeV EGS banks. The algorithm uses linear interpolation for the pulse height and the standard deviation of all the clusters in the window with pulse height above the cut (400 counts in Y and 200 counts in Z). Given an event with energy E, if E_1 is the closest energy from the EGS bank and E_2 the second closest (such that $E_1 \le E \le E_2$), we take an event from the E_1 bank and scale each strip pulse height by:

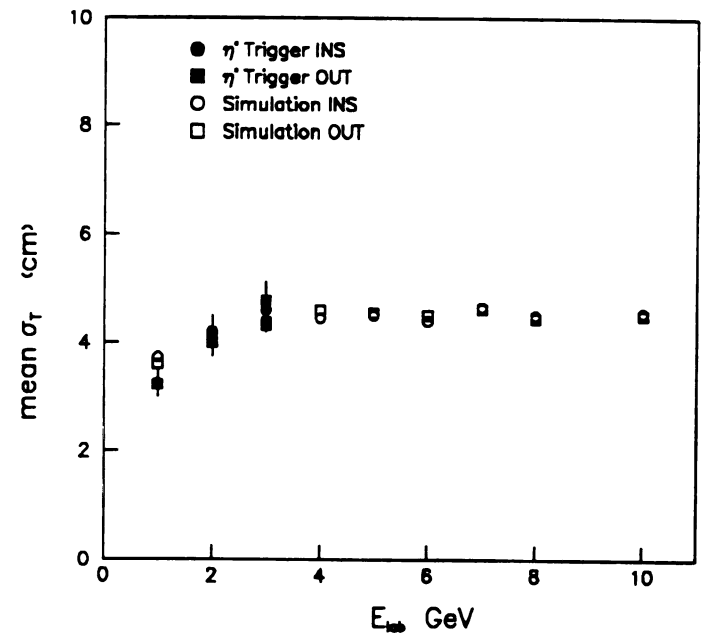


Figure V-23: Mean of the σ_{t} Distributions vs. Energy for Single Photons from the η^{o} Trigger and Simulation.

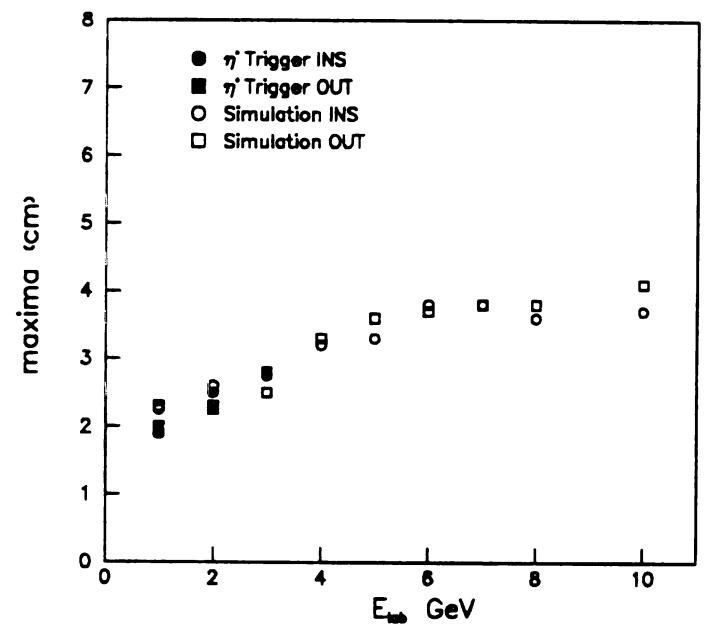


Figure V-24: Maxima of the σ_t Distributions vs. Energy for Single Photons from the η° Trigger and Simulation.

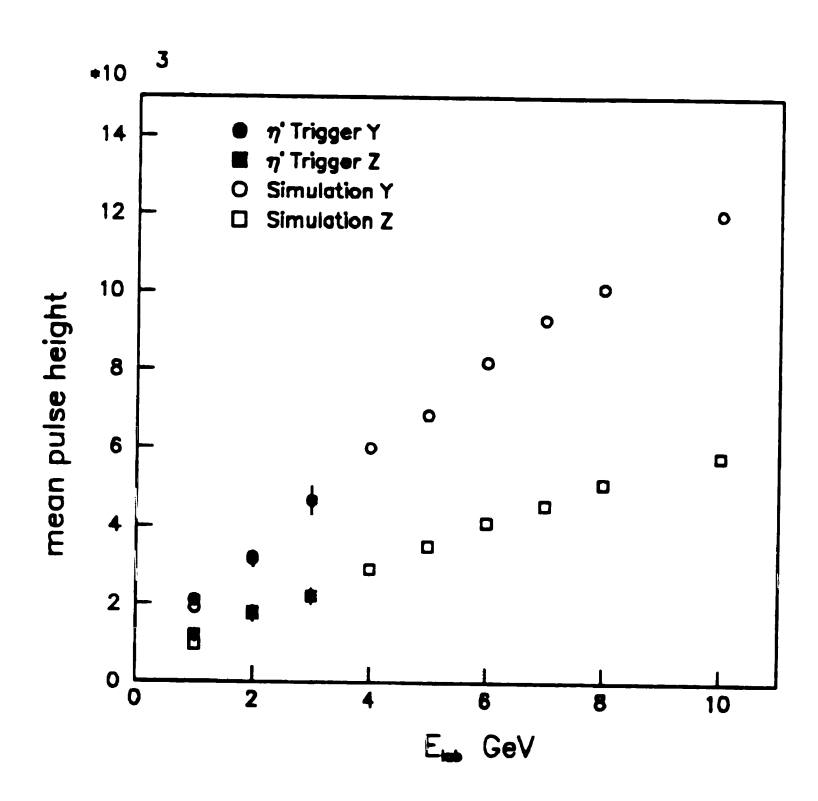


Figure V-25: Mean Pulse Height vs. Energy for Single Photons from the η° Trigger and Simulation.

 $\text{PHT}_{\mathbf{i}}(E) = \beta \cdot \text{PHT}_{\mathbf{i}}(E_1), \text{ with } \beta = \frac{\langle \text{PHT}_{\mathbf{in}} \rangle_E}{\langle \text{PHT} \rangle_{E_1}}, \text{ where } \langle \text{PHT} \rangle_{E_1} \text{ is the mean}$ $\text{pulse height of the cluster in } E_1, \text{ and } \langle \text{PHT}_{\mathbf{in}} \rangle_E \text{ is the linear}$ interpolated mean pulse height at energy E, as:

$$\begin{split} &\langle \text{PHT}_{\text{in}}\rangle_E = \langle \text{PHT}\rangle_{E_1} + \big[\langle \text{PHT}\rangle_{E_1} - \langle \text{PHT}\rangle_{E_2}\big] \cdot (E-E_1)/(E_1-E_2) \,. \text{ The width of } \\ &\text{the clusters is also scaled. Every strip is scaled by a factor α, while keeping the centroid of the cluster fixed. Thus, if x_i is the strip position and $\langle x \rangle$ the centroid position, $[x_i(E) - \langle x \rangle \langle E)] = $\alpha \cdot [x_i(E_1) - \langle x \rangle \langle E_1)]$, with $\alpha = \frac{\sigma(E) + \langle \sigma_{in} \rangle_{E^-} \langle \sigma \rangle_{E_1}}{\sigma}, \text{ where } \langle \sigma_{in} \rangle_{E} \text{ is the interpolated mean standard deviation as: } \langle \sigma_{in} \rangle_{E} = \langle \sigma \rangle_{E_1} + \big[\langle \sigma \rangle_{E_1} - \langle \sigma \rangle_{E_2}\big] \cdot (E-E_1)/(E_1-E_2). \text{ A rebinning of the pulse height information into 1 cm strips is performed after the width scaling.} \end{split}$$

After the interpolation we apply the "chamber response algorithm" to the energy distributions to obtain the pulse height information. Once we have created an event sample of pure single photon events we use the standard algorithm to calculate the $\sigma_{\rm t}$ distributions in the $p_{\rm T}$ range of 4.5 to 10 GeV.

For the multiphoton case we proceed in a similar way. Now for each of the events generated in the neutral decay MC we have two or more strip chamber positions at which we should insert the appropriate chamber signal from the EGS bank. Due to the kinematical properties of the decay (discussed in Appendix B), the photons cover a large range of energies. For this reason we ran EGS simulations for incident photons as low as 0.5 GeV. Below 0.5 GeV the probabilities that this photon passes through the front glass and produces a signal in the chamber are very low (see figure V-19).

The same interpolation of chamber properties from the EGS bank as described above was used. Then the "chamber response algorithm" was applied to the joint information of the photons. The multiphoton sample obtained was analysed using the standard algorithm to obtain the $\sigma_{\rm t}$ distributions.

V-9. A Front/All cut.

A study of the counting matrices of figure V-9, the Front/All histograms of figure IV-9, and the $\sigma_{\rm t}$ data distributions of figure V-15 showed an excess of data events with no strip chamber clusters, low Front/All, and lower $\sigma_{\rm t}$ values than those expected from the simulation. We studied a sample of these events and concluded that they correpond to several sources distinct from direct photons or neutral meson decays. These included side splashes (beam-gas or beam-pipe interactions), "glass misfireds" (large energies in a single cell with no neighbors) and a small hadron background (to be discussed in section VI-9). These classes of backgrounds will tend to give low $\sigma_{\rm t}$ and low Front/All.

The ratio Front/All was defined in section IV-7. The ratio measures the fraction of energy deposited in the front glass array, or how deeply in the glass array the shower had started.

A requirement of a minimum Front/All could ,then, clean the sample of these spurious events. Figure V-26 shows a scatter plot of Front/All vs. $\sigma_{\rm t}$. The region of low Front/All (< 0.14) has excess concentration of low $\sigma_{\rm t}$ events with few events at high $\sigma_{\rm t}$. Requiring

Front/All greater than 0.14 improved the agreement between made MC $\sigma_{\mbox{\scriptsize t}}$ simulations and data.

This cut must be taken into account in the acceptance correction for the observed signal. The correction affects the single and multiphoton samples differently. Therefore we need to know both Front/All distributions.

Front/All distributions for single photons were obtained directly from the EGS simulation (Appendix C). The multiphoton Front/All distributions were obtained using the EGS output in combination with the meson decay simulation. For each photon we obtained from EGS Front/All = $(F/A)_i$. An event with n photons, of energy E_i will have Front/All given by:

Front/All =
$$\frac{\sum_{i}^{n} E_{i} \cdot (F/A)_{i}}{n}$$
 (V-m)

To find if the simulation was correct, two checks were done. First, a special electron initiated EGS run at 4 GeV was made to compare with a 4 GeV PS test run done with a front-glass back-glass configuration [NIC82]. The test and simulation distributions are shown in figure V-27. Evidently, the simulated values are lower than the PS measurements.

A second check was performed using the direct photon trigger data. For a given p_T bin, a simulation of the data was taken as a combination of C_{γ} % single photons and $(1-C_{\gamma})$ % of multiphotons. Figure V-28 shows the data Front/All distributions for the data and the

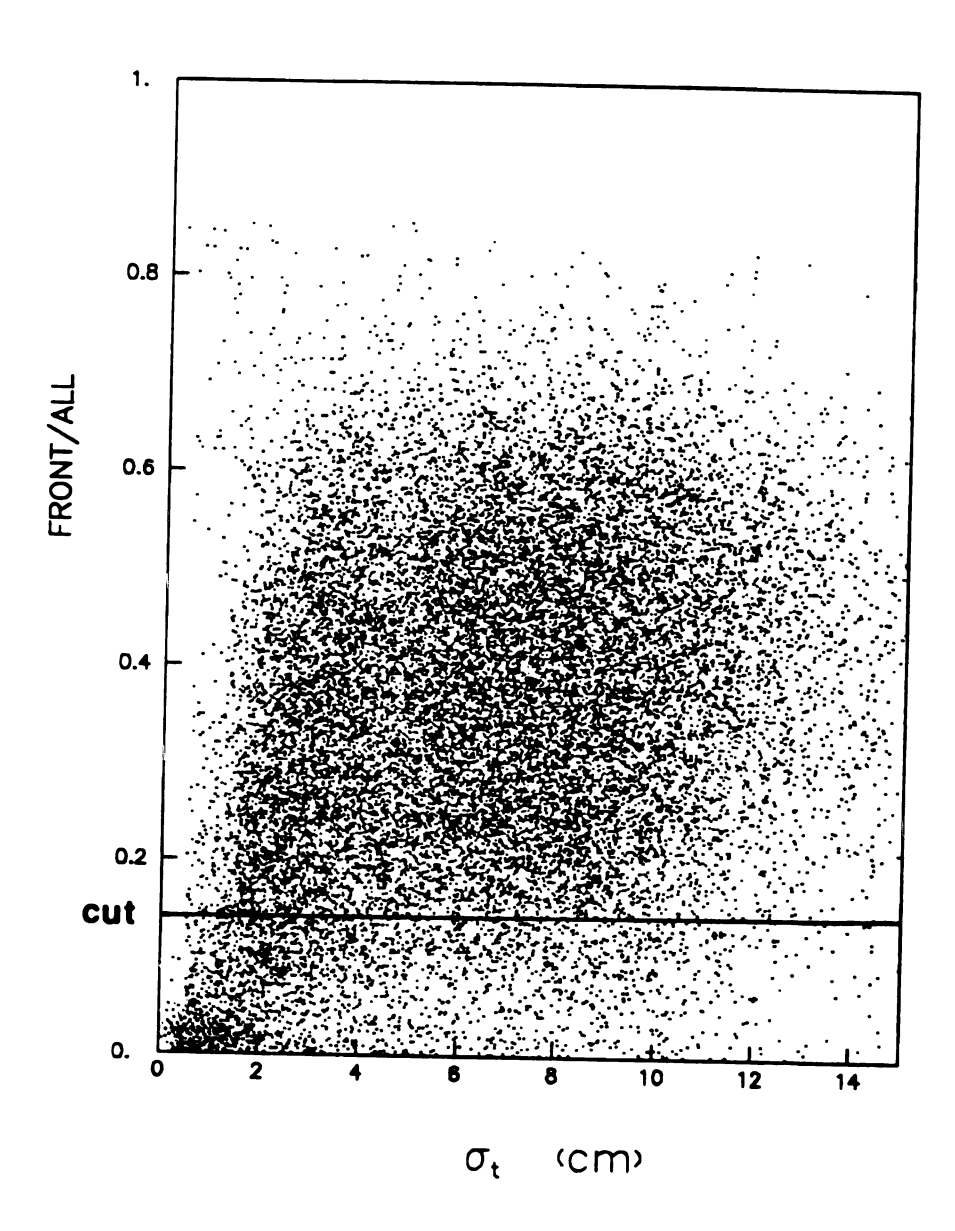


Figure V-26: Front/All vs. σ_{t} for the Direct Photon Trigger Data.

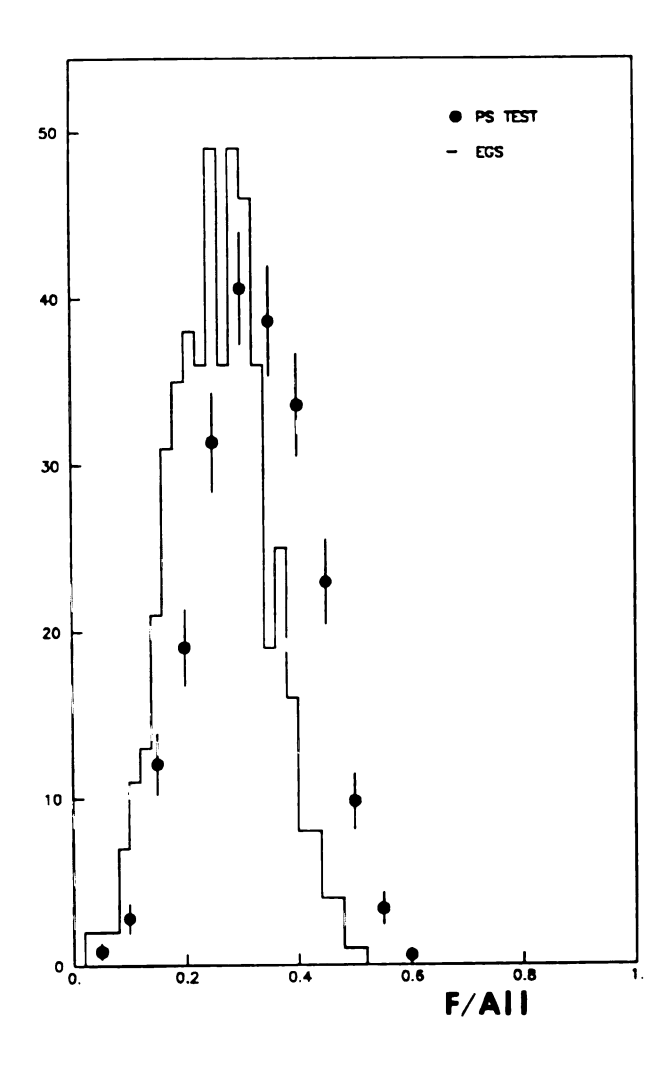


Figure V-27: Front/All distribution for 4 GeV EGS Electron Initiated Shower Simulation and 4 GeV Electron PS Test Data.

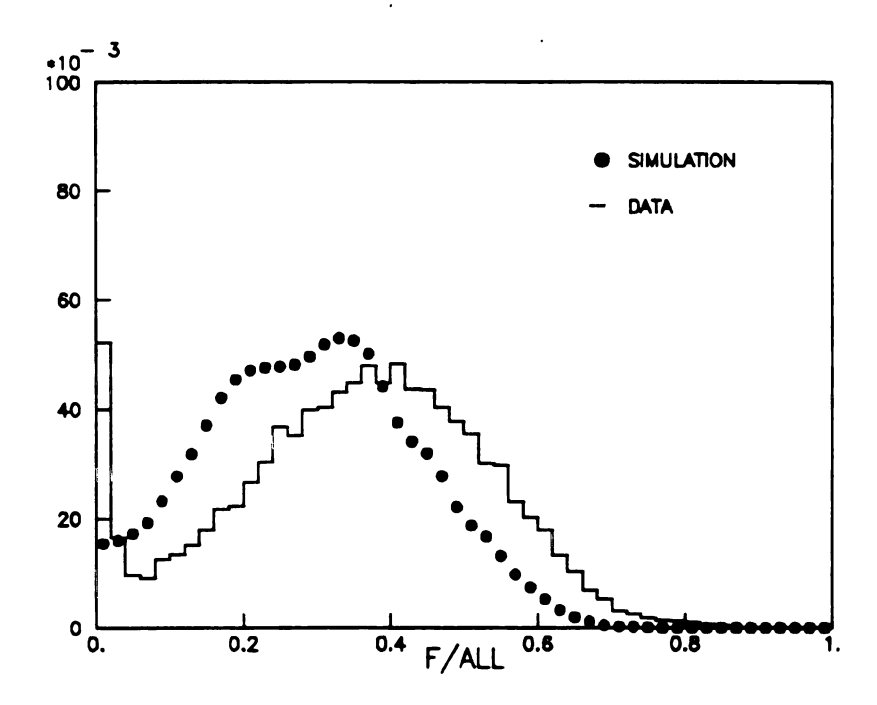


Figure V-28: Front/All Distributions for the Direct Photon Data and EGS Simulation in the Range Δp_T^- 4.5-5 GeV/c.

simulation in the Δp_T = 4.5-5 GeV/c bin. Here also the simulated values are lower than the data.

The simulation does not agree with the data. There are two ways to explain the disagreement: either the simulation is wrong or the evaluation of the data Front/All is wrong.

This last possibility is related to how the front plus back glass arrays were calibrated at the PS [HUM83] using a 4 GeV electron beam. The calibration constants were determined such that Front + Back = 4 GeV and setting the ratio Front/(Front + Back) such that minimized the energy resolution. There are problems with the method, because the fluctuations that cause the resolution smearing are induced not only by the shower fluctuations but also by dissimilar light collection.

The simulation presents two main problems; first one has to be sure to take the full shower simulation down to the Cerenkov threshold, and second, the light collection was not modelled.

It is not obvious how to add light collection effects within reasonable simulation times, and how this will affect the results. There are more low-energy shower electrons in the back glass than in the front glass array. Low energy electrons have their light emitted farther forward than high energy electrons. Due to the geometry of the arrays, this will make the lower energy electrons have better collection probability in the back than in the front since they are, in average, pointing forward. This effect then will tend to lower the Front/All ratio. On the other hand, low energy electrons are produced at larger angles, therefore half of the time this will help some low energy electrons in the front glass but the other half they will point away

from the photomultiplier tube. All these effects would tend to lower Front/All in the simulation.

For the direct photon trigger data we may consider also the effect of associated particles and the clustering in the front glass (complicated due to the poor spatial granularity) which will tend to increase the Front/All ratio of the data.

Due to these considerations we decided to adjust the Front/All distributions phenomenologically. We changed the Front-to-Back balancing of the Monte Carlo energy depositions such that the 4 GeV electron Front/All simulation and PS data agree. This requires:

Front/All $_{new}$ = Front/All $_{old}$ /(.78 + .23·Front/All $_{old}$) . For each p_T bin, random numbers from the Front/All histogram for photons (and mesons) were generated to recalculate new Front/All using the previous relation. New histograms were then produced and from them the acceptances were calculated. The Front/All distribution for photons are shown in figure V-29 and for mesons in figure V-30.

A new comparison of the simulation with the data, shown in figure V-31, shows a good agreement between distributions. At low Front/All the excess showed by the data is in agreement with the expected background. Note that energy scale nonlinearities are implied in this MC Front/All transformation. Changing the front-to-back energy balancing at one energy produces an energy shift in the calibration (see section VI-4).

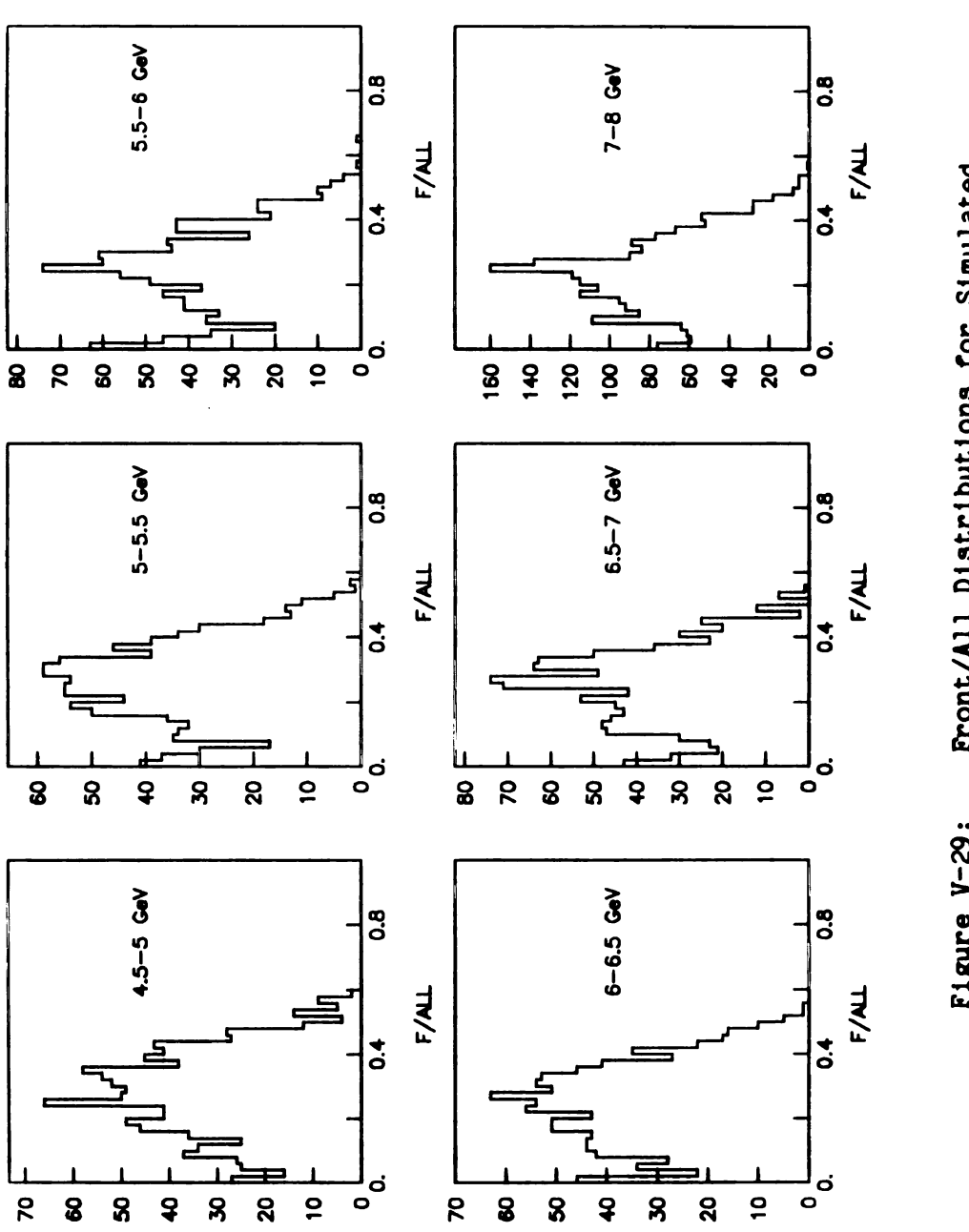


Figure V-29: Front/All Distributions for Simulated Single Photons.

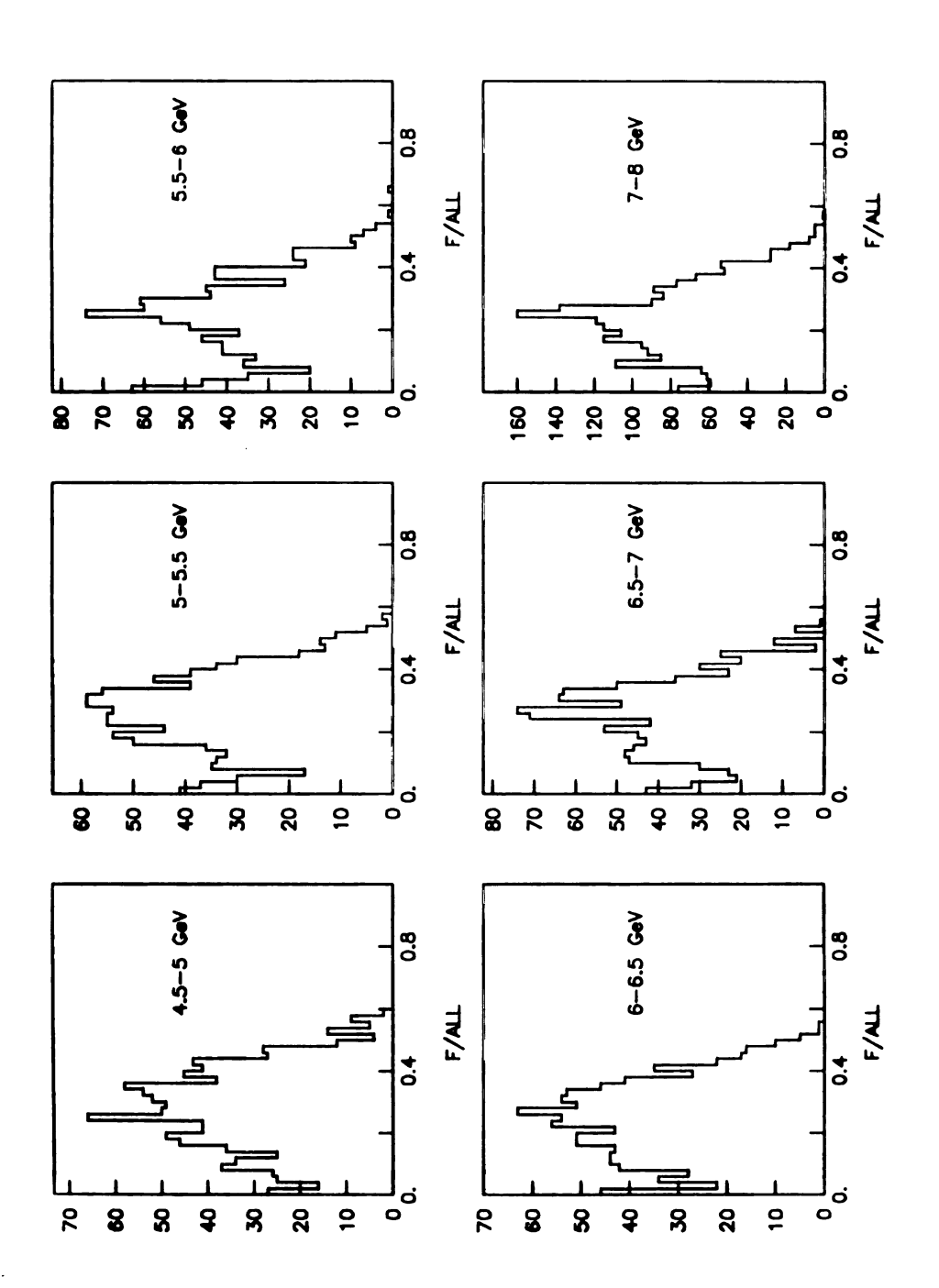


Figure V-29: Front/All Distributions for Simulated Single Photons.

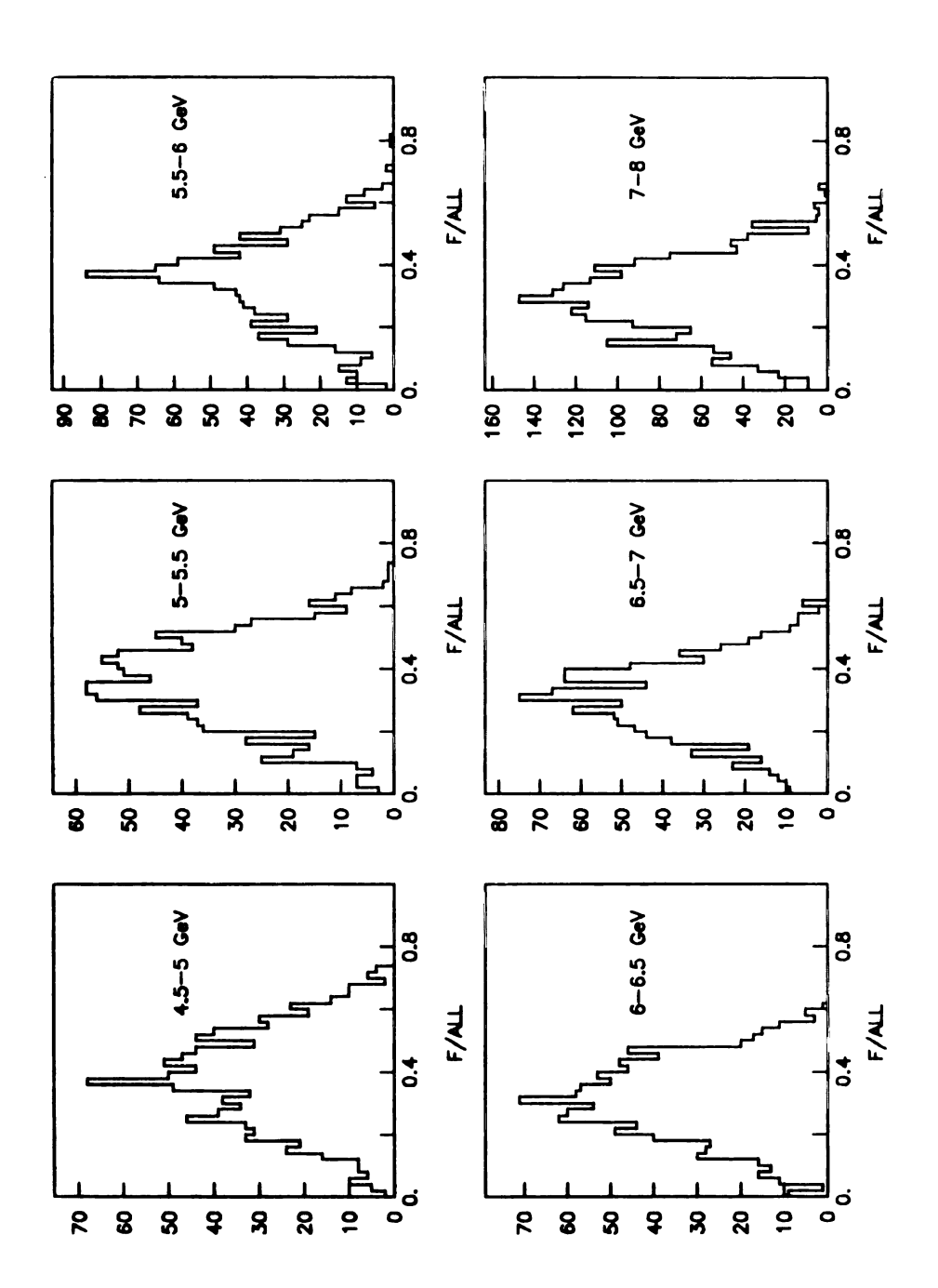


Figure V-30: Front/All Distributions for Simulated

Multiphotons.

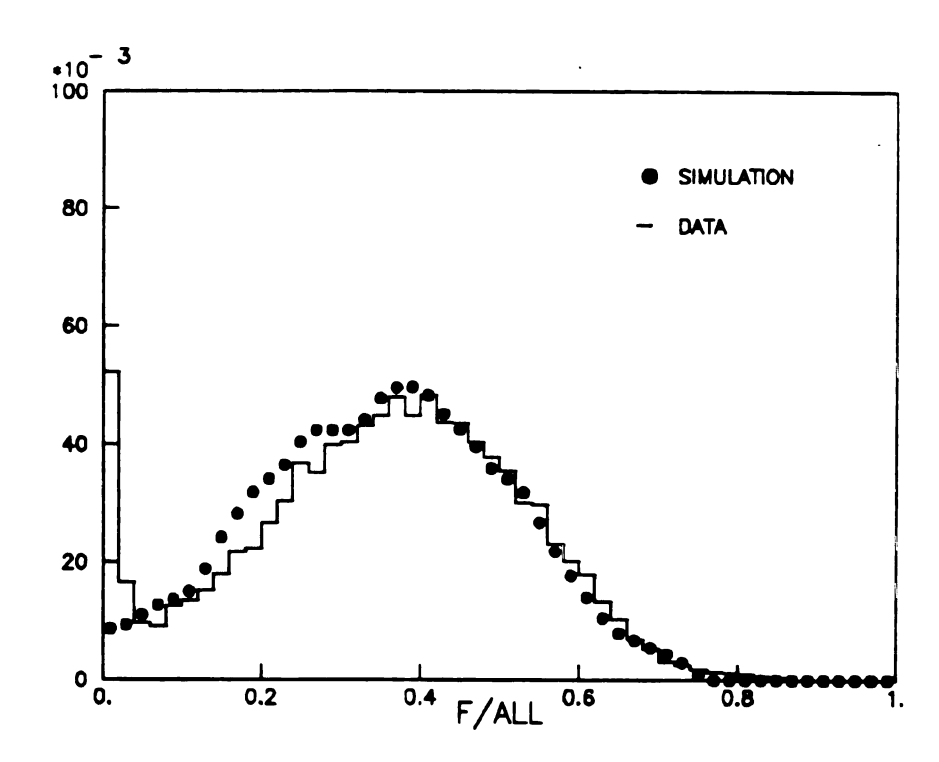


Figure V-31: Front/All Distributions for the Direct Photon Data and EGS Simulation in the Range Δp_T = 4.5-5 GeV/c After Rebalance of Front and Back.

perfort

sich th

kere, Migger

tiltiph

dene (

Fents

100 to 1

Elisiz 31 30

V-10. Fits to the σ_t Distributions.

A maximum likelihood fit [EAD82] to the data histogram was performed to find C_{γ} (fraction of single photons in the data sample) such that:

$$f_d = C_{Y} \cdot f_{Y} + (1 - C_{Y}) \cdot f_{\pi^0}$$
 (V-n)

where, f_d is the normalized σ_t distribution for the direct photon data trigger, f_γ and f_{π^0} are the normalized σ_t distributions for photon and multiphotons.

The likelihood function for binned data [EAD82] is defined as:

$$L = \prod_{i=1}^{N} \frac{(f_{di})^{n_{i}}}{n_{i}!}$$
 (V-o)

where the sum is over the bins of the histogram and n_i is the number of events in the i-th bin.

The most probable value of C_{γ} is obtained by making the most probable f_d distribution as a combination of f_{γ} and f_{π^0} . The value C_{γ} maximizes the likelihood function:

$$\frac{\partial L}{\partial C_{\gamma}} = 0$$
 or minimizes $\{-Ln(L)\}: -\frac{\partial ln(L)}{\partial C_{\gamma}} = 0$ (V-p)

The CERN library subroutine MINUIT [JAM87] was used to find the minimum of $\{-Ln(L)\}$ for each of the p_T bins.

ļ

0

weptan

frect ph

Ţ

emys, A

me sing

stip of .

is our de

-

ŗ

J;

tare No Doublin

Higround

Er Litiphor

12

^{te}efore

V-11. Corrections to the Direct Photons Observed.

Once C_{γ} (fraction of single photons) is obtained, we make acceptance and background corrections in order to extract the number of direct photons produced by nature.

The meson decay Monte Carlo provided the acceptance for meson decays, \mathbf{A}_{m} , and the background of single photons from meson decays in the single photon sample. This can be described by $\Upsilon / \Upsilon \Upsilon \mid_{\mathrm{meson}}$: the ratio of single to multiphoton produced events by neutral meson decays in our detector.

For each \mathbf{p}_{T} bin the number of single photons observed is given by:

$$Y_{obs} = C_{Y} \cdot N_{D}$$
 $(V-q)$

where N_D is the total number of events in the p_T range considered, Δp_T . To obtain the number of direct photons observed we need to subtract the background of single photons due to neutral meson decay:

$$\gamma_{\text{Dobs}} = \gamma_{\text{obs}} - \gamma_{\text{background}}$$
 (V-r)

From the MC we obtained Y / YY $\big|_{meson}$. If N_{YY} is the number of multi-photons in Δp_T , the number of background single photons is:

$$\gamma_{\text{back}} = \frac{\gamma}{\gamma \gamma}$$
 mesons $N_{\gamma \gamma}$

but

$$N_{\gamma\gamma} = (1 - C_{\gamma}) \cdot N_{D}$$

therefore

$$\gamma_{D_{ODS}} = C_{\gamma} \cdot N_{D} - \frac{\gamma}{\gamma \gamma} \Big|_{\text{mesons}} \cdot (1 - C_{\gamma}) \cdot N_{D}$$
 (V-s)

€ere Y

wineot.

i the

iige o

Stain

Potage

Hesan

Nice.

, Hi Sh

13 (a

Qin .

To find the total number of direct photons produced we must correct by the apparatus acceptance. Therefore:

$$Y_{Dp} = \frac{1}{A_{Y}} \cdot Y_{D}$$

$$\gamma_{Dp} = \frac{1}{A_{\gamma}} \cdot N_{D} \cdot \{ C_{\gamma} - \frac{\gamma}{\gamma \gamma} |_{mesons} \cdot (1 - C_{\gamma}) \}$$
 (V-t)

where Υ_{Dp} is the number of direct photons produced by nature in this Δp_T range over the rapidity Δy and the azimuthal angle $\Delta \phi$ range considered in the Monte Carlo calculation of A_{γ} .

It is conventional to express the result of the direct photon measurements as the ratio of direct photons to π° -mesons produced. To obtain this ratio we first calculate the number of neutral mesons produced,

(mesons) =
$$(1 - C_{\gamma}) \cdot N_{D}$$
 (V-u)

Since some neutral mesons are observed as single photons, the total number of neutral mesons is really:

$$(mesons)_{obs} = (mesons) + \gamma_{background}$$
 (V-v)

Using (V-u) and (V-v) we obtain:

(mesons)_{obs} =
$$(1 - C_{\gamma}) \cdot N_{D} + \frac{\gamma}{\gamma \gamma} \Big|_{\text{mesons}} \cdot (1 - C_{\gamma}) \cdot N_{D}$$
 (V-x)

Dividing by the acceptance, $\mathbf{A}_{\mathbf{m}}$, given by the meson decay MC we obtain the number of neutral mesons produced:

$$(\text{mesons})_{p} = \frac{1}{A_{m}} \cdot N_{D} \cdot (1 - C_{\gamma}) \cdot \{1 + \frac{\gamma}{\gamma \gamma} |_{\text{mesons}}\}$$
 (V-y)

the subscript p refers to the number produced in the Monte Carlo range of $\Delta \phi$, Δy and Δp_T . The ratio of produced direct photons to neutral mesons is then:

$$\frac{\Upsilon_{D}}{\text{(mesons)}}\Big|_{p} = \frac{A_{m}}{A_{\gamma}} \cdot \frac{\left\{\frac{C_{\gamma}}{1 - C_{\gamma}} - \frac{\gamma}{\gamma \gamma}\Big|_{\text{mesons}}\right\}}{\left\{1 + \frac{\gamma}{\gamma \gamma}\Big|_{\text{mesons}}\right\}}$$
 (V-z)

To obtain the ratio of direct photons to π° -mesons we form:

$$\frac{\Upsilon_{D}}{(\text{mesons})} |_{p} = \frac{\Upsilon_{D}}{\pi^{\circ} + \text{other neutral mesons}} |_{p}$$

$$= \frac{\Upsilon_{D}/\pi^{\circ}|_{p}}{1 + \text{other neutral mesons}} |_{p}$$

therefore

$$\frac{\Upsilon_{D}}{\pi^{0}} |_{p} = (1 + \frac{\text{other neutral mesons}}{\pi^{0}})_{p} \cdot \frac{\Upsilon_{D}}{\text{(mesons)}} |_{p} \quad (V-A)$$

where the ratio of other neutral mesons to π° -mesons produced can be calculated knowing the production cross sections and branching ratios of all the neutral meson decays considered.

In Appendix A the neutral meson decays that contribute to our background are discussed. They were included in the neutral meson decay Monte Carlo. In Appendix A we found that:

$$(1 + \frac{\text{other neutral mesons}}{\pi^0})_p = 1.627$$

therefore:

$$\frac{\Upsilon_{D}}{\pi^{0}}\Big|_{p} = 1.627 \cdot \frac{A_{m}}{A_{\gamma}} \cdot \frac{\left\{\frac{C_{\gamma}}{1 - C_{\gamma}} - \frac{\gamma}{\gamma \gamma} \middle|_{mesons}\right\}}{\left\{1 + \frac{\gamma}{\gamma \gamma} \middle|_{mesons}\right\}}$$
 (V-B)

V-12. Statistical Errors.

This section describes the calculation of the statistical errors associated with the number of direct photons and the quantities derived from it.

The error in a bin i of the data σ_{t} sample distributions is, using a multinomial model for the distribution f_{D} [EAD82]:

$$\sigma_{D_i} = \frac{\sqrt{n_i}}{N_D} = \frac{\sqrt{f_{Di}}}{N_D}$$
 (V-C)

where n_i is the number of events in the σ_t bin, N_D is the total number of events in the p_T range considered and $f_{Di} = n_i/N_D$.

Since the errors of the $\sigma_{\rm t}$ distributions for the single and multiphoton samples depend on both the neutral meson decay simulation and the EGS shower simulation, they are not easy to calculate directly. For the multiphoton sample, part of the statistical error came from the statistics of the neutral meson decay Monte Carlo, the number of mesons generated. This gives a lower limit to the real statistical error. The

true error also involves the number of events generated by the EGS Monte Carlo, which is smaller. However, the number of independent combinations of EGS photon showers available to the decay Monte Carlo is large compared with $N_{\rm EGS}$, so this correction is small. The error in $f_{\rm mi}$ is approximated by:

$$\sigma_{m_{i}} = \frac{\sqrt{n_{mi}}}{N_{m}} = \sqrt{\frac{f_{mi}}{N_{m}}} \qquad (V-D)$$

where n_{mi} is the number of events in the σ_t bin (generated by the meson decay MC), N_m the total number of events generated in the p_T range and f_{mi} is the normalized number in the σ_T bin, $f_{mi} = n_{mi} / N_m$.

For the single photon sample we considered both N_{EGS} , the total number of showers from the two energies used to interpolate for the p_T bin, and N_{γ} , the number of events generated by the single photon Monte Carlo in the p_T range. The number of independent entries in the σ_t distribution is limited by N_{EGS} , not the number of single photons generated by the Monte Carlo N_{γ} . The statistical error of $f_{\gamma i}$ is:

$$\sigma_{\Upsilon_{1}} = \sqrt{\frac{n_{\Upsilon_{1}}}{N_{EGS} \cdot N_{\Upsilon}}} = \sqrt{\frac{f_{\Upsilon_{1}}}{N_{EGS}}}$$
 (V-E)

where n_{Yi} is the number of events in the σ_t bin and $f_{Yi} = n_{Yi} / N_{Yi}$.

Since we were not able to run the Monte Carlo long enough to make the MC statistical error negligible with respect to the data statistical error, the standard maximum likehood error formulas did not apply.

The error associated with the fit was found by a Monte Carlo simulation of the variations expected for each of the distributions. This MC repeatedly generated $f_{\rm d}$, f_{γ} and $f_{\rm m}$ from Poisson distributions with appropriate number of entries and the observed values as the means, and performed a fit for each set of fluctuated distributions. A distribution of C_{γ} resulting from these fits was formed for each p_T bin as shown in figure V-32. The error, ΔC_{γ} , for each p_T bin was calculated by two methods. the first method took the rms of the distribution of the values of C_{γ} . The second method took different right and left side C_{γ} errors such that 68% of the distribution fell within their limits. The error ΔC_{γ} quoted for each p_T bin was taken as the largest of the three values, rms, $\left|C_{\gamma+}-C_{\gamma}\right|$, $\left|C_{\gamma-}-C_{\gamma}\right|$. The ΔC_{γ} values are shown in table VI-1. The statistical errors were dominated by the Monte Carlo statistics for the lower p_T bins $(p_T < 6.5 \ \text{GeV/c})$ and by the data statistics for the higher p_T bins $(p_T > 6.5 \ \text{GeV/c})$.

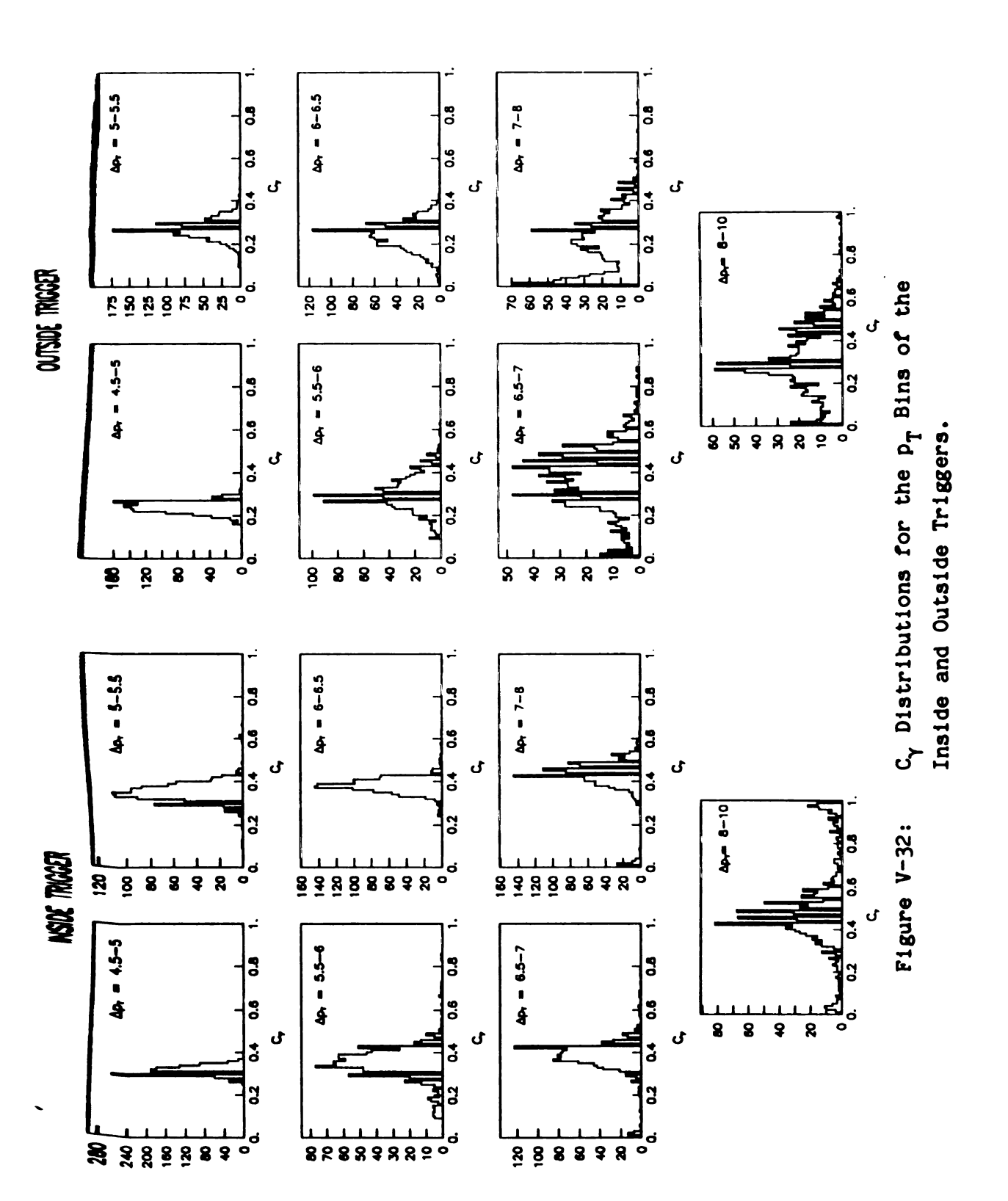
Applying propagation of errors to calculate the error in the number of direct photons of formula (V-t) we obtain:

$$\Delta \gamma_{Dp} = \frac{1}{A_{\gamma}} \cdot \sqrt{\left\{C_{\gamma} - \frac{\gamma}{\gamma \gamma} \middle|_{m} \cdot (1 - C_{\gamma})\right\}^{2} \cdot N_{D} + N_{D}^{2} \cdot \left\{1 + \frac{\gamma}{\gamma \gamma} \middle|_{m}\right\}^{2} \cdot \Delta C_{\gamma}^{2}}$$

(V-F)

The error in the ratio of direct photons to neutral mesons or π° -meson is from formulas (V-z) and (V-B):

$$\Delta \left\{ \begin{array}{c|c} \gamma \\ \hline m \end{array} \middle| p \right\} = \frac{A_m}{A_{\gamma} \cdot \left\{ 1 + \frac{\gamma}{\gamma \gamma} \middle| m \right\}} \cdot \frac{\Delta C_{\gamma}}{(1 - C_{\gamma})^2} \qquad (V-G)$$



$$\Delta \left\{ \left. \frac{\Upsilon}{\pi^0} \right|_{p} \right\} = 1.627 \cdot \Delta \left\{ \left. \frac{\Upsilon}{m} \right|_{p} \right\}$$

(V-H)

CHAPTER VI

RESULTS AND CONCLUSIONS

VI-1. Fraction of Single Photons.

Figures VI-1 and VI-2 show the inside and outside trigger σ_{t} distributions for the single and multiphoton simulations, the data and f t he maximum likelihood fit for each of the p_T bins. As explained previously, the simulation of the strip chamber response was only approximate, ignoring electronic cross-talk, shower particle propagation Deyond simulation cut-offs, etc. We add a resolution in σ_t , $\Delta\sigma_t$, as a Phenomenological description of these effects. For each Monte Carlo event we calculated the σ_t value from a Gaussian distribution with mean σ_{t} (the value calculated by the response algorithm) and rms = $\Delta \sigma_{t}$. The Value of $\Delta \sigma_t$ was parametrized as: $\Delta \sigma_t = A \cdot (\sigma_t + \beta)$, where the values of A and β were chosen to best fit the data. The values were β = 0.6 for all energies and A= 0.1 for $E_{lab} \le 5$ GeV , A = 0.07 for 5 GeV $\le E_{lab} \le 7$ GeV and A = 0.05 for E_{lab} > 7 GeV. The $\Delta\sigma_t$ dependence on σ_t can be viewed as an uncertainty associated with the distance between photons in multiphoton decays. The other term can be associated with the

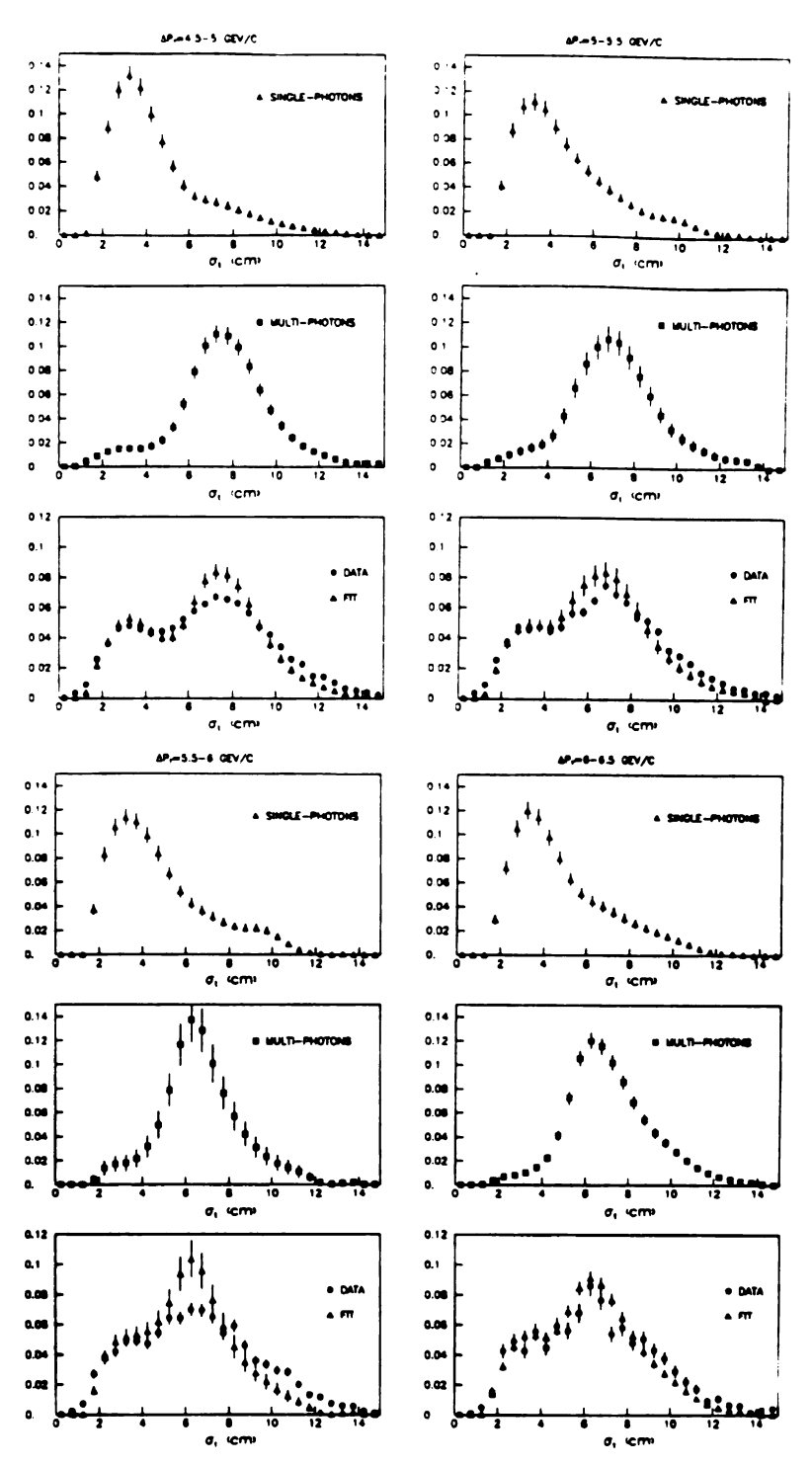


Figure VI-1: Non-smeared σ_{t} Distributions for the Inside Trigger Single and Multiphoton Simulations, Direct Photon Trigger Data and Likelihood Fit for Various ρ_{T} (C.M.) Bins.

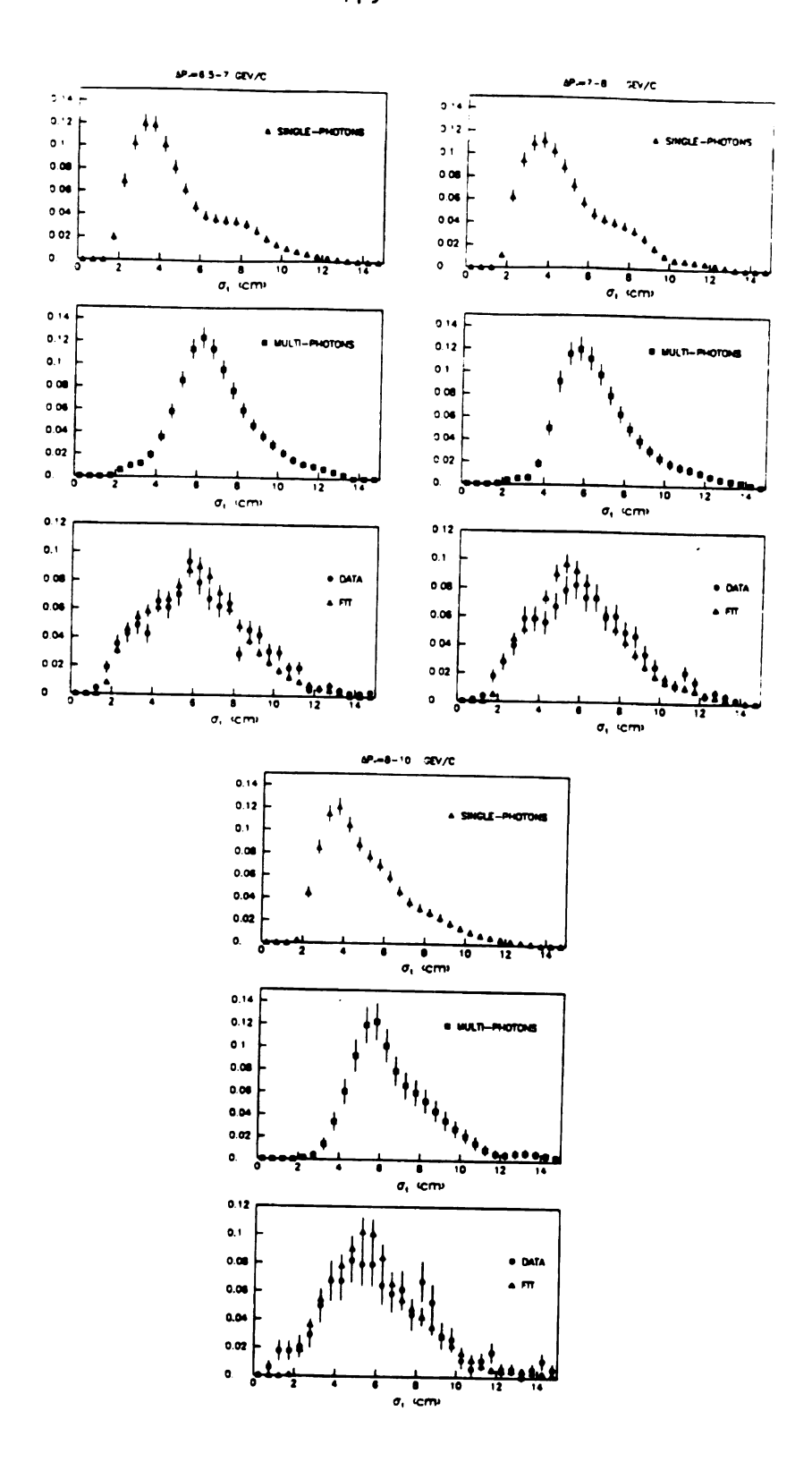


Figure VI-1: Continuation.

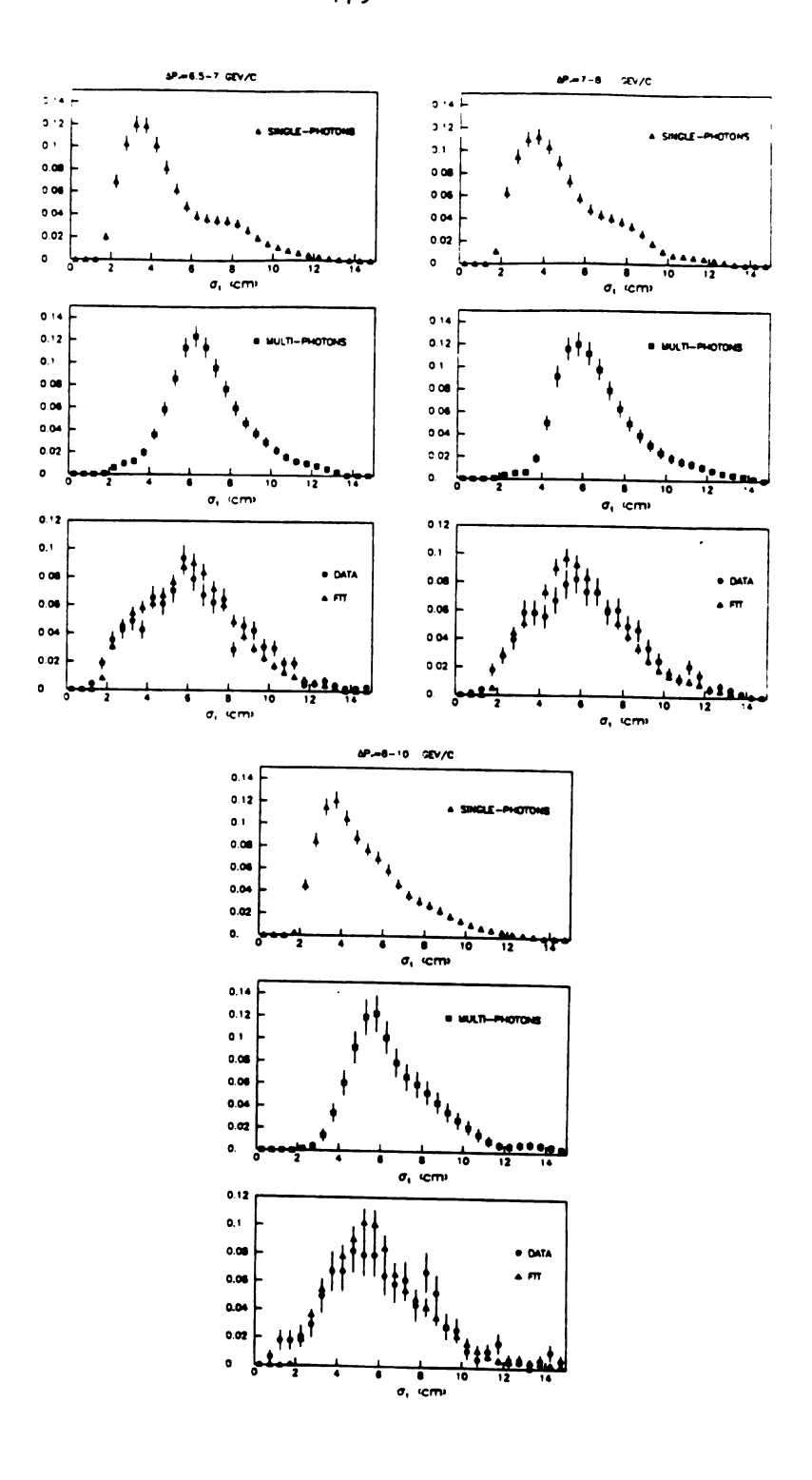


Figure VI-1: Continuation.

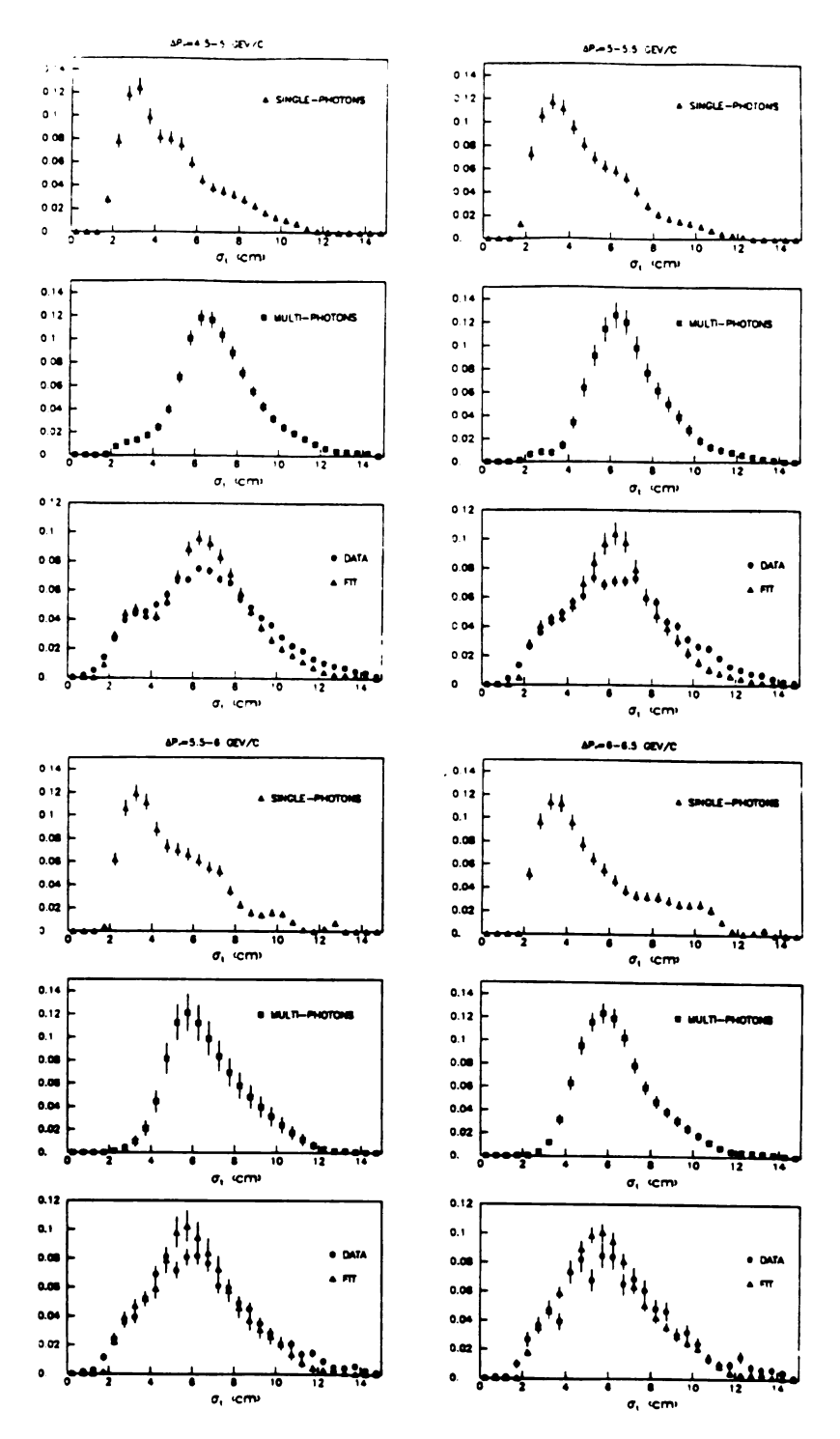


Figure VI-2: Non-smeared \mathfrak{o}_{t} Distributions for the Outside Trigger Single and Multiphoton Simulations, Direct Photon Trigger Data and Likelihood Fit for Various p_{T} (C.M.) Bins.

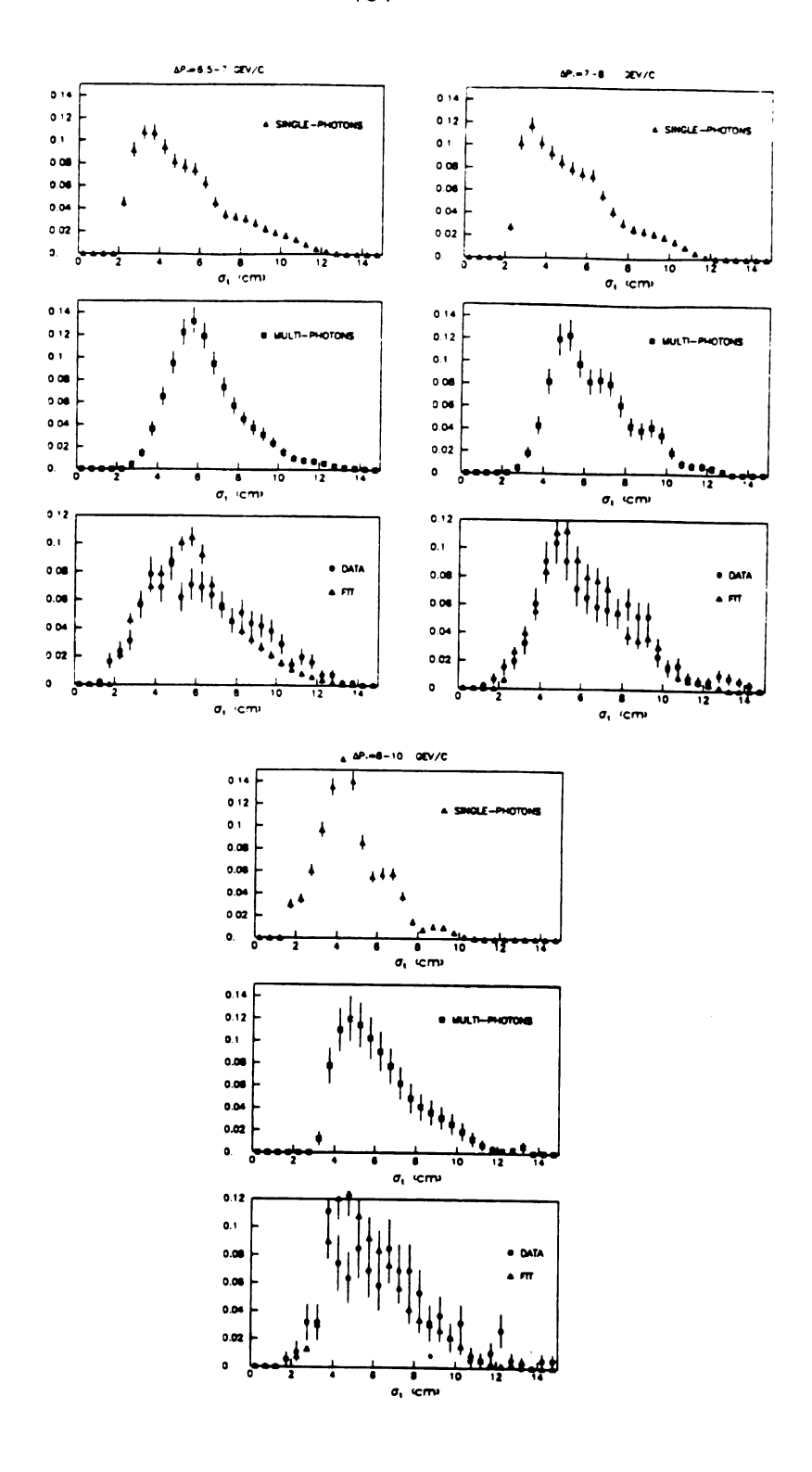
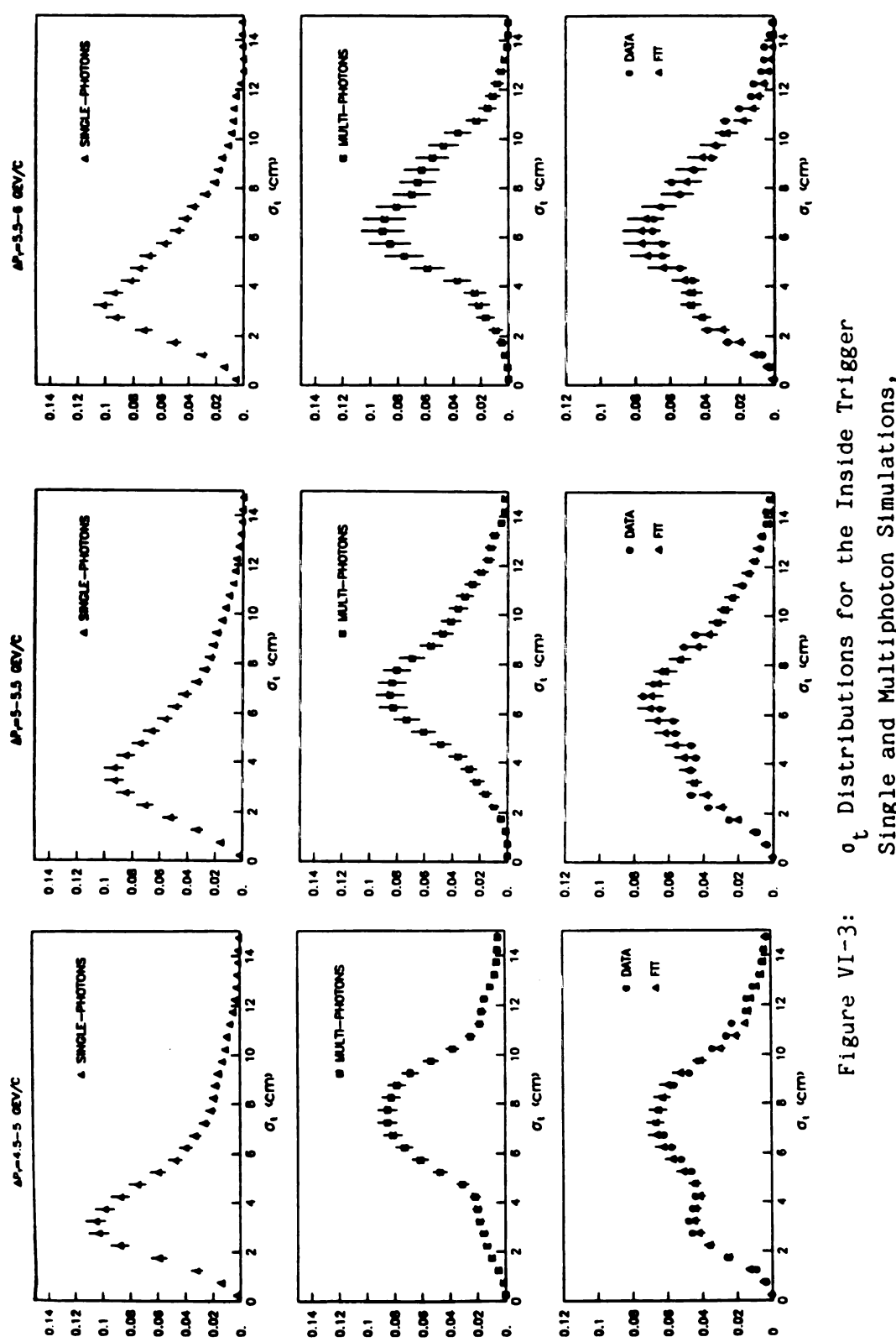


Figure VI-2: Continuation.

uncertainties in the single photon $\sigma_{\rm t}$ distributions. Thus, the error in the model is expected to decrease for increasing lab energies, as indeed it does.

Figures VI-3 and VI-4 show the σ_{t} distributions for simulations, data and likelihood fit after introducing this smearing. It can be seen that there is a considerable improvement in the fits, especially for the width of the distributions. The maxima remain practically in the same position. Figure VI-5 shows the ratios between smeared and non-smeared versions of the cross section. As can be seen, they do not differ by more than 15%. This shows that the likelihood fits are driven by the positions of the maxima of the σ_{t} distributions and not their widths. The smeared set of distributions fit the data clearly better but do not change the final answer significantly. We took the smeared set of C_{γ} values as our best results.

Table VI-1 shows the values of acceptance, luminosity, C_{γ} and other parameters used to calculate our results. The inside and outside triggers are given independently. As can be seen from the C_{γ} fit distributions of figure V-31 and errors of table VI-1, the values obtained from the last two outside p_T bins are very unstable and have large uncertainties. This is due to the fact that at these lab energies, π° 's are really merged, as can be seen from the σ_t distributions of figure VI-4. The final results (for Y/π° , Y/all, direct photon and meson cross sections) were obtained by an error-weighted average between the inside and outside triggers. If $\phi_{ins} \pm \Delta \phi_{ins}$ is the value of ϕ (a given



Single and Multiphoton Simulations, Direct Photon Trigger Data and Likelihood Fit for Various p_T (C.M.) Bins.

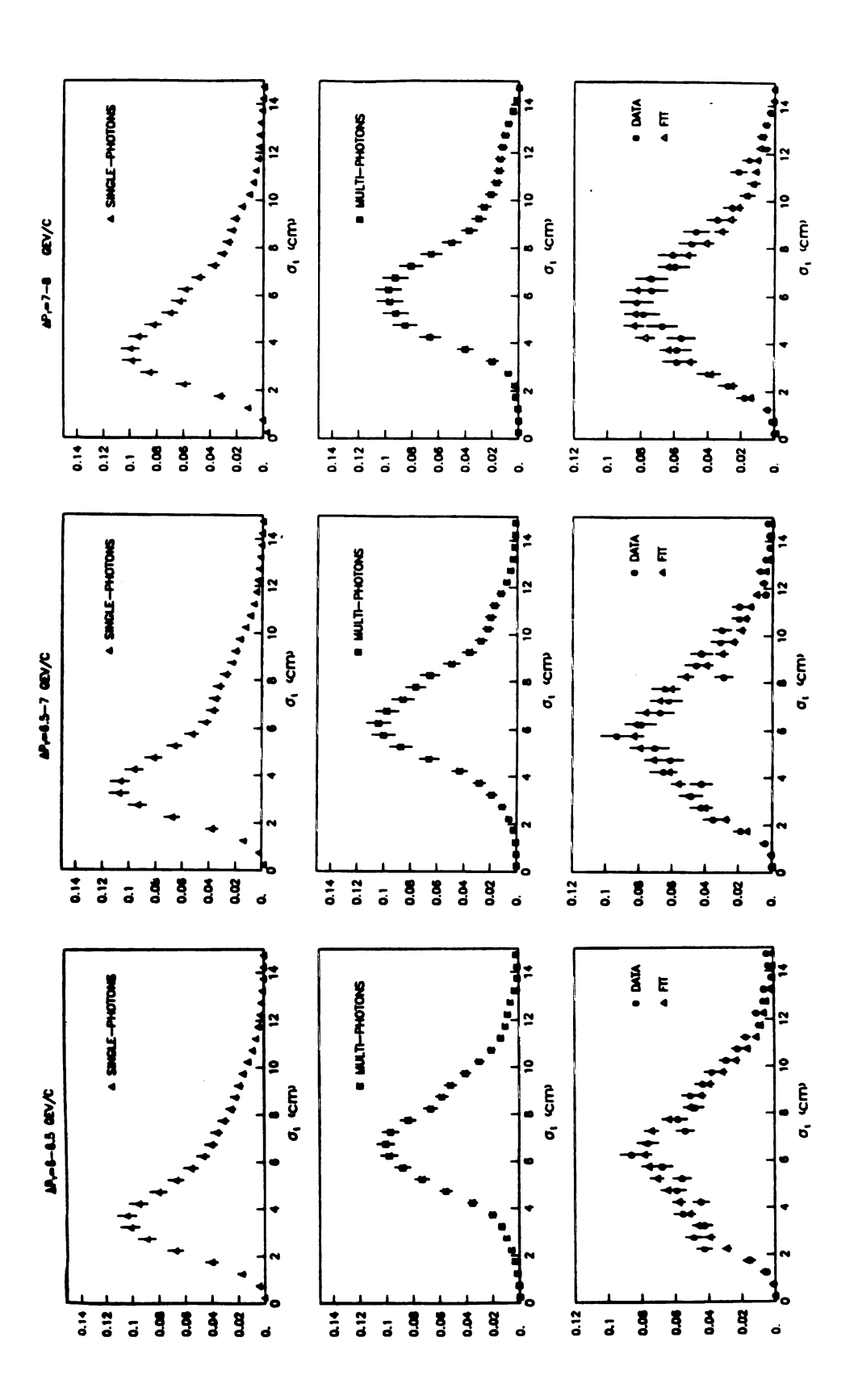


Figure VI-3: Continuation.

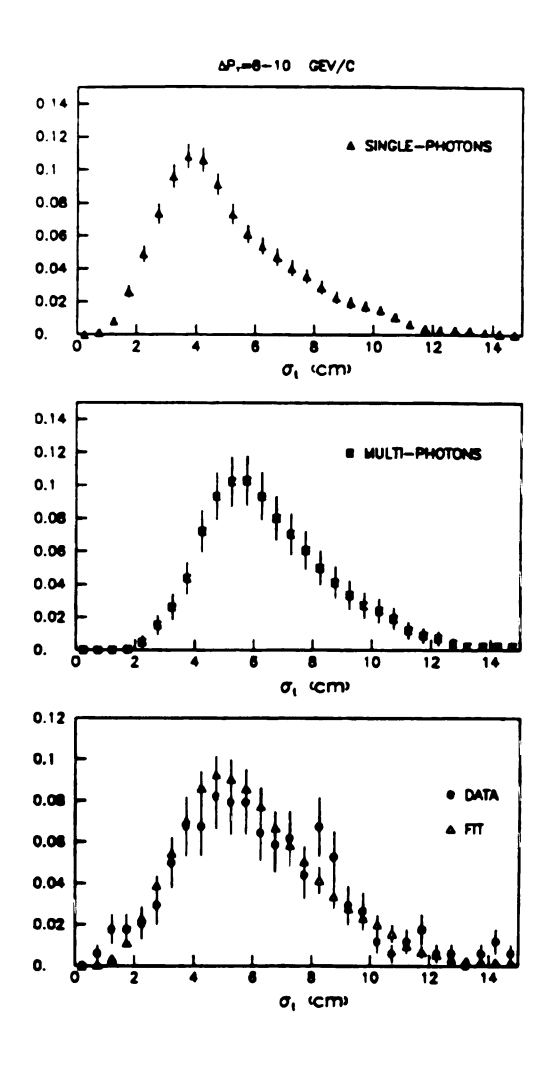
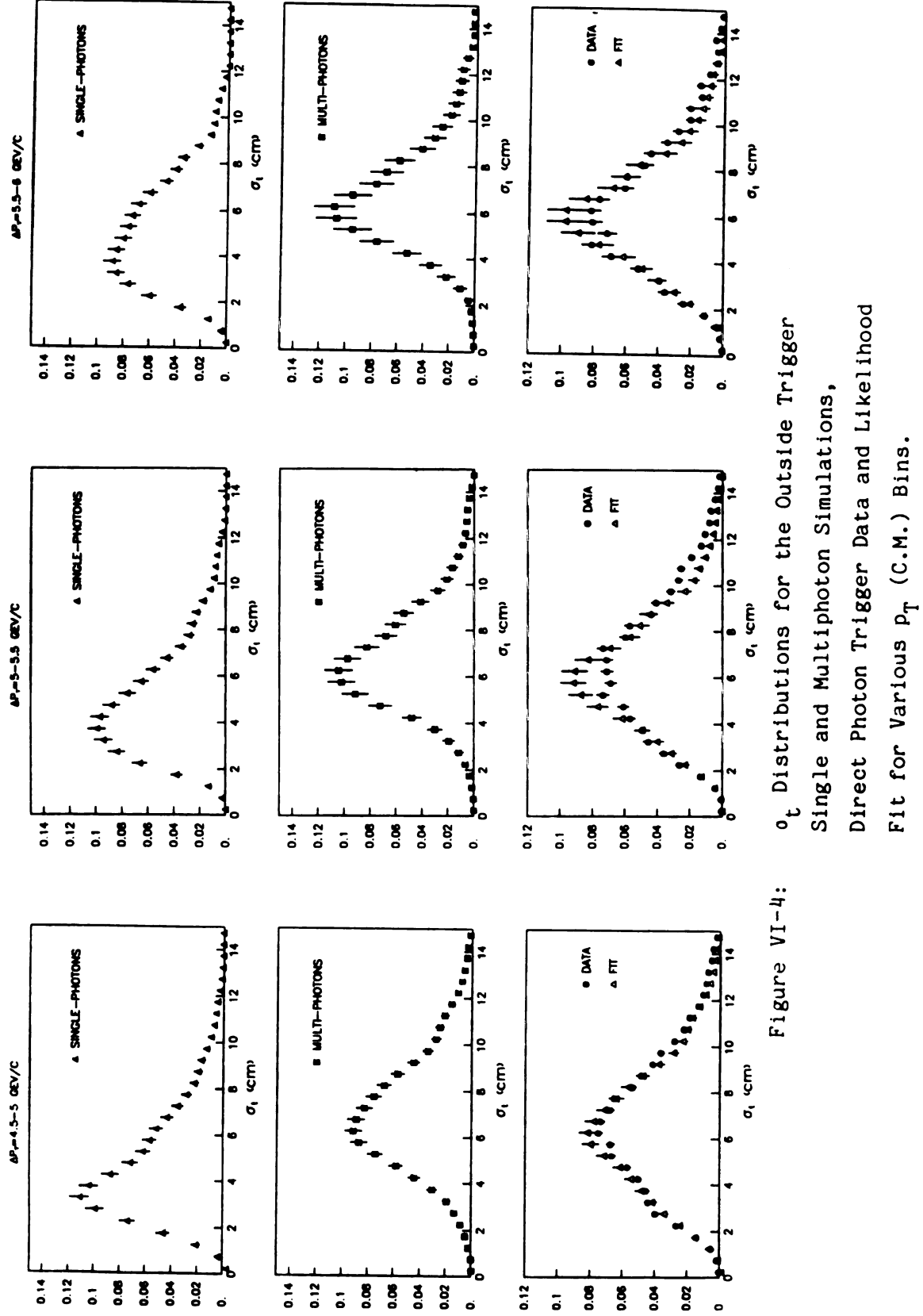


Figure VI-3: Continuation.



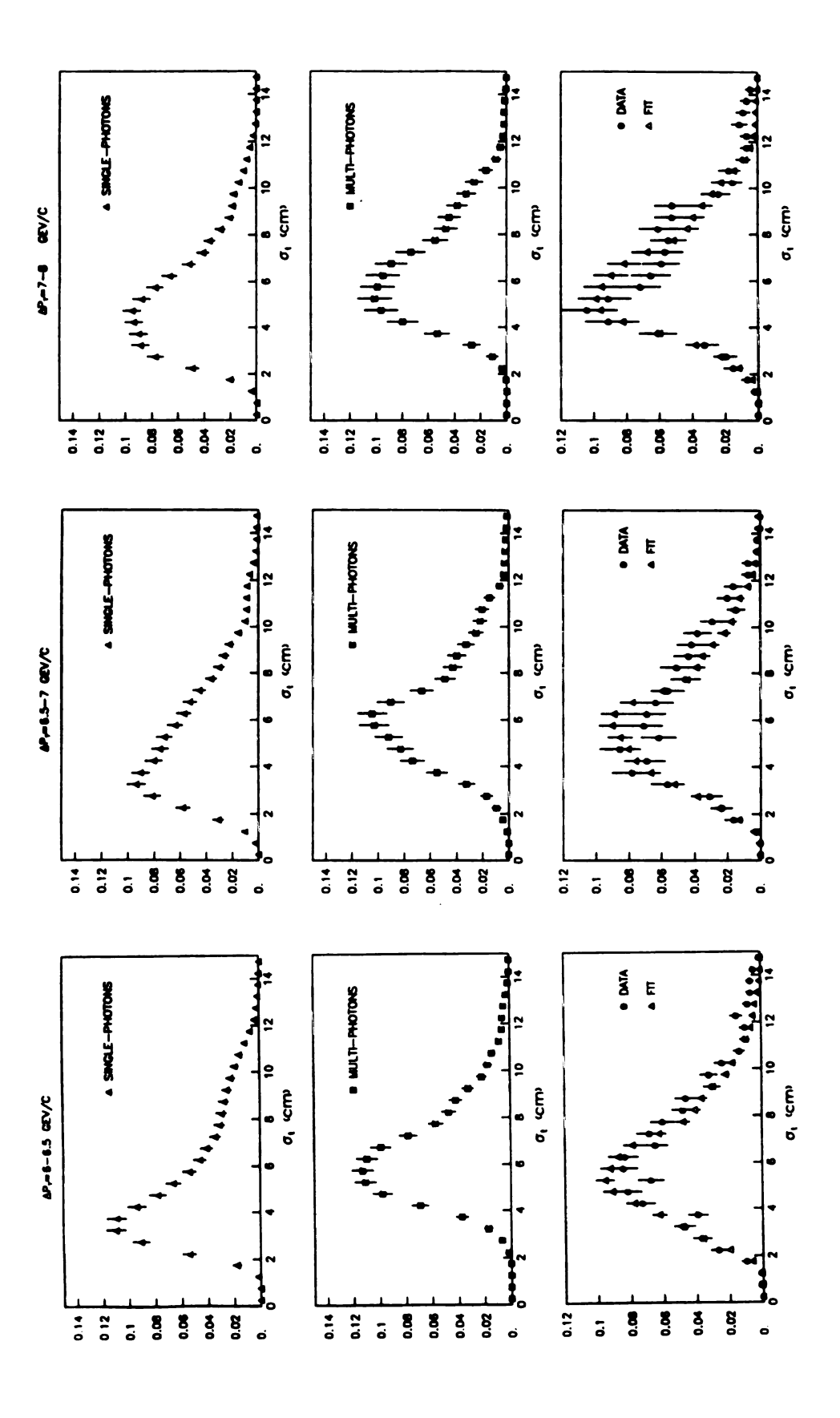


Figure VI-4: Continuation.

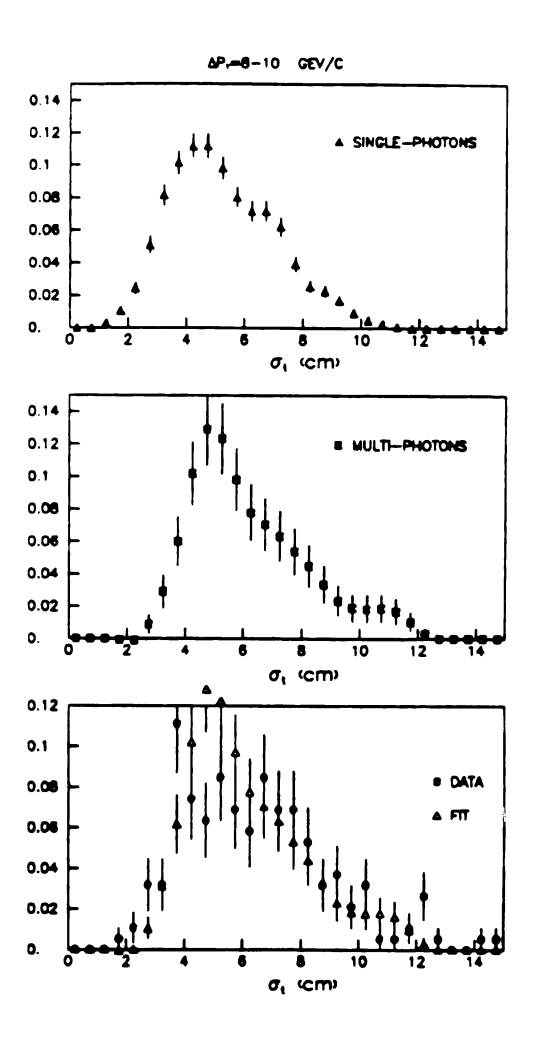


Figure VI-4: Continuation.

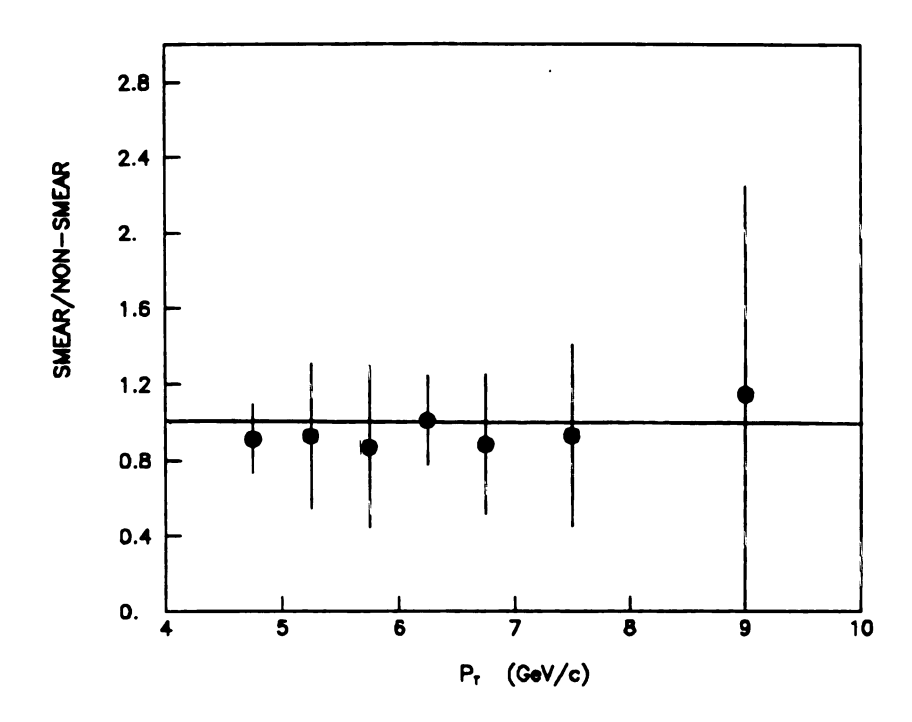


Figure VI-5: Ratio of Smeared to Non-smeared Versions of the Direct Photon Cross Sections as Function of \textbf{p}_{T} (C.M.).

Rm 0.013 0.014 0.014 0.013 0.014 0.014 0.013 0.014 0	e I bins			su)	Inside Trigger	ger		
0.013 0.013 0.013 0.013 0.013 0.013 0.013 0.013 0.013 0.013 0.013 0.013 0.013 0.013 0.013 0.013 0.037 0.037 0.037 0.037 0.037 0.03 0.212 0.192 0.175 0.161 0.149 0.12 0.212 0.13 0.19 0.19 0.19 0.19 0.19 0.10 0.13 0.31 0.32 0.32 0.33 0.33 0.33 0.33 0.33 0.33	6eU/c	4.5-5	5-5.5	5.5-6	6-6.5	6.5-7	7-8	8-10
0.040 0.039 0.038 0.037 0.037 0.5 0.5 0.5 0.5 0.5 0.5 0.5 0.5 0.5 0.5 15120 8051 3867 1967 1025 0.212 0.192 0.175 0.161 0.149 0.22 0.21 0.19 0.19 0.149 0.22 0.21 0.19 0.19 0.17 0.22 0.21 0.19 0.19 0.17 0.22 0.21 0.19 0.19 0.17 0.22 0.21 0.19 0.19 0.17 0.22 0.23 0.33 0.34 0.37 0.02 0.06 0.08 0.04 0.08 4.72 5.22 5.72 6.23 6.73 6.73	A m	0.013	0.013	0.013	0.013	0.013	0.013	0.012
6.5 6.5 0.5 0.5 0.5 0.5 15120 8051 3867 1967 1025 0.212 0.192 0.175 0.161 0.149 0.22 0.21 0.19 0.19 0.19 0.10 0.31 0.33 0.38 0.37 0.02 0.06 0.08 0.04 0.08 4.72 5.22 5.72 6.23 6.73	Ay	0.040	0.039	0.038	0.037	0.037	0.036	0.034
0.5 0.5 0.5 0.5 0.5 15120 8051 3867 1967 1025 0.212 0.192 0.175 0.161 0.149 0.22 0.21 0.19 0.19 0.17 0.22 0.21 0.19 0.19 0.17 0.31 0.33 0.38 0.37 0.02 0.06 0.08 0.04 0.08 4.72 5.22 5.72 6.23 6.73	7			5.	97x 10 ³	21		
15120 8051 3867 1967 1025 0.212 0.192 0.175 0.161 0.149 0.22 0.21 0.19 0.19 0.19 0.31 0.33 0.33 0.38 0.37 0.02 0.06 0.08 0.04 0.08 4.72 5.22 5.72 6.23 6.73	ΔPT	0.5	0.5	0.5	0.5	5.0	1.0	2.0
0.212 0.192 0.175 0.161 0.149 1.92 1.92 0.22 0.21 0.19 0.17 0.31 0.33 0.33 0.37 0.02 0.06 0.08 0.04 0.08 4.72 5.22 5.72 6.23 6.73	z	15120	8051	3867	1961	1025	811	352
m 0.22 0.21 0.19 0.19 0.17 r 0.31 0.33 0.33 0.38 0.37 r 0.02 0.06 0.08 0.04 0.08 r 4.72 5.22 5.72 6.23 6.73	<1//>////	0.212	0.192	0.175	0.161	0.149	0.135	0.115
m 0.22 0.21 0.19 0.19 0.17 0.31 0.33 0.33 0.38 0.37 0.02 0.06 0.08 0.04 0.08 4.72 5.22 5.72 6.23 6.73	8 0 ♦ 0				1.92			
0.31 0.33 0.33 0.38 0.37 0.02 0.06 0.08 0.04 0.08 4.72 5.22 5.72 6.23 6.73	1/m m	!	0.21	0.19	0.19	0.17	0.17	0.12
0.02 0.06 0.08 0.04 0.08 4.72 5.22 5.72 6.23 6.73	C,	0.31	0.33	0.33	0.38	0.37	0.42	0.43
4.72 5.22 5.72 6.23 6.73	ΔCγ	0.02	90.0	0.08	0.04	0.08	0.10	0.21
	p ₁ o	4.72	5.22	5.72	6.23	6.73	7.42	8.72

p _T bins			Out	Outside Trigger	gger		
GeU/c	4.5-5	5-5.5	5.5-6	6-6.5	6.5-7	82	8-10
E E	0.028	0.028	0.028	0.028	0.027	0.026	0.025
Яy	0.068	0.068	0.064	0.064	0.062	0.058	0.055
J				2.57H10 37	37		
ΔP _T	0.5	0.5	0.5	0.5	9.0	1.0	2.0
Z	14032	6735	3064	1484	746	610	249
<1/b	0.212	0.192	0.175	0.161	0.149	0.135	0.115
R Φ Φ Φ				1.92			
m 14./ t	91.0	0.14	0.13	91.0	0.13	0.13	0.10
ις	0.27	0.31	0.30	0.35	0.39	0.21	0.24
ΔCγ	0.06	0.00	0.11	80.0	0.17	0.17	0.21
o 1 d	4.72	5.22	5.72	6.23	6.73	7.42	8.72

R $_m$ = Neutral Meson Acceptance; R $_\gamma$ = Direct Photon Acceptance L = Integrated Luminosity (cm $^{-2}$) $_\Delta$ p $_T$ = bin range (GeV/c)

 $\mathsf{N_0}_{-}$ - Number of Dete Events in the $\mathsf{p_T}$ bin

(1/ p_T) = 1/ p_T fiverage (Cross Section Weighted) in $\Delta\,p_T$ (c/GeV).

∆♦ ∆ y = (Azimuthal Angle)×(Rapidity) Renges (rad).

 $\gamma/\Upsilon \mid_{\ m}$ = Fraction of Single Photons to Multiphotons from Neutral Meson Decays.

 C_{γ} = Fraction of Single Photons in the p_{T} bin.

 ΔC_{γ} = Error in C_{γ} from fit and Statistics

 ρ_To = Value for plotting the Cross Section in the ρ_T bin (GeV/c).

Table VI-1: Inside and Outside Values of the Parameters Used to Calculated the Cross Sections, γ/all and γ/π° .

result) for the inside trigger and $\phi_{\text{out}}^{\pm} \Delta \phi_{\text{out}}$ for the outside trigger, the final result was obtained by [BEV69]:

$$\phi = \frac{\phi_{\text{ins}} \cdot (1/\Delta \phi_{\text{ins}})^2 + \phi_{\text{out}} \cdot (1/\Delta \phi_{\text{out}})^2}{(1/\Delta \phi_{\text{ins}})^2 + (1/\Delta \phi_{\text{out}})^2}$$
 (VI-a)

and the error:

$$\Delta \phi = \sqrt{\frac{1}{(1/\Delta \phi_{ins})^2 + (1/\Delta \phi_{out})^2}}$$
 (VI-b)

where only statistical errors were considered. The discussion of systematic errors will be reserved for section VI-4.

VI-2. Direct Photon to π° -meson and Direct Photon to Neutral Meson ratios.

It has been common in the literature to give the ratio of produced direct photon to π° -meson as the experimental result of direct photon measurements. This is generally the case among the experiments using a direct technique to differentiate π° triggers from direct photon triggers on an event by event basis. Giving a ratio of the two quantities measured with the same detector minimizes the systematic errors.

Ratios of direct photons to "all" also have been given in the literature. In this case the term "all "can be misleading, since it has to be clearly specified what was included in the "all" definition. We define "all neutral mesons" by the list of decays included in Appendix A, and "all" as "all neutral mesons" plus "direct photons".

Table V-2 and Table V-3 show the Υ/π° and Υ/all resulted from the inside and outside triggers. Table V-4 shows the error-weighted averages.

The CCOR collaboration (experiment R108) [ANG80] has given values of direct photon to all found using the conversion method. In figure VI-6 our values of direct photons to neutral mesons plus direct photons ("all") are shown. The R108 results are also shown.

The ratios of direct photons to π° -mesons produced are better defined. Figure VI-7 shows our values of the direct photon to π° -mesons ratios. The values for the ISR experiment R806 [ANA82] are also shown. However, they depend on both how well the direct photon signal is measured and how well the π° - meson signal to noise ratio has been evaluated. We believe that this double measurement made the interexperiment comparison more difficult. The easiest and least biased comparison is to compare directly the direct photon signal, as is done in section VI-5.

VI-3. Direct photon cross section.

The invariant direct photon cross section as a function of \mathbf{p}_{T} , ϕ (azimuthal angle) and y (rapidity) can be written as:

$$E \frac{d\sigma}{d^3p} = \frac{d\sigma}{p_T dp_T \cdot d\phi \cdot dy} \qquad (VI-e)$$

For a given phase space volume $\Delta p_T \Delta \phi \Delta y$, the average in this volume can be calculated as:

$$\langle E \xrightarrow{d\sigma} \rangle_{\Delta p_T \Delta \phi \Delta y} = \langle \frac{d\sigma}{p_T dp_T \cdot \Delta \phi \cdot \Delta y} \rangle =$$

Table VI-2: Results for the Inside Trigger.

hi= - (0-11/-)			Inside Tri	gger - Re	sults		
p T bins (GeV/c)	4.5-5	5-5.5	5.5-6	6-6.5	6.5-7	7-8	8-10
Direct Photon	2.21 ± 0.34	1.31± 0.05	6.30 ± 2.96	3.91± 0.72	1.89 ± 0.68	8.53 ± 3.11	1.88± 1.22
Cross Section	x 10 ⁻³⁴	x 10 ⁻³⁴	x 10 -35	× 10 ⁻³⁵	× 10 ⁻³⁵	× 10 ⁻³⁶	× 10 ⁻³⁶
Neutral Meson	3.62 ± 0.11	1.68 ± 0.15	7.24± 0.87	3.14 ± 0.21	1.51 ± 0.20	4.99 ± 0.88	9.39± 3.50
Cross Section	x 10 ⁻³³	x 10 -33	x 10 ⁻³⁴	× 10 ⁻³⁴	x 10 ⁻³⁴	x 10 ⁻³⁵	x 10 ⁻³⁶
"All"	3.84 ± 0.11	1.81± 0.16	7.87 ± 0.92	3.53± 0.22	1.70 ± 0.21	5.84± 0.93	1.13 ± 0.37
Cross Section	x 10 ⁻³³	x 10 ⁻³³	x 10 ⁻³⁴	× 10 ⁻³⁴	x 10 ⁻³⁴	x 10 ⁻³⁵	x 10 ⁻³⁵
γ/ mesons	0.061	0.078	0.087	0.125	0.125	0.171	0.200
	± 0.010	± 0.031	± 0.042	± 0.024	± 0.048	± 0.069	± 0.150
γ/ all	0.057	0.072	0.080	0.111	0.111	0.146	0.167
	± 0.009	± 0.028	± 0.039	± 0.021	± 0.042	± 0.058	± 0.122
γ/π°	0.099	0.127	0.141	0.203	0.204	0.278	0.325
	± 0.015	± 0.050	± 0.069	± 0.040	± 0.077	± 0.113	± 0.244

All Cross Sections in cm 2 c 3 GeV 2

Table VI-3: Results for the Outside Trigger.

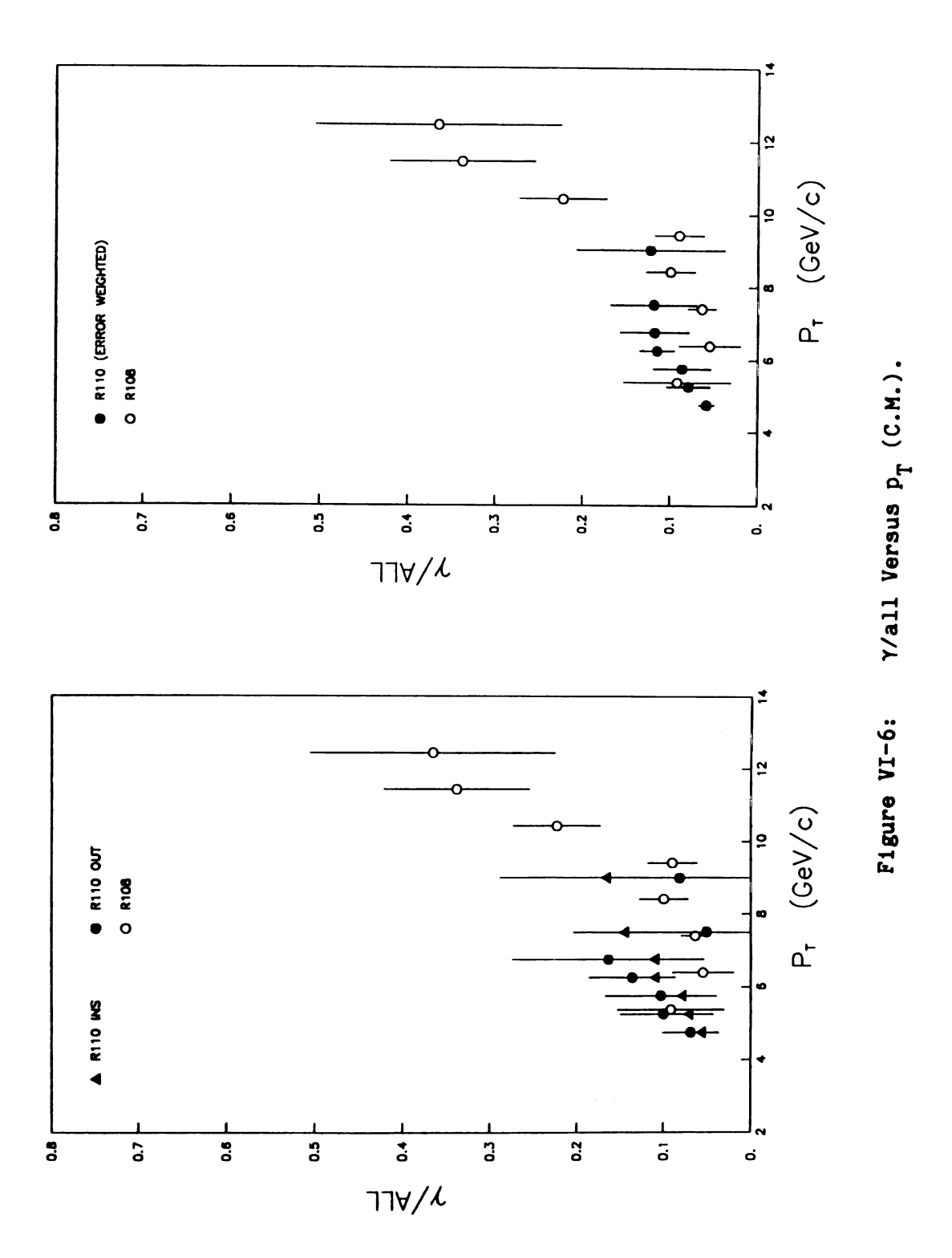
			Outside T	rigger - A	esults		
p T bins (GeV/c)	4.5-5	5-5.5	5.5-6	6-6.5	6.5-7	7-8	8-10
Direct Photon Cross Section	2.72± 1.23 × 10 ⁻³⁴	1.64 ± 0.79 x 10 ⁻³⁴	7.10 ± 4.22 x 10 ⁻³⁵	4.02 ± 1.37 × 10 ⁻³⁵	2.26± 1.40 x 10 ⁻³⁵		
Neutral Meson	3.65± 0.30	1.47± 0.19	6.14 ± 0.97	2.54 ± 0.32	1.15± 0.32	5.73 ± 1.25	9.70 ± 2.75
Cross Section	x 10-33	x 10 ⁻³³	x 10 ⁻³⁴	× 10 ⁻³⁴	x 10 ⁻³⁴	x 10 -35	x 10 ⁻³⁶
"All"	3.92± 0.32	1.64 ± 0.21	6.85± 1.06	2.94 ± 0.35	1.37± 0.35	6.04 ± 1.37	1.06 ± 0.30
Cross Section	x 10 ⁻³³	x 10 ⁻³³	x 10 ⁻³⁴	x 10 ⁻³⁴	x 10 ⁻³⁴	x 10 ⁻³⁵	x 10 ⁻³⁵
γ/ mesons	0.074	0.112	0.116	0.158	0.196	0.054	0.089
	± 0.034	± 0.056	± 0.071	± 0.057	± 0.133	± 0.097	± 0.128
γ/ all	0.069	0.100	0.104	0.136	0.164	0.051	0.082
	± 0.032	± 0.050	± 0.064	± 0.049	± 0.110	± 0.092	± 0.118
γ/π°	0.121	0.182	0.188	0.257	0.319	0.088	0.145
	± 0.056	± 0.090	± 0.116	± 0.094	± 0.217	± 0.158	± 0.209

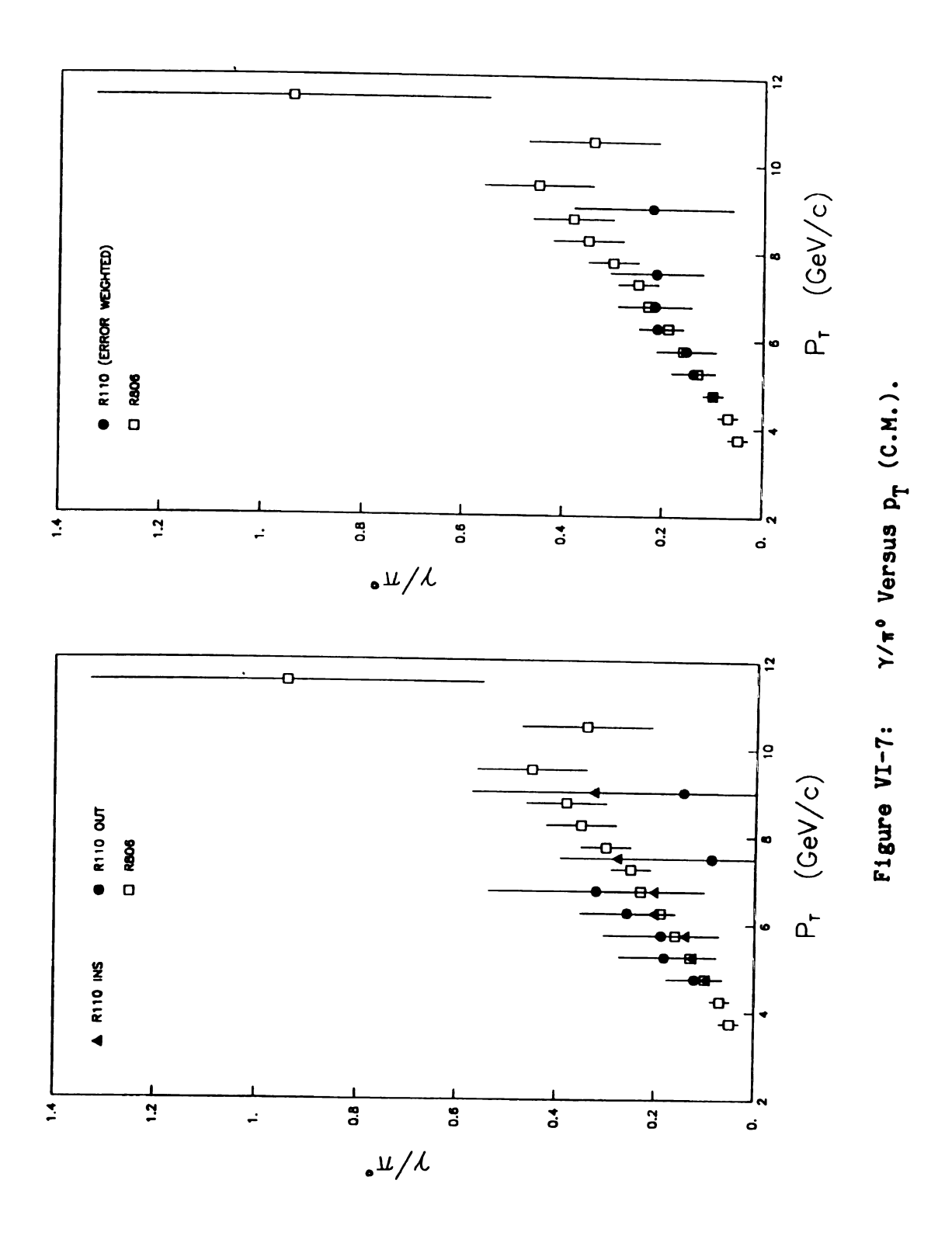
All Cross Sections in cm 2 3GeV-2

Table VI-4: Final Average Results of the Cross Sections, γ/all and γ/π° .

			Veighted	Weighted Average - Results	- Results	40	
p T Dins (ven/c)	4.5-5	5-5.5	5.5-6	6-6.5	6.5-7	8-2	8-10
Direct Photon	2.25± 0.33	1.41± 0.42	6.56±2.42		3.94± 0.63 1.96± 0.61	$7.21 \pm 2.72 \ 1.37 \pm 0.86$	1.37± 0.86
Cross Section	× 10 ⁻³⁴	x 10 ⁻³⁴	× 10 ⁻³⁵		× 10 ⁻³⁵ × 10 ⁻³⁵	× 10^{-36} × 10^{-36}	× 10 -36
Neutral Meson	3.62± 0.10	1.60 ± 0.12	6.75± 0.65	6.75± 0.65 2.95± 0.18 1.41± 0.17 5.23± 0.72 9.58± 2.16 x 10 ⁻³⁴ x 10 ⁻³⁴ x 10 ⁻³⁵ x 10 ⁻³⁶	1.41 ± 0.17	5.23 ± 0.72	9.58± 2.16
Cross Section	× 10 ⁻³³	x 10 -33	× 10 ⁻³⁴		× 10-34	× 10 ⁻³⁵	× 10-36
"AII" Cross Section	3.85± 0.11 × 10 ⁻³³	1.75± 0.13 × 10 ⁻³³	7.43±0.69 × 10-34	i	3.35±0.19 1.62±0.18 5.90±0.77 x 10 ⁻³⁴ x 10 ⁻³⁵	5.90± 0.77 x 10 ⁻³⁵	1.08 ± 0.23 × 10-35
γ/mesons	0.062	0.086	0.094	0.130	0.133	0.131	0.136
	± 0.009	± 0.027	± 0.036	± 0.022	± 0.045	± 0.056	± 0.097
γ/ all	0.058	0.079	0.086	0.115	0.118	0.119	0.123
	± 0.009	± 0.025	± 0.033	± 0.020	± 0.039	+ 0.049	± 0.085
γ/π°	0.101	0.139	0.154	0.211	0.217	0.214	0.221
	± 0.015	± 0.044	± 0.059	± 0.036	± 0.073	± 0.092	± 0.159

All Cross Sections in cm 2 $^3\mathrm{GeV}^{-2}$





$$= \frac{1}{\Delta p_{T} \cdot \Delta \phi \cdot \Delta y} \int_{\Delta p_{T}} \int_{\Delta \phi} \int_{\Delta y} \frac{1}{p_{T}} \cdot \frac{d\sigma}{dp_{T} d\phi dy} \cdot dp_{T} d\phi dy$$
(VI-d)

assuming that $d\sigma(\phi,y)$ is flat in the $\Delta\phi\Delta y$ sub-space (since our rapidity acceptance is small), we can write:

$$E \xrightarrow{d\sigma} = \langle E \xrightarrow{d\sigma} \rangle_{\Delta p_{T} \Delta \phi \Delta y} = \frac{1}{\Delta p_{T} \cdot \Delta \phi \cdot \Delta y} \int_{\Delta p_{T}} \int_{\Delta \phi} \int_{\Delta y} \frac{1}{p_{T}} \cdot \frac{d\sigma}{dp_{T}} \cdot dp_{T} d\phi dy =$$

$$= \frac{1}{\Delta p_{T} \cdot \Delta \phi \cdot \Delta y} \langle \frac{1}{p_{T}} \rangle_{\Delta p_{T}} \int_{\Delta p_{T}} \int_{\Delta \phi} \int_{\Delta y} \frac{d\sigma}{dp_{T}} \cdot dp_{T} d\phi dy \qquad (VI-e)$$

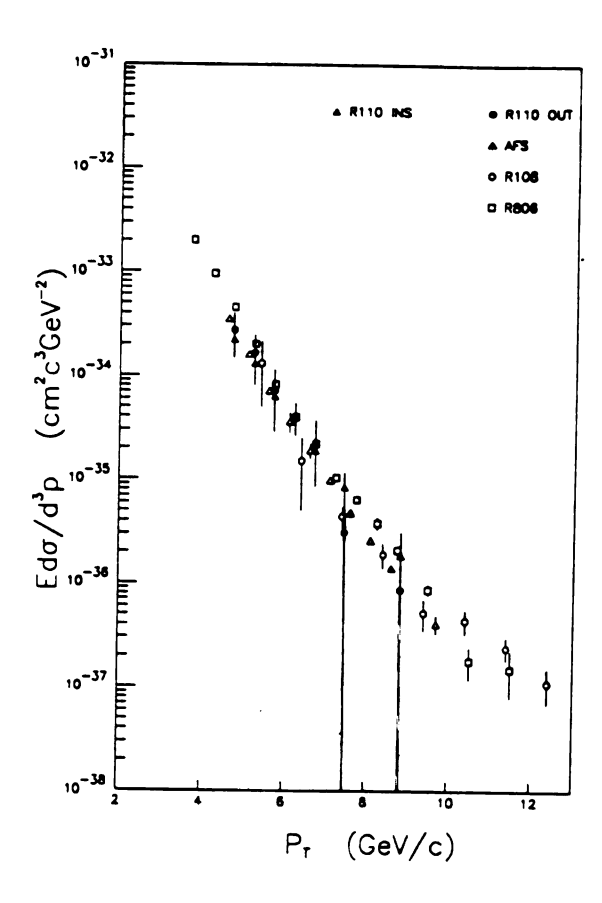
where we have dropped the average symbol on $E\frac{d\sigma}{d^3p}$ for notational convenience. Now

$$\int_{\Delta p_T} \int_{\Delta \phi} \int_{\Delta y} \frac{d\sigma}{dp_T} \; dp_T d\phi \, dy \; = \frac{\gamma_{Dp}}{L} \; , \; \text{therefore:} \;$$

$$E \frac{d\sigma}{d^3p} = \frac{\gamma_{Dp} \langle \frac{1}{p_T} \rangle}{L \cdot \Delta p_T \Delta \phi \Delta y} \qquad (VI-f)$$

where $\langle \frac{1}{p_T} \rangle$ is the average of $\frac{1}{p_T}$ in the bin Δp_T wide; γ_{Dp} , from equation (V-t), is the number of direct photons produced in the volume $\Delta p_T \Delta \phi \Delta y$. L is the accumulated luminosity of the sample. L was $5.97 \cdot 10^{37}$ cm⁻² for the inside and $2.57 \cdot 10^{37}$ cm⁻² for the outside and $\Delta \phi \Delta y = 1.92$ is the $(\phi - y)$ sub-space volume used in the Monte Carlo for acceptance calculations.

Tables VI-2 and VI-3 show the values of the cross section for the seven $\mathbf{p_T}$ bins considered in the inside and outside configurations. Figure VI-8 shows the R110 cross section for the inside and outside



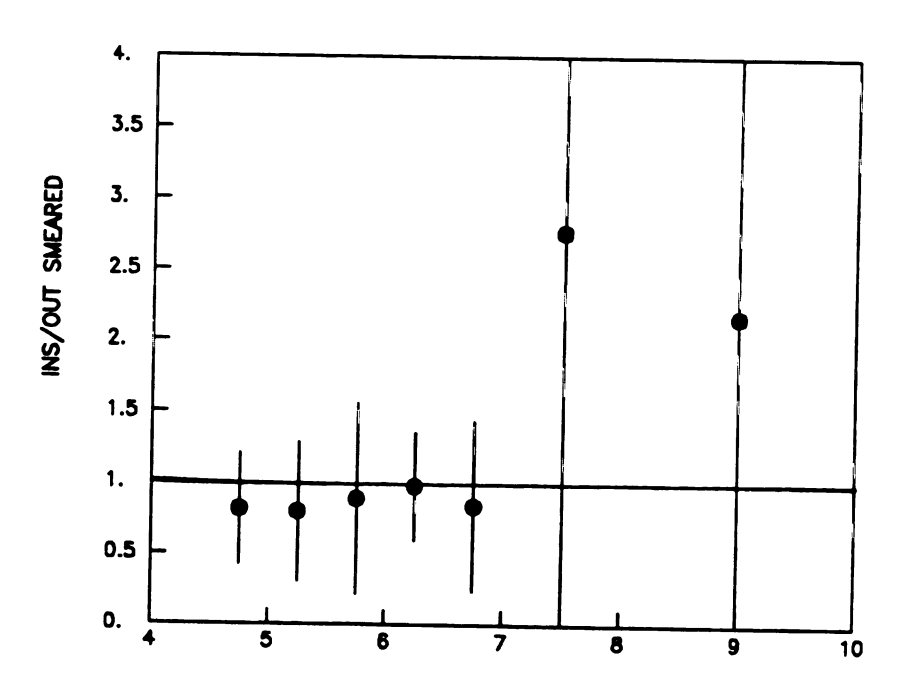


Figure VI-8: Direct Photon Invariant Cross Section for the Inside and Outside Triggers and their Ratio.

samples and their ratios. Figure VI-9 shows the values of the cross section calculated from the error-weighted average of the inside and outside values. Table VI-4 gives the final results for the seven $p_{\rm T}$ bins.

The values of the cross section were plotted at values \mathbf{p}_{T_0} such that:

$$\langle E \frac{d\sigma}{d^3p} \rangle_{p_{T_0}} = \frac{1}{\Delta p_T} \int_{\Delta p_T} E \frac{d\sigma}{d^3p} dp_T$$
 (VI-g)

 $\mbox{$p$}_{T_{\,0}}$ was determined iteratively starting with the bin centers. Only two iterations were necessary. The final values are shown in table VI-1.

The statistical errors of the measured direct photon cross section were calculated using:

$$\Delta(\langle E | \frac{d\sigma}{d^3p} \rangle) = \langle E | \frac{d\sigma}{d^3p} \rangle \cdot (\Delta \Upsilon_{Dp} / \Upsilon_{Dp})$$
 (VI-h)

where $\Delta\Upsilon_{\mbox{\scriptsize DD}}$ is given by formula (V-F).

VI-4. Systematic errors.

There were five main sources of systematic error in the evaluation of the direct photon cross section: luminosity measurement, energy calibration of the detector, selection of strip chamber information (strip chamber cuts and windows), modeling of the detector

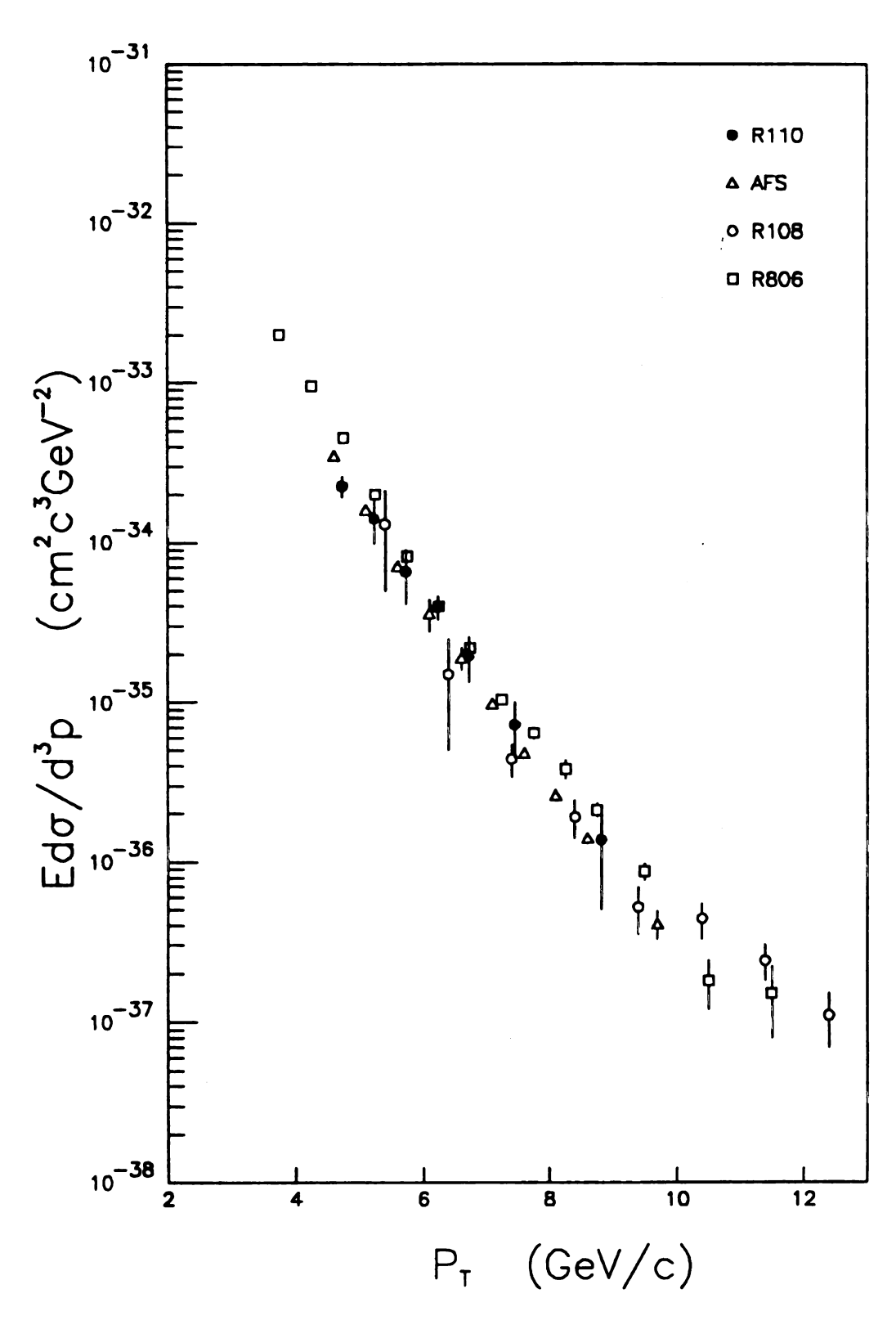


Figure VI-9: Direct Photon Invariant Cross Section Compared with other ISR Experiments.

and physics processes (strip chamber response algorithm and EGS) and acceptance calculation.

The error associated with the luminosity measurement was about $\Delta L/L = 10\%$ and thus $\Delta (cross section)/(cross section) = 10\%$.

The overall energy scale uncertainty due to the uncertainty in the beam momentum during the PS calibration of the NaI(Am) sources, and the uncertainty in their deterioration with time was estimated to be less than 5% in the energy scale. There are additional effects due to the relative calibration of the front plus back arrays, discussed below with the Front/All cut acceptance.

In the evaluation of \mathfrak{a}_{t} , there were several parameters used to select strip chamber information. We studied how the uncertainty in the determination of these parameters propagates to the value of the cross section. The most important influence on the cross section is through the shape of the \mathfrak{a}_{t} distributions. The most sensitive parameter was the cut on total pulse height of the cluster, used to determined the limits of the information window (section V-2). We set the pulse height cut as low as we could, while still rejecting noise. The cut could potentially bias our sample. Low energy photons from asymmetric decays may have their clusters fail to pass this cut, giving a \mathfrak{a}_{t} more like a single photon than a multiphoton. Therefore, the impact of the cut value in the \mathfrak{a}_{t} distribution shape is substantial. We found that a 5% increase in the cut (which was the largest we felt was credible) produced a 10% increase in the cross section due to our uncertainty in all the strip chamber cut values.

The study of systematic errors associated with the EGS simulation is difficult, since it would take large amounts of time to run with all the cut-off and geometry possibilities. We chose to run several cut-offs (0.5,1 and 3 MeV). In the course of our simulations, we used several different detector geometries. Studying the variation produced in the shape of the strip chamber energy deposition by the different parameters, propagating these variations to the 0th distribution, and fitting to get the cross sections, we have concluded that a systematic error of about 5% in the cross section can be attributed to uncertainties in the EGS simulation.

The systematic errors in the acceptance calculations come from the cut simulations introduced in the Monte Carlos. We studied the most important cuts: the B veto, the Front/All cut and the trigger simulation in the case of mesons. In section V-6 we discussed the B-veto simulation and how it compares with the data values. From the comparison between data and simulated acceptances we estimate an uncertainty in the cross section of about 2.5% from the B-veto acceptance.

For multiphoton decays, the trigger was simulated by defining a merging window in the back glass array. Photons hitting the back glass at distances less than 30 cm produced one cluster in the Monte Carlo simulation (see Appendix D). We changed the merging distance to 35 cm. The shift changed the total meson acceptance by 1.7 %. The only effect in the direct photon cross section is through the value of $\gamma/\gamma\gamma|_m$. The effect on the direct photon cross section of the $\gamma/\gamma\gamma|_m$ change is negligible.

As explained in section V-9, the Front/All cut rejected spurious events that populated the low end tail of the $\sigma_{\rm t}$ distributions. The problem was that the direct EGS simulated Front/All distributions do not agree with the data. There are reasons to believe that both data and simulation are erroneous. Light collection is not modelled in the Monte Carlo and the Front-Back calibration of the array was done ignoring the energy variation in the light collection ratio between the front and back.

We opted, then, to phenomenologically adjust the Monte Carlo to the data. Comparing the calculated Front/All acceptance and the observed data acceptance in the first \mathbf{p}_{T} bin, where the extra background events are less important, we associated a 2 % systematic error for the acceptance Front/All simulation.

Associated with the Front/All simulation problems, there is a balancing front-back uncertainty in the energy calibration. We evaluated this uncertainty by two methods. First, we calculated the data energy shift for making PS data and simulated Front/All agree. The energy shift resulted in: $E_{\text{new}} = E_{\text{old}} = (1.08 - .24 \cdot \text{Front/All})$. The ratio $E_{\text{do}} = (p_{\text{Told}}) = (1.08 - .24 \cdot \text{Front/All})$. The ratio the energy change. Energy shifts from 1% in the first $p_{\text{Told}} = (1.08 - .24 \cdot \text{Front/All})$. The ratio the energy change. Energy shifts from 1% in the first $p_{\text{Told}} = (1.08 - .24 \cdot \text{Front/All})$. This method overestimates the values of cross section shifts since does not account for possible backgrounds present in the direct photon sample. The second

me thod calculates, event by event, the recalibrated data cross section. Since the Front/All of data and simulation will now agree, the Front/All acceptance is calculated directly from the EGS Front/All distributions. The shifts in the cross sections using this method ranged from -2% in e first bin to 12% in the last p_T bin. This method accounts for exceptance in the direct photon sample. However, they are not all accounted for in the acceptance correction (other hadrons and extra exceptance with low o_t). We believe that the values of the systematic errors associated with the front-back balancing uncertainty lie between the ese results.

If we add in quadrature all of the systematic errors discussed above, then the total systematic error in the direct photon cross section should range from 18% at the lowest p_T bin to 30% at the highest.

VI-5. Comparison with QCD Predictions and with Other Experiments.

Other experiments have measured pp + YX reactions at the ISR.

Figure VI-9 compares our direct photon invariant cross section with

ther ISR measurements at \(\sigma = 63 \) GeV, the CCOR (R108) collaboration

[ANG80], the AFS collaboration [TRE85] and experiment R806 [ANA82].

Ratios among experimental cross sections are showed in figure VI-10.

They represent the cross section ratios of AFS, R108 and R806 values to

Our R110 measurements, calculated from a functional form fit discussed

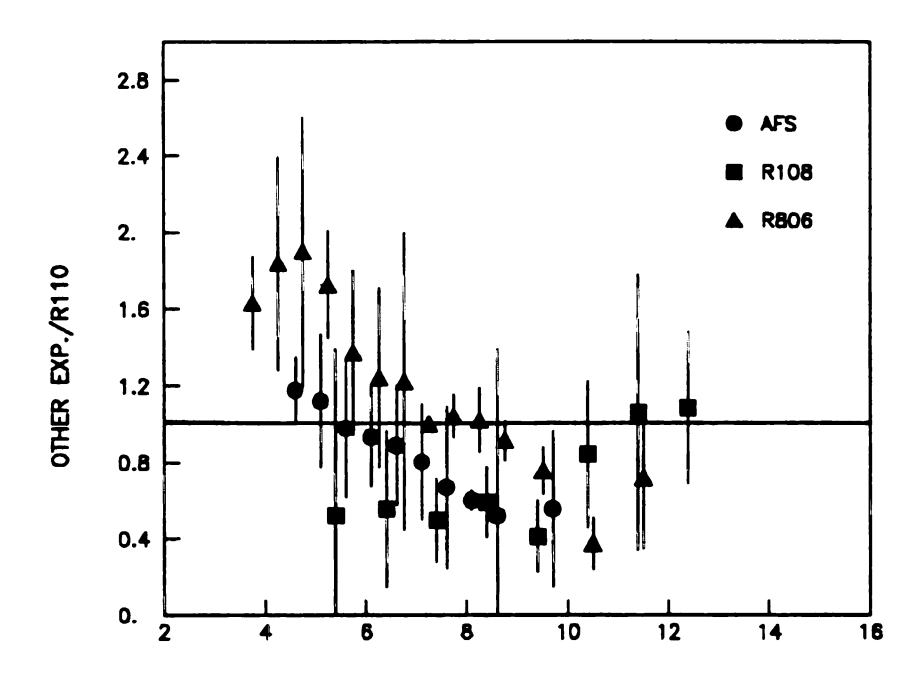


Figure VI-10: Ratios between Direct Photon Cross

Sections Measured in Other Experiments
and R110.

below. Our results agree better with R806 for values between 6 < $\rm p_T$ < 9 GeV/c, but for lower $\rm p_T$ values our cross section is lower, near the AFS measurements. The R108 values are lower but for high $\rm p_T$ ($\rm p_T$ > 10 GeV) their values are consistent with the trend of our results.

As in others inclusive hadron reactions [ANG78], the direct photon cross section can be parametrized as:

$$E \frac{do}{d^3p} = A \cdot p_T^{-n} (1 - x_T)^m \qquad (VI-i)$$

where $x_T = 2p_T / \sqrt{s}$.

A three parameter fit to our data values gives $A = 7.66 \pm 0.38 \times 10^{-30}, \ n = 6.06 \pm 0.36 \ \text{and m} = 5.76 \pm 1.31 \ \text{with a } \chi^2/\text{D.O.F.} = 0.78 \ (\text{D.O.F.} = 4). \ \text{As this experiment covers only a short range in } \chi_T = 0.15 \le \chi_T \le 0.286) \ \text{and has only one } \sqrt{s} \ \text{value, we used data from other} = 0.15 \le \chi_T \le 0.286) \ \text{and has only one } \sqrt{s} \ \text{value, we used data from other} = 0.15 \le \chi_T \le 0.286) \ \text{and has only one } \sqrt{s} \ \text{value, we used data from other} = 0.15 \le \chi_T \le 0.286) \ \text{and has only one } \sqrt{s} \ \text{value, we used data from other} = 0.15 \le \chi_T \le 0.286) \ \text{and has only one } \sqrt{s} \ \text{value, we used data from other} = 0.15 \le \chi_T \le 0.286) \ \text{and p} = 0.286$ and p parameter of the fitting. The experiment NA24 [DEM87] at the SPS fixed target program has given data at $\sqrt{s} = 24 \ \text{GeV}$ in a $\chi_T = 0.27 \le \chi_T \le 0.5$, and experiment WA70 [BON87] also at the SPS have data at $\sqrt{s} = 23 \ \text{GeV}$ in the range $0.27 \le \chi_T \le 0.496$. Fitting again (VI-1) to the three sets of measurements we obtained A= $0.03 \pm 0.96 \times 10^{-30}$, n= $0.03 \pm 0.03 \pm 0.039$, with $\chi^2/\text{D.O.F.} = 0.95$ (D.O.F.= 14). In figure VI-11 the scaling plot $p_T^{4.91} \to \frac{d_0}{d^3 p}$ vs χ_T is shown including NA24,

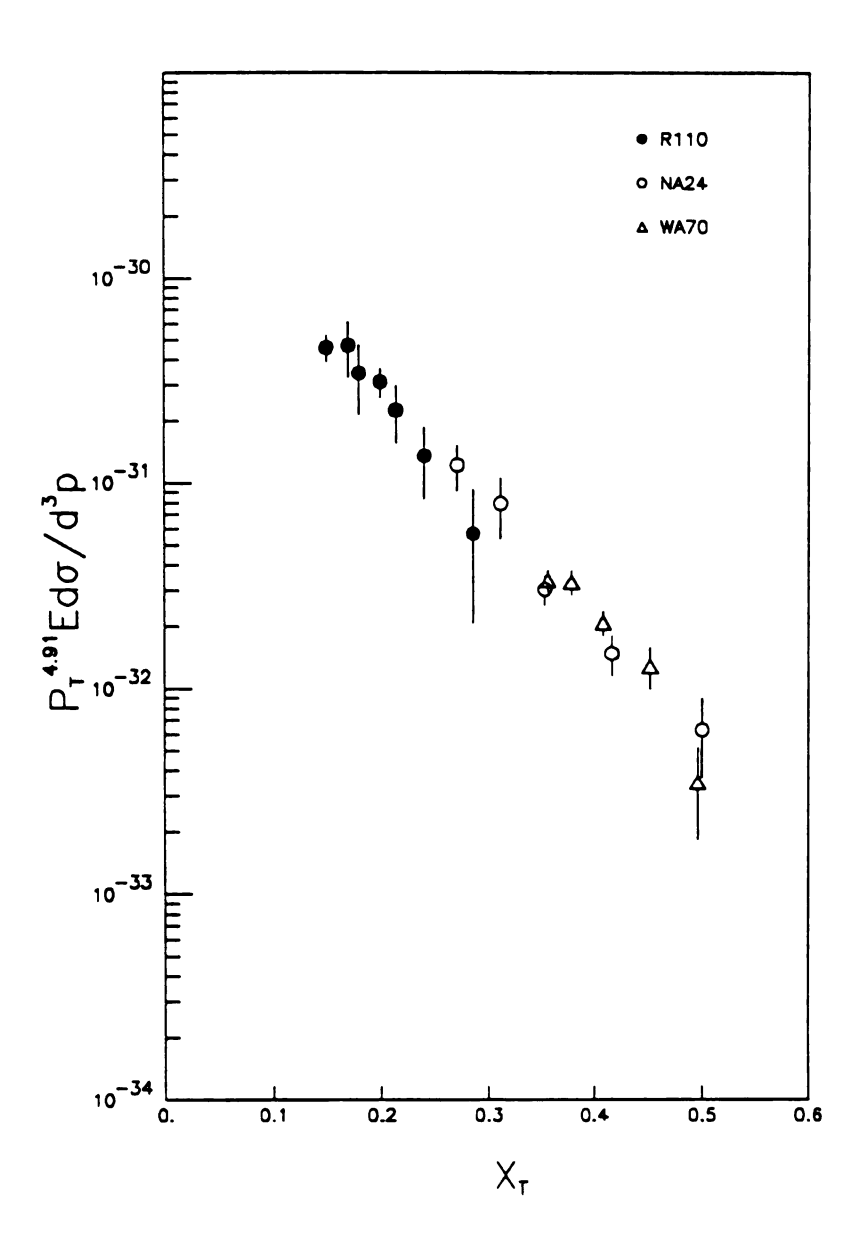


Figure VI-11: $p_T^{4.91}$ E $\frac{d\sigma}{d^3p}$ vs. x_T , for Experiments NA24, WA70 and R110.

WA70 and R110 values (only statistical errors are shown).

As explained in the first chapter there are QCD perturbative predictions for the direct photon invariant cross section. Using the Bielefeld-LAPP-Orsay (BLO) group [AUR88] calculations we can compare QCD predictions with different set of structure functions to the data. This group used the two sets of structure function parametrizations of Duke and Owens [DUK84]. These sets are the result of a leading logarithm analysis of DIS, Drell-Yan pair production and production of heavy conances. Set I corresponds to a soft gluon distribution and a value $\Lambda_{\overline{MS}}$ 200 MeV, whereas the set II corresponds to a harder gluon and a larger value of $\Lambda_{\overline{MS}}$ 400 MeV. Both gluon distributions are represented in figure VI-12. The sets differ chiefly in the gluon structure functions, parametrized as [DUK84]:

$$\mathbf{x} = G(\mathbf{x}, Q^2) = 1.564 \cdot (1 + 9\mathbf{x}) \cdot (1 - \mathbf{x})^6$$
 Set I (soft), $\Lambda = 200 \text{ MeV/c}$
 $\mathbf{x} = G(\mathbf{x}, Q^2) = 0.879 \cdot (1 + 9\mathbf{x}) \cdot (1 - \mathbf{x})^4$ Set II (hard), $\Lambda = 400 \text{ MeV/c}$
at $Q^2 = 4 \text{ (GeV/c)}^2$

Figure VI-13 shows our data and the optimized ("PMS") prediction to the second order for the set I, set II and Born terms. The dashed curve represents the second order optimized prediction when no bremsstrahlung terms are considered. A good agreement is found when set is used. Set II predicts larger rates than we observe.

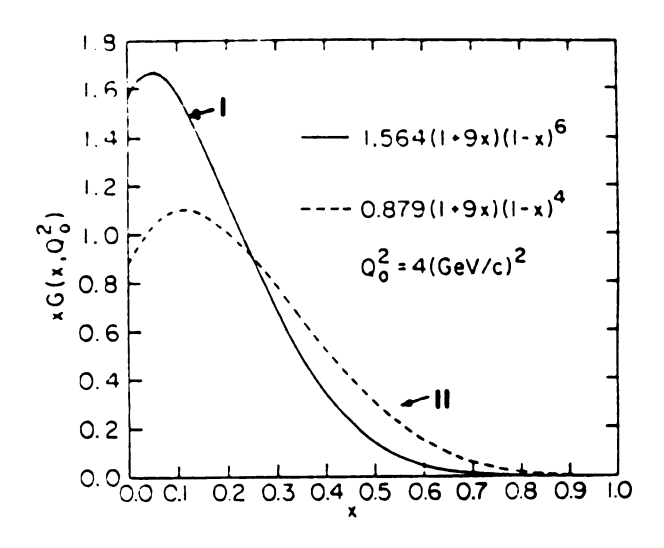


Figure VI-12: Gluon Structure Functions for the Duke and Owens [DUK84] Set I and II.

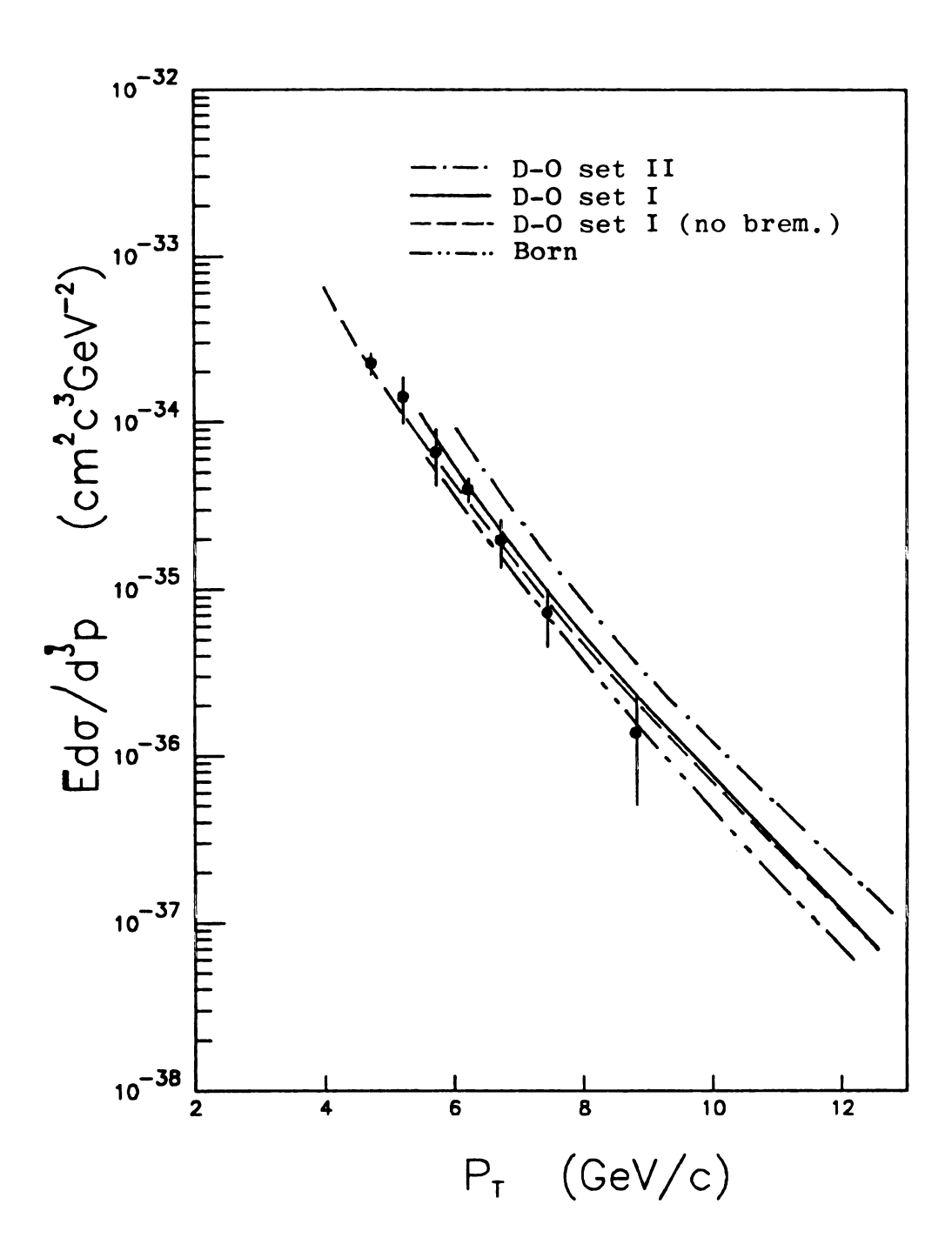


Figure VI-13: Measured Direct Photon Cross Section
Compared with QCD Predictions by
Aurenche et al. [AUR88].

dire GeV.

simi

calc

dire

pred

stru

[KOD]

and t

Pred

(als

COMP

sect:

expe

diffe

The group of Contogouris et al. [ARG84] has also calculated a direct photon cross section for proton-proton interactions at $\sqrt{s} = 63$ GeV. Using a leading-logarithm approximation, k_T smearing and K factors calculated in the soft-gluon approximation [ARG84], they arrive at very imilar results. Figure VI-14 shows Contogouris et al. [ARG87] QCD predictions for DO set I, DO set II and our experimental results for the direct photon cross section.

Our data points favor, in both cases, Duke and Owens set I = tructure functions with a value of $\Lambda_{\overline{MS}} \le 200$ MeV.

A different parametrization has been used by the BLO group BAI88]. They used the gluon distribution in the universal convention

KOD78]:

$$x \cdot G(x, Q_0^2 = 2 \text{ GeV}^2) \sim (1 - x)^{\eta}$$
 (VI-j)

and the QCD scaling prediction for the direct photon cross section of $\mathbf{p_T}^{-6}$ [BER82]. Figure VI-15 shows $\mathbf{p_T^6} \cdot \mathbf{E} = \frac{d\sigma}{d^3\mathbf{p}}$ vs $\mathbf{x_T}$ for different QCD predictions based in different values of \mathbf{n} , and our experimental results (also R108 and R806 results are shown). Our best estimate of \mathbf{n} from this comparison is $\mathbf{n} = 5$ to 6.

As a by-product of our measurements, a meson invariant cross section was extracted. Figure VI-16 shows the "all" = meson + direct Photon cross section as function of p_T. These values were compared with measurements made with the back array only by an predecessor of our experiment (experiment R108) [ANG78]. The values agree within a 15% of ifference.

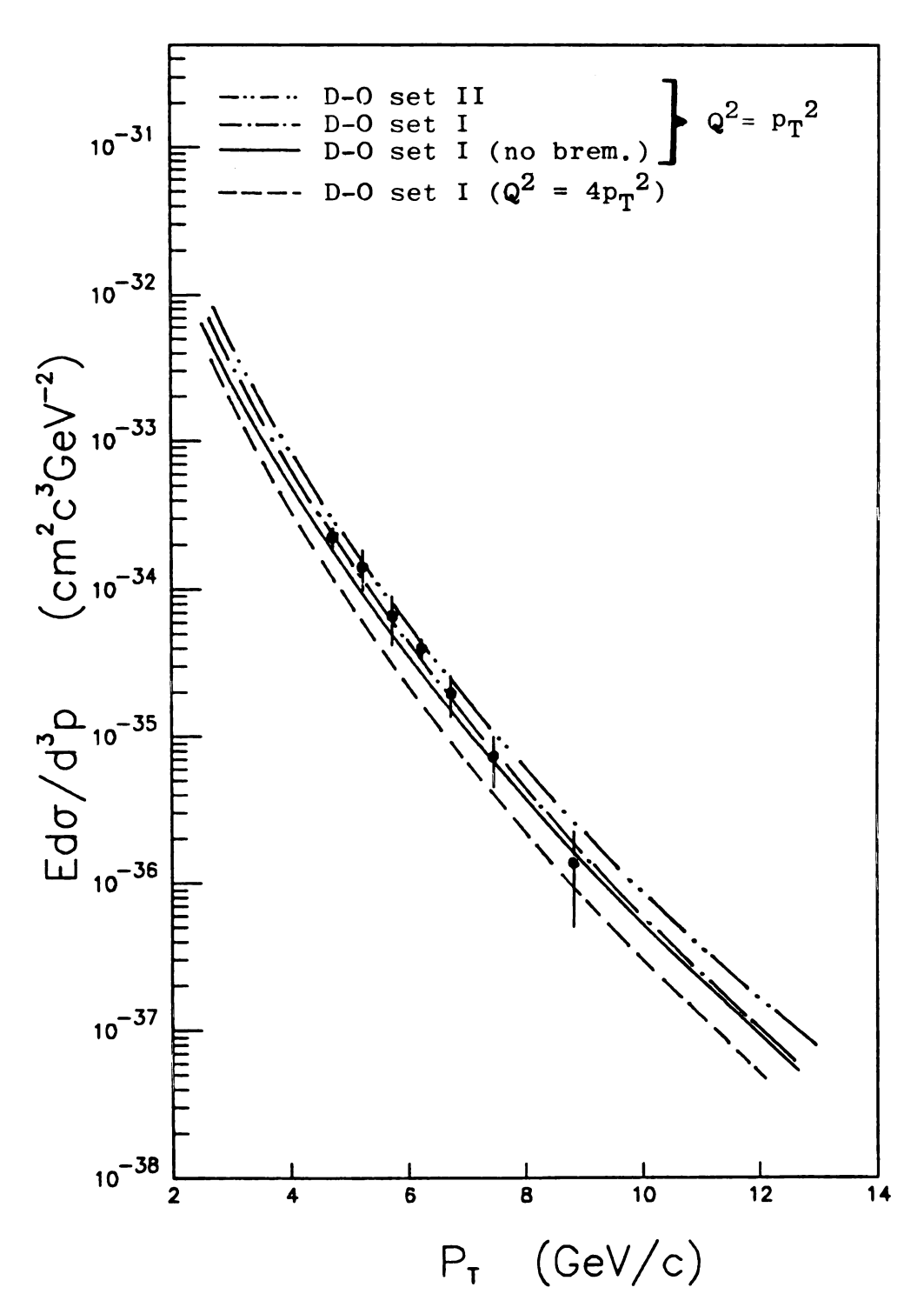


Figure VI-14: Measured Direct Photon Cross Section
Compared with QCD Predictions by
Contogouris et al. [ARG87].

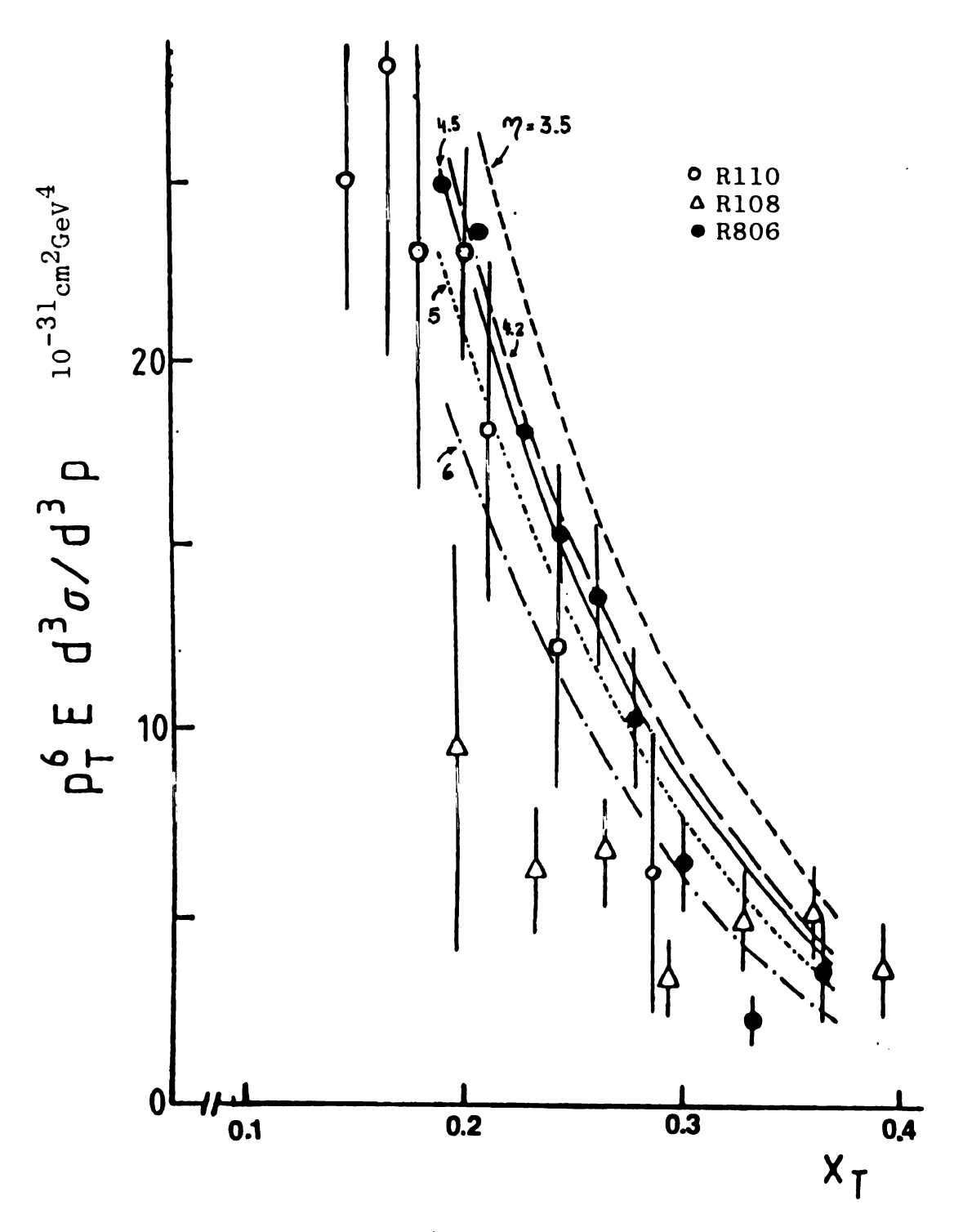


Figure VI-15: $p_T^6 \cdot E \frac{d\sigma}{d^3p}$ vs. x_T , for Different QCD Predictions and Experimental Results for R806, R108 R110.

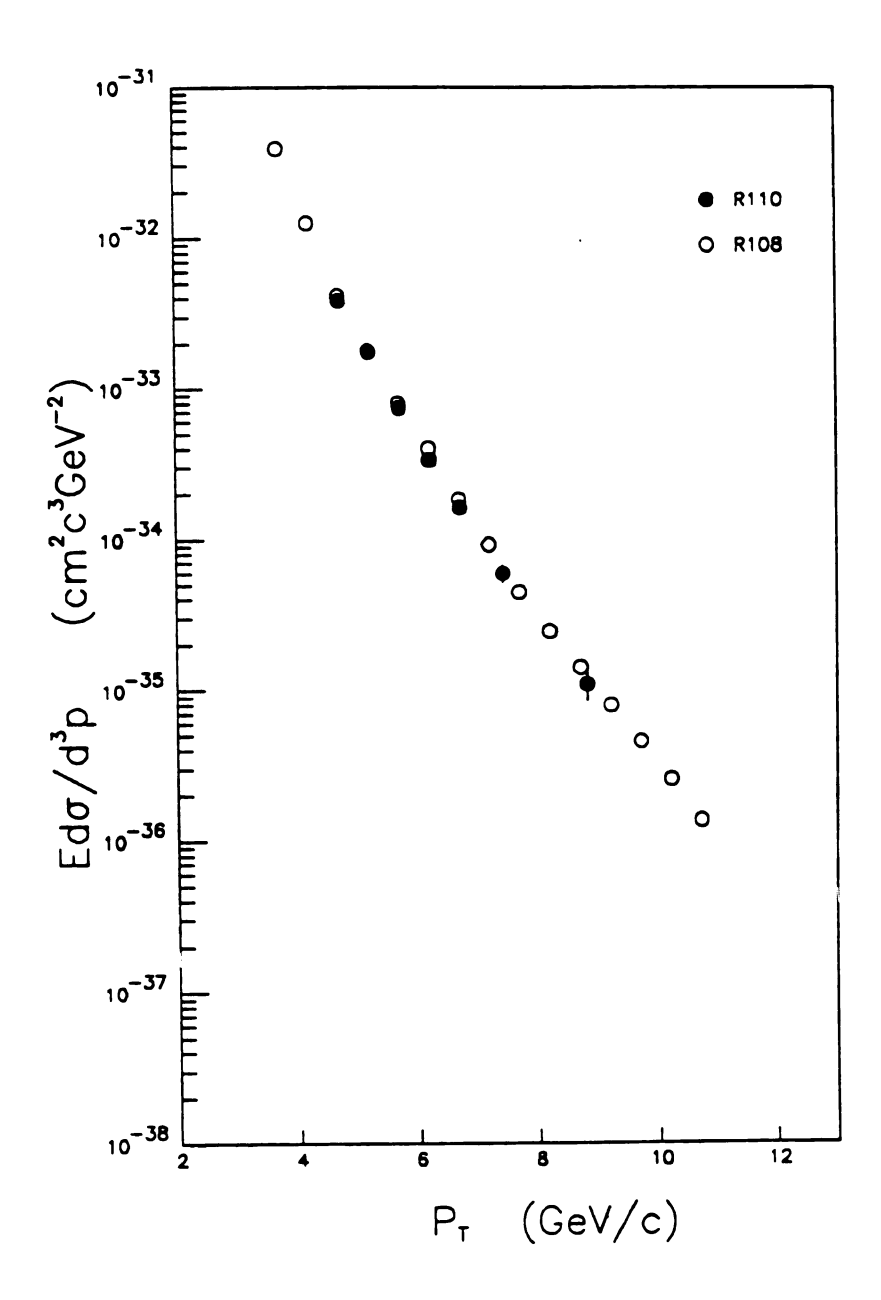


Figure VI-16: "All" (Direct Photon + Neutral Mesons)

Invariant Cross Section vs. p_T (C.M.)

for Experiment R108 and R110.

VI-6. Direct photon event correlations.

Is produced directly from a parton interaction of the constituents of the beam particles. The structure of the direct photon event is not as quantitatively calculable as the cross section. However there is qualitative understanding as to how these events should look within the ramework of Quantum-Chromodynamics (QCD) [HAL80].

To isolate a relatively pure sample of direct photons is very a lifficult. The selection of direct photons tends to bias the structure revents in an unknown way and small backgrounds are able to ontaminate the results noticably in certain regions of phase space.

A direct method of observation is the most appropriate to produce the best possible direct photon sample, since it will remove most of the background, especially in the p_T range where Y/all ratios are much smaller than one. In our case we do not have a complete separation between the single and multiphotons samples but we do have a model to determine their ratio in any data sample.

Our method of extracting a direct photon sample is again based on the σ_t distributions. We determine a σ_t value (σ_{cut}) such that all the events in the data sample with values of σ_t less than σ_{cut} form the sample of "direct photons". The signal is determined by the single photon component and the noise (neutral meson background) by the ultiphoton component. We can determine the best value of σ_{cut} to btain a reasonable signal-to-noise ratio and a reasonable number of

events. After a value of $\sigma_{\rm cut}$ was chosen, the Monte Carlo $\sigma_{\rm t}$ distributions can be used to calculate the signal-to-noise ratio and to estimate the background from multiphotons still present in the sample.

VI-7. Subtraction of the neutral meson background.

We are trying to measure a certain property, ϕ , of the direct photons. Using the $\sigma_{\rm cut}$ value, we divide each sample in two. We denote ith the subscript 1, events with $\sigma_{\rm t} \leq \sigma_{\rm cut}$ (direct photon candidates) and 2 with $\sigma_{\rm t} \geq \sigma_{\rm cut}$ (neutral meson candidates). However each sample is mix of direct photons and neutral mesons. We can assume that the property ϕ is given by a combination of the property for pure direct photons, ϕ_{γ} , and for pure neutral mesons, $\phi_{\rm m}$. Thus we assume that the property ϕ is not correlated with $\sigma_{\rm t}$, and therefore is independent of the cut. ϕ only depends on the proportion of pure direct photons and pure neutral mesons. Therefore we can write:

$$\phi_1 = \omega_1 \cdot \phi_{\Upsilon} + (1 - \omega_1) \cdot \phi_{m^1}$$

$$\phi_2 = \omega_2 \cdot \phi_{\Upsilon} + (1 - \omega_2) \cdot \phi_{m^2}$$
(VI-k)

where ω_1 is the probability of the event being a direct photon for the sample 1, and ω_2 for the sample 2. Since we assume the total sample is

composed only of direct photons and neutral mesons, the probability for being a meson is $(1-\omega_i)$, for i=1,2.

Each of these probabilities can be written in the form: $\omega_i = P_{\gamma i} \cdot P_{\gamma D i}, \text{ where } P_{\gamma i} \text{ is the probability of being a single photon and } P_{\gamma D_i} \text{ is the probability of this single photon being a direct photon.}$

We now define the notation illustrated in figure VI-17. Let f be a normalized σ_{t} distribution and F be its integral over a restricted region, thus, f_{γ} , f_{m} and f_{D} represent the normalized σ_{t} distributions for single photons, multiphotons and simulated data respectively. For any value of σ_{t} :

$$f_{D} = C_{Y} \cdot f_{Y} + (1 - C_{Y}) \cdot f_{m} \qquad (VI-1)$$

where C_{γ} is the fraction of single photons in the data sample extracted by the likelihood fit explained in section V-10.

Therefore, integrating (VI-1) over region i and letting,

$$F_{x_i} = \int_{i} f_{x}(\sigma_t) d\sigma_t; \text{ region 1 is 0 to } \sigma_{cut}$$

region 2 is
$$\sigma_{\text{cut}}$$
 to 0, and x= D, Y or m,

we obtain

$$F_{Di} = C_{\Upsilon} \cdot F_{\Upsilon i} + (1 - C_{\Upsilon}) \cdot F_{mi} \qquad (VI-m)$$

The probability $P_{\gamma i}$ of being a single photon is then:

$$P_{\gamma i} = \frac{C_{\gamma} \cdot F_{\gamma i}}{F_{D4}} \qquad i=1,2 \qquad (VI-n)$$

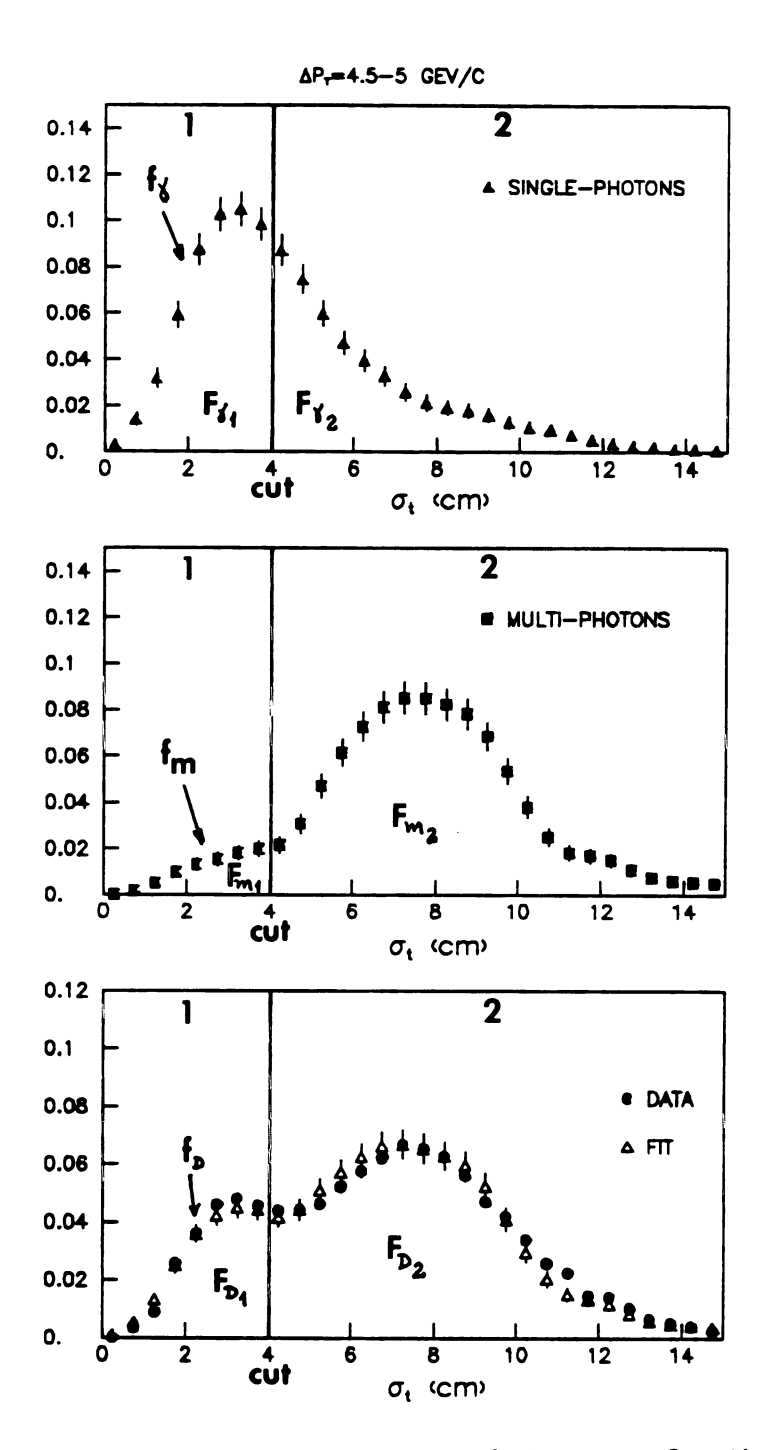


Figure VI-17: Representation of the ocut for the Extraction of a Direct Photon Sample and Correction of the Neutral Meson Background.

and the fraction of direct photons in the single photon sample, $P_{\gamma Di}$; is given by:

where we assume that this fraction remains constant for different $\sigma_{\mbox{\scriptsize t}}.$

Therefore:

$$\omega_{i} = P_{\gamma i} \cdot P_{\gamma D i} = \frac{F_{\gamma i}}{F_{D i}} \cdot \left[c_{\gamma} - \frac{\gamma}{\gamma \gamma} \Big|_{m} \cdot (1 - c_{\gamma}) \right] \qquad (VI-p)$$

gives the probabilities, from the simulated values of $F_{\gamma i}$ and F_{mi} where F_{Di} is given by $F_{Di} = C_{\gamma} \cdot F_{\gamma i} + (1 - C_{\gamma}) \cdot F_{mi}$.

Solving the system of two equations in (VI-k) we obtain:

$$\phi_{\gamma} = \frac{1}{(\omega_1 - \omega_2)} \cdot [(\phi_1 - \phi_2) - (\omega_2 \phi_1 - \omega_1 \phi_2)] \qquad (VI-q)$$

and

$$\phi_{\rm m} = \frac{1}{(\omega_1 - \omega_2)} \cdot (\omega_1 \phi_2 - \omega_2 \phi_1) \qquad (VI-r)$$

The errors can be calculated by propagation as:

$$(\Delta \phi_{\gamma})^{2} = (\partial \phi_{\gamma}/\partial \omega_{1})^{2} \cdot (\Delta \omega_{1})^{2} + (\partial \phi_{\gamma}/\partial \phi_{1})^{2} \cdot (\Delta \phi_{1})^{2} + (\partial \phi_{\gamma}/\partial \omega_{2})^{2} \cdot (\Delta \omega_{2})^{2}$$

$$+ (\partial \phi_{\gamma}/\partial \phi_{2})^{2} \cdot (\Delta \phi_{2})^{2}$$

$$(\Delta \phi_{m})^{2} = (\partial \phi_{m}/\partial \omega_{1})^{2} \cdot (\Delta \omega_{1})^{2} + (\partial \phi_{m}/\partial \phi_{1})^{2} \cdot (\Delta \phi_{1})^{2} + (\partial \phi_{m}/\partial \omega_{2})^{2} \cdot (\Delta \omega_{2})^{2}$$

$$+ (\partial \phi_{m}/\partial \phi_{2})^{2} \cdot (\Delta \phi_{2})^{2}$$

$$(VI-s)$$

Note that,

$$\Delta \phi = \phi_{m} - \phi_{\gamma} = \frac{\phi_{1} - \phi_{2}}{(\omega_{1} - \omega_{2})} \qquad (VI-t)$$

If the starting distribution values do not show already an appreciable difference between samples 1 and 2, or if the efficiency of the cut for separating direct photons from mesons is low $(\omega_1 \approx \omega_2)$, this method of extracting the background is not applicable. We must start with sufficient signal-to-noise to obtain meaningful results.

The determination of $\sigma_{\rm cut}$ was done by studying the ratio signal-to-noise as function of the cut ($\sigma_{\rm cut}$). The ratio signal-to-noise is defined as the fraction of direct photons divided by the fraction of neutral mesons in the direct photon sample defined by $\sigma_{\rm cut}$. In terms of ω , the ratio can be written as:

signal-to-noise =
$$\frac{\omega}{1-\omega_1}$$
 (VI-u)

Figure VI-18 shows the signal-to-noise ratio as function of p_T for various values of the cut $\sigma_{\rm cut}$. For each p_T , there is a maximum for a 100% efficient cut where the signal-to-noise is given by the fraction of direct photons in the sample. The minimum corresponds to $\sigma_{\rm cut}$ = 0 (no cut). The ratio increases with p_T as the data gets richer in direct photons. The highest signal-to-noise ratios were found using $\sigma_{\rm cut}$ = 4 cm. The average signal-to-noise ratio for the total sample was 1.01, but the ratio reaches 2 for p_T values greater than 7 GeV/c.

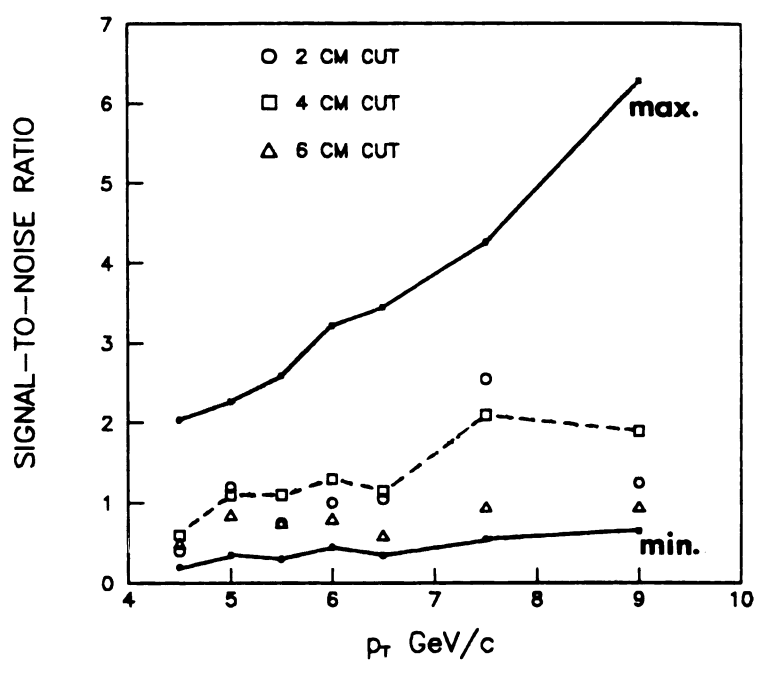


Figure VI-18: Signal-to-Noise ratios vs. p_{T} for various values of o_{cut} .

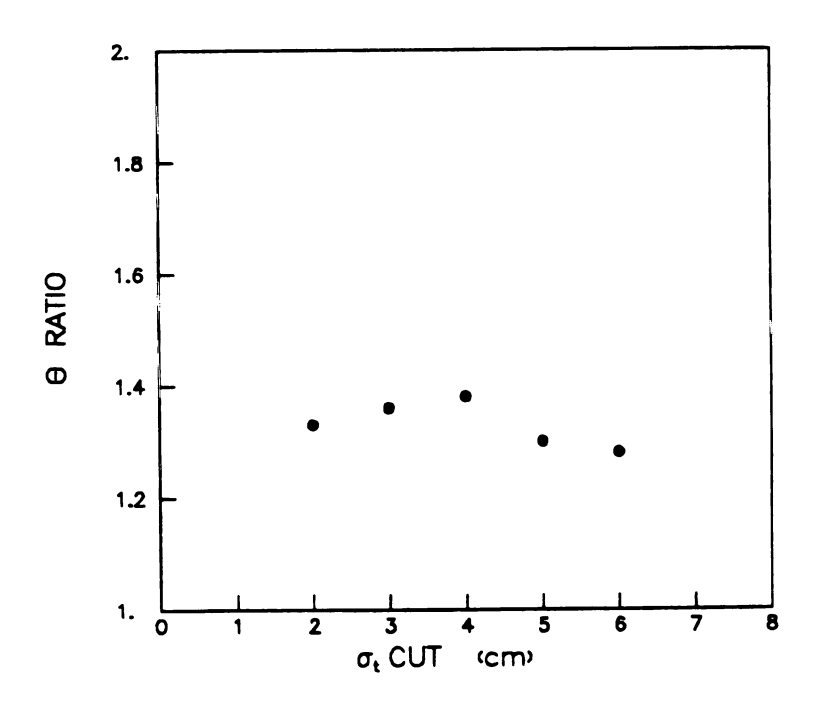


Figure VI-19: Values of θ vs. σ_{cut} .

Another variable was studied to determined the best possible value of $\sigma_{\rm cut}$. The idea was to find $\sigma_{\rm cut}$ such that it maximizes the difference between direct photons and mesons in the variable under study. The variable chosen was the azimuthal distribution of associated particles as defined in section VI-9. We defined the varible 0, as the sum of the differences between samples 1 and 2 for the first five bins of the azimuthal distribution, $|\Phi| \leq 36^{\circ}$, where a noticable difference of the variable between samples 1 (photons) and 2 (mesons) is expected. Using (VI-u), we define:

$$\Theta = \sum_{i=1}^{5} \left| \frac{\phi_{1i} - \phi_{2i}}{(\omega_{1} - \omega_{2}) \cdot \sqrt{(\Delta \phi_{mi})^{2} + (\Delta \phi_{\gamma i})^{2}}} \right| \qquad (VI-v)$$

as the error weighted difference. $(\Delta\phi_{mi})$ and $(\Delta\phi_{\gamma i})$ are given by (VI-s). Figure VI-19 shows the variable 0 for different values of the cut. Again the most favorable situation occurs for σ_{cut} = 4 cm. Therefore, a value of σ_{cut} = 4 cm was chosen.

VI-8. Estimation of other backgrounds.

While discussing the Front/All cut we have already mentioned that there are backgrounds other than neutral meson decays. We study here the class of background produced by hadrons that can most influence the associated particle distributions.

low "ele trig as e of c conce cham possi

> parti (espe

> > conta

since

proto

For th In ad

stabbe

rates

lesons

detect

:onsid cut and

Charged mesons, mostly π^+ and π^- , if they are superimposed on a low energy neutral decay, can produce a spurious high energy "electromagnetic" cluster in the calorimeter. We have a cut to remove triggers with charged particles pointing to the trigger cluster region, as explained in section IV-7. In figure IV-8 we showed the distribution of charged particle hits on the back glass face. There is a small concentration of charged particles in the trigger region. As the drift chambers are not perfectly efficient, we have to consider the possibility of events passing this cut.

The B-veto cut should also rule out most of this class of events since we cut on a B pulse height lower than the minimum ionizing particle value. However, as seen in figure IV-8, this cut is inefficient (especially in position determination). There is some charged hadron contamination in the events.

Another charged particle which will contribute is the antiproton, \bar{p} , especially since it can annihilate in the glass giving E > p. For the same reason the anti-neutron, \bar{n} , is a good background candidate. In addition, because it is neutral, it is not tracked by the drift chambers. Other neutral hadrons produced in proton-proton collisions at rates big enough to contribute to the background are neutrons (n) and K_L^o mesons.

A Monte Carlo was written to determine the acceptances for the detection of π^+ , π^- , n, K_L^o , \bar{p} and \bar{n} . This simple Monte Carlo only considered the most important analysis requirements: B-veto, Front/All cut and charged particle cut. The trigger was simulated by an energy cut

after energy smearing. The hadron response of the calorimeter was extracted from previous PS tests [BEA74] and the drift chamber track efficiency was taken to be 90 % [NIC82].

The ratios of production for the hadrons with respect to neutral mesons were extracted from the literature and assumed to have the same p_T dependence as the neutral mesons. $(\pi^+ + \pi^-)/(\text{neutral mesons}) = 2.0$ [AKE84], $(n+K_L^0)/(\text{neutral mesons}) = 0.55$ [DRI82] and $\bar{p}/\text{mesons} = \bar{n}/\text{mesons}$ = p/mesons = 0.12 [AKE84]. The resulting Monte Carlo acceptances were:

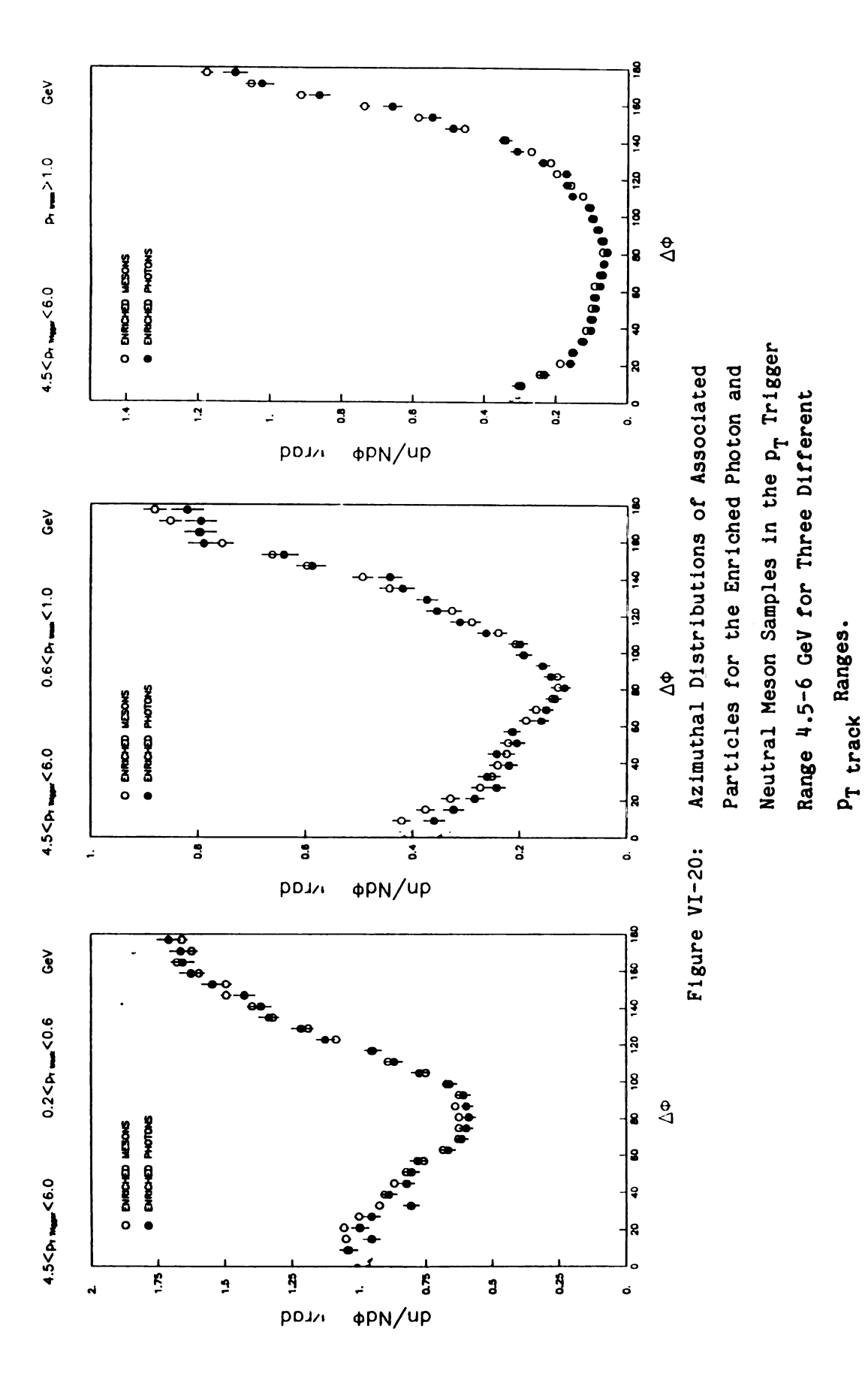
	4.5-5 GeV/c	7-8 GeV/c	
$A_{(\pi^{+}+\pi^{-})}/A_{m}$	0.024	0.037	
A(n+K°)/Am	0.028	0.061	
A_n^-/A_m	0.050	0.123	
A-/A p m	0.031	0.108	

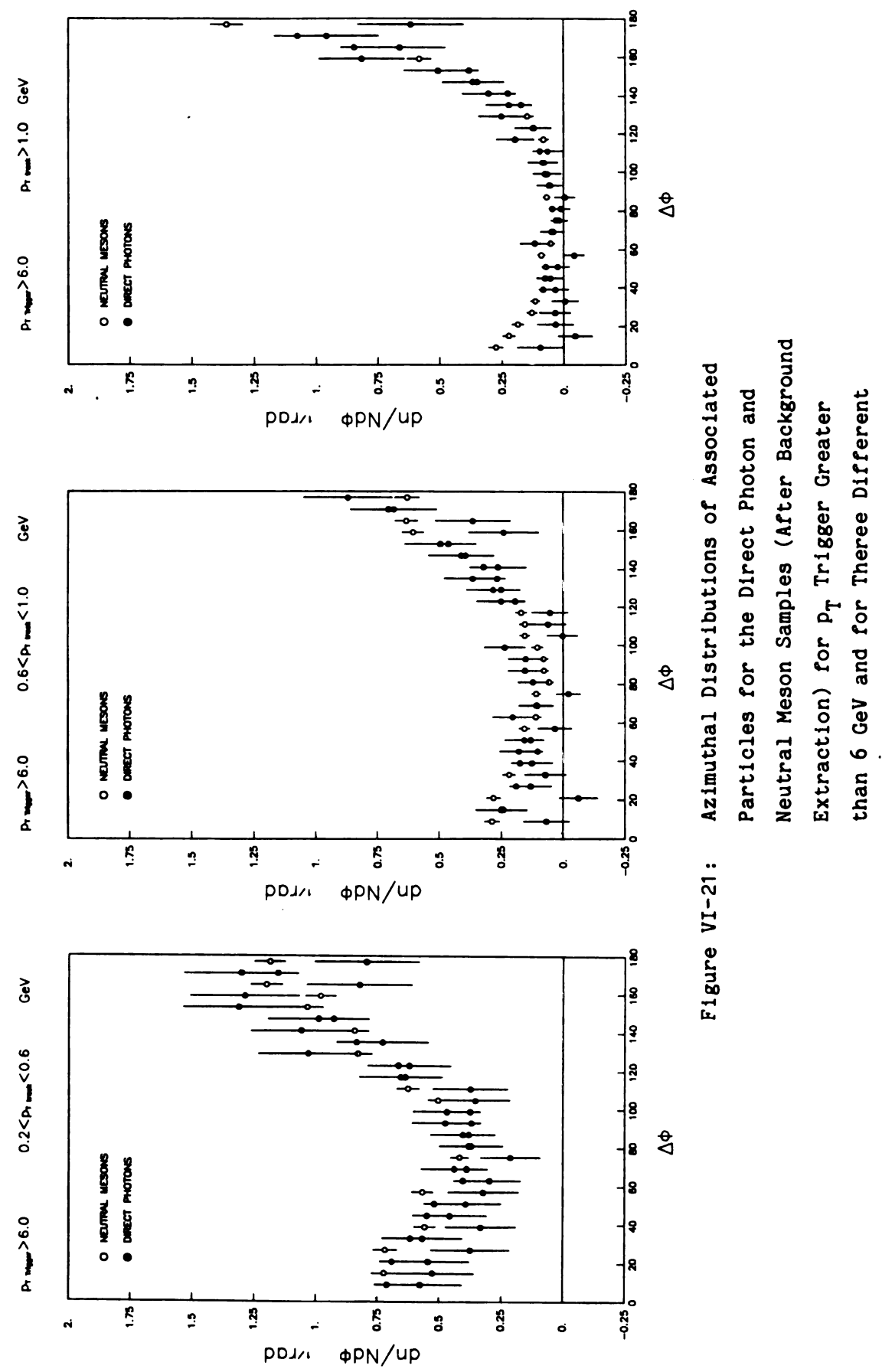
The Monte Carlo simulation showed that most of these backgrounds produce very low Front/All ratios, with 96% below the Front/All cut of 0.14. We estimate the total hadron contamination to be less than 5 % of the observed neutral meson background for the low \mathbf{p}_{T} bins, rising to 12% for the high \mathbf{p}_{T} bins. These backgrounds will be concentrated at low Front/All and low σ_{t} values. In the worst scenario, we could consider all these background events present in the direct photon sample defined by σ_{t} < 4 cm.

VI-9. Charged particle distributions.

Hadrons on the same side as the direct photon, i.e., having an azimuthal angle ϕ relative to the trigger particle within \pm 90°, originate mainly from bremsstrahlung processes. On the other hand, the Compton and annihilation terms are characterized by isolated high-p $_{_{\mathbf{T}}}$ photons. Figures VI-20 shows azimuthal distributions of associated charged particles. The value of $\Delta n/N\Delta \phi$ is plotted versus ϕ , where ϕ is the azimuthal angle relative to the Y or meson trigger. N is the total number of events in the Δp_T trigger interval considered and Δn the number of charged particles. The first bin $(0^{\circ}-6^{\circ})$ has been omitted since it corresponds to the region vetoed by the B counters cut. Events were selected with 4.5 \leq p_T trigger < 6.0 GeV/c for three different requirements in the p_T of the tracks plotted: 0.2 \leq $p_{T \text{ track}} <$ 0.6, $0.6 \le p_{T,track} < 1.0$ and $p_{T} \ge 1.0$ GeV/c. Requirements were imposed on the tracking algorithm to reject poorly measured tracks (on the χ^2 , number of space points and extrapolated distance to the event vertex).

The large peak at $\phi = \pi$ is from the recoiling jet, while the smaller peak at $\phi = 0^{\circ}$ in the meson case is due to hadrons of the jet associated with the trigger. Clear two jet structure is shown. The same side for both enriched photon and meson samples looks much alike, contrary to QCD predictions and other measurements [AKE82]. The signal-to-noise ratio is approximately one (as discussed in section VI-7) assuming only the neutral meson background. There are then reasons to believe that the separation we obtain is not good enough to observe





p_T track Ranges.

the effect predicted. However, for high p_T triggers, and after the subtraction of the neutral meson background by the method explained in section VI-7, the direct photon sample started to show the trend expected by QCD calculations. Figures VI-21 shows the azimuthal distributions for events with p_T trigger > 6 GeV/c with the neutral meson background extracted and the same track requirements as in figure VI-19. The direct photon sample shows a lack of charged associated particles on the same side of the trigger if compared with neutral meson sample. Unfortunately, we have insufficient statistics to make a more detailed study in this p_T range.

VI-10. Away Side Studies.

The away side associated particles, those having an azimuthal angle ϕ relative to the photon (or meson) that is larger than \pm 90°, will present different characteristics for meson and direct photons. In the case of the Compton process the recoiling jet will be caused by the fragmentation of a quark, whereas for the annihilation process it will be a gluon.

In proton-proton collisions the ratio of u quarks to d quarks on the away side will be approximately:

$$C_q = \frac{N_u \cdot (Z_u \alpha)^2}{N_d \cdot (Z_d \alpha)^2} = 2 \frac{(^2/_3)^2}{(^1/_3)^2} = 8$$
 (VI-x)

This ratio 8-to-1 at the quark level will give a large ratio of positive to negative hadrons in the away side. This is, however, not totally correct since u quarks can give rise to negative hadrons and d quarks to positive hadrons. One might hope to approach this ratio with leading hadrons, which might remember the charge of the parent parton.

Figure VI-22 shows the ratio of positive-to-negative associated hadrons in a 45° semicone centered at 180° of the trigger direction for both direct photon and meson background corrected samples. The ratios for the direct photon and neutral meson samples are shown versus $\mathbf{z}_{\mathbf{F}}$, where $\mathbf{z}_{\mathbf{F}}$ is defined as:

$$z_{F} = \frac{|\overrightarrow{p}_{track} \cdot \overrightarrow{p}_{trigger}|}{p_{trigger}^{2}} \quad (VI-y)$$

In the same plot the QCD predictions for direct photons and neutral mesons are shown [HAL80]. For high values of \mathbf{z}_{F} , where the predicted differences are greater, the measured uncertainties are higher due to the rarity of fragmentation at high \mathbf{z}_{F} , making it difficult to reach a definite conclusion.

VI-11. Summary and Conclusions.

Data were taken at \sqrt{s} = 63 GeV from p-p collisions at the CERN ISR, triggering on electromagnetic shower deposition in a lead glass array calorimeter. A MWPC was used to discriminate between single- and multi-photon triggers. Unfortunately, the characteristics of the MWPC



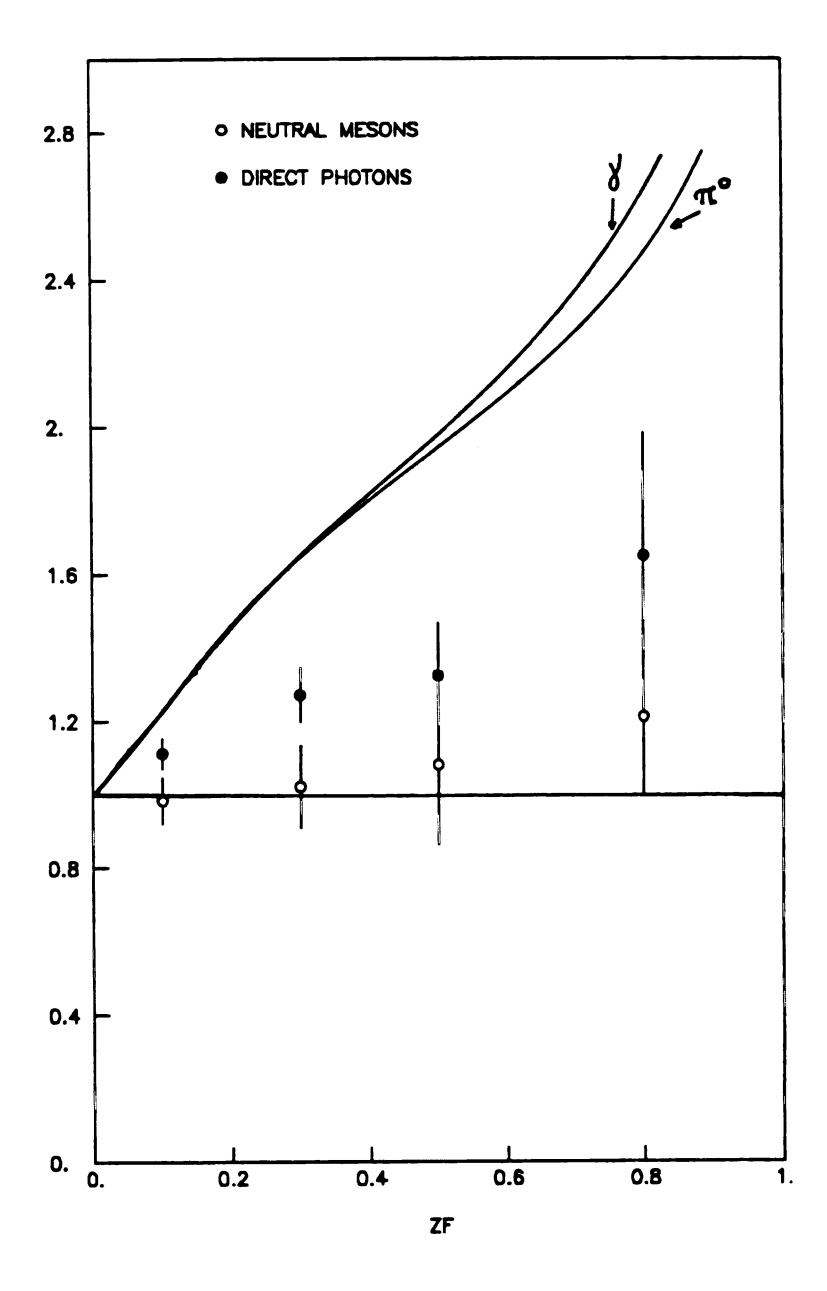


Figure VI-22: Ratio of the Number of Positive to Negative Charged Hadrons in the Away Side vs. \mathbf{z}_{F} , for the Direct Photons and the Neutral Mesons Samples. Also QCD Predictions [HAL80] are shown.

were such that a direct count of single photon showers proved difficult. A method was devised to discriminate between single and multiphoton triggers based on the transverse shower shape study of the trigger shower. The data were compared with simulated single and multiphoton characteristics. In this way the fraction of single photons present in the data sample was obtained. The simulation of the MWPC response introduced one the most important cause of systematic uncertainties.

A Monte Carlo simulation of the single photon background was used to correct the total fraction of single photons and obtain the inclusive direct photon cross section. The measured direct photon cross section agrees well with other ISR experiments, especially with experiment R806 [ANA82]. The R108 measurements are somewhat lower than ours, but the high \mathbf{p}_{T} R108 values follow the trend for high \mathbf{p}_{T} values. We compared our photon cross section results with QCD perturbative predictions of Aurenche et al. [AUR88] and Contogouris et al. [ARG87]. Our best agreement comes using Duke & Owens [DUK84] set I of structure functions and when bremsstrahlung is neglected (Due to our cleaning cuts our cross section will be strongly biased towards non-bremsstrahlung events).

We can put some constraints on the gluon structure function of the nucleon and the value of the strong coupling constant $\Lambda_{\overline{MS}}$. Due especially to our systematic errors we cannot rule out Duke & Owens set II definitively. It can be said, though, that given a gluon structure function of the form:

$$x \cdot G(x, Q_0^2) \propto (1 - x)^{\eta}$$
 (VI-z)

we strongly favor a value of η between 5 and 6 (slightly softer than Duke and Owens set I value) and a value of $\Lambda_{\overline{MS}} \leq$ 200 MeV.

We also studied the associated particles of the direct photon events. There are signs that the QCD predicted direct photon event structure is present in the data. The azimuthal angle distribution of associated particles, when comparing direct photons and meson triggers, showed an excess of associated particles in the trigger hemisphere for the neutral meson triggers with \mathbf{p}_T greater than 6 GeV/c. Due to the method used to obtain the sample, this study did not show significant differences for low \mathbf{p}_T triggers. The differences are more manifest at high \mathbf{p}_T where the sample is richer in direct photons. The away jet charge ratio shows a statistically weak trend towards the QCD predictions.

We conclude that the agreement between our data and the QCD predictions, including second order calculations, were very good. Taking our data in conjunction with all other measurements we can be confident in using the QCD predictions to extrapolate direct photon properties for future experiments in different energy regimes. There are already various "third generation" experiments taking data that will test further the prediction of more precise QCD calculations [FER86].

APPENDICES

APPENDIX A

Single Photon Background from Neutral Meson Decays

Many of the single photon triggers in our data are caused by neutral meson decays to two or more photons where only one of the photons succeeded in passing the requirements imposed by the geometrical acceptance or the analysis cuts. Therefore, the single photon sample extracted from our data is a mixture of direct photons and single photons produced by neutral meson decays.

Neutral mesons decay very quickly to a combination of photons and mesons of lower masses. The least massive neutral meson, the π° meson, decays to two photons with a branching ratio of almost 99% and with a lifetime of only 0.87×10^{-16} seconds. It is by far the most important cause of background in the p_{T} range of this study. Neutral Meson Branching Ratios were taken from the particle data tables [PDT86]. Production Ratios were taken from the literature [BUS76a,ALP75,KOU80 and DIA80] and were assumed to be all independent of p_{T} . After candidate meson decays were selected they were allowed to decay through the detector simulation Monte Carlo described in Appendix D to find out if, in the conditions of our measurements, they produced a significant yield

Table A-1: Neutral Meson Decays.

1	2	က	4	2	9	7	8
particle	mass GeV	$\frac{prod./\pi^{\bullet}}{\sigma}$	decay	# of photons	branching ratio	σ br./ $_{\pi^{m o}}$	% in the sample
π°	.135	1.	ÅÅ	2	1.	1	61.4
ىل	.549	• 55	ÅÅ	2	38	.209	12.8
μ	.549	.55	иии	9	08.	.165	10.1
, N	.498	.40	υυ	4	.31	.124	7.6
ത	.783	.50	μγ	3	60*	.045	2.8
ىلا ,	.957	1.	ນ ນ ໄ	9	.084	.084	5.2

of s

func

the

prod

prod

two

the

inst

the

of t

"all

or:

This

of single photon triggers. The contributions were calculated as a $\text{function of } p_T \text{ of the triggering photon.}$

Table A-1 shows the neutral mesons chosen as contributions to the background. The production rates are given in relation to the π^o production. The last column gives the fraction of each neutral meson production to the sum of all the six mesons considered. The K_S^0 decays to two π^o with a rather long lifetime of 0.89×10^{-10} seconds; however for the purpose of our analysis we have assumed that all the decays occur instantaneously after being created in the proton-proton reaction, at the vertex of the event.

To calculate the ratio of $\pi^{\circ}\text{-mesons}$ to all mesons we assume that "all" includes all neutral mesons of table A-1, so that, adding column 7 of the table:

"all mesons" / π° -mesons=

$$1. + .209 + .165 + .124 + .045 + .084 = 1.627$$

or:

$$\pi^{\circ}$$
-mesons/ all mesons = 0.615

This is the ratio of production introduced in section 10 of chapter V.

APPENDIX B

Neutral Meson Decay Kinematics

Two-body Decays.

Let us consider the two-body decay $M \to A + B$. Figure B-1 defines the kinematics of the decay in the neutral meson center of mass and in the laboratory frames. If the neutral meson has zero spin (as π° , η° and K_{s}^{0}) the angular distributions of the decay particles in the center of mass frame are uniform in solid angle.

Let us take as an example the decay $\pi^{\circ} \rightarrow \Upsilon\Upsilon$, the most important background decay. The Lorentz transformations between the center of mass (CM) frame (π° rest frame) and laboratory (LAB) frame of the four momenta of the photons, as defined in figure B-1, are given by (ignoring the Z coordinate which is unaffected by the boost):

$$\begin{vmatrix} 1 & 0 & 0 \\ 0 & E/m & -p/m \end{vmatrix} \cdot \begin{vmatrix} (m/2) \cdot \sin \theta \\ (m/2) \cdot \cos \theta \end{vmatrix} = \begin{vmatrix} E_{\gamma^1} \cdot \sin \phi_1 \\ E_{\gamma^1} \cdot \cos \phi_1 \end{vmatrix}$$
 for photon 1

i gare

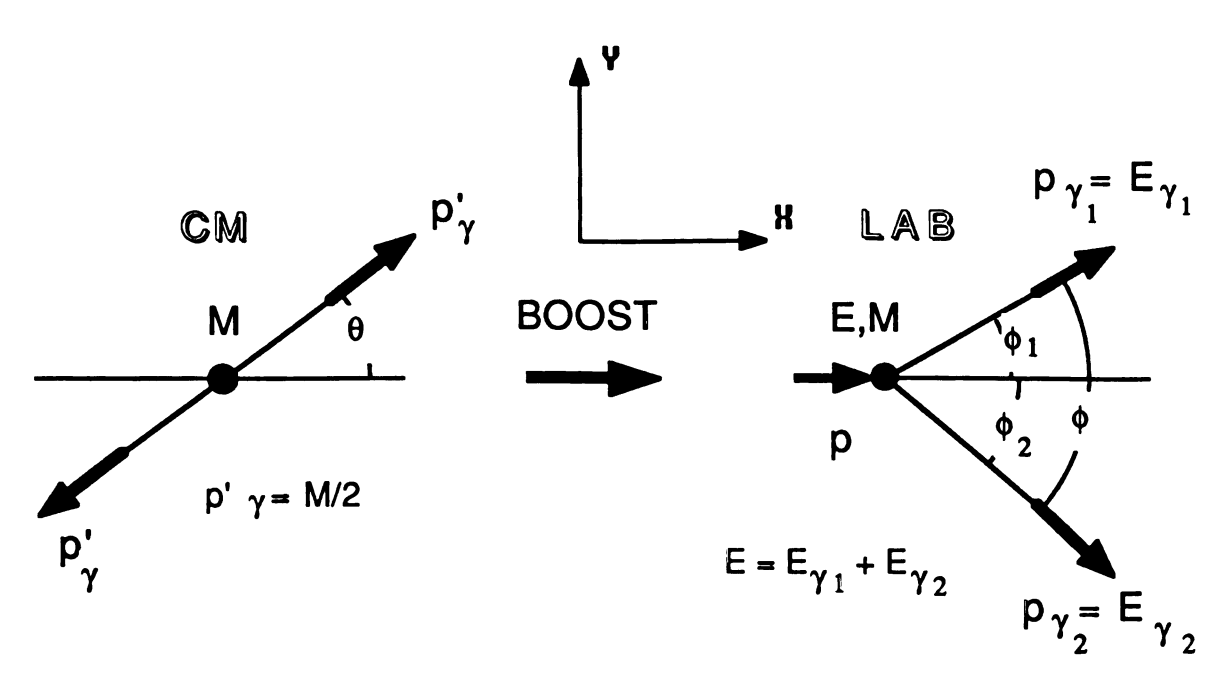
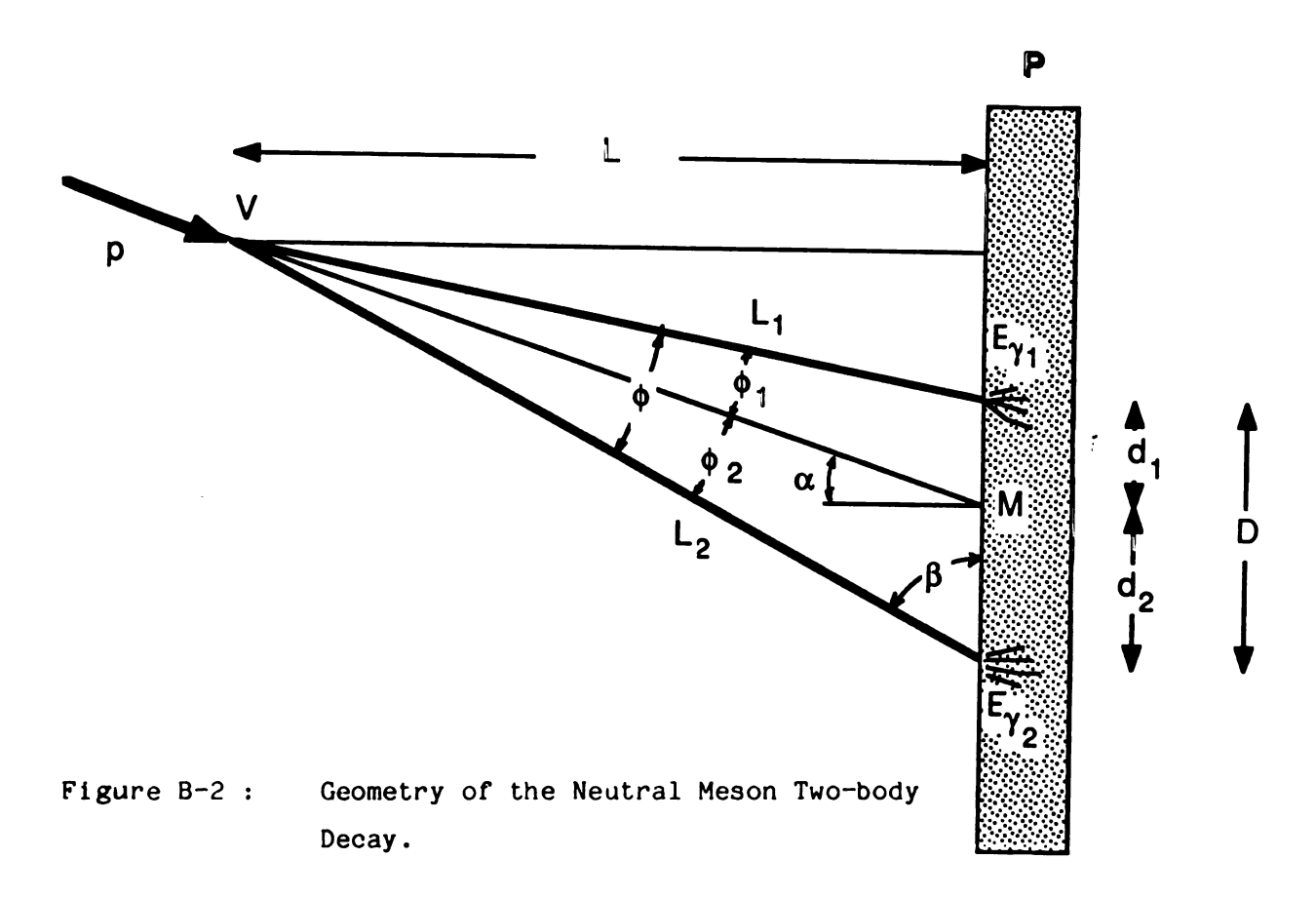


Figure B-1: Neutral Meson Two-body Decay Kinematics.



and

0 1

where

energy the LA

the me

respec

and

$$\begin{vmatrix} 1 & 0 & 0 \\ 0 & E/m & -p/m \end{vmatrix} \cdot \begin{vmatrix} -(m/2) \cdot \sin \theta \\ -(m/2) \cdot \cos \theta \end{vmatrix} = \begin{vmatrix} E_{\gamma^2} \cdot \sin \phi_2 \\ E_{\gamma^2} \cdot \cos \phi_2 \end{vmatrix}$$
 for photon 2

where m is the mass of the neutral meson, p and E the momentum and energy in the LAB system; EY_1 and EY_2 are the energies of the photons in the LAB frame and ϕ_1 and ϕ_2 the angles of the photon momenta respect to the meson momentum in the LAB frame. θ is the angle of the photon with respect to the boost in the CM frame.

That produced the equations:

$$(m/2) \cdot \sin \theta = E_{\gamma 1} \cdot \sin \phi_1$$
 (B-a)

$$(E/2) \cdot \cos \theta + p/2 = E_{\gamma 1} \cdot \cos \phi_1$$
 (B-b)

$$(p/2) \cdot \cos \theta + E/2 = E_{\gamma 1}$$
 (B-c)

$$-(m/2) \cdot \sin \theta = E_{\gamma 2} \cdot \sin \phi_2$$
 (B-d)

$$-(E/2) \cdot \cos \theta - p/2 = E_{\gamma^2} \cdot \cos \phi_2 \qquad (B-e)$$

$$-(p/2) \cdot \cos \theta + E/2 = E_{\gamma^2}$$
 (B-f)

Since
$$m^2 = E^2 - p^2$$

= $(E_{\gamma 1}^1 + E_{\gamma 2}^2)^2 - (p_{\gamma 1}^1 + p_{\gamma 2}^1)^2$

but:

there

or

Where

relat

:s eq

the as

$$m^{2} = E_{\gamma 1}^{2} + E_{\gamma 2}^{2} + 2E_{\gamma 1}E_{\gamma 2} - p_{\gamma 1}^{2} - p_{\gamma 2}^{2} - 2|p_{\gamma 1}||p_{\gamma 2}| \cdot \cos(\Phi)$$

but:

$$E_{\gamma 1}^2 = p_{\gamma 1}^2$$
 and $E_{\gamma 2}^2 = p_{\gamma 2}^2$

therefore:

$$m^2 = 2E_{\gamma^1}E_{\gamma^2}(1 - \cos(\phi))$$

or

$$m^2 = 4 \cdot E_{\gamma 1} \cdot E_{\gamma 2} \cdot \sin^2 (\Phi/2)$$
 (B-g)

where $\Phi = \phi_1 + \phi_2$, the angle between both photons in the LAB frame. Relation (B-g) can also be written as:

$$m^2 = (E^2 - p^2 \cdot \cos^2 \theta) \cdot \sin^2 (\Phi/2) \qquad (B-h)$$

The asymmetry of the decay is defined as

$$A = \frac{E_{\gamma^1} - E_{\gamma^2}}{E_{\gamma^1} + E_{\gamma^2}}$$

By (B-c) and (B-f), $A = (p/E) \cdot \cos \theta$, and for the extreme relativistic case p = E, therefore $A = \cos \theta$.

In the case of zero spin particles (such as π° 's and η 's), cos θ is equally probable (flat distribution) between -1 and 1, and therefore the asymmetry distribution is also flat.

Consider a neutral meson decay from a point $V:(x_0,y_0,z_0)$ at a distance L from the plane P, with the direction of \vec{p} (meson momentum) forming an angle α with the plane. Figure B-2 describes the geometry and the notation for the decay. We will calculate the general form for the distance (D) between the two photon hits at the plane.

We can write:

$$d_{2} = \frac{L_{2} \cdot \sin \phi_{2}}{\sin (90 + \alpha)} \qquad d_{1} = D - d_{2} = \frac{L_{1} \cdot \sin \phi_{1}}{\sin (90 - \alpha)}$$

therefore

$$D = d_1 + d_2 = \frac{1}{\cos \alpha} \cdot (L_2 \cdot \sin \phi_2 + L_1 \cdot \sin \phi_1)$$

or using (B-a) and (B-d):

$$D = \frac{m}{2} \cdot \frac{\sin \theta}{\cos \alpha} \cdot \left(\frac{L_2}{EY_2} + \frac{L_1}{EY_1}\right)$$
 (B-i)

From this relation we find that the minimum distance between photons ($\partial D/\partial\theta=0$) occurs for $\theta=0^\circ$ and $\theta=90^\circ$. But, for decays with both photons hitting the plane, not all the values of θ are allowed. From (B-h) we see that $E^2-p^2\cdot\cos^2\theta$ has to be ≥ 0 , therefore values of $\theta<\theta_L$ are forbidden, where θ_L is such that $\cos\theta_L=\frac{p}{E}$. Thus the only minimum is at $\theta=90^\circ$.

The distance between photons perpendicular to the direction of the meson \vec{p} is :

$$D_{T} = 1_{1} + 1_{2} = L \cdot (\tan \phi_{1} - \tan \phi_{2})$$

using (B-a)/(B-b) and (B-d)/(B-e):

 $\tan \phi_1 = (m \cdot \sin \theta)/(p - E \cdot \cos \theta)$; $\tan \theta_2 = (m \cdot \sin \theta)/(p + E \cdot \cos \theta)$ therefore:

$$D_{T} = L \cdot m \cdot \sin \theta \left(\frac{1}{p + E \cdot \cos \theta} + \frac{1}{p - E \cdot \cos \theta} \right)$$

=
$$2 \cdot L \cdot m \cdot \sin \theta \cdot \frac{p}{p^2 - E^2 \cdot \cos^2 \theta}$$
 (B-j)

but

$$D = \frac{1}{\cos \alpha} \cdot D_{T}$$

therefore:

$$D = \frac{2 \cdot L \cdot m \cdot \sin \theta}{\cos \alpha} \cdot \left(\frac{p}{p^2 - E^2 \cdot \cos^2 \theta} \right)$$
 (B-k)

Considering small angles (L is large compared with D, α = 0°) and the extreme relativistic case p = E, then :

$$D = \frac{2 \cdot m \cdot L}{E \cdot \sin \theta}$$
 (B-1)

and the minimum at $\theta = 90^{\circ}$ is :

$$D_{\min} = \frac{2 \cdot L \cdot m}{E}$$
 (B-m)

Figure B-3 shows D vs. E for the π° + YY and η° + YY decays in the energy range study for this dissertation.

To find the analytic form for the distribution of D for given values of m, L and E, we calculate the probability, $Prob(d\langle D)$, of d being less than D.

In the CM system
$$\frac{dP}{d\cos\theta} = \frac{dP}{dx} = 1/2$$
, calling $x = \cos\theta$,

0 < x < 1, for the forward photons.

From (B-1),
$$D(x) = \frac{2 \cdot m \cdot L}{E \cdot \sqrt{1 - x^2}}$$
 (B-n)

(relativistic π° , i.e. E > 1 GeV).

Therefore:

$$Prob(d < D) = \int_{\text{min}}^{D} \frac{dP}{dD} \cdot dD = \int_{\text{min}}^{D} \frac{dP}{dx} \cdot \frac{dx}{dD} \cdot dD = \int_{\text{min}}^{x(D)} \frac{dP}{dx} \cdot dx$$

$$Prob(d < D) \rightarrow \int_{\text{min}}^{x(D)} dx$$

from (B-n),
$$x(D) = \sqrt{1 - (E \cdot D/ 2 \cdot m \cdot L)^2}$$

then:

or

Prob(d < D) =
$$\sqrt{1 - (D_{min}/D)^2}$$
 (B-o)

This is the distribution of D shown in figure B-4.

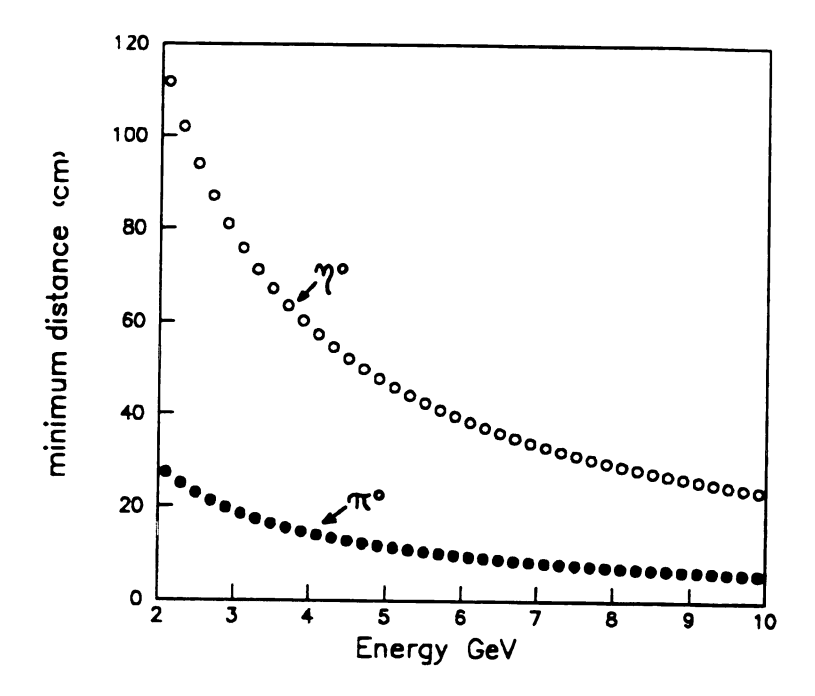


Figure B-3: D_{min} vs E for π° + YY and η° + YY.

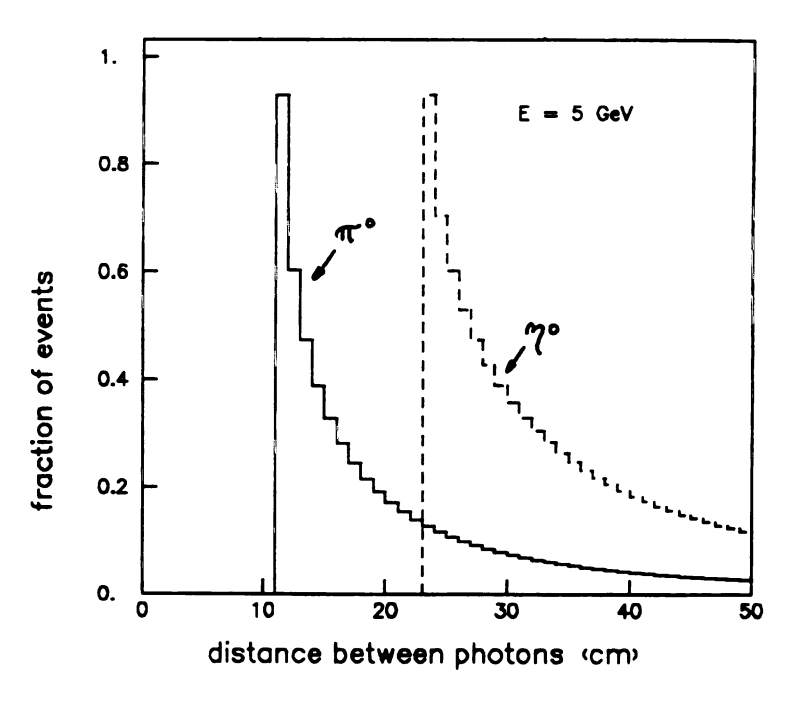


Figure B-4: Distribution of the Distance Between Photons for 5 GeV $\pi^{\,0}$ and $\eta^{\,0}$ Decays.



Another important quantity is the energy distribution of each photon in the LAB system, given by P(E): the probability of the photon having the energy E.

$$\frac{dP(E)}{dE} = \frac{dP}{d\Omega} \cdot \frac{1}{dE} \quad ; \quad \frac{dE}{d\Omega} = \frac{dE}{d\cos \theta \cdot d\phi} \quad \text{which is a constant as can be}$$

shown by differentiating equation (B-c). $\frac{dP}{d\Omega}$ is a constant for zero spin neutral mesons, therefore, $f(E) = \frac{dP(E)}{dE}$ is constant between zero and the maximum energy of $E_{\gamma} = E_{meson}$.

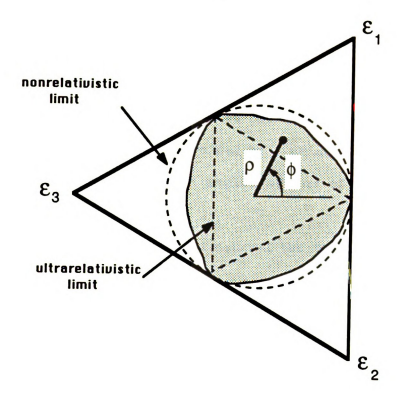
Most of the two-body decays considered in this dissertation were spinless mesons. However, the decay $\omega^o \to \pi^o \Upsilon$, involves the spin one ω^o meson. The distribution of the decay particles in the CM of ω^o frame is given by $(1 + \cos^2 \theta)$.

Three-body Kinematics.

The Dalitz plot [HAG64] is the most appropriate way to represent three-body decays as $\eta^o \to \pi^o \pi^o \pi^o$ and $\eta^* \to \eta^o \pi^o \pi^o$. The Dalitz plot is shown in figure B-5.

We assumed that these decays were just controlled by the available phase space. Therefore the only constraints in the decay were given by the conservation of energy and momentum:

$$\varepsilon_1 + \varepsilon_2 + \varepsilon_3 = Q = M - (m_1 + m_2 + m_3)$$



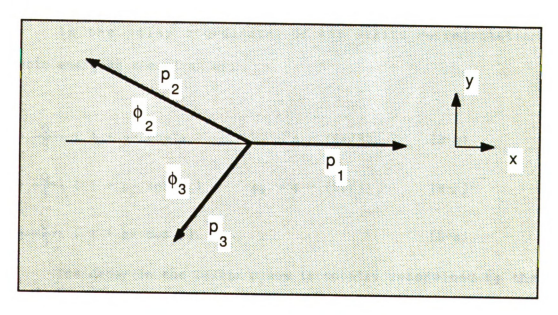


Figure B-5 : Dalitz Plot and Kinematics of Three Body Neutral Meson Decays.

$$\stackrel{\rightarrow}{p_1} + \stackrel{\rightarrow}{p_2} + \stackrel{\rightarrow}{p_3} = 0$$
 (B-p)

where ϵ_i are the kinetic energies and \vec{p}_i the momenta of the particles.

The last equation implies that the three decaying particles lie in a plane. The decay is determined by 5 parameters, chosen to be two kinetic energies and the Euler angles of one of the momenta in the parent frame.

Because of their vectorial nature, the momenta have to obey the relation:

$$\frac{p_1 - p_2 - p_3}{2 \cdot p_3 \cdot p_2} \le 1$$

which gives the boundary curve of the allowed region of the Dalitz plane.

In the polar coordinates of the Dalitz representation the kinetic energies are given by:

$$\varepsilon_1 = \frac{Q}{3} \cdot (1 + \rho \cdot \cos \phi_1)$$
 $\phi_1 = \phi - (2\pi/3)$ (B-q)

$$\varepsilon_2 = \frac{Q}{3} \cdot (1 + \rho \cdot \cos \phi_2)$$
 $\phi_2 = \phi - (2\pi/3)$ (B-r)

$$\varepsilon_3 = \frac{Q}{3} \cdot (1 + \rho \cdot \cos \phi)$$
 (B-s)

The decay in the Dalitz plane is totally determined by the two coordinates 0 \leq ρ \leq 1 and 0 \leq φ \leq 2π .

Then:

$$p_1^2 = 2 \cdot m \cdot \epsilon_1 + \epsilon_1^2$$

$$p_1^2 = 2 \cdot m \cdot \epsilon_2 + \epsilon_2^2 \qquad (B-t)$$

$$p_3^2 = 2 \cdot m \cdot \epsilon_3 + \epsilon_3^2$$

and in the plane of the decay (see Figure B-4) the momenta of the three particles are then:

$$(p_1, 0, 0); (p_2, p_2(1 - \cos^2\phi_2), 0); (p_3\cos\phi_3, -p_3\sin\phi_3, 0)$$

where:

$$\cos \phi_3 = \frac{p_2^2 - p_3^2 - p_1^2}{2 \cdot p_1 \cdot p_3} \qquad \cos \phi_2 = \frac{-p_1 - p_3 \cdot \cos \phi_3}{p_2}$$
(B-u)

Given the Euler angles $\alpha,\;\beta,\;$ and Υ of $\overset{\rightarrow}{p_1}$ the decay is totally defined.

Appendix C

Shower Simulations (EGS Monte Carlo)

As part of the data analysis we needed to know the characteristics of single photons in the energy range from 0.5 to 10 GeV in our detector. We had a sample of well identified photons from η° decays (Appendix E) in the range from 0.5 to 4 GeV.

To simulate the electromagnetic cascades (showers) produced by a single photon in our detector, we used the standard code developed by Nelson et al. [NEL85] at SLAC called EGS (Electron-Gamma Shower). Using its IV version (EGS4).

The EGS4 code is explained in the SLAC report 265. It is a "general purpose package for the Monte Carlo simulation of the coupled transport of electrons and photons in an arbitrary geometry for particles with energies above a few keV up to several TeV". I will explain here only the special characteristics of our EGS4 running, our geometry and materials; refering to the SLAC report for the description of the EGS simulation itself.

We were particularly interested in transverse shower shapes as observed in the strip chambers. The chambers were sensitive to very low

energy δ rays. Therefore, our simulation gave great attention to the production and transport of charged particles of low energy.

EGS4 allowed energy cut-offs as low as 10 KeV correcting some errors in the former EGS3 code low energy interactions, and introducing Rayleigh scattering. EGS4 also allowed us to include Landau fluctuations in the active region of the strip chamber, as well as the ability to change the low energy electron transport algorithm (see PRESTA below).

Landau fluctuations were added simply by replacing the energy fluctuations macro with a call to a subroutine, for energy deposition in the active region of the strip chamber. In this subroutine the energy deposited was fluctuated according to a Landau distribution. Even for electrons with kinetic energy as low as 30 KeV the thickness of the strip chambers still made the Landau distribution the correct one. If the resulting fluctuated energy was greater than the charged particle cut-off of 30 KeV, a new attempt to fluctuate the energy was made, since then, EGS4 would simulate new depositions.

Since it was the shower shapes that interested us, the path of charged particles was of great importance. With these low cut-off energies, EGS4 did not do a good job of transporting charged particles. To improve it we added the Parameter Reduced Electron-Step Transport Algorithm (PRESTA) [BIE87]. This replaced the Fermi-Eyges multiple scattering theory which EGS4 used (and which worked well at energy cut-offs above 40 MeV), with the Moliere scattering theory which allowed the use of large step sizes. Using PRESTA, there was no longer a noticeable dependence on the electron step-size. PRESTA also included a lateral correlation algorithm to account for large steps (in EGS4 the step-size is restricted such that these corrections are negligible). Finally, a

new boundary crossing algorithm was emplyed. This requires a particle to cross a boundary if its actual path did so even if the starting and ending points of the step were on the same side of the boundary.

The detector geometry was simulated from outside of the B counters through the end of the back glass, since only photons that had not showered before the front glass array were of interest. All materials were considered to be of finite extent in X and infinite extent in Y and Z.

The regions considered in the simulation are indicated in figure C-1. All regions are formed of isotropic and homogeneous materials. In the simulation of the strip chamber we decided not to include the Kapton or Mylar, since they only contributed 0.2 % of the total strip chamber radiation length, which we believe is of the order of the uncertainty of the thickness of the Epoxy layer. In addition we did not include the anode wires, support wires or spacers in the active region of the strip chamber nor did we use Styrofoam. Instead we replaced that material with Argon gas, since the open cell of the Styrofoam made that region mostly Argon. The 70-30 Argon-Ethane mixture was simulated by pure Argon.

The materials are defined as follows:

Air: 78% of Nitrogen gas and 21% of Oxygen gas by volume at 1 atm and density of 1.29.10⁻³ g/cc

Iron: Elemental Iron standard density, 7.86 g/cc, [CRC74]

Lead Glass: Relative amount of atoms by weight of 51.1 Pb, 25.97 O, 18.2 Si, 3.23 K, and 1.33 Na at a density

of 4.08 g/cc

Argon: Elemental gas [CRC74] at 1 atm density of

EGS IV + PRESTA

Detector Geometry

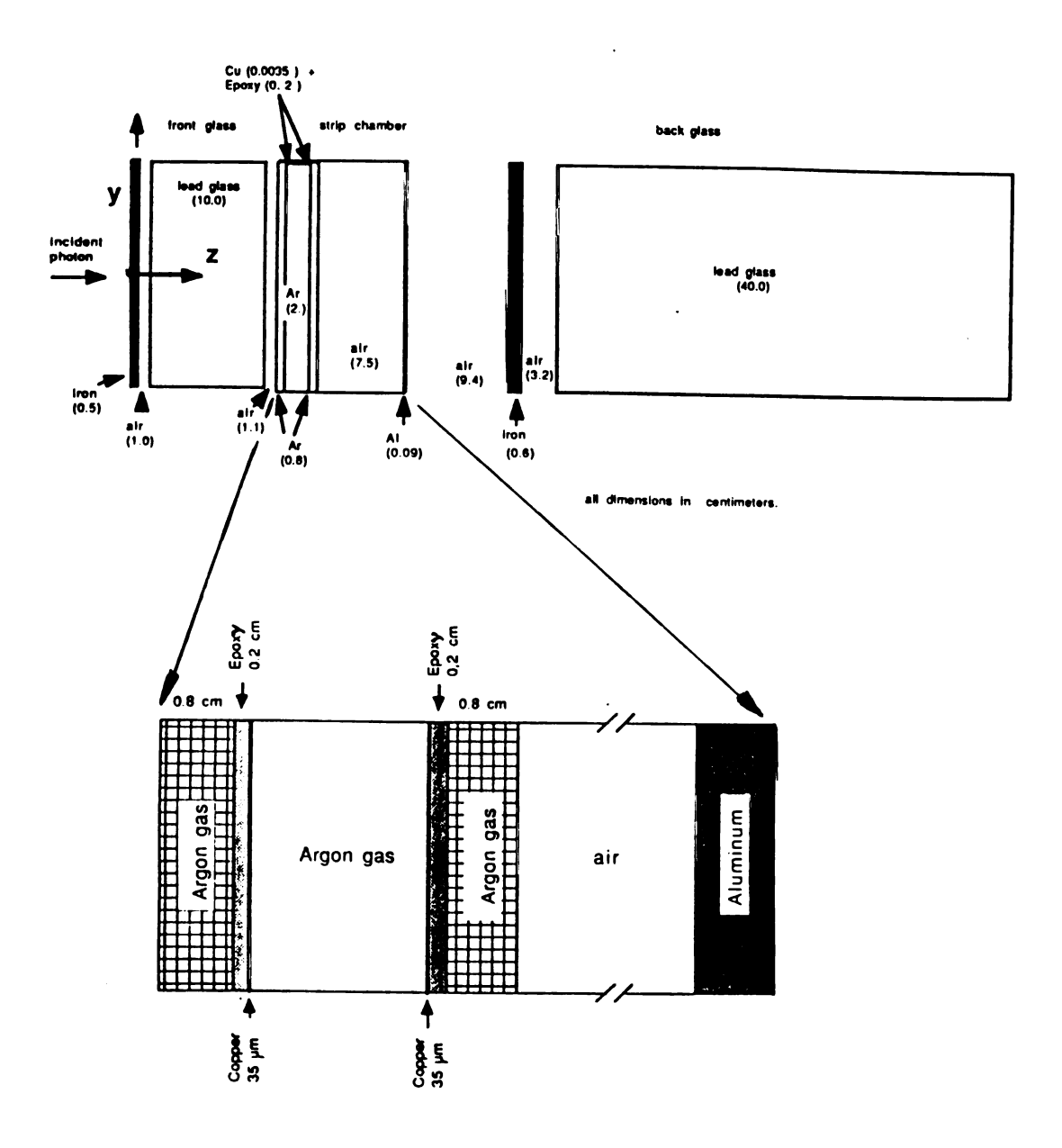


Figure C-1: EGS4 Detector Geometry.

 $1.78 \cdot 10^{-3}$ g/cc.

Epoxy: A compound of $C_{39}-H_{52}-O_{11}$ and a density of

1.14 g/cc.

Copper: Elemental Copper, standard density, 8.93 g/cc, [CRC74].

Aluminum: Elemental Aluminum, standard density, 2.70 g/cc, [CRC74].

The incident photon started in the front face of the iron, in front of the front glass, in the positive direction of X at an angle with the normal to the surface randomly chosen according to a fit of a distribution of incident angles measured from the single gammas of the trigger data. The fit gives: $(20 \cdot \arccos [1-2 \cdot \operatorname{randomnumber}]/3)$. The angle ϕ is chosen randomly between 0 and 2π . The initial Y and Z coordinate was randomly chosen in the range -0.5 to 0.5 cm to avoid any systematic bin edge effects in the histograms (the histograms were bin red in one cm. bins).

Particles were transported through the 19 regions defined in figure C-1. Any shower particle exiting the rear of the back glass had all of its energy deposited in the air behind it. The importance of considering the materials after the strip chamber for the shower shapes in the chamber was shown to be relevant due to an important albedo effect. Especially, low energy photons produced in the back glass or the iron between glasses and emitted backwards could initiate showers still detectable in the strip chamber.

Particles were transported until the particle total energy fell below a cut-off. For photons that cut-off was set at 500 keV and for

^{ch}arged particles it was 541 keV (30 keV of kinetic energy). These cut
^{offs} are rather arbitrary and were fixed after some trials with

^qtherent values, choosing the one than best fit the η^o trigger data

Tho ton σ_t distributions at 2 GeV.

Any particle produced with an energy below the cut-off was approximated by a local energy loss at the beginning of the step. In the active region of the strip chamber, however, this energy was distributed uniformly in millimeter increments along the straight line path of the particle.

For the lead glass regions, where the energy deposited is measured by the Cerenkov light produced, only charged particles up to the Cerenkov cut-off value (index of refraction = 1.67) of 127 keV (kinetic energy) were considered in calculating the amount of energy measured by the lead glass.

A photon's shower can be fully contained in the front glass or it may not begin showering before passing through the strip chamber. The se effects are important in determining if low energy photons of neutral meson decays will be detected in the strip chamber and back glass. Special EGS runs were done at energies as low as 0.25 GeV with a photon total energy cut-off of 30 keV (allowing photons leaving the front glass to create charged particles in the strip chamber). This probability for photons to produce no signal in the strip chamber was measured as a function of incident photon energy. Table C-1 gives the number of events for each of the incident energies.

The normalization of energy deposited in the Argon gas to strip

Chamber pulse height was done at 2 GeV. In order to minimize any

Table C-1: EGS4 runs.

Incident photon energy GeV	photon GeV	.25	.50	75	-	1.5 2	2	က	4	5	9	7	8	10
number of events	r ts	2000	CU	2000	1000 2000 1000 1000	1000	1000	1000 1000 1000 1000 1000	1000	1000	1000	1000	900	009

Hi qu al di en po re Эľ Se

١,

differences between the EGS simulated events and the sample of single photons from resolved η° 's, the 2 GeV EGS events were run with incident energies distributed in the same way as in the single photon sample. In runs at other energies, all incident photons had the same energy.

The most important information extracted from the EGS simulation entered directly in the analysis in the form of the transverse shape of the energy deposited for the shower traversing the strip chamber. Histograms were made to look at the transverse profile of three quantities, the number of particles (separated into charged particles, all particles and particles moving in the positive and negative X direction), the distance traveled in crossing the strip chamber and the energy deposited in the strip chamber. These last energy weighted position diagrams, taken in bins of 1 cm were used as a model for the response of the chambers. In addition the energies measured in the front and back glass were used to calculate the ratio front/(front+back), and the energy deposited in the iron plates between glass arrays was used to correct the energy measured in the glass. All this information was store for each individual event.

No effort was made to simulate the Cerenkov light propagation and collection in the Cerenkov counters so the agreement between data and simulation in the ratio Front/All must be seen as approximate (see section V-9).

Ξà

ācci

Appendix D

Neutral Meson Decay Monte Carlo

A multi-purpose simulation for the decay of neutral mesons through the detector was written to assist in the data analysis. Three main outputs were extracted from this simulation. After trigger and cut simulations were applied, positions at which photons struck the strip chambers and their measured energy were calculated. With this information and the pulse height distributions from EGS, it was possible to calculate $\sigma_{\rm t}$ for each multi-photon event. Secondly, the number of single photons produced by neutral meson decay was extracted as the ratio of single to multi-photons in each $\rm p_T$ bin. Finally, the total acceptance of the detector for neutral mesons was extracted by comparing input and output in the simulation.

All the neutral mesons mentioned in Appendix A were run independently and, later, their results were combined. To combine the results the rates and initial conditions had to be considered for each case to calculate the total number of events to run. Then the events accepted were simply added linearly.

For each event a single neutral meson was generated in the center of mass of the ISR. The angle ϕ was chosen randomly in the interval $\Delta \phi = \pm 0.6$ rad and the rapidity y was also chosen randomly in the range $\Delta y = \pm 0.8$. The transverse momentum was chosen randomly but according to the total neutral meson cross section published by the experiment R108 [ANG78]. The absolute rate was scaled from the π^0 rate (Appendix A) by the branching ratio and cross section. The vertex of the event was taken from a flat probability distribution within a diamond form in the plane X-Z (long axis: 85 cm, short axis: 11 cm) and Y was taken = 0. This defined the parent four momentum in the CM-ISR frame.

All decay photons were first defined in the rest frame of their parents. Then, transformed to obtain the photon four momenta in the laboratory frame. The kinematics of the decays were discussed in appendix B. For example, in the case of the decay $K_S^0 \to \pi^0\pi^0 \to \gamma\gamma\gamma\gamma$, each of the photons four-momenta satisfies the following matrix relation:

 $Q_{CM-p} = B_{\pi} \cdot R_{\pi} \cdot B_{K} \cdot R_{K} \cdot B_{ISR} \cdot Q_{LAB} = M \cdot Q_{LAB}$ with $M = B_{\pi} \cdot R_{\pi} \cdot B_{K} \cdot R_{K} \cdot B_{ISR}$ where B are Lorentz boosts, R are 4-dimensional rotations and Q_{LAB} and Q_{CM-p} are the 4-momenta of the photons in the LAB and parent CM respectively. The four-momentum of the photon in the laboratory is found by inverting the matrix M,

$$Q_{I,AB} = M^{-1} \cdot Q_{CM-D}$$

The positions of photons at the back glass and strip chambers were calculated from their LAB four-momenta. The first cut requires that

at least one photon position lies inside the geometric acceptance of the back glass.

A simple clustering algorithm was applied to all the photons in the back glass. Photons were said to belong to the same cluster if their distances in Y and Z were less than 30 cm, the value extracted by considering π° and η° merging in the η° trigger data. The only unit of analysis became now the cluster, formed by single or multi-photons. The 4-momenta of the clusters were calculated adding the 4-momenta of all contributing photons. Clusters with energies below 0.15 GeV were rejected. Then the energy deposited was smeared using the resolution relation measured at the PS [ANG82]:

 $E_{smeared}$ = {1+ 0.05•R1}•{E+ R2•(0.004•E+ 0.43• \sqrt{E})}, where R1 and R2 are two random numbers between 0 and 1. As a consequence, positions of multiphoton clusters were also smeared since they were derived from the energy measurements.

The trigger simulation accepted the event if at least one smeared cluster energy was more than 3.4 GeV for the inside or 4.5 GeV for the outside.

The same series of cuts applied in the data analysis were then applied, in the same order, as discussed below. Table D-1 shows the list of cuts and their respective acceptances. Since we did not simulate associated particles, cuts relating to these particles were not applied.

When more than one cluster was found in the back glass the Position of the second cluster was required to be outside a square of \pm 20 cm around the triggering cluster. If still there were two clusters, the most energetic one only was considered. Only clusters with their

INSIDE						
4.5-10 GeV/c	π-21	17 ~ _u	η - -61	K1	w•3€	1,-61
Back Glass geom. acceptance (1)	0.26	0.35	0.49	0.42	94.0	0.57
Trigger (2)	0.82	0.32	0.02	0.14	0.37	40.0
Only one cluster in Back Glass (3)	0.96	0.45	0.22	0.20	0.99	0.10
Front Glass geom. acceptance (4)	0.53	0.47	0.47	84.0	0.49	0.46
Front Glass fld.	0.65	19.0	0.61	89.0	0.65	09.0
B-veto (6)	0.33	0.54	91.0	0.31	0.23	0.52
Shower reaching the Strip Chamber	0.47	0.96	0.95	0.97	0.99	0.99
Front/All cut (8)	0.95	0.45	0.45	0.45	0.45	0.45
No Strip Chember Clusters (9)	860	96.0	95.0	81.0	84.0	3 K.0
Totel	0.021	100.0	0.0001	100.0	0.01	0.0003

			OUTSIDE							
-36	ח'-בוֹ		4.5-10 GeV/c	π-21	η*-24	η*.επ	K44	w~33	μ-61	
-	0.57		Back Glass geom.	0.45	0.53	89.0	0.61	0.56	0.74	
72	0.04		Trigger (2)	0.88	0.58	0.12	0.38	0.50	0.44	
44	0.10		Only one cluster in Back Glass (3)	0.97	0.21	80.0	0.11	8.	0.04	
<u>-</u>	0.46		Front Glass geom.	0.54	0.50	85.0	0.46	0.61	85.0	
٠Ç	09.0		Front Glass fid.	99.0	99.0	9.65	0.65	79.0	0.65	
23	0.52		B-veto (6)	0.34	0.54	0.26	0.30	0.26	0.50	
-6	0.99		Shower reaching the Strip Chamber	86.0	0.96	0.44	0.99	8.	6.8	
15	0.45		Front/All cut (8)	0.90	08.0	0.90	0.00	0.90	0.40	
••	3 K:0		No Strip Chamber Clusters (9)	0.49	0.99	96.0	99.0	0.44	0.99	
-	0.0003		Total ',	240.0	0.010	0.0005	0.00	0.026	ት000.0	
		l								

Table D-1: Values of the Simulated Cut Acceptances in the Neutral Meson Decay Monte Carlo.

front glass positions inside a fiducial region 13 cm from the border of the front glass were accepted. A simulation of the B veto cut was then applied (as discussed in section V-6).

The next cut simulations used input from the EGS runs. A random number was compared with the probability (computed in EGS) that a photon shower of this energy produced nothing observable in the Strip Chamber. The Front/All cut of .14 applied to the data was applied to the Front/All calculated for each event (see section V-9).

The algorithm for clustering pulse height information in the strip chambers was applied, included some pulse height cuts that could reject events (called "00 events": no-Y, no-Z clusters).

Events passing all these cuts were then taken as observed. These events were used to calculateee $_m$ (neutral meson acceptance), Y/YY $|_m$ (ratio of single to multiphotons produced by neutral meson decays) and were used to fill the σ_+ plots.

Appendix E

The nº Trigger Data

The only source of well-identified single photon candidates in the detectors were decays of η° + YY and π° + YY . For a good identification a mass determination is indispensible. Therefore the photons have to be separated in the back glass in order to get both energy measurements.

We had two separate periods of η° trigger running, both with the same geometry as the normal direct photon trigger; in Spring 1983 and in December 1983. From the Spring '83 run we had an integrated luminosity of L = 9.9×10^{36} cm⁻² for the outside and L = 9.2×10^{36} cm⁻² for the inside trigger. Two condensed tapes (CON) were produced: one only with inside events and another with only outside events. The number of events was 26536 inside and 45636 outside. Only one third of these events had vertices and most events had only one good cluster.

The main features of the Spring'83 analysis are the following: the hardware trigger consisted of "glass singles" events where either side could trigger. B counters in veto were used.

The symbolic expression for the trigger is:

where A refers to the A counters, B to the B counters and ${\bf G}_{\bar{\bf I}}$ and ${\bf G}_{\bar{\bf O}}$ to the back glass arrays (inside and outside).

The DST filter accepted events with one or more good clusters. The good cluster selection included: energy of cluster ≥ 0.12 GeV; events inside the front glass acceptance; total front glass energy greater or equal to 0.02 GeV, and a B veto passed. Events with two or more good clusters were accepted without further energy cuts. One-cluster events were accepted only if their energy were greater or equal to 3 GeV inside or 3.5 GeV outside. No additional filtering was done in the CON tape stage.

The December'83 data was taken with the inside retracted geometry at the same time as the normal direct photon trigger was being taken. No outside η^o data was taken at this time. A double glass trigger hardware configuration was utilized that required two cluster triggers having a summed energy \geq 3.5 GeV. The DST filtering of these η^o data required two clusters passing a B veto test with energies summing to 3 GeV . Direct photon triggers passing these requirements were also kept. No front glass energy cut was made for the Dec '83 η^o data and no additional cuts were applied in making the CON tape. This CON tape contains 7304 events.

The mass spectra were calculated from samples of events with two good back glass clusters. These events passed a vertex test and a NaI-trigger test similar to the ones used in the direct photon analysis. In

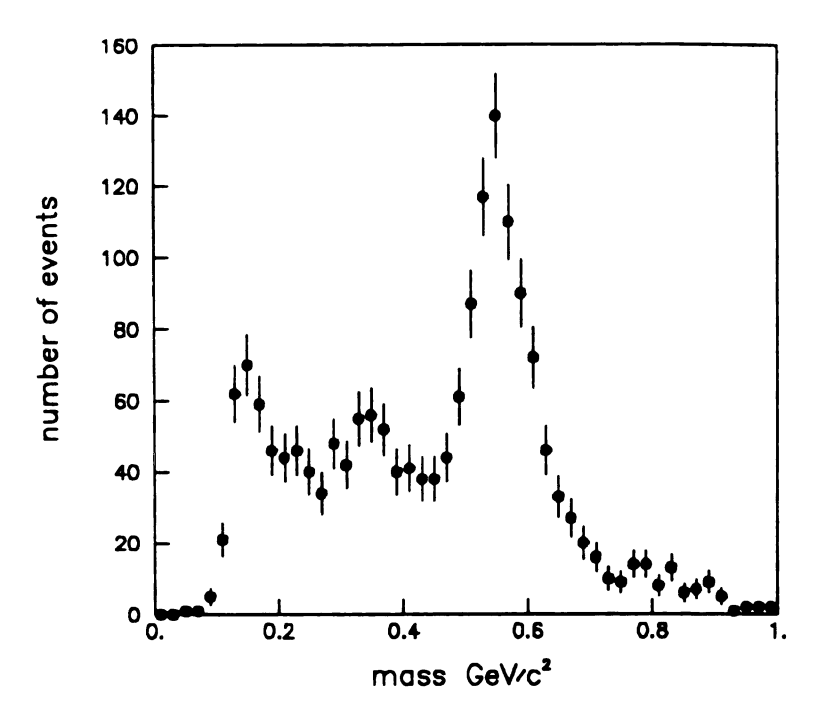


Figure E-1 : η° Mass Spectrum.

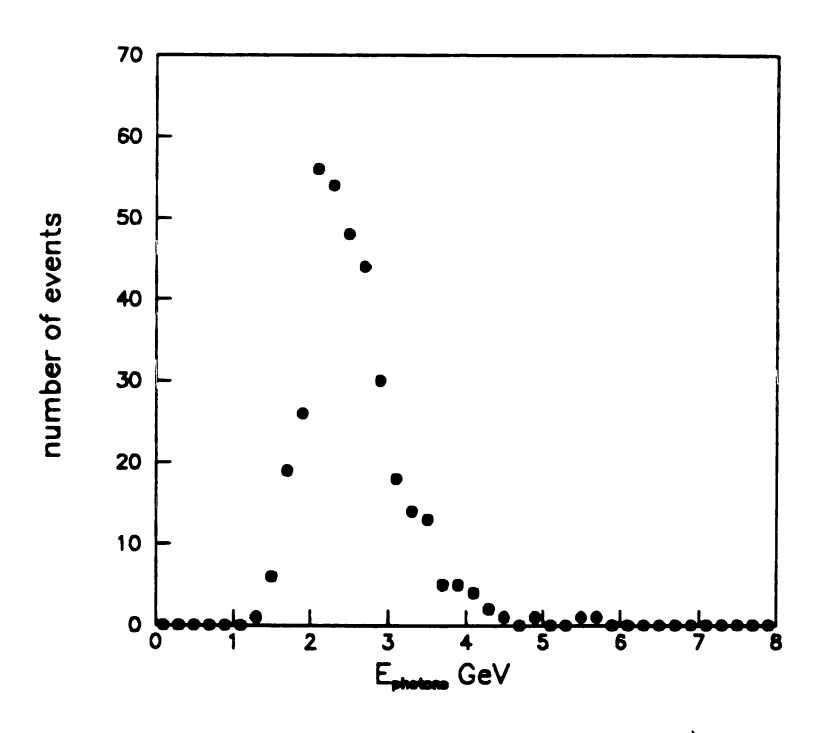


Figure E-2: Energy Spectrum of Single Photons from $\eta^{\,o}$ Decays.

addition events with a number of back glass clusters less than two were rejected. Events with front glass cluster "only" and with excessive "unclustered" energy were also rejected. From events with exactly two clusters a mass was calculated. The mass spectrum is shown in figure E-1.

The best η° candidates were extracted from the mass band .48 \leq m \leq .62 GeV/c². An energy cut in the second energy cluster of the event (0.5 GeV for the inside, and 0.75 GeV for the outside) was also required.

Every η° event gave, then, two single photons. The single photon energy spectrum is shown in figure E-2. The glass and strip chamber information of these photons were stored in two "banks" (one from the outside and one from the inside) and each photon was indexed by its energy.

LIST OF REFERENCES

LIST OF REFERENCES

[AKE82]	Akesson, T. et al.; Phys. Lett. 118B(1982)178.
[AKE83]	Akesson, T. et al.; Phys. Lett. 123B(1983)367.
[AKE84]	Akesson, T. et al.; Nucl. Phys. B246(1984)408.
[AKE85]	Akesson, T. et al.; Phys. Lett. 158B(1985)282.
[AKE86]	Akesson, T. et al.; Z. Phys. C32(1986)491.
[AK077]	Akopdjanov, G.A. et al.; N.I.M. 140(1977)441.
[ALP75]	Alper, B. et al.; Nucl. Phys. B87(1975)19.
[ALT77]	Altarelli, G. and Parisi G.; Nucl. Phys. B126(1977)298.
[AMA78]	Amaldi, E. et al.; Phys. Lett. 77B(1978)240.
[ANA82]	Anassontzis, E. et al.; Z. Phys. C13(1982)277.
[ANG78]	Angelis, A.L.S. et al.; Phys. Lett. B79(1978)505.
[ANG80]	Angelis, A.L.S. et al.; Phys. Lett. 94B(1980)106.
[ANG81]	Angelis, A.L.S. et al.; Phys. Lett. 98B(1981)115.
[ANG82]	Angelis, A.L.S.; Oxford University, D. Phil. Thesis, 1982.

[ANG84a]	Angelis,	A.L.S.	et al.;	Phys.	Lett.	141B(1984)140.
----------	----------	--------	---------	-------	-------	----------------

[ANG84b] Angelis, A.L.S. et al.; Phys. Lett. 147B1(1984)472.

[APP86] Appel, J.A. et al.; Phys. Lett. 176B(1986)239.

[ARG84] Argyres, E. N. et al.; Phys. Rev. D29(1984)2527.

[ARG87] Argyres, E. N. et al.; Phys. Rev. D35(1987)1584.

[AUR84] Aurenche, P. et al.; Phy. Lett. 140B(1984)87.

[AUR85] Aurenche, P. et al.; Z. Phys. C29(1985)423.

[AUR86] Aurenche, P. et al.; Phys. Lett. 169B(1986)441.

[AUR87] Aurenche, P. et al.; Nucl. Phys. B286(1987)509.

[AUR88] Aurenche, P. et al.; Nucl. Phys. B297(1988)661.

[BAD86] Badier, J. et al.; Z. Phys. C31(1986)341.

[BAI86] Baier, R.; in The Quark Structure of Matter, pp.113, ed.

Jacob-Winter, World Scientific Publishing, Co., (1986).

[BAL80] Baltrusaitis, R.M. et al.; Phys. Rev. Lett. 44(1980)122.

[BEA74] Beale, J.S., et al.; N.I.M., 117 (1974)501.

[BEN83] Benary, O. et al.; Z. Phys. C16(1983)211.

[BER82] Berger, E. L.; Phys. Rev. D26(1982)105.

[BER87] Bernasconi, A., et al.; Preliminary Results on Inclusive Cross Section in pp collision at √s=24.3 GeV

from UA6 Experiment, Presented by M.-T. Tran, Proceeding of the Institute of the Europhysical Conference on High-Energy Physics, Uppsala, (1987).

- [BIE87] Bielajew, A.F. and Rogers, D.W.O.; N.I.M. B18(1987)165.
- [BLA88] Blair, R.; CDF Direct Photon Analysis. Talk given at the 7th Topical Workshop on Proton-Antiproton Collider Physics, Fermilab (1988).
- [BON87] Bonesini, M. et al.; Production of High Transverse Momentum Prompt Photons and Neutral Pions in Proton-Proton Interactions at 280 GeV/c, preprint CERN-EP/87-185.
- [BRE77] Breskin, A. et al.; N.I.M. 143(1977)29.
- [BRO75] Brodsky, S.J. and Farrar G.R.; Phy. Rev. D11(1975)1309.
- [BUR80] Buras, A.; Asymptotic Freedom in Deep Inelastic Processes in the Leading Order and Beyond. Rev. of Mod. Phys. 52(1980)199.
- [BUS73] Busser, F.W. et al.; Phys. Lett. B46(1973)471.
- [BUS76a] Busser, F.W. et al.; Nucl. Phys. B106(1976)1.
- [BUS76b] Busser, F.W. et al.; Nucl. Phys. B113(1976)189.
- [CAM78] Camilleri, L. et al.; A System of Cylinderical Drift Chambers in a Superconducting Solenoid. N.I.M. 156 (1978)275.
- [CHA70] Charpak, G. et al.; N.I.M. 80(1970)13.
- [CHA78] Charpak, G. et al.; N.I.M. 148(1978)471.

[CON81] Contogouris, A.P.S. et al.; Nucl. Phys. B179 (1981) 461.

[CON86a] Contogouris, A.P.S.; Optimal, Complicated and Unnatural Scales in Large -P_T Physics. McGill University Report, (1986).

[CON86b] Contogouris, A.P.S. and Tanaka, H.; Phys. Rev. D33 (1986) 1265.

[CON87] Contogouris, A.P.S. et al.; Phys. Rev. D35(1987)1590.

[COX82] Cox, B. et al.; Fermilab Report. 82/75-76-Exp.

[CRC74] CRC <u>Handbook of Chemistry and Physics</u>, R.C Weast ed. 55th edition, CRC Press (1974).

[DAR76] Darriulat, P. et al.; Nucl. Phy. B110(1976)365.

[DEM87] DeMarzo, C. et al.; Phys. Rev. D36(1987)8.

[DIA80] Diakonou, M. et al.; Phys. Lett. 89B(1980)432.

[DIC87] DiCiaccio, A. et al.; Jets, Direct-photons, W & Z production vs QCD in UA1. Proceedings of the Int. Europhysical Conference on High-Energy Physics, Uppsala, (1987).

[DIM78] Dimcovski, Z. et al.; Use of a Cathode Read-out Multiwire Proportional Chamber for Separation of Electromagnetic and Hadronic Showers, N.I.M. 156(1978)123.

[DOU84] Douiri, A.; Annecy Report LAPP-TH-100 (1984).

[DRE70] Drell, S.D. and Yan, T-M.; Phy. Rev. Lett. 25(1970)316.

[DRI82]	Drijard.	D.	et al.	: Z.	Phys.	C12	(1982)217.

- [DUK84] Duke, D.W. and Owens, J.F.; Phys. Rev. D30(1984)49.
- [DUK85] Duke, D.W. and Roberts, R.G.; Determinations of the QCD Strong Coupling α_s and the scale Λ_{QCD} . Physics Reports, 120(1985)275.
- [D084] DO Design Report, The DO Experiment at the Fermilab Antiproton-Proton Collider (1984).
- [EAD82] Eadie, W.T. et al.; Statistical Methods in Experimental Physics, North-Holland, 2nd reprint (1982).
- [ERS82] Erskine, G.A.; N.I.M. 198(1982)325.
- [ESC75] Escobar, C.O.: Nucl. Phys. B98(1975)173.
- [FAR76] Farrar, G.R. and Frautschi S.C.; Phys. Rev. Letts. 36 (1976)1017.
- [FER84] Ferbel, T. and Molson, W.R.; Direct Photon Production in High-Energy Collisions, Rev. of Mod. Phys. 56(1984)181.
- [FER86] Ferbel, T.; Acta Phys. Polonica, B17(1986)435.
- [GAT79] Gatti, E. et al.; N.I.M. 163(1979)83.
- [HAG64] Hagedorn, R.; Relativistic Kinematics, W.A. Benjamin, Inc., 1964.
- [HAL80] Halzen, F. et al.; Phys. Rev. D22(1980)1617.
- [HUB77] Hubner, K.; ISR Performance for Pedestrians, CERN 77-15 (1977).

[HUM83]	Humphries,	B.;	R110	internal	memo	#	105	(1983).
---------	------------	-----	------	----------	------	---	-----	---------

[HUM88] Humphries, B.; Michigan State University, Ph.D Thesis, in progress.

[JAC75] Jackson, J.D.; <u>Classical Electrodynamics</u>, 2nd edition, John Wiley & Sons, (1975).

[JAC80] Jacob, M.; <u>Jet Phenomena</u>. Techniques and Concepts of High-Energy Physics, ed. T. Ferbel, Plenum Press, (1980).

[JAM87] James, F. and Ross, M.; CERN Computer Center Program Library (GENLIB), long write-up D506, revised (1987).

[JOH75] Johnson, R.A.; University of California, Berkeley, Ph.D. Thesis (1975).

[KOU80] Kourkoumelis, C. et al.; CERN preprint EP/80-160.

[LEA82] Leader, E. and Predazzi, E.; An Introduction to Gauge
Theories and the 'New Physics'. Cambridge University
Press, (1982).

[LIN82] Linnemann, J.T.; R110 internal memo # 89 (1982).

[MAT84] Mathieson, E. et al.; N.I.M. 227(1984)277.

[MCL83] McLaughlin, M. et al.; Phys. Rev. Lett. 51(1983)971.

[MOR77a] Morpurgo, M.; N.I.M. 17(1977)89.

[MOR77b] Morpurgo, M. and Pozzo, G.; N.I.M. 17(1977)87.

- [NEL85] Nelson, W.R., Hirayama, H. and Rogers, W.O.; The EGS4
 Code System, SLAC-Project-265, (1985).
- [NIC82] Nickerson, R.B.; Oxford University, D. Phil. Thesis, (1982).
- [OWE87] Owens, J.F.; Rev. Mod. Physics 59(1987)465.
- [PDT86] Particle Data Group; Phys. Lett. 170B(1986).
- [PIU82] Piuz, F. el al.; N.I.M. 196(1982)451.
- [POR79] Pordes, S. H.; CCOR internal memo #387 (1979).
- [QUI83] Quigg, C.; Gauge Theories of Strong, Weak and Electromagnetic Interactions. Benjamin-Cummings, (1983).
- [REY81] Reya, E.; Perturbative Quantum Chromodynamics. Physics Reports 69(1981)195.
- [RUT11] Rutherford, E.; Phil. Mag. 21(1911)669.
- [SAU77] Sauli, F.; Principles of Operation of Multiwire Proportional and Drift Chambers. CERN Report 77-09 (1977); also in Experimental Techniques in High Energy Physics, ed. T. Ferbel, Addison-Wesley Publishing Co., (1987).
- [SAX85] Saxon, D.H.; Jet Fragmentation. Proceedings of the International Europhysics Conference on High-Energy Physics, Bari, (1985).
- [SIV76] Sivers, D.S.J. et al.; Phys. Rep. 23C(1976)1.
- [STE81] Stevenson, P.M.; Phys. Rev. D23(1981)2916.

[TRE85]	Treille, D.; Ha	rd Scattering of	Hadrons and Photons.
	Proceedings of	the International	Europhysics Conference
	on High-Energy	Physics, Bari, (19	985).

- [VAN86] Van der Graaf, H. et al.; N.I.M. A252(1986)311.
- [VAN68] Van der Meer, S.; Calibration of the Effective Beam Height in the ISR, CERN Divisional Report, ISR-PO/68-31, (1968).
- [YEL81] Yelton, J.M.; Oxford University, D. Phil. Thesis, (1981).
- [YND83] Yndurain, F.J.; Quantum Chromodynamics., Springer-Verlag, (1983).